UNIVERSITY OF SOUTHAMPTON

FACULTY OF PHYSICAL AND APPLIED SCIENCES

Optoelectronics Research Centre

Controlling light localization with nanophotonic metamaterials

Tsung-Sheng Kao

Thesis for the degree of Doctor of Philosophy

July 2012

UNIVERSITY OF SOUTHAMPTON

ABSTRACT

FACULTY OF PHYSICAL AND APPLIED SCIENCE

OPTOELECTRONICS RESEARCH CENTRE

Doctor of Philosophy

CONTROLLING LIGHT LOCALIZATION WITH NANOPHOTONIC METAMATERIALS

by Tsung-Sheng Kao

Light localization plays an important role in developing high resolution imaging and precision technologies in nanophotonics. In order to create and control nanoscale light localizations, this thesis has investigated into two research topics with different types of nanophotonic metamaterials: precise control of near-field light localizations and subwavelength light concentration beyond the near field.

For the first topic, (i) I have demonstrated for the first time that a planar fish-scale metamaterial can be used as a controllable template for nanoscale light localizations. By tuning the polarization and wavelength of an incident light beam, the positions of energy hot-spots on the landscape of the metamaterial can be efficiently controlled. Moreover, it has been found that the locations of the hot-spots show a high correlation with the nanostructure, the unit cell size, and the dipole absorption resonance of the fish-scale metamaterial.

In an array of discrete asymmetrically split-ring meta-molecules system, (ii) I have also demonstrated for the first time that the well-isolated subwavelength energy hot-spots can be created and positioned on the metamaterial landscape by the coherent control of a monochromatic continuous light beam with a spatially modulated phase profile. Due to the strong optically induced interactions between meta-molecules, a well-isolated energy hot-spot of a fraction of wavelength has been created. By simply tailoring the phase profile, the hot-spot positions on the metamaterial can be prescribed and moved at will from one meta-molecule to another in a digital fashion with an accurate moving step around $\lambda/2$. In my experiments, (iii) I have integrated a scanning near-field optical microscope and a spatial light modulator to demonstrate the coherent control process. Via this approach, an energy concentration on the nanoscale and accurate control of the energy hot-spots have been achieved.

For the second topic, based on optical super-oscillation, (iv) I have first created an isolated focused spot by using a super-oscillating binary masks with radially symmetric quasi-periodic arrangement of nanoholes. The well-isolated focused spot around 0.45 λ has been acquired in a wide field of view about 90 λ. (v) Discovering another exploitation of nanohole arrays, it has been shown that a quasi-periodic nanohole array can be used as a conventional lens with a high numerical aperture around 0.89.

Contents

List of Figures

DECLARATION OF AUTHORSHIP

I, Tsung-Sheng Kao, declare that the thesis entitled "Controlling light localization with nanophotonic metamaterials" and the work presented in the thesis are both my own, and have been generated by me as the result of my own original research. I confirm that:

- this work was done wholly or mainly while in candidature for a research degree at this University;
- where any part of this thesis has previously been submitted for a degree or any other qualification at this University or any other institution, this has been clearly stated;
- where I have consulted the published work of others, this is always clearly attributed;
- where I have quoted from the work of others, the source is always given. With the exception of such quotations, this thesis is entirely my own work;
- I have acknowledged all main sources of help;
- where the thesis is based on work done by myself jointly with others, I have made clear exactly what was done by others and what I have contributed myself;
- parts of this work have been published as the journal papers and conference contributions listed in Appendix C.

Signed: _____

Date: _____

Acknowledgements

I am very grateful to my supervisor, Prof. Nikolay Zheludev, for his inspiration and guidance through my academic research. I would like to thank Dr. E. T. F. Rogers for his help with experimental and calculation techniques. I would also like to thank all my collaborators, Dr. Y. Chen, Dr. S. D. Jenkins, and Dr. J. Ruostekoski for offering helpful discussions. For sample fabrications and experimental assistance, I would like to thank Dr. T. Uchino, J. Y. Ou and M. Ren. I would also like to thank V. Savinov for his design in one of the binary masks. A big thanks goes to all the people who have helped me on the journey of pursuing my PhD degree. I would also like to express my gratitude towards Prof. D. P. Tsai and his wife for their encouragement and my family for their support. Finally, I would like to especially thank my wife, my dearest princess, Chen-Yi. Without her, this work could not be finished.

1 Introduction

1.1 Motivation

With the rapid development of nanophotonics, there has been increasing attention on localizing and concentrating the optical energy of a light beam to form a subwavelength ($\ll \lambda$) focused spot. Thus, within the last few decades, a number of promising concepts of subwavelength optical field generation and detection have been widely proposed and experimentally demonstrated [1–10], some of which have made significant breakthroughs in biological specimen imaging and nanostructure fabrication [11–19]. Meanwhile, a great deal of effort has been made in controlling and manipulating focused subwavelength spots at will [20–31]. However, it is found that most of these techniques are restricted to certain wavelengths, limited nanosystems or fail to achieve nanoscale accuracy in optical manipulation.

To overcome the limitations above, this thesis will focus on manipulating characteristics of light and using various kinds of nanostructures, with the aim of easily and precisely creating and controlling nanoscale light localizations. Fundamental theories and experimental methods relevant to this theme will be discussed below. It is hoped that through this work, a new scheme of light localization can be developed and hence applied in practical areas such as super-resolution imaging [1–7,11–13,32–78], ultra-high density data storage [79–88], optical nanolithography [14–19, 89, 90] and nanoluminescent bio-assay labeling [91–93].

1.2 Light localization in the near field

1.2.1 Diffraction limit

In terms of subwavelength light localization, the first challenge encountered will be the diffraction limit [94], which is inherent in the nature of light and will affect the image resolution. The origin and impact of the diffraction limit are now discussed.

For an electromagnetic wave (EM wave) incident upon on a screen or a sample as in the diagram schematically shown in Fig. 1.1, the transmitted EM wave behind the screen can be given by

$$Ae^{i(\vec{\kappa}\cdot\vec{r}-\omega t)} = Ae^{i(\kappa_x X+\kappa_y Y+\kappa_z Z-\omega t)} \tag{1.1}$$

where A is the amplitude of the transmitted EM wave and $\vec{\kappa}$ is the wavevector, indicating the wave propagation direction [42, 95]. The wavevector $\vec{\kappa}$ has a value, $|\vec{\kappa}| = \kappa_0 = \sqrt{\kappa_x^2 + \kappa_y^2 + \kappa_z^2}$, where κ_0 is the wavenumber and κ_i are the wavenumber components associated with the wave propagation in the X, Y and Z directions. Therefore, the transmitted wave can be expressed again as follows.

$$Ae^{i(\kappa_x X + \kappa_y Y - \omega t)} e^{i(\kappa_z Z)} = Ae^{i(\kappa_x X + \kappa_y Y - \omega t)} e^{i(\sqrt{\kappa_0^2 - (\kappa_x^2 + \kappa_y^2)} Z)} \tag{1.2}$$

Along the Z direction, the types of wave propagation can be categorized as follows.

- **Propagating waves** ($\kappa_0^2 > \kappa_x^2 + \kappa_y^2$): κ_z is real, meaning that the transmitted waves have the form, $Ae^{i(\kappa_x X + \kappa_y Y - \omega t)} e^{i(\sqrt{\kappa_0^2 - (\kappa_x^2 + \kappa_y^2)}\, Z)}$. Such waves will propagate to the far-field region as propagating waves and can be captured in conventional optical systems.

- **Surface waves** ($\kappa_0^2 = \kappa_x^2 + \kappa_y^2$): $\kappa_z = 0$. The form of the wave propagation becomes $Ae^{i(\kappa_x X + \kappa_y Y - \omega t)}$. Only the waves with the wavenumber components κ_x and κ_y exist and form surface waves travelling on the interface between different media in the X and Y directions.

- **Evanescent waves** ($\kappa_0^2 < \kappa_x^2 + \kappa_y^2$): The transverse spatial frequency $\kappa_{\|} = \sqrt{\kappa_x^2 + \kappa_y^2}$ is greater than the free space wavenumber κ_0, meaning that the longitudinal wavenumber κ_z, associated with the wavevector components in the Z direction, becomes imaginary and the transmitted waves have the form,

  $$Ae^{i(\kappa_x X + \kappa_y Y - \omega t)} e^{-(\sqrt{|\kappa_0^2 - (\kappa_x^2 + \kappa_y^2)|}\, Z)} \tag{1.3}$$

  This indicates that the amplitude of these transmitted waves decreases exponentially in the Z direction and is confined to a distance close to the interface between different media. Therefore, an evanescent wave, or evanescent field, is a near-field standing wave exhibiting exponential decay with distance away from the boundary and cannot propagate to the far-field region. Thus the evanescent waves, which carry detailed information from objects with high spatial frequencies κ_x and κ_y, are lost in the far-field region. As E. K. Abbe mentioned, such

loss causes inaccuracy of detection in conventional far-field optics and thus images generated are diffraction-limited [94, 96, 97].

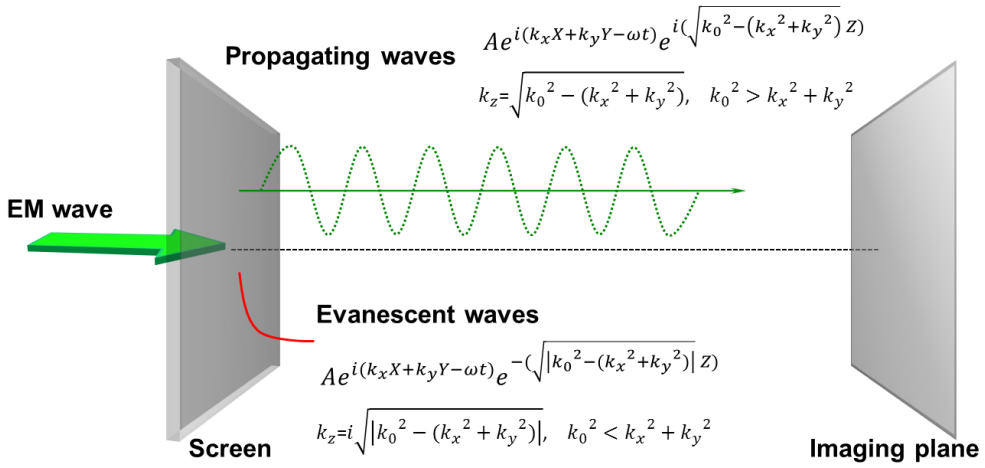

Figure 1.1: ***Imaging the free space field behind a screen.*** *Schematic representation. For an electromagnetic wave (EM wave) incident upon on a screen, the transmitted EM wave behind a screen can be diffracted into propagating waves ($\kappa_0^2 > \kappa_x^2 + \kappa_y^2$), surface waves ($\kappa_0^2 = \kappa_x^2 + \kappa_y^2$) and evanescent waves ($\kappa_0^2 < \kappa_x^2 + \kappa_y^2$). For the evanescent waves, the wavenumber κ_z associated with the propagation in the Z direction is imaginary, which indicates that the amplitude of the evanescent field decreases exponentially in the Z direction.*

For over a century, it has been generally accepted that, due to the loss of high spatial frequencies κ_x and κ_y in the far-field region, the smallest focused spot and the maximum spatial resolution of a conventional optical imaging system are both limited by the diffraction of light. As E. K. Abbe suggests, the resolution of an imaging instrument is not restricted by the quality of the components, but limited by the wavelength (λ) of the incident light beam and the numerical aperture ($N.A.$) of the optics. Therefore, as shown in Fig. 1.2, the minimum resolving distance ($\triangle$) of adjacent illuminated spots is determined by the Abbe-Rayleigh diffraction limit [94]

$$\triangle = \frac{0.61\lambda}{N.A.}. \tag{1.4}$$

Here $N.A.$ is equal to $n\sin\theta$. n is the refractive index of the medium where the lens is working and θ is the half-angle subtended by the lens with respect to an object or a point light source as shown in Fig. 1.3. The value of $N.A.$ indicates the light harvesting or emitting ability of a lens. In a microscope system, the minimum resolving distance -

denoted as the maximum spatial resolution - is often estimated to be half the wavelength of an incident light beam. The conventional and intuitive way to increase the spatial resolution in an optical microscope system is choosing a shorter wavelength of incident light beam and selecting a higher numerical aperture objective lens.

Take an objective lens immersed in oil of high refractive index ($n = 1.515$) for example, the largest value of $N.A.$ is around 1.38. When the wavelength $\lambda = 500$ nm of a visible light source is applied, the best spatial resolution of a conventional optical system is approximately 0.45 λ, suggesting 220 nm as the best resolution achievable in a conventional optical microscope. Such performance is unable to meet the requirements of modern technology. However, there is one obvious solution to break this limitation: to recover the evanescent wave which is lost during light propagation.

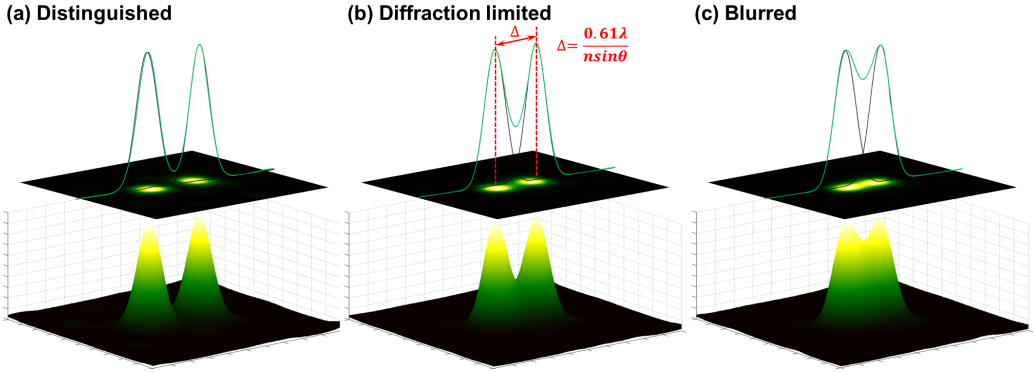

Figure 1.2: ***Abbe-Rayleigh diffraction limit in a conventional optical imaging system.*** *Schematic representation. When the separation between two light sources is less than the diffraction limited distance $\triangle$, the combined diffraction pattern shows that the two light sources are no longer clearly distinguished. According to the Abbe-Rayleigh rule, the two light sources cannot be resolved when the central maximum of one falls inside the location of the first minimum of the other [94].*

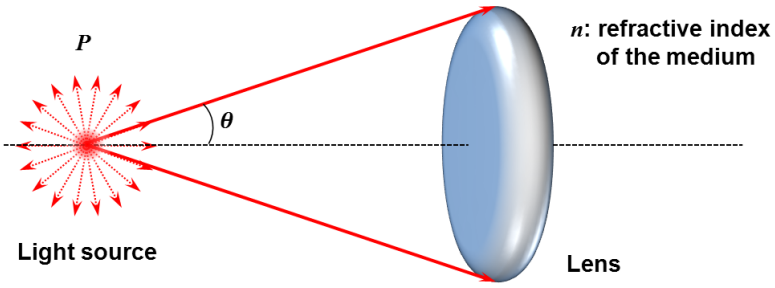

Figure 1.3: ***Numerical aperture (N.A.).*** *Schematic representation.* $N.A. = n \sin\theta$. *n is the refractive index of the medium where the lens is working and θ is the largest angle of the diverging light beams which can be collected by the lens. The value of N.A. indicates the ability of light harvesting/emitting by a lens [97].*

1.2.2 Evanescent waves

Although the evanescent field cannot propagate very far along the Z direction, nor can it be detected by a conventional far-field optical imaging system, it is still a physical field and exists on the structure surface in the near-field region. Moreover, the wavenumber components κ_x and κ_y, associated with propagation in the X and Y directions respectively, can be larger than the free space wavenumber $\kappa_0 = |\vec{\kappa}|$,

$$\kappa_x > \kappa_0 \quad \text{and/or} \quad \kappa_y > \kappa_0 \tag{1.5}$$

The corresponding wavelengths in the X and Y directions, λ_x and λ_y, are hence shorter than the ordinary wavelength $\lambda = 2\pi/\kappa_0$, *i.e.* ,

$$\lambda_x < \lambda \quad \text{and/or} \quad \lambda_y < \lambda \tag{1.6}$$

As it is travelling on the sample surface, the evanescent field may interact with the existing nanostructure patterns or any object located in the near-field region, such as fine gratings, scattering particles or other subwavelength nanostructures. Moreover, the evanescent wave may excite surface plasmon polaritons (SPP) [98,99] – a collective oscillation of electrons or a plasma wave travelling on a metal surface. With the existence of evanescent waves, subwavelength light localizations can be formed in the near-field region, while the confined photons can tunnel out to a waveguide (ex. a fibre) and be detected. In the near-field region, evanescent waves with high spatial $\vec{\kappa}$ vectors govern the interactions between subwavelength nanostructures. Therefore, the intensity dis-

tribution of nanoscale light localizations in the near-field region can be controlled and manipulated by different types of nanostructures. Research on generation or conversion of the evanescent fields has led to many practical applications, such as high-resolution imaging [50–52, 100, 101], bio-sensing [102, 103], solar energy devices [104].

On the other hand, from the viewpoint of Fourier optics [105], the formation of a nanoscale light localization confined within a subwavelength-sized ($\ll \lambda$) region is mainly composed of wave components with high spatial frequencies, such as the evanescent waves. Therefore, the evanescent waves provides an opportunity to develop techniques for high-resolution imaging or fine nanostructure milling. Due to the fact that evanescent waves only exist in the near-field zone and thus subwavelength light confinement is always bound to the sample surface, such techniques need to be performed in the near-field region and carried out a very short distance from the sample surface.

1.2.3 Scanning near-field optical microscopy (SNOM)

While there are different interpretations of the near-field region, in this thesis it is defined as the distance away from the sample surface less than a wavelength of incident radiation. To understan and use the near field well, it is important to first realize how theories of near-field optics and the related techniques have been developed. Some critical breakthroughs are summarized as follows. In 1928, E. H. Synge proposed the original concept of scanning near-field optical microscopy (SNOM) [1]. He suggested a thin, opaque metallic plate with a tiny aperture of about 100 nm be placed in immediate proximity to a sample surface. With a plane wave illuminating the plate from one side, an illumination spot should be generated on the other side. In near-field region, the size of this illumination spot would be not limited by the diffraction of light, but the aperture size in the metallic plate. Then the transmitted light could be collected by a microscope and the intensity could be measured by a photoelectric cell. In order to establish the optical image of the sample, the aperture should be moved and scanned point by point. In this process, the spatial resolution of the established images would be limited by the size of the aperture, instead of the wavelength λ of the incident light beam. Synge's idea was first experimentally demonstrated by E. A. Ash and G. Nicholls in 1972 [33]. They used an aperture with a diameter of 1.5 mm, illuminated with 3 cm waves and successfully imaged subwavelength line gratings with period of

0.5 mm. Subwavelength imaging with a resolution of $\lambda/60$ was obtained and such a result demonstrated that the Abbe's diffraction limit could be broken in the microwave region.

Later, thanks to the development of scanning probe microscopy (SPM) techniques in 1980s [106], the distance between the scanning probe and sample could be precisely controlled. In 1984, both A. Lewis and D. W. Pohl's groups managed to obtain subwavelength images at optical frequencies [2, 34]. They used a sharp, metal-coated pointed tip with a subwavelength aperture and a feedback control mechanism on the tip oscillation frequency to finely adjust the distance between the tip and sample. As a result, the distance between the sample and the probe could be maintained within only a few nanometres and the resolution of the subwavelength optical images could be as small as 25 nm ($\lambda/20$).

In summary, SNOM has the following characteristics. First, a probe is placed into the subwavelength vicinity ($\ll \lambda$) of a sample and the optical distribution can be imaged point by point by scanning along the illuminated sample surface. Second, the spatial resolution of such a microscope system is not diffraction limited and only relates to the aperture size of the probe.

Fig. 1.4 shows the schematic representation of conventional far-field (a) and scanning near-field (b-c) optical microscopy arrangements. The intensity distributions of electromagnetic waves at different cross-sections along the propagation direction are displayed illustrating the loss of spatial resolution, which is especially pronounced for the far-field microscopy arrangement as shown in Fig. 1.4 (a). In contrast, in near-field scanning arrangements, scattered power can be detected by a probe with a subwavelength aperture (Fig. 1.4 (b)) or a tiny scatterer (Fig. 1.4 (c)), scanning over the sample which can produce higher resolution images.

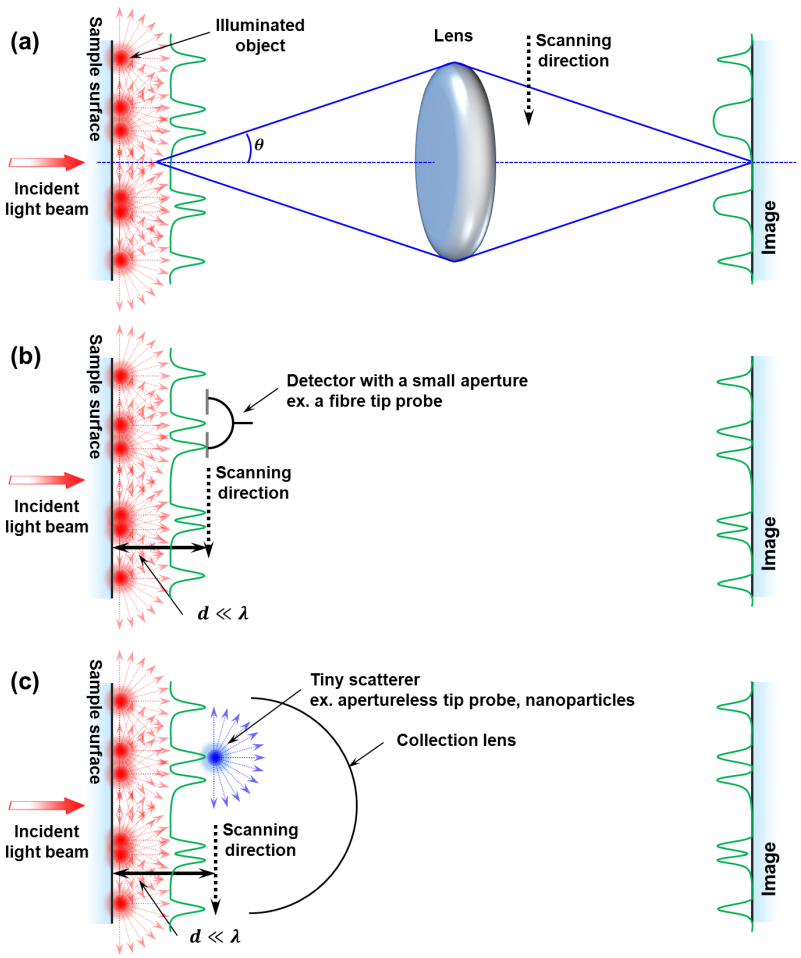

Figure 1.4: ***Conventional far-field and scanning near-field optical microscopy arrangements.*** *Schematic representation. (a) Conventional far-field and (b-c) SNOM arrangements. (a) shows the conventional imaging with an objective lens, where θ is the maximum angle that the objective lens can accept, (b) shows the near-field scanning apparatus with a aperture scanning tip, and (c) shows the near-field scanning arrangement with a tiny scatterer. With a subwavelength aperture or a tiny scatterer, the image is established point by point. In that case, the spatial resolution of the established image depends on the size of aperture or the scatterer. Figure is re-established from Ref. [107].*

Since SNOM was first developed, substantial research has started to look into the confined photons between the scanning probe and the sample. Techniques using different types of scanning probes have been extended to a wide range of applications [108–116]. Fig. 1.5 shows the various configurations with each type of scanning probes employed in SNOM. Examples include

- **illumination SNOM** (see Fig. 1.5 (a)): The fibre probe is employed to guide the radiation from a light source to the tip aperture that illuminates samples.

Light transmitted/reflected by the sample is collected by detectors [108–110].

- **collection SNOM/the photon scanning tunnelling microscope (PSTM)** (see Fig. 1.5 (b)): The transmitted/reflected light from the sample is collected by a pointed, apertured scanning probe [111–113].
- **apertureless SNOM/the surface field enhancement effects near sharp pointed metal-coated probes** (see Fig. 1.5 (c)): The pointed end of an apertureless probe is used as a tiny scatterer to scatter the transmitted/reflected light from the sample to a large detector [114–116].

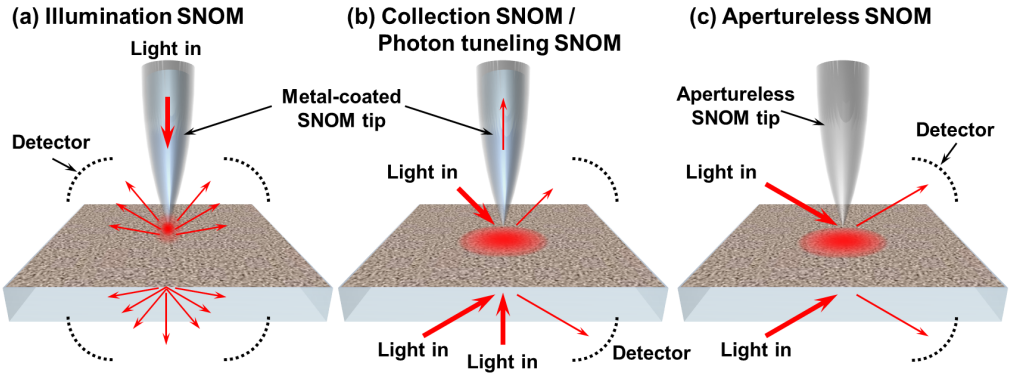

Figure 1.5: ***Different configurations of SNOM.*** *Schematic representation. (a) Illumination mode of SNOM. The light beam is launched into a fibre tip and illuminates the sample as a point light source. (b) Collection mode or photon tuneling mode of SNOM. A SNOM tip is used for collecting near-field optical fields. (c) Apertureless mode of SNOM. A silicon tip or a cantilever is employed for scattering near-field optical fields. The spatial resolution of apertureless SNOM can be down to* $1 - 10$ nm *[116]. Figure is re-established from Ref. [107].*

By means of the interactions between evanescent waves and nano-objects in the near-field region, nanoscale light localizations can be produced and controlled by different types of nanostructures. As a result, the development of SNOM technologies not only allows us to directly observe and understand the important optical phenomena occurring near the illuminated surface structure on the nanoscale, but also provides a link to the macroscopic optical behaviour in the far-field region.

1.3 Light localization with metamaterials

1.3.1 Artificial atoms/molecules

Besides utilizing the evanescent waves to generate the subwavelength light localization and using the near-field scanning technique to obtain optical super-resolution images in near-field region, there is another approach to concentrate light beams into a small volume and increase the spatial resolution of an optical system. By changing the size, shape or arrangements of atoms or molecules in matter, one can tailor the behavior of light. However, the composites and arrangements of atoms or molecules in matter have to follow the natural rules and are very difficult to change at will. Therefore, for a long period, scientists have tried to fabricate artificial "atoms" or "molecules" with specific arrangement in 2D or 3D in order to control electromagnetic waves [6, 117–122]. For example, in 1948, W. E. Kock made a pioneering contribution to the construction of artificial complex materials [117]. He suggested making light-weight microwave lenses by replacing a heavy high-permittivity refractive medium with a periodic arrangement of conducting spheres, disks or strips. His work involved an arrangement of metallic elements in a 3D array or lattice structure to mimic the crystalline lattices. The constructed metallic elements of the dielectric lens effectively tailored the refractive index of the artificial media, which was regarded as a new way of producing materials. With this method, the size of the artificial elements was on a much smaller scale than the operating wavelength, and the tailored electromagnetic behavior resulted from the processes occurring in the artificial elements. Since then, artificial complex materials have become a popular research subject.

Like the development of SNOM, research on artificial complex materials also encountered some technical difficulties, one of which was that the size of artificial elements had to be smaller than the wavelength of light. Consequently, it was difficult to experimentally demonstrate and realize artificial complex materials operating in the optical range. Fortunately, with the rapid development of fabrication techniques in recent years, such as focused ion beam (FIB) milling [123–125], electron beam lithography (EBL) [126, 127]and self-assembly (SA) of materials [128–130], the size of the constructed artificial elements can be down to few tens of nanometres. Such promising techniques provide more convenience and diversity of sample design and its fabrication.

1.3.2 Negative refraction of light

Novel ideas of material synthesis and fabrication techniques have recently allowed the size of the artificial elements to be much smaller than the wavelength of optical radiation. With various designs of nanostructures and different composite materials, artificial electromagnetic composites can mimic known material responses or generate new physical response functions that do not occur or may not be available in nature. In artificial complex media, the elements in turn interact with the incident electromagnetic waves and the alternating electromagnetic fields between each element, influencing the macroscopic effective permittivity ε and permeability μ of the composite medium. Recently, the idea of complex materials with negative values of both the permittivity and permeability at a certain frequency has aroused tremendous interest. Originating from V. G. Veselago's theory in 1968 [120], this idea involved the investigations of plane wave propagation in a material whose permittivity and permeability were assumed both to be negative. Negative ε and μ lead to a medium with negative index of refraction n and therefore electromagnetic wave propagation will show a reversal of the Snell's law at the interfaces of positive and negative refractive index medium. Adopting this idea, J. B. Pendry harboured the ambition of creating a "perfect lens", which consisted of a medium with negative refractive index [6]. Such a promising concept can be used in a subwavelength optical imaging system and will be able to beat the diffraction limit. Fig. 1.6 shows a schematic diagram of the comparison between a conventional material ($n > 0$) and a material with negative refractive index ($n = -1$). As light passes through the conventional material, all the diverging rays from a point light source obey the Snell's law and cannot focus again to form a focused spot. However, in the negative refractive index media, the diverging rays will be re-directed and concentrated into a focused spot. Particularly, the evanescent waves, which contain detailed information from an illuminated object, can be amplified and propagated to the other side of the negative refractive index lens [6]. Thus, in principle, the size of the focused spot can be infinitesimal and the point source can be perfectly imaged; however, the property of negative refractive index cannot be found in any current natural materials.

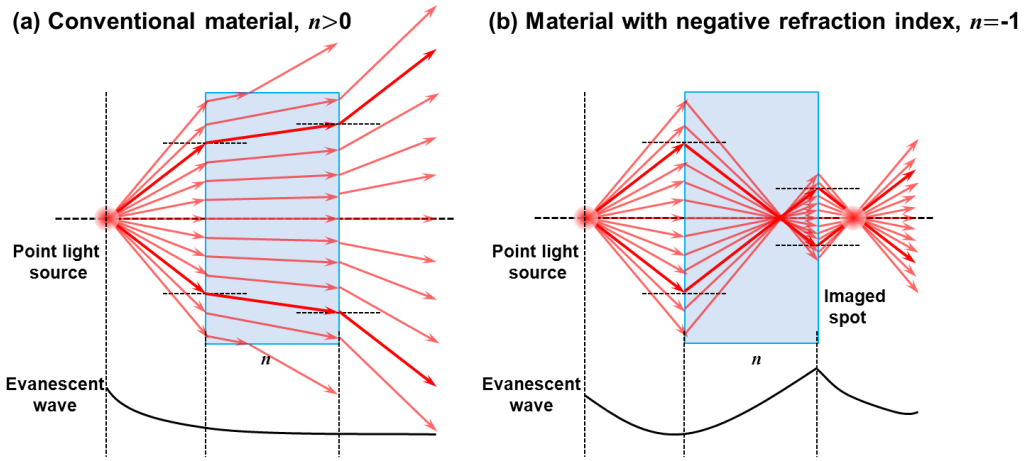

Figure 1.6: ***Perfect imaging of a point light source by a negative refractive index medium.*** *Schematic representation. (a) conventional material with refractive index $n > 0$; (b) A negative refractive index medium with $n = -1$. In a negative refractive medium, light diverging from a point source is set in reverse and converges back to a point. The black line shows the intensity of the evanescent wave. Figure is re-established from Ref. [6, 7]*

Despite this problem, the idea of exploiting artificial complex media to achieve negative refraction of light is still fascinating, especially in terms of its ability to harvest the evanescent waves. Therefore, several concepts based on different types of artificial negative refractive medium to achieve super-resolution images have been proposed in recent years. In 2001, D. R. Smith *et al.* first realized negative refraction in the microwave region by using a combination of wires and split-ring resonators [122]. In their results, electromagnetic waves could be bent to a negative angle with the surface normal and propagated in the direction opposite to that predicted by Snell's law. Since then, such artificial media of negative refractive index, which can practically overcome the diffraction limit, have been known as "superlenses". Inspired by the experimental realization of the superlens in the microwave region, the attention of the negative refraction research has shifted towards to the range of visible light. Many purposely designed structures and material combinations were used to enhance the evanescent fields to contribute to subwavelength imaging. For example, in 2005, the first high-resolution, sub-diffraction-limited image was obtained by an optical superlens [78], which contained a thin silver slab (35 nm). The image was recorded on a photo-resist layer by optical lithography at the wavelength of 365 nm. A grating was imaged with spatial resolution of around 63 ± 4 nm ($\sim \lambda/6$). A year later, a better

feature resolution of $\lambda/20$ was achieved by a SiC superlens [11], at a mid-infrared frequency with phonon excitations. Although both of the silver slab and SiC superlenses have improved the image resolution, the lenses still needed to be placed close to the objects and the sub-diffraction-limited images could only be produced in the near-field region.

In order to obtain subwavelength images in the far field, a silver superlens-based device, termed the "far-field superlens" (FSL), was proposed to project a sub-diffraction-limited image into far field [12]. The FSL is constructed by adding a subwavelength grating as a coupling element onto a silver slab superlens. With the coupling element, the enhanced evanescent waves can be coupled into propagating waves. High-resolution images can be reconstructed by collecting the far-field signals from the far-field superlens. Another approach to transfer evanescent waves into propagating wave is hyperlens [13], using a piece of artificial strongly anisotropic metamaterial to transfer the subwavelength information into the far-field. With the help of the hyperlens geometry, the waves gradually reduce their wavevector values along the propagation direction in the metamaterial, and thus the waves continue to propagate even after leaving the hyperlens. Different types of superlenses with artificial negative refractive medium are summarized and shown in Fig. 1.7.

1.3.3 Metamaterials

After Pendry's initial ground-breaking work on negative refraction of light and the following related studies on different types of artificial complex medium, researchers suggested that electric and magnetic resonances could be tailored by regulating the artificially engineered metamaterials [132–134]. Metamaterials gain unusual electromagnetic properties from structure rather than composition. They consist of a large number of artificial subwavelength nanostructures in an array of subwavelength unit cells. The size of the metamaterial unit cell is much smaller than the wavelength of an incident light beam, and the elementary building block of a metamaterial, i.e. the metamaterial unit cell, is called a meta-molecule. With properly designed metamaterials, the properties and behaviour of electromagnetic waves can be tuned as emitters, enhancers and so on [135, 136].

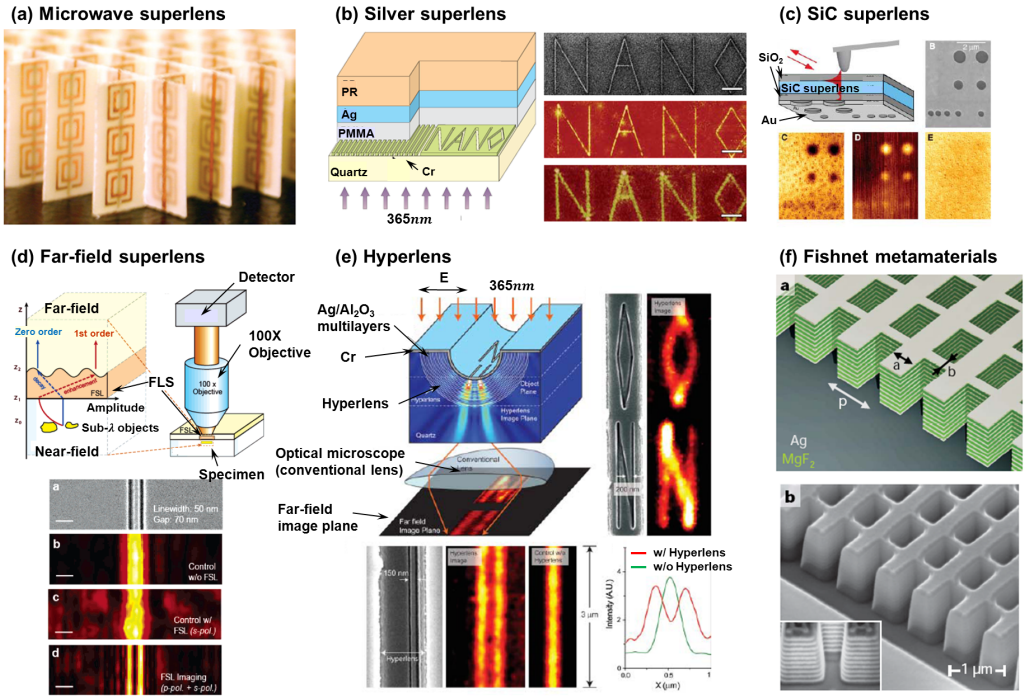

Figure 1.7: ***Different types of superlenses with artificial negative refractive medium and their results.*** *Schematic representation. (a) The microwave superlens, which is the combination of wires and split-ring resonators, first successfully demonstrated the negative refraction phenomena [122]. (b) The optical superlens of a thin silver slab demonstrated sub-diffraction-limited imaging with resolution of $\lambda/6$ in the optical range ($\lambda = 365$ nm) [78]. (c) The SiC superlens successfully demonstrated a deep subwavelength resolution of $\lambda/20$ in the mid-infrared frequency range [11]. (d) The far-field superlens (FSL). By adding a subwavelength grating as a coupling element onto a silver slab superlens, the evanescent waves can be transferred into propagating waves and the subwavelength features can be reproduced in the far-field region [12]. (e) The hyperlens. With a strongly anisotropic metamaterial, the evanescent waves are transferred to propagating waves, which can keep propagating even after leaving the hyperlens [13]. (f) The fishnet metamaterial. A low-loss negative refractive index medium contains 21 layers of fishnet nanostructures [131]. Figures are from Ref. [11–13, 78, 122, 131].*

With the wide exploration of metamaterials in the last few years, it has been realized that the potential of metamaterials in applications could be much broader. Nowadays transformation optics has merged with metamaterials studies, being able to precisely control electric and magnetic material properties [137, 138]. One of the most remarkable applications would be invisibility cloaking, which was designed by guiding electromagnetic waves around a hidden object and has already been experimentally demonstrated in both the microwave and optical region [139–142]. Besides invisibility cloaking, transformation optics has also been used for other optical transformation devices, such as electromagnetic concentrators, electromagnetic field and polarization

rotators, and electromagnetic-wave bending structures.

1.4 Light localization through optical super-oscillations

In order to obtain subwavelength light localization and optical super-resolution imaging, many of the studies mentioned above depend on the exploitation or recovery of evanescent waves, containing fine details of the electromagnetic field distribution in the immediate proximity of the testing objects. Nevertheless, among these methods, either the objects need to be placed in the near-field region or the imaged patterns would be generated very close to the sample surface. Such requirements are unfavourable to many applications of imaging. In an attempt to overcome these restrictions, we should consider the following issue. Is the existence of evanescent fields necessary to form subwavelength optical concentrations or to reveal nanoscale features? More specifically, is it possible to generate subwavelength light localizations or image patterns with super-resolution far away from the sample surface? To answer these questions, we shall start from research on signal processing and then try to find solutions through optical super-oscillations.

1.4.1 Optical super-oscillations

It is generally thought that a signal band-limited to the maximum frequency f_{max} cannot change substantially in an interval shorter than $1/f_{max}$. However, such a statement is incorrect. In fact, in a local region, band-limited signals may oscillate rapidly at a frequency arbitrarily faster than the maximum frequency that they contain. These localized transient variations are now known as super-oscillations [9, 143–145] − the phenomenon of a function oscillating faster than its fastest Fourier component. To show that a super-oscillating signal can be created locally, many examples of super-oscillating functions have been identified [146–148]. For instance, a 1D function $f(x)$ with a limited series of harmonics, an example taken from Ref. [146], is given as follows,

$$f(x) = \sum_{n=0}^{5} a_n \cos(2\pi n x). \tag{1.7}$$

In this 1D function $f(x)$, there are only five frequency components, while the highest one is $f_{max}(x) = \cos(2\pi \times 5x)$. By appropriately choosing the coefficients a_n, the limited series of harmonics can form a super-oscillating function $f(x)_{super-oscillating}$, considering $f(x)$ with $a_0 = 1$, $a_1 = 13295000$, $a_2 = -30802818$, $a_3 = 26581909$, $a_4 = -10836909$, and $a_5 = 1762818$. This new super-oscillating function can be well approximated by a harmonic function near $x = 0$.

$$f(x)_{super-oscillating} \approx 0.5(\cos(2\pi \times 43.6x) + 1) \tag{1.8}$$

The 1D function $f(x)$, a limited series of 5 frequency components with coefficients a_n, and its highest harmonic function $f_{max}(x) = \cos(2\pi \times 5x)$ are plotted in Fig. 1.8 (a) and (b), respectively. As shown, in a range of $x = [-1, 1]$, all the signals seem to oscillate slower than the highest frequency component $f_{max}(x)$. However, in the close-up at x close to 0 (indicated by the green square), it is observed that a super-oscillating feature is created near $x = 0$ as shown in Fig. 1.8 (c). This feature oscillates nearly nine times faster than the highest harmonic function $f_{max}(x)$ and can be well approximated by a harmonic function, as the red dotted line indicates. Thus, a super-oscillating feature can be generated in a local area by appropriately choosing the weights of the frequency components contained in a band-limited system.

Although the 1D function $f(x)$ successfully demonstrates that a super-oscillating feature can be created near $x = 0$, such a simple example of 1D super-oscillating function is still difficult to obtain physically. First, with an increase on the oscillation frequency of a localized super-oscillating signal, the corresponding coefficients of individual frequency components will dramatically increase. Moreover, a slight variation of the coefficients may destroy the super-oscillations or generate another super-oscillating feature somewhere else. Thus, the super-oscillation process is delicate. However, how to practically generate super-oscillating fields becomes an interesting issue and will be discussed below.

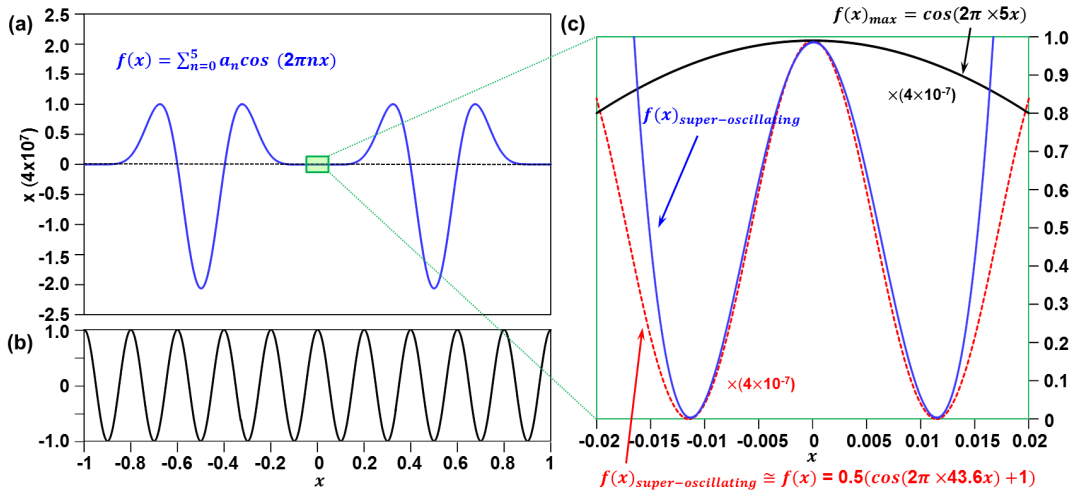

Figure 1.8: ***Super-oscillating feature generated by a limited series of frequency components.*** *Calculation results. A 1D function $f(x)$ with a limited series of harmonics, $f(x) = \sum_{n=0}^{5} a_n \cos(2\pi nx)$, is plotted in plate (a) in a range of $x = [-1, 1]$, while plate (b) shows the highest Fourier harmonic $f_{max}(x) = \cos(2\pi \times 5x)$. Near x=0, a super-oscillating feature can be created and changes nearly nine times faster than the highest harmonic as shown in plate (c).*

1.4.2 Super-oscillating masks

In 2006, M. V. Berry and P. Popescu, starting from earlier works on quantum mechanics, suggested that light diffraction on a subwavelength grating structure, producing propagating waves that entirely exist in the optical field, could create nanoscale light localizations or subwavelength features at a distance far away from the grating. Thus, such a grating produces subwavelength features without the existence of evanescent waves [9]. They related such an effect to the super-oscillations of the optical fields, the fact that band limited functions are able to oscillate arbitrarily faster than the highest Fourier components whose spatial frequency is $2\pi/\lambda$. In fact, based on the same underlying physics of tailoring the interference of several coherent light sources, in 1952, G. Toraldo Di Francia demonstrated that the size of a subwavelength light localization in the far-field can be modulated by a pupil design with a series of concentric ring apertures [149]. By increasing the number of the constituent ring apertures and adjusting their positions in the super-resolving pupils, a nearly dark zone surrounding the central localized spot can be enlarged as desired. The expense is that the amplitude variations between individual ring apertures become larger and larger, similar to the coefficients obtained in the 1D function $f(x)$ (Equ. 1.7). Consequently, with every attempt to re-

duce the size of the central diffraction spot, the brightness of side rings must necessarily increase. Such a subwavelength optical concentrator can be employed as a focusing device in a super-resolution scanning optical microscope or used as a super-resolving filter in confocally scanned imaging systems [149–152]. In the apparatus, the testing objects are placed several wavelengths away from the device as the schematic diagram shows in Fig. 1.9, thus removing the main limitation of near-field instruments.

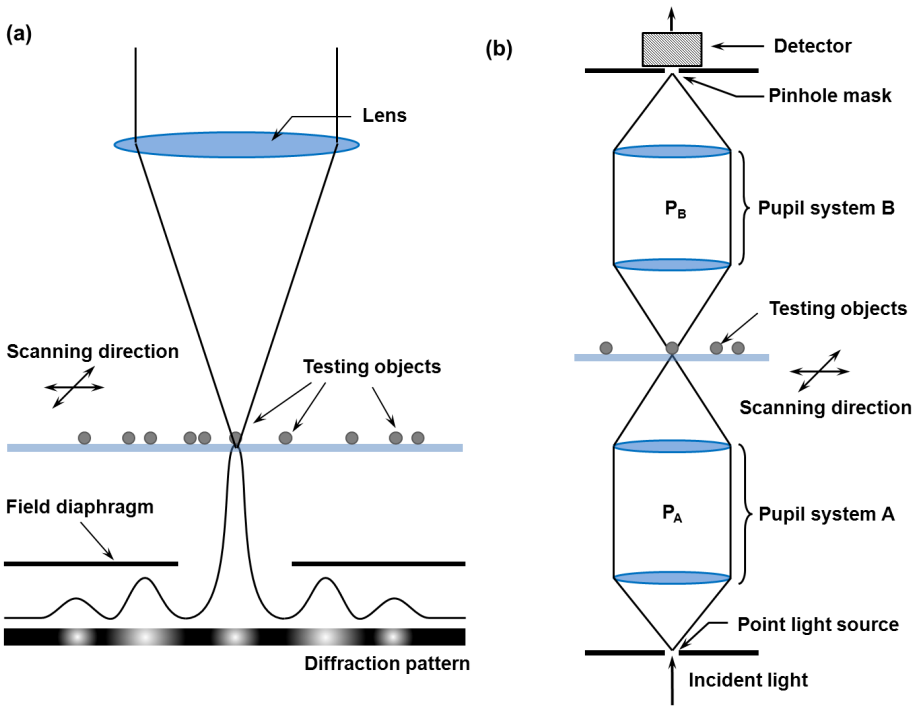

Figure 1.9: ***Proposals to achieve super-resolution with optical pupils.*** *Schematic representations. (a) A subwavelength feature in a diffraction pattern can be created by adjusting the amplitudes and positions of ring apertures in a pupil design. By an arrangement with field diaphragms screening out the larger luminous rings of the diffraction pattern, the retained subwavelength feature can be used as focused spot in a scanning optical system . (b) shows the principle of confocally scanned imaging with the pupil systems. The schematic diagrams are re-established from Ref. [149, 150].*

Before G. Toraldo Di Francia's work, research on constructing antennas to beat the wave diffraction limit had been contemplated by the microwave community for some time, aiming at creating a narrow beam of electromagnetic radiation. In 1943, S. A. Schelkunoff analyzed the radiation patterns of a linear array of dipoles and proved that a much narrower radiation pattern could be achieved by properly adjusting the individual radiating elements [153]. Beginning from his pioneering work, researchers started to look for the most directive current distributions on an array of antennas. But very

soon, C. J. Bouwkamp and N. G. de Bruijn proved that no such optimum distribution exists, meaning that there was no upper limit to the gain obtained [154]. However, as a consequence, when the sharpness of an electromagnetic radiation beam increases, the power to the antennas also needs to be increased to maintain the signal level. Due to its impracticality, the concept of super-directive antennas was not pursued.

However, the idea of super-oscillating fields generated by light diffraction on sub-wavelength grating structures to achieve subwavelength features generated without evanescent waves, proposed by M. V. Berry and P. Popescu, had an independent revival recently in the domain of optics [8–10,146,152]. To design a subwavelength grating structure which can be used as a "super-oscillating mask" to generate a subwavelength light localization at distances away from the mask, F. M. Huang *et al.* [155] theoretically demonstrated that a 1D super-oscillating mask $t(x)$ can be designed through a series of complicated calculations. A 1D prescribed subwavelength field distribution $h(x)$ can be created when the super-oscillating mask is illuminated by a plane wave at wavelength of λ as shown in the schematic diagram in Fig. 1.10.

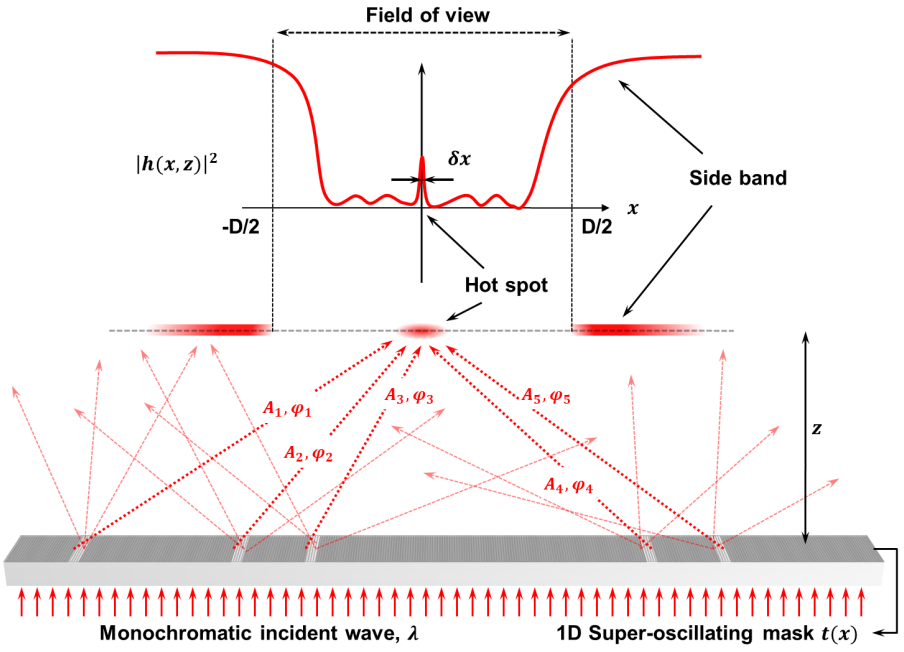

Figure 1.10: ***A 1D super-oscillating mask*** $t(x)$ ***can be designed to create a prescribed super-oscillating field in a limited range.*** *Schematic diagram. As described in the text, a 1D super-oscillating mask* $t(x)$ *with complex intensity and phase profile can be designed [155]. By shining a monochromatic plane wave on the mask* $t(x)$*, a subwavelength optical localization of* δx *can be obtained at a distance* z *away from the mask.*

The main step in designing the 1D super-oscillating mask is to present the desired super-oscillating feature as a series of band-limited functions which can be decomposed into free-space plane waves of a given wavelength λ. Therefore, by using the prolate spheroidal wave functions, a complete set of band-limited functions developed by D. Slepian and H. O. Pollark [156], desired subwavelength features with the size of δx located in a field of view $[-D/2, D/2]$ can be approximately described as shown in Fig. 1.11 (a). Any prescribed subwavelength feature can be obtained by increasing the number of prolate spheroidal wave functions used to approximate the field distribution. Then, by presenting the prolate spheroidal wave functions as a series of plane waves and using the scalar angular spectrum description of light propagating from the mask to the super-oscillating feature, the intensity and phase profile of the required complex mask transmission function $t(x)$ for generating a super-oscillating feature of $\delta x = 0.21\lambda$ at a distance of $z = 20\lambda$ can be readily derived as shown in Fig. 1.11 (b).

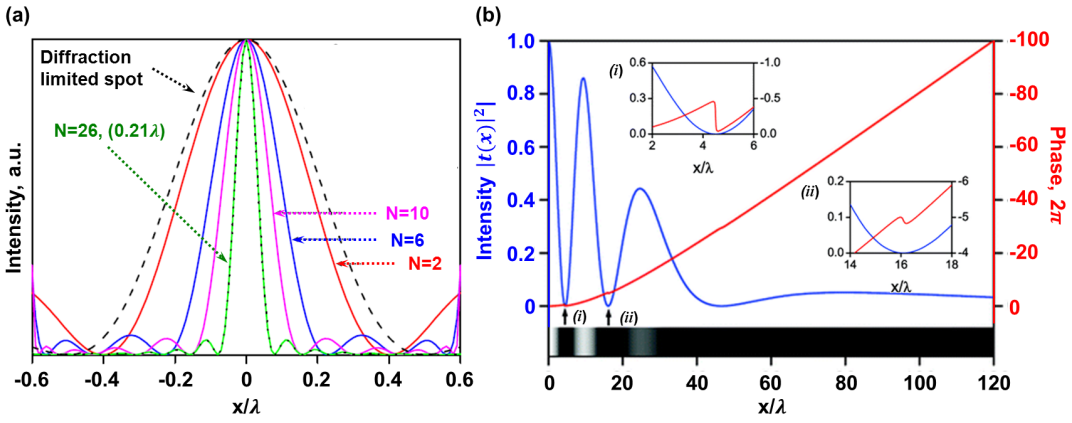

Figure 1.11: ***Normalized intensity profiles of prescribed subwavelength hot-spots with the size of*** δx ***through the approximation process and the intensity and phase profile of a designed super-oscillating mask*** $t(x)$ ***to generate a sub-wavelength spot of*** $\delta x = 0.21\lambda$**.** *(a) shows the normalized intensity profiles of prescribed subwavelength features through approximation by a series of band-limited prolate spheroidal wave functions with different numbers of components N. A subwavelength hot-spot with the width of* 0.21λ *as a target field distribution can be obtained with N=26. Through complex calculations, a super-oscillating mask* $t(x)$ *can be designed whose intensity and phase profile are shown in the plate (b). The insets show the detail of kinks in the phase profile as the arrows (i) and (ii) indicate. Images are obtained from Ref. [155].*

With a monochromatic wave illuminating this designed 1D super-oscillating mask, a subwavelength focused spot with prescribed size and shape can be created beyond the evanescent fields as shown in Fig. 1.12 (a). Thus, a 1D super-oscillating mask can be

designed through a series of complicated calculations to generate desired subwavelength features away from the mask. Such a 1D super-oscillating mask can also be employed in an optical apparatus to generate a subwavelength spot for the super-resolution imaging beyond the diffraction limit. Moreover, from their calculation results, such a mask may not only be used as a focusing device but also can mimic the lens functions as a super-resolution imaging device to image two close objects as shown in Fig. 1.12 (b).

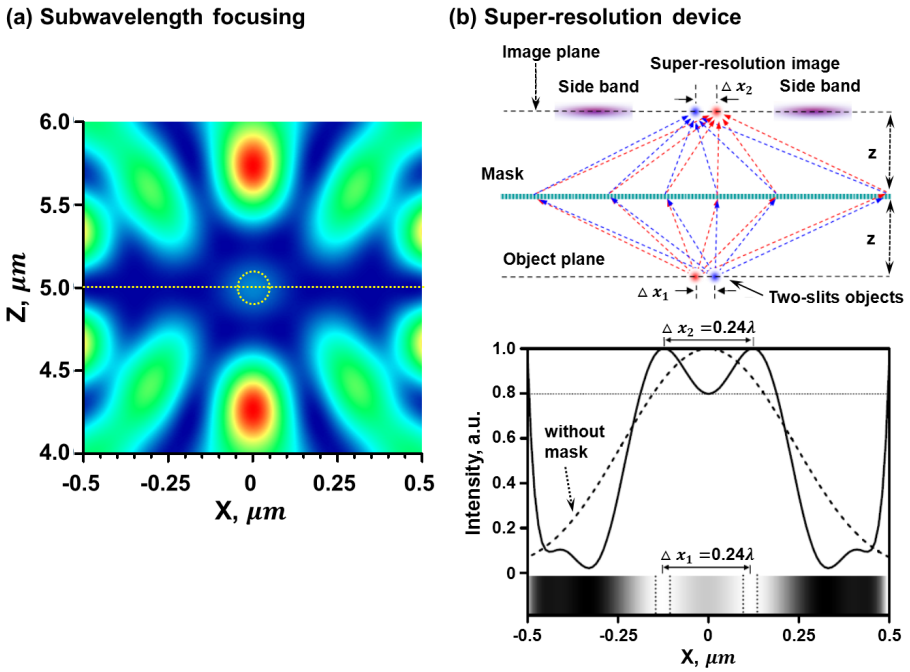

Figure 1.12: ***The designed super-oscillating mask can be used as a subwavelength focusing device or a super-resolution imaging device.*** *(a) shows that a subwavelength focused spot can be created by the designed 1D super-oscillating mask $t(x)$ along the Z direction within a limited range. (b) shows that two closed objects can be imaged and distinguished on the other side of the designed super-oscillating mask. The super-oscillating mask can mimic the lensing function of a conventional lens with high numerical aperture. Images are obtained from Dr. F. M. Huang's work and Ref. [155].*

However, to design such a super-oscillating mask is not easy. First, the approximation process of a prescribed subwavelength field distribution by a series of band-limited prolate spheroidal wave functions, as shown in Fig. 1.11 (a), requires a greater number of components, the smaller the required hot-spot. Also, the field of view of the subwavelength spot is limited, and sidebands will arise outside the prescribed range. From the point of view of producing the designed subwavelength light localizations experimentally, since the super-oscillations process is based on the precise and delicate

interference of waves, the prescribed focused hot-spot can be created only by precisely controlling the amplitude and the phase on each pixel of the complex super-oscillating mask.

So how can we create a super-oscillating mask without sophisticated design or precise control? Inspired by the simple example of 1D function $f(x)$ and the suggestions from Berry *et al.* , an intuitive and direct way is adopted to extend the 1D subwavelength grating structure to a 2D nanohole array, making it a super-oscillating binary mask capable to generating a subwavelength energy hot-spot beyond the near field as shown in the schematic diagram in Fig. 1.13. Through appropriate arrangements of the constituent nanoholes on a metal screen, a super-oscillating field may be created at a long distance from the nanohole array binary mask.

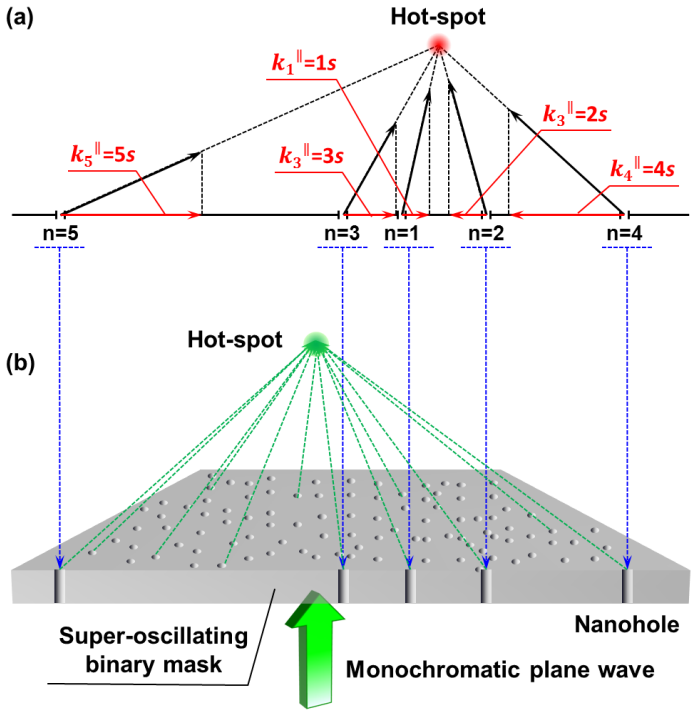

Figure 1.13: ***Schematic configuration of a super-oscillating binary mask.*** *(a) The physical interpretation of a 1D super-oscillating function with a limited series of harmonics. To generate a super-oscillating feature, the constituent Fourier components can be realised as optical scatterers, microwave emitters or light diffracted on the nanohole array in a real physical system. (b) An idea to extend the 1D grating to a 2D binary masks with nanoholes. By properly choosing the positions of nanoholes, super-oscillating hot-spots can be generated by using the super-oscillating binary mask.*

However, how to arrange the numerous nanoholes to construct super-oscillating fields is still a problem to be resolved. Fortunately, in 2007, F. M. Huang, *et al.* suc-

cessfully demonstrated in experiments that an array of nanoholes with quasi-periodic arrangements could be used as a super-oscillating binary mask to generate subwavelength focused spots as shown in the SNOM scanning results in Fig. 1.14 (a) [10, 146]. In their studies, subwavelength energy hot-spots were obtained by illuminating a 5-fold symmetry quasi-periodic nanohole array. Moreover, the focal plane of such focused spots was tens of wavelengths away from sample surface and the focused spots were separated a few micrometres from each other. This breakthrough not only verifies the theory of optical super-oscillations but also provides relatively simple solutions to the design of super-oscillating masks. Through differently designed nanohole arrays, the size and position of the subwavelength light localization can be controlled. Meanwhile, F. M. Huang *et al.* also found that such super-oscillating masks with nanoholes in quasi-periodic arrangements could be used as a high $N.A.$ lens to image complex structures which are composed of multiple point sources [157]. Fig. 1.14 (b) shows calculation results resolving multiple point light sources by using the quasi-periodic nanohole array as a lens. Such results show that the nanohole arrays have great application potential, such as focusing a light beam into a small spot or mimicking the imaging function of a conventional lens.

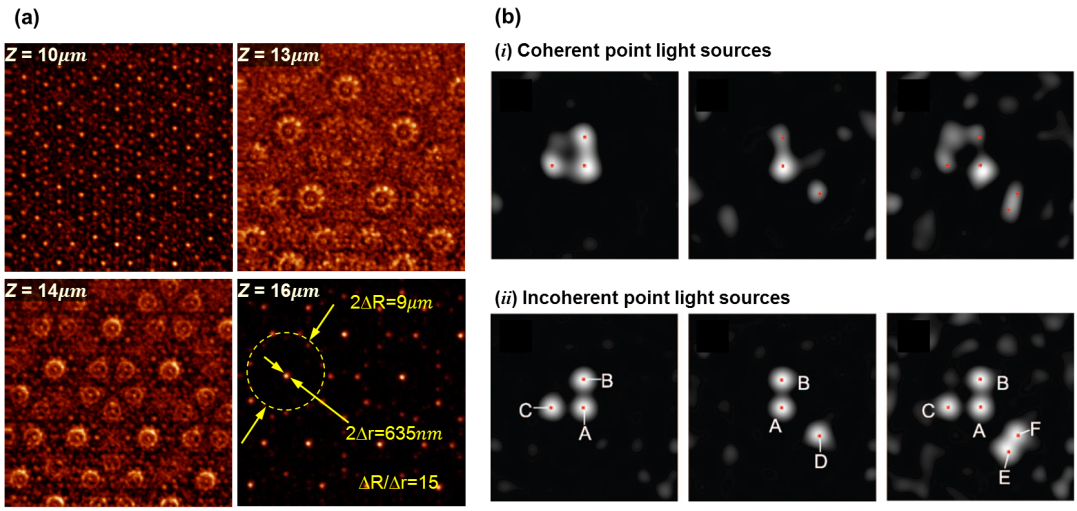

Figure 1.14: ***Quasi-periodic nanohole arrays can be used as subwavelength light focusing device and mimic the imaging functions of a high*** *N.A.* ***lens.*** *(a) Field maps at different distances Z above a 5-fold symmetry quasi-periodic nanohole array. The illumination wavelength of a monochromatic plane wave is* $\lambda = 500$ nm. *Note that highly isolated energy hot-spots can be observed at* $Z = 16$ μm. *(b) Calculation results. Quasi-periodic nanohole arrays can be used as a lens to image multiple coherent (i) and incoherent (ii) point light sources of* $\lambda = 660$ nm. *The red spots indicate the positions of the point light sources. As with a conventional lens, the resolving power of a nanohole array lens is better for incoherent illumination. Images are obtained from Ref. [10, 157].*

1.5 Thesis Overview

As shown in the literature review and discussions above, creating light localizations with a subwavelength scale in an optical system is a way to image and acquire optical super-resolution images beyond the diffraction limit. The size of the localized optical spots represents the light concentration ability of an optical system and thus the smallest resolving distance between two close objects. In general, light localization is essentially the focusing ability, while imaging is where the objects can be actually imaged. Regarding the different optical imaging methods, as long as one can construct an optical image, showing fine detail and the difference between target objects, the approach can be regarded as a super-resolution technique and practically employed to image objects with nanoscale separations or biological specimens. In some of these practical approaches, the spatial discrimination between the target objects can be much smaller than the size of the localized optical spot obtained in the optical systems [43, 44, 158–160]. Several optical super-resolution techniques and their methods are summarized below.

- **Recovery or conversion of an evanescent wave**: scanning near-field optical microscopy (SNOM) [1, 2, 32–34, 40, 41, 106], total internal reflection fluorescence microscopy (TIRFM) [100, 101], etc.

- **Negative refraction index with a metamaterial**: Pendry's perfect lens [6, 120], superlens [11, 12, 78], hyperlens [7, 13], etc.

- **Interference of surface plasmons**: surface plasmon microscopy [50, 51], plasmonic structured illumination microscopy (PSIM) [52], etc.

- **Functional super-resolution techniques with special strategies**: stimulated emission depletion microscopy (STED) [3, 53–57], reversible saturated optical fluorescence transitions (RESOLFT) [4, 59, 60], photo-activated localization microscopy (PLAM) [58,61–63], stochastic optical reconstruction microscopy (STORM) [64, 65], ground state depletion (GSD) [5, 66, 67], etc.

Moreover, optical images with subwavelength discrimination can also be acquired by other approaches such as multiple colour [161–163], structured illumination [164–166], four-wave mixing [70, 71], two-photon luminescense (TPL) [72, 73], second harmonic generation (SHG) [74, 75] or saturated structured illumination [76, 77], etc. Fig. 1.15 shows a measure of the resolving ability, the full width of the smallest spot at its half maximum (FWHM), between different optical super-resolution techniques.

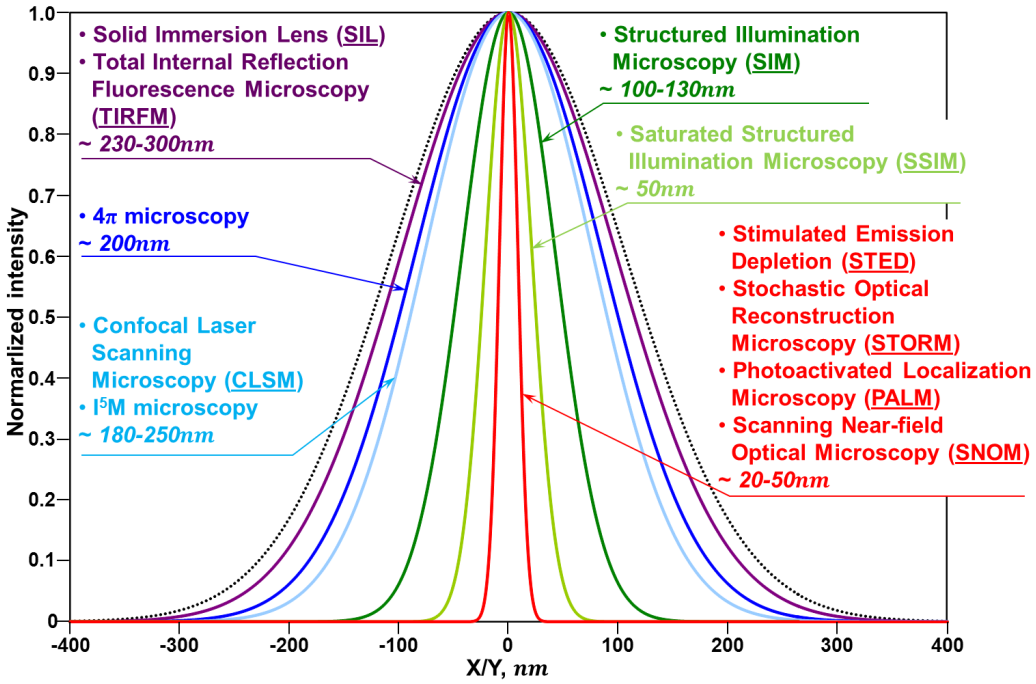

Figure 1.15: ***Comparison of resolving ability between different optical super-resolution techniques.*** *A schematic representation of the smallest spot size which can be resolved by different optical super-resolution techniques, while the dashed black line indicates the spot size (FWHM) which can be obtained for a conventional lens at* $\lambda = 488$ nm *and N.A.=0.85.*

Generally, for a given wavelength, a decrease in focal spot size is accompanied by a decrease of the optical energy in the subwavelength spot and an increase in sideband intensity. For a practical super-resolution instrument, the trade-off between spot size, spot energy and sideband intensities must be optimised for a particular application. Therefore, the imaging performance of an optical super-resolution technique should be characterized by both the value of spot size and the Strehl ratio S. Strehl ratio S is defined as the ratio between the observed peak intensity from a point source at the detection plane and the theoretical peak intensity of the Airy pattern in a perfect imaging system [151, 167, 168]. For a given resolution, the best performance will be achieved when the Strehl ratio is maximized. The maximum Strehl ratio which can be obtained by the Solid Immersion Lens (SIL) technique is around $S = 0.5$ with the focused spot size slightly smaller than the diffraction-limited spot [169–173]. The focused spot size can also be slightly squeezed beyond the diffraction limit by using a pupil filter with optimized amplitude and phase distribution. The Strehl ratio in a

pupil filter system is between 0.1 and 0.4, depending on spot size [174–178].

In a confocal laser scanning microscope (CLSM) system, the Strehl ratio is around 0.6 and the spatial resolution is around 200 nm [47,179–182]. This low efficiency in the confocal laser scanning system is because only the signal produced very close to the focal plane can be detected. Most of the energy (out-of-focus signal) is eliminated by a pinhole in front of a detector. In the functional super-resolution techniques, since the resolution is quite high, the aberration of lenses becomes an important factor affecting the Strehl ratio and the corresponding spot size in the system [183]. For example, with aberrations in a stimulated emission depletion microscopy (STED) system, the value of the Strehl ratio is around 0.724 and the corresponding spot size is around 87.1 nm. In aberration-free conditions, the size of the focused spot is 75.7 nm, a decrease of 15%. STED requires a high-intensity excitation pulse for the excitation of fluorophores and a stimulated emission depletion pulse for the de-excitation of fluorophores. Similar to a confocal laser scanning system, only fluorescent light originating from the spontaneous decay of the fluorophores remaining in their excited state can be detected. In the stochastic optical reconstruction microscope (STORM) system, by sequentially activating and deactivating the numerous fluorophores, the position of each fluorophore can be determined with high precision. Much of the energy is wasted in both methods. Although the spatial resolution is high in the near-field optical scanning technique, the resolving power is dependent on the aperture size of the scanning fibre tip. Therefore, to achieve high spatial resolution, only few photons can pass through the subwavelength aperture and be detected by a sensitive photo multiplier (PMT). In the view of the above, the balance between the spot size and the efficiency of an imaging system is an important factor in the development of all optical super-resolution techniques.

Although light localization on a subwavelength scale is not the only way to achieve the optical super-resolution in a microscope system, the new scheme for generating nanoscale light localizations is still interesting and therefore an interesting challenge. This thesis will explore light localization by manipulating the characteristics of light and using various kinds of nanostructures, aiming to develop new schemes which can be applied to imaging instruments with nanoscale resolution, ultra-high density data storage or bio-sensing devices, etc. Topics will range from tailoring nanoscale light localization with metamaterials to the focusing ability and lensing function of a quasi-periodic

nanohole array. Theoretical analysis and experimental results will be presented, with the structure organized as follows.

In **Chapter 2**, it is reported how a metamaterial can be used as a controllable template for nanoscale light localization. Through numerical simulations and analytical calculations, the plasmonic resonant response will be investigated in detail.

In **Chapter 3**, an integration of a SNOM and a spatial light modulator (SLM) will be proposed to fire a single meta-molecule in a metamaterial system and to generate a single subwavelength hot-spot by modulating the light beam on a much larger scale. In this approach, the strong optically induced interactions between meta-molecules and coherent light beam with a spatially tailored phase profile will be used to generate isolated nanoscale energy hot-spots. With a simple adjustment of the phase profile, the energy hot-spot can be moved at will.

In **Chapter 4**, following a successful experimental demonstration through a super-oscillating binary mask with a 5-fold symmetry quasi-periodic nanohole array, a series of further investigations on different types of super-oscillating binary masks will be included. A well-isolated focused spot will be created by using a high-radial symmetry quasi-periodic nanohole array.

Chapter 5 will discuss the lensing function of different types of quasi-periodic nanohole arrays: (1) one-to-one imaging of a point light source and (2) a linear displacement of an imaged spot accompanied with a linear movement of a point light source. Through the imaging of complex configurations, the imaging resolutions of a nanohole array lens will be shown to be comparable to those of high numerical aperture lenses.

Finally, **Chapter 6** will summarize all of the research results contributing to this thesis, and then will provide an outlook suggesting possible applications based on primary findings.

2

Metamaterial as a controllable template for nanoscale light localization

2.1 Synopsis

In this chapter, a planar metamaterial with fish-scale nanostructures will be used as a new controllable template for nanoscale light localizations. With this double-periodic nanowire metamaterial, the subwavelength light localizations on the metamaterial landscape can be efficiently controlled by the polarizations and wavelengths of incident radiation.

To understand the resonant electromagnetic properties of fish-scale metamaterials, a brief introduction about unusual electromagnetic properties of the fish-scale metamaterials will be given in Section 2.2. In Section 2.3, a detailed description of the experimental arrangement, including a scanning near-field optical microscope (SNOM), and the geometry of fish-scale metamaterials will be provided. Then, Section 2.4 will summarize the experimental results of far-field spectroscopic measurements and near-field intensity mappings, while Section 2.5 will include theoretical investigations and comparisons to the experimental measurements. Finally, in Section 2.6, the array's resonant features in transmission and their dependence on the characteristic dimensions of the fish-scale pattern will be discussed, followed by conclusions of the chapter presented in Section 2.7.

2.2 Electromagnetic properties of fish-scale metamaterials

As described in Section 1.3, metamaterials constructed from artificial meta-molecules exhibit unusual electromagnetic properties that may not be found in nature, such as extraordinary optical transmission (EOT) through subwavelength nanohole arrays [184, 185], negative refraction of light in a medium whose effective permittivity ε and permeability μ are both negative [6, 186, 187], and invisibility over a narrow bandwidth of incident electromagnetic waves with gradient-index materials [139–142]. Usually, metamaterials gain their particular far-field electromagnetic properties from the nanoscale interactions between meta-molecules and the plasmonic responses of the composite nanostructures, which are mainly influenced by the structure or arrangement of the constituent meta-molecules rather than the material composition. Thus, with small

inhomogeneities or asymmetric structural changes on a subwavelength scale, effective macroscopic behaviours of electromagnetic waves can be created or controlled. The ability to manipulate electromagnetic properties allows metamaterials to have diverse potential applications, including super-resolution imaging apparatus, bio-sensing detectors, solar energy devices, high-gain and high-frequency antennas for communications, ultra-high density data storage, invisible shielding, and on-chip optical interconnects for future exascale computing systems, etc.

What is more, metamaterial nanostructures can be used as a controllable template for nanostructured optical field localizations. To illustrate this idea, a double-periodic subwavelength nanowire structure, a fish-scale pattern, will be used as an example for tailoring nanoscale light localizations [30]. Such a metamaterial with fish-scale nanostructures manifests rich resonant electromagnetic properties [188–190]. For example, when mounted on a metal backing plate, the fish-scale metamaterial acts as a "magnetic mirror" that reverses the magnetic field of the incident wave upon reflection rather than the electric field as a conventional mirror (see Fig. 2.1(a)) [188, 189]. Therefore, the magnetic field is cancelled in the plane of the magnetic mirror, which makes the magnetic mirror with fish-scale metamaterials act as a superconductor at optical frequency [189]. In other words, such a nanostructure can act as a local field concentrator and a resonant amplifier of losses in the underlying dielectric [188]. Furthermore, tilted fish-scale patterns that lack a plane of symmetry belong to the category of planar chiral nanostructures and show asymmetric transmission of light in opposite directions. This effect is different from the conventional gyrotropy of bulk chiral media and the Faraday Effect for its co-rotating elliptical polarization eigen-states [190, 191].

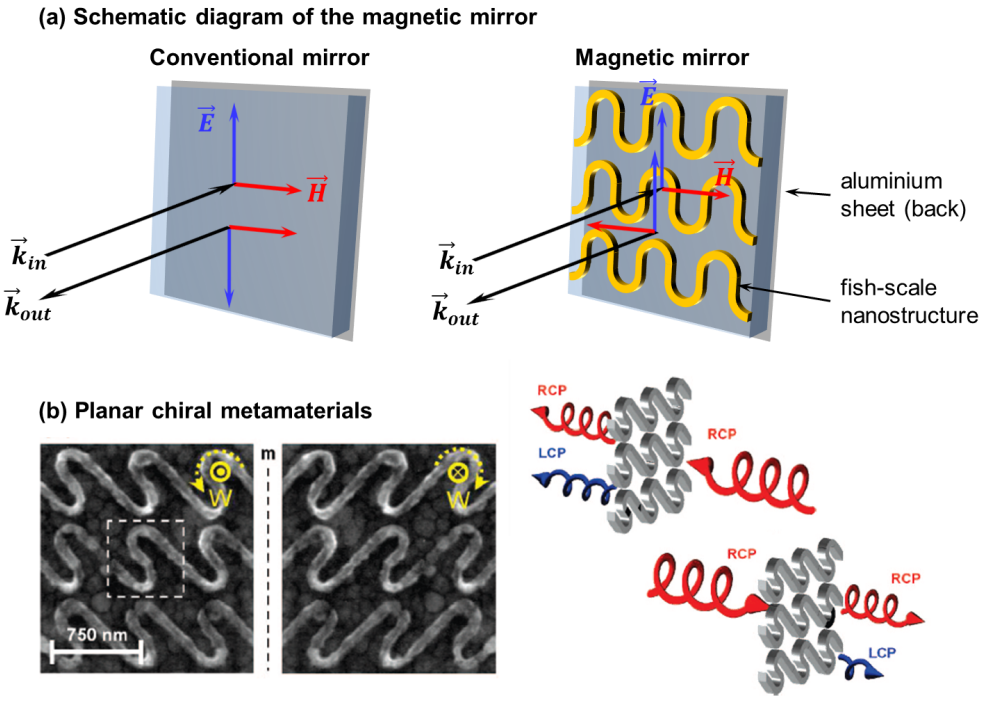

Figure 2.1: ***Electromagnetic properties of fish-scale metamaterials.*** *(a) Magnetic mirror with fish-scale metamaterials. Schematic diagram. Unlike a conventional mirror, the magnetic fields change upon reflection from a magnetic mirror and are cancelled in the plane of the mirror [189]. (b) Asymmetric transmission of light in opposite directions. Illustration of transmission and polarization conversion of circularly polarized light by a planar fish-scale metamaterial. The fish-scale metamaterials also support the enantiomerically sensitive plasmon excitations. Figures are from ref. [190].*

2.3 Experimental configuration

A fish-scale metamaterial array is used as an example of a controllable template for nanoscale energy hot-spots and plasmonic excitations in the immediate proximity of the metamaterial landscape is mapped by a SNOM with nanoscale spatial resolution. A schematic diagram of the experimental configuration and nanostructure of the fish-scale metamaterial samples are shown in Fig. 2.2 (a) and (b), respectively. For near-field mapping, a SNOM (Omicron Co., Twin-SNOM) is used and operated in collection mode, employing polarization-insensitive metal-coated SNOM tapered fiber probes (Jasco Inc.) with a 60 nm aperture. The SNOM scanning probe module is operated in the shear-force mode, while the distance between the tip and the sample is controlled by a feedback mechanism on the phase difference of the oscillating tip. By fixing a SNOM probe and linearly shifting the sample piezo stage (PI Co.), the transmitted

light is collected point by point to construct a near-field optical image. The pixel resolution of the constructed optical images is determined by the size of scanning area and the number of scanned points. To study the field distributions at different excitation wavelengths and polarization states, the samples are illuminated with a supercontinuum laser source (Fianium Co., SC450-2) through bandpass spectral filters with a bandwidth of 40 nm and a linear polarizer (used for determining the polarization direction). Also, the experiment is complemented by normal incidence far-field transmission measurements between 500 nm and 1900 nm using a microspectrophotometer (CRAIC Tech., QDI 2010). These spectral results can help us to understand the resonant features of the fish-scale metamaterial array and to choose the excitation wavelengths at which to examine the field distributions on the metamaterial landscape.

The fish-scale metamaterials were fabricated by Dr. Y. Chen at Rutherford Appleton Laboratory in the U.K. Aluminium nanowires of approximately 50 nm thickness and 50 nm width were fabricated using electron-beam lithography (EBL) on a 500 μm thick transparent silica substrate. The metamaterial samples consisted of double-periodic round fish-scale patterns with 440 ×440 nm^2 unit cells as shown in the schematic diagram in Fig. 2.2 (b). The total length S of the aluminium nanowire in a fish-scale meta-molecule unit cell was around 850 nm and the minimum gap between neighboring strips was 170 nm. The overall fish-scale metamaterial structure contained about 1.2×10^6 fish-scale meta-molecules and had lateral dimensions of 500 ×500 μm^2.

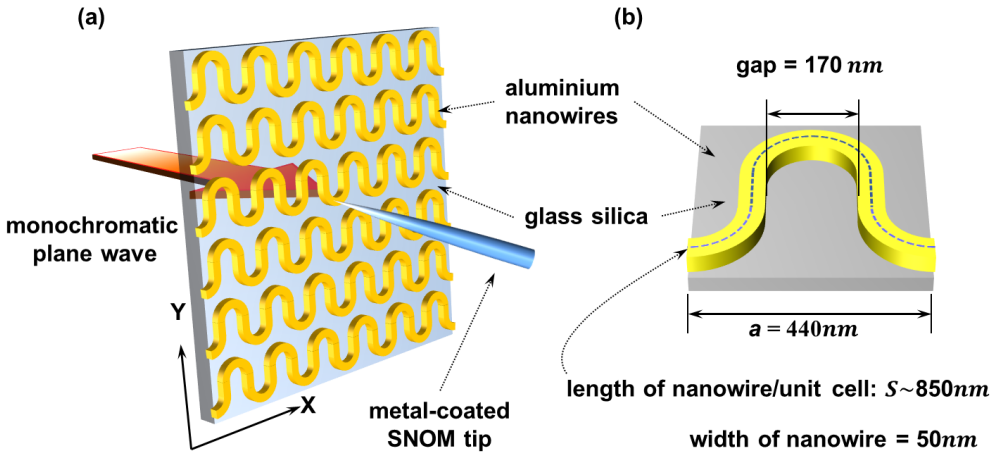

Figure 2.2: ***Mapping near-field light localizations on the landscape of double-periodic nanowire arrays.*** *Schematic diagram of experimental configuration. (a) With monochromatic plane wave illumination on a double-periodic nanowire array, the near-field intensity distributions in the immediate proximity of the metamaterial landscape are directly measured by using a SNOM. The X- and Y-axis indicate the polarization directions of the incident light beam. Plate (b) schematically shows the configuration of an aluminium fish-scale meta-molecule. The aluminium nanowires are etched on a silica substrate with a* 440 $\times$440 nm^2 *unit cell and the total length of the nanowire S in a unit cell is around* 850 nm.

2.4 Experimental results

2.4.1 Far-field optical transmission spectra of fish-scale metamaterials

Fig. 2.3 shows the measured geometry of the fabricated fish-scale metamaterial and the far-field optical transmission spectra of the metamaterial array at X (red) and Y (blue) polarizations. Fig. 2.3 (a) is a fragment of the scanning electron microscope (SEM) image of the fish-scale nanostructure, and Fig. 2.3 (b) is one of the sample topographies taken simultaneously with the near-field optical measurements. It is found that the topographic images correspond to the SEM image of a fabricated sample and are repeatable during each near-field optical measurement, suggesting that the dramatic difference of the field maps is not due to topography-related artifacts [192, 193] but a genuine manifestation of the intrinsic difference in the interaction of the nanostructures with light at different excitation wavelengths and polarizations. The X- and Y-axis indicate the polarization direction of the incident light beam.

The choice of wavelengths used for field mapping is explained in Fig. 2.3 (c), which shows the experimental transmission spectra of the fabricated sample for X-(red) and

Y-(blue) polarized light. It can be seen that the X-polarized spectrum (red) shows a resonant dip in transmission at around 700 nm, while the resonant frequency of around 1.15 µm at Y-polarization is linked to the known dipole excitation [188, 189]. The wavelengths used for SNOM mapping, indicated by the green dashed lines, are selected on the two wings of the transmission dip (550 nm and 850 nm) and close to its center (660 nm) in X-polarization.

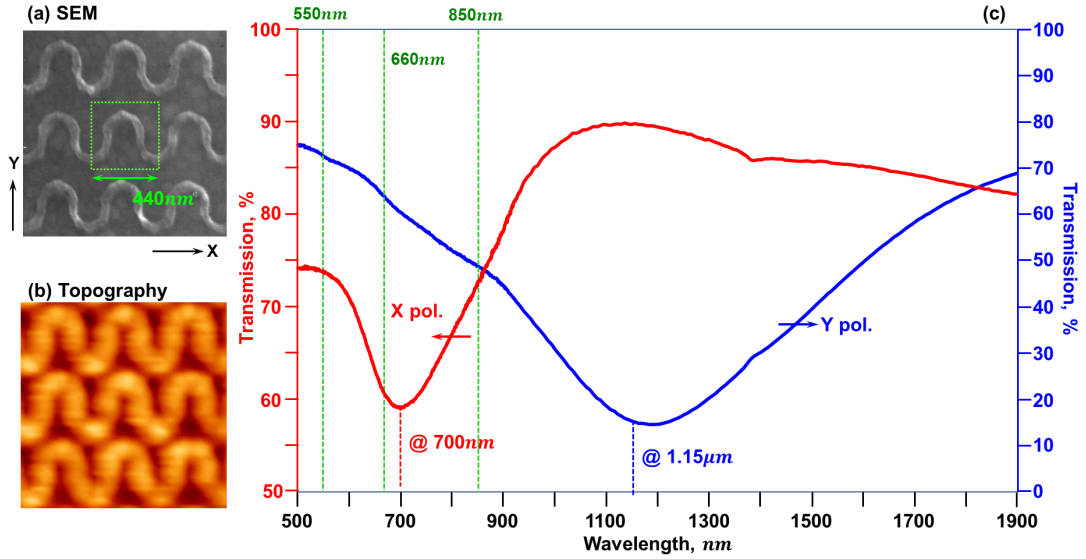

Figure 2.3: ***Measured geometry of the double-periodic nanowire arrays and the far-field optical transmission spectra at*** X ***and*** Y ***polarizations.*** *(a) shows the SEM image of the fish-scale nanostructure. (b) The sample topography taken simultaneously with the near-field optical measurements shows correspondence to figure (a). (c) Far-field optical transmission spectra of the double-periodic nanowire arrays. A resonant dip in transmission is at around* 700 nm *at x-polarization, while the resonant frequency is around* 1.15 µm *at y-polarization. The green dashed lines indicate the wavelengths used for SNOM mapping of* 550 nm, 660 nm, *and* 850 nm.

2.4.2 Near-field optical mapping on the fish-scale metamaterial landscape

Near-field mapping results for two orthogonal polarizations along and perpendicular to the nanowire meander and for three characteristic wavelengths are shown in Fig. 2.4. The green dashed fish-scale patterns indicate the corresponding locations of the fish-scale meta-molecules, which are taken from the simultaneous topographic measurements as shown in Fig. 2.3 (b). The dimension of the schematic green fish-scale pattern is close to the structural design as shown in Fig. 2.2 (b).

From Fig. 2.4, it can be clearly observed that nanoscale optical fields are able to be controlled by the wavelengths and polarizations of the incident light. For instance, X-polarized excitation appears to create subwavelength energy hot-spots with periodic field distributions. With a change of excitation wavelength from 550 nm to 660 nm, the hot-spot patterns are dramatically altered as Fig. 2.4 (a) and (b) indicate. A double periodic arrangement of deeply subwavelength hot-spots (125 nm, 0.23 λ) located at the vertical sections of the meander pattern at wavelength of 550 nm becomes a single periodic chess-board pattern of bigger hot-spots (175 nm, 0.27 λ) at 660 nm, occurring at the peaks and valleys of the meander. At the wavelength of 850 nm, though the size of the energy hot-spots can be as small as 130 nm (0.16 λ), the hot-spots pattern becomes blurred and ill-defined on the metamaterial landscape as Fig. 2.4 (c) shows. It can be found that the period and the locations of these subwavelength energy hot-spots correspond to the unit cell size and the positions of the fish-scale meta-molecules. Therefore, the maximum separation between the hot-spots on the fish-scale metamaterial landscape is the size of the unit cell, 440 nm. Regarding the Y-polarization, Fig. 2.4 (d) to (f) show that the hot-spots appear to be located between the meander rows at the wavelength of 550 nm, move to the areas between vertical sections of the meander design at 660 nm, and become a continuous strip pattern of ill-defined spots attached to the vertical sections of the meander at 850 nm. Such results show that the locations of the hot-spots show a high correlation with the nanostructure, the unit cell size, and the dipole absorption resonance of the fish-scale metamaterial.

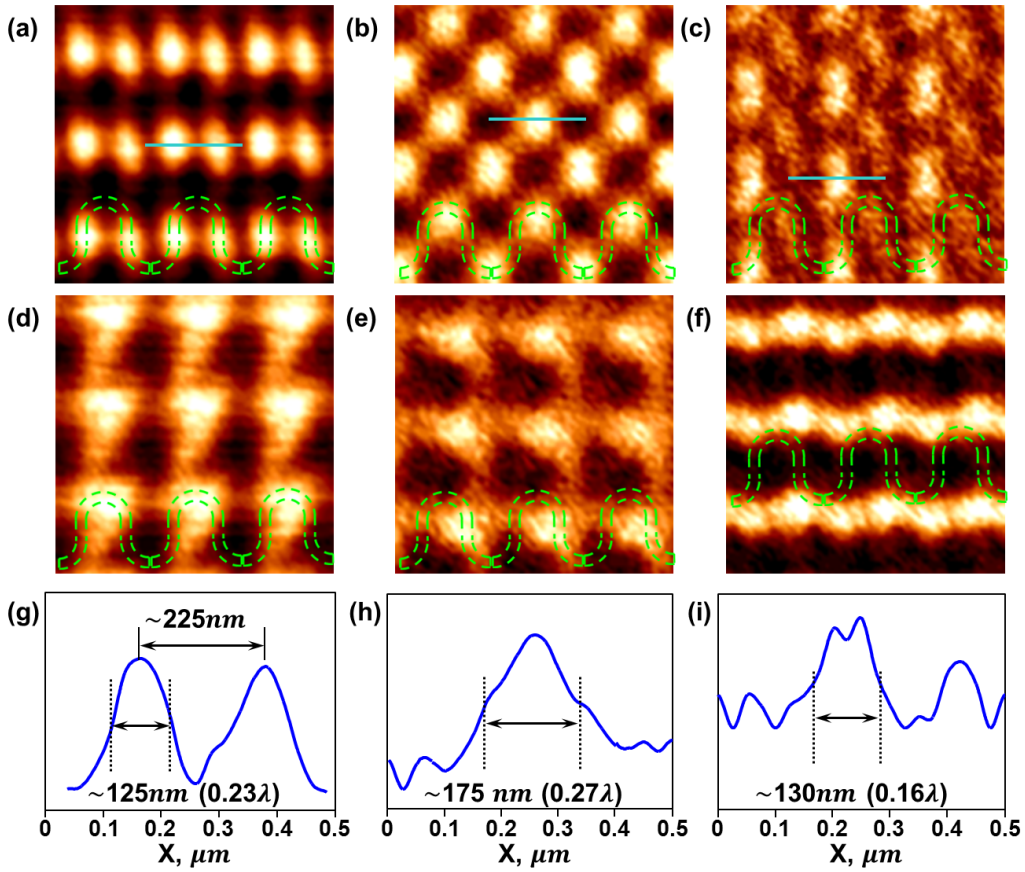

Figure 2.4: ***SNOM mapping of a double-periodic nanowire array (fish-scale pattern) at different wavelengths and polarizations.*** *The first and second rows show the near-field intensity maps for excitation polarized along (X) and perpendicular (Y) to the nanowire meander, respectively. Columns correspond to measurements at* 550 nm, 660 nm, *and* 850 nm *(from left to right). The bottom row shows field intensity profiles at the position indicated in the x-polarization maps. All maps are* 1.32×1.32 μm^2. *The green dashed fish-scale patterns indicate the corresponding locations of the fish-scale meta-molecules, which are taken from the simultaneous topographic measurements.*

2.5 Theoretical investigations

To understand the origin of the plasmonic field variations and the metamaterial array's resonant features, theoretical simulations of the far-field optical transmission spectra and the near-field distributions on the landscape of fish-scale metamaterials are conducted by using a 3D Maxwell solver (COMSOL). The comparisons between the simulation results and the experimental measurements will be analyzed and discussed below.

2.5.1 Far-field optical transmission spectra of fish-scale metamaterials

The COMSOL model for the calculating the far-field optical spectra of a fish-scale metamaterial array and the near-field intensity distributions on the landscape of fish-scale nanostructures are shown in Fig. 2.5. The fish-scale nanostructure within an unit cell of 440 ×440 nm^2 is placed on a semi-infinite silica substrate with a refractive index of 1.515, while incident illumination is from the bottom as in the experiments. The X and Y axes indicate the polarization directions of an incident light beam. The realistic material parameters and Joule loss factors of the aluminum nanowires are obtained from a well-established data of the dielectric parameters of the metal [194] as a function of excitation wavelength. In this numerical model, two perfectly matched layers (PML) are set to be at the top and the bottom domain to reduce interference effects in the numerical modeling. The boundaries in the X and Y directions are set to periodic boundary conditions, simulating an infinite fish-scale metamaterial array. Regarding the geometric structure of the fish-scale meta-molecules, a fish-scale nanostructure with the same structural design as the fabricated sample described in Fig. 2.2 (b) is used and two parameters which may change as a result of the fabrication processes are also varied in the simulations. One is the thickness t of the aluminium nanowires, while the other is the length l between the upper and the lower semicircles. The outer and inner radius of the semicircle are $R = 135$ nm and $r = 85$ nm (see Fig. 2.5), respectively. Thus, the width of the aluminium nanowires is fixed at 50 nm.

By integrating the power flow on the two integration planes, P_1 and P_2, with and without the existence of the metamaterial, simulated far-field optical transmission T, reflection R and absorption A spectra can be obtained through the following calculations.

$$T = |\vec{P}_{1,\,meta}|/\vec{P}_{1,\,air} \tag{2.1}$$

$$R = (|\vec{P}_{2,\,air}| - |\vec{P}_{2,\,meta}|)/|\vec{P}_{2,\,air}| \tag{2.2}$$

$$A = 1 - T - R \tag{2.3}$$

Simulated far-field optical transmission spectra of the aluminium fish-scale metamaterials with different geometric parameters are compared to the experimental measurements below.

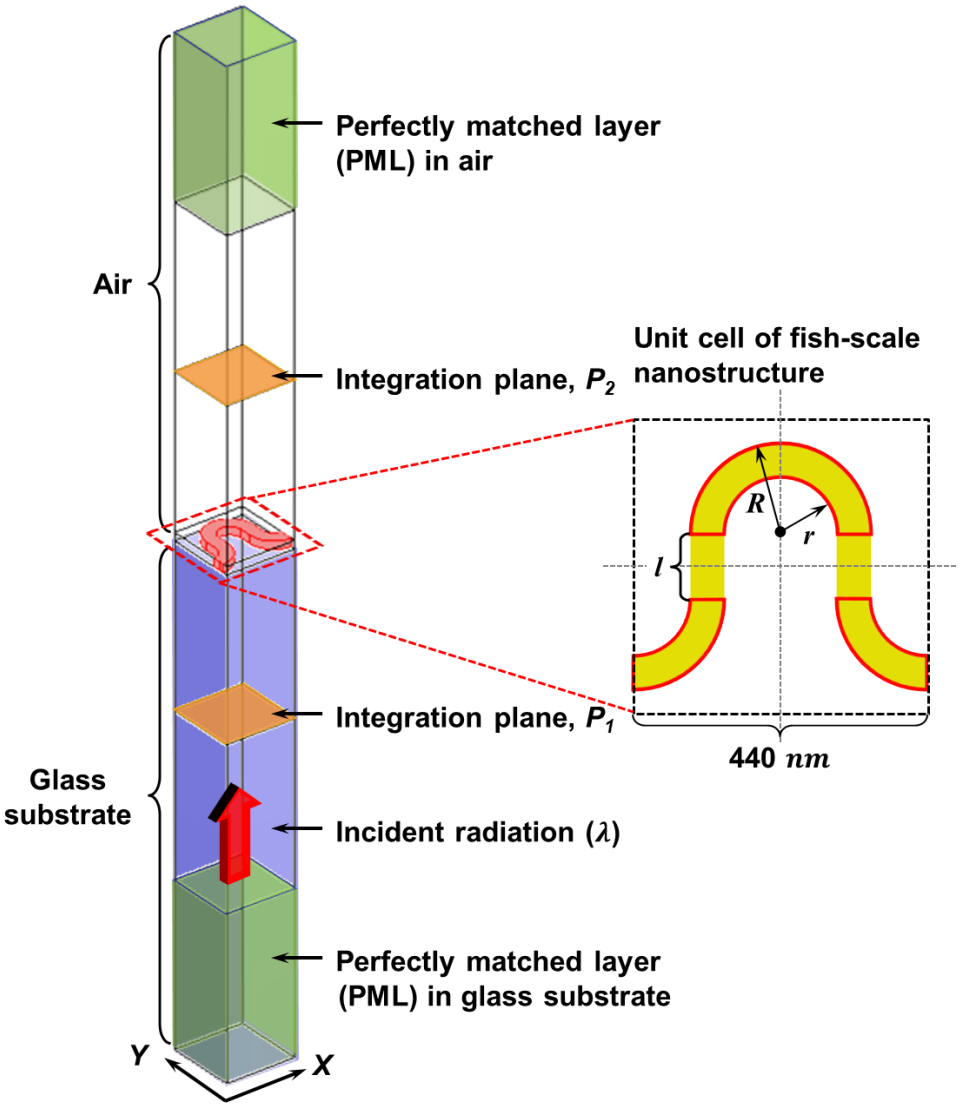

Figure 2.5: ***A model established in the COMSOL numerical simulations.*** *To acquire the simulated far-field optical spectra of a fish-scale metamaterial array and the near-field intensity distributions on the landscape of nanostructures, a model with a fish-scale nanostructure in an unit cell of* 440 ×440 nm^2 *is shown in the schematic diagram. Two PMLs are set to be at the top and the bottom domain for absorbing the outgoing waves. The boundaries in the* X *and* Y *directions are set to periodic boundary conditions, making the simulation results equal to the simulations of an infinite metamaterial array. The pattern of the fish-scale nanostructure is shown in the inset of the diagram and two geometric parameters of the nanostructure are varied in the numerical simulations: the thickness* t *of the aluminium nanowires and the length* l *between the upper and lower semicircles.*

Fig. 2.6 (a) and (b) show the comparisons between the experimental measurements of the fabricated sample and the simulated far-field optical transmission spectra of fish-scale metamaterials with different thickness t and lengths l with X- and Y-polarized excitation, respectively. In the geometric design which is the same as the fabricated

metamaterial sample (described in Fig. 2.2 (b)), the thickness of constituent nanowires is 50 nm and the length l between the top and bottom semicircles is 80 nm. The simulated far-field optical transmission spectra of such fish-scale nanostructures with X- and Y-polarized excitation are shown in Fig. 2.6 (a) and (b) by red lines. Both of the simulated optical transmission spectra display a qualitative agreement with the experimental spectra measurements (black dashed lines). The simulated spectrum with X polarization shows a narrow resonant dip in transmission at around 620 nm, while the experimental transmission spectrum shows the resonance at 700 nm. Also, with Y polarization, broad resonances occur at around 1 μm and 1.15 μm in the spectral simulations and experimental measurements, respectively.

These differences in the resonant frequencies may come from slight geometric changes in the fabrication process. Therefore, to match the experimental spectral measurements, the thickness t of the aluminium nanowires and the length l between the upper and lower semicircles are considered as possible structural changes and are varied in a series of simulations. As the gray lines show in Fig. 2.6 (a) and (b), a fish-scale metamaterial with a thickness of $t = 30$ nm shows resonances at 650 nm and 1.05 μm under X and Y polarization, respectively. In both the polarization directions, the resonances of the fish-scale metamaterials with smaller thickness are moved to longer resonant wavelengths. Moreover, by increasing the length l between the upper and lower semicircles to 150 nm, the resonances under the two orthogonal polarized excitations are matched well to the experimental spectra as the blue lines indicate in Fig. 2.6 (a) and (b), showing a narrow resonant dip in X polarization at around 690 nm, while a broad resonance in Y polarization is at 1.05 μm. The resonant features of a fish-scale nanowire array can be interpreted as described in Sec. 2.6.

From the simulated far-field spectra results, it is found that the structural changes of the fish-scale meta-molecules may cause a resonant frequency shift under both X and Y polarizations. With a length ($l = 150$ nm) between the upper and lower semicircles, the simulated resonant frequencies correspond to those in the experimental spectra. Such a length is nearly double the original structural design; however, such a large change is not seen in the SEM image and topographic measurements shown in Fig. 2.3 (a) and (b). A small difference from the original structural design is possible and it may come from the fabrication process. Another factor which might affect the resonant frequency

of the fish-scale metamaterials is dielectric parameters of the aluminium nanowires used in the simulations. However, different aluminium material parameters were not tested in my simulations.

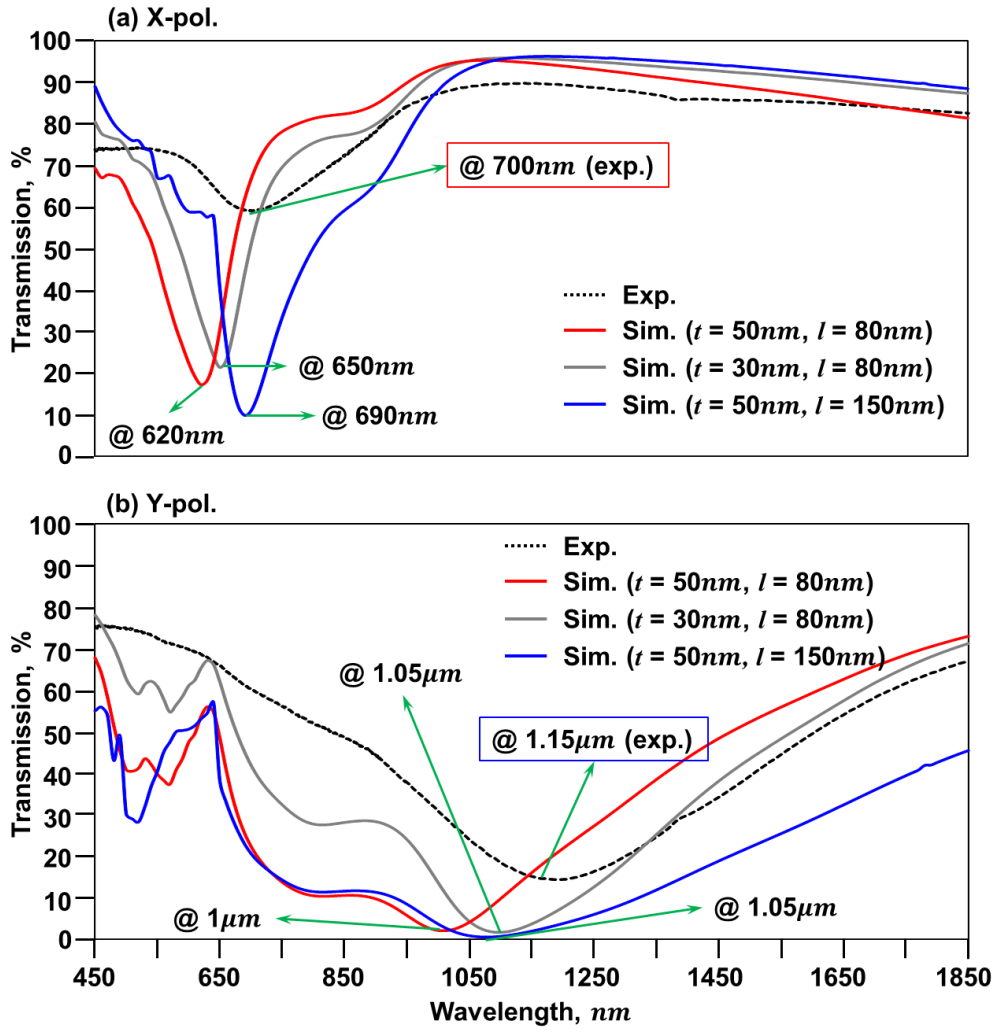

Figure 2.6: ***Comparison of far-field optical transmission spectra of the aluminium fish-scale metamaterials at different polarization directions.*** *Plates (a) and (b) display the comparison between the experimental spectra measurements (dashed black lines) of the fabricated fish-scale metamaterial sample and the simulated far-field optical transmission spectra of fish-scale nanostructures with different thickness t and lengths l at the X and Y polarizations, respectively. In this figure, the red lines represent the simulated far-field optical transmission spectra of a fish-scale metamaterial whose thickness t of nanowires and the length l between the upper and bottom semicircles are same as the fabricated fish-scale metamaterial sample ($t = 50$ nm; $l = 80$ nm). Gray lines indicate the simulated transmission spectra of the fish-scale nanostructures with a thinner thickness of* 30 nm, *while the blue lines display the simulation results as the fish-scale nanostructure with a longer length l of* 150 nm.

Besides the different resonant wavelengths, the different resonant depths shown in the comparisons of far-field optical transmission spectra may result from the defects in the fabricated samples, which make meta-molecules not identical to each other, causing a lower depth at the resonant dip [195]. Similarly, in the simulations, the another factor that influences the depth of the resonant dip is the dissipative parameter of the silica substrate. As the simulated transmission spectra show in Fig. 2.7, a broader resonance with a lower resonant depth will be obtained with an increase of the dissipative parameter ε''. These results were obtained from Dr. Zengbo Wang, who now is in the School of Electronic Engineering in Bangor University, U.K.

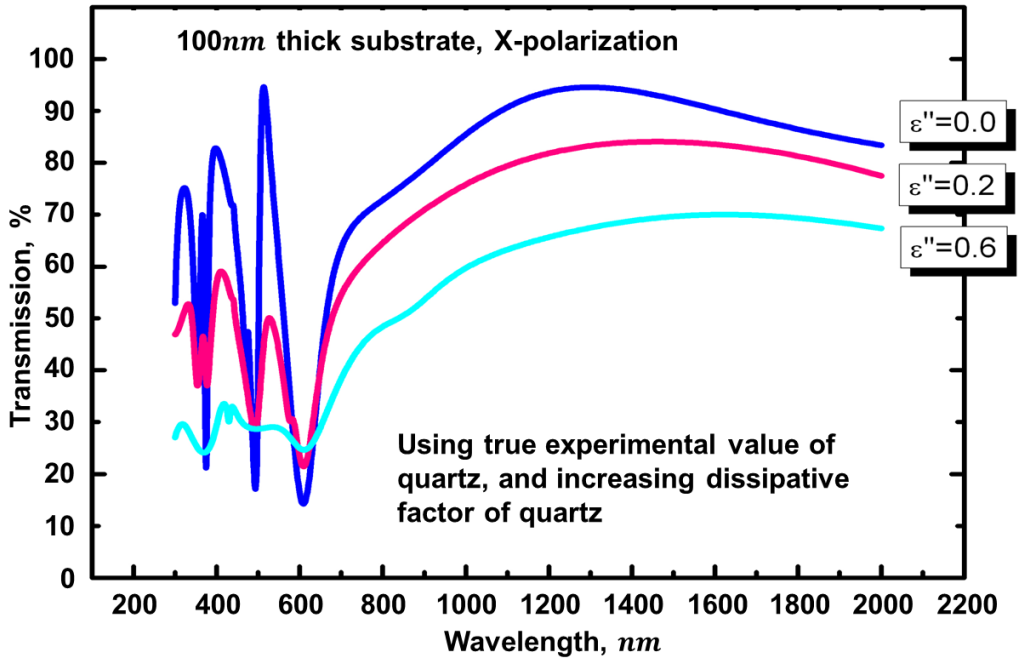

Figure 2.7: ***Simulated far-field optical transmission spectra of fish-scale metamaterials with different dissipative parameters of the underlying silica substrate.*** *Simulation results were obtained from Dr. Zengbo Wang, who now is in the School of Electronic Engineering in the Bangor University, U.K. The fish-scale metamaterial in the simulations has the same structural design as the fabricated metamaterial sample (unit cell:* $440 \times 440\ \mathrm{nm}^2$*, length* $l = 80$ nm *and thickness* $t = 50$ nm*) with different dissipative parameter* ε'' *of the silica substrate. As shown, a broader resonance with a lower resonant depth will be obtained by increasing the dissipative parameter.*

2.5.2 Near-field optical mapping on the fish-scale metamaterial landscape

By using the COMSOL 3D Maxwell equations solver, theoretical near-field optical field maps with different characteristic wavelengths and polarization directions can also be acquired. For comparison with the experimental SNOM mappings shown in Fig. 2.8 (a) under X-polarized excitation, Fig. 2.8 (b) shows the simulated plasmonic field distributions in the immediate proximity of the fish-scale nanostructure with the same structural design as the fabricated metamaterial sample. The excitation wavelengths employed in plate (*i*) to (*iii*) in (b) are 500 nm, 620 nm and 800 nm, respectively. The choice of these excitation wavelengths corresponds to the resonant dip, (red line in Fig. 3.6 (a)) which occurred at $\lambda = 620$ nm in the simulated optical transmission spectrum and two other wavelengths that are below (500 nm) and above (800 nm) the resonance. Here the simulation maps show the intensity distributions in the near-field region, selected as 10 nm above the surface of the fish-scale metamaterials. The variation of field distributions is similar to the pattern transition in the experimental results. However, such results still do not quite correspond to the experimental near-field mappings.

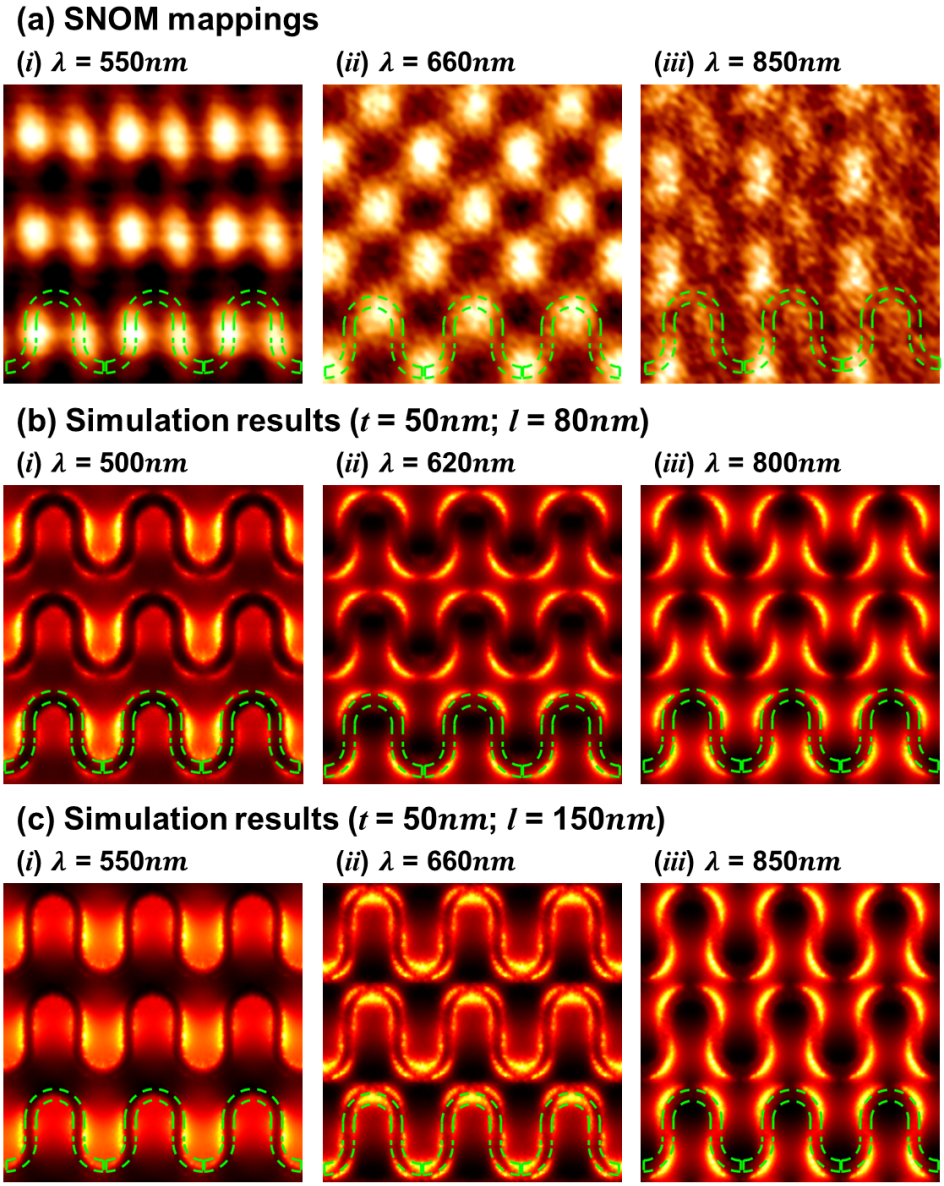

Figure 2.8: ***Comparisons of the plasmonic field distributions on the fish-scale nanowires array landscape: X polarization.*** *(a) SNOM maps. Plates (i) to (iii) in (a) show the near-field maps at wavelengths of* 550 nm, 660 nm *and* 850 nm, *respectively. (b) and (c) are the simulated field distributions. The fish-scale nanostructure in (b) is the same as the fabricated fish-scale metamaterial sample and the excitation wavelengths are* 500 nm, 620 nm *and* 800 nm. *The fish-scale meta-molecules in (c) have a longer length* $l = 150$ nm *in the nanostructure and the excitation wavelengths are the same as employed in the experiments. All maps have a size of* 1.32×1.32 μm^2.

To match the experimental optical near-field maps, a series of simulations with varying structural parameters of the fish-scale meta-molecules has been conducted. According to the far-field optical transmission spectra of fish-scale metamaterials as

shown in Fig. 2.6, the fish-scale meta-molecules with an increased length $l = 150$ nm has approximately the same resonances as the fabricated fish-scale metamaterial sample. Thus, such a fish-scale nanostructure with an increased length is simulated to examine the field distributions on the landscape of the metamaterial array. With the same excitation wavelengths and under X polarization, plates (i) to (iii) in Fig. 2.8 (c) show the intensity distributions on the surface of the fish-scale meta-molecules array at the wavelength of 550 nm, 660 nm and 850 nm, respectively. As shown, at a wavelength of 550 nm, the optical energy is concentrated as a pair of energy hot-spots on the two sides of fish-scale meta-molecules, while at $\lambda = 660$ nm, the energy hot-spots occur at the peaks and valleys of the meander and are attached to the vertical sections of the meander at the excitation wavelength of 850 nm. Such simulated intensity distributions are similar to the experimental mappings and a similar pattern transition across the resonant frequency is observed here.

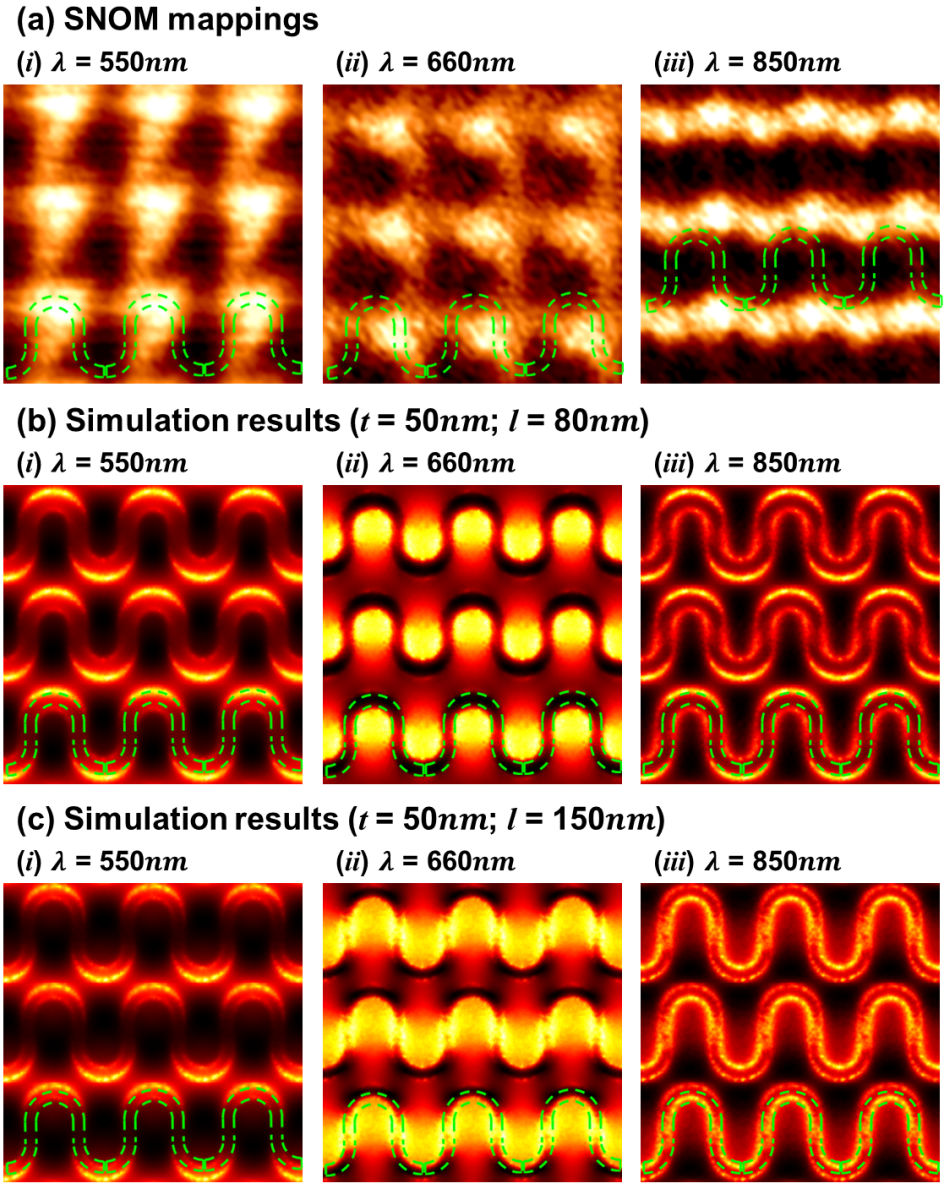

Figure 2.9: ***Comparisons of the plasmonic field distributions on the fish-scale nanowires array landscape: Y polarization.*** *(a) SNOM maps. Plates (i) to (iii) in (a) show the near-field maps at wavelengths of* 550 nm, 660 nm *and* 850 nm, *respectively. (b) and (c) are the simulated field distributions. The fish-scale nanostructure in (b) is the same as the fabricated fish-scale metamaterial sample and the excitation wavelengths are* 500 nm, 620 nm *and* 800 nm. *The fish-scale meta-molecules in (c) have a longer length* $l =$ 150 nm *in the nanostructure and the excitation wavelengths are same as what is employed in the experiments. All maps are in size of* 1.32×1.32 μm^2.

At the same wavelengths and under Y-polarised excitation, simulations on the two kinds of fish-scale nanostructures are shown in Fig. 2.9. In Fig. 2.9, plate (a) displays the experimental SNOM maps on the fabricated fish-scale metamaterial sample, while

plate (b) shows the simulated intensity distributions at 10 nm above the fish-scale metamaterial with the same structural design. Fig. 2.9 (c) represents the simulation results of the field distributions on an array of fish-scale meta-molecules with an increased length $l = 150$ nm. The corresponding excitation wavelengths are indicated in the figure and all the wavelengths are below the broad resonance at around $\lambda = 1.05$ μm. In the simulation results, the field distributions show a variation with wavelength and the optical energy is usually distributed over the nanowires, rather than generating localized energy hot-spots on the metamaterial landscape. However, compared with the experimental results shown in Fig. 2.9 (a), the simulated field distributions fail to reveal the same patterns.

The theoretical calculations above cannot achieve exact quantitative correspondence with the far-field spectral measurements or the near-field optical mappings probably due to the structural changes from sample fabrication process or oxidization, the displacement between tip aperture and fish-scale nanowire array in near-field measurements, the choice of dielectric parameters in the simulations, etc. However, a good qualitative agreement still demonstrates that the plasmonic field distributions can be efficiently controlled by manipulating the wavelengths of excitation and the polarization states. Although there are justifiable concerns on SNOM scanning probes causing disturbance to the near-field distributions [192, 193], our SNOM scanning results indicate that the influence of near-field probe does not dramatically change the field distributions and that the experimental data may indeed be interpreted as real near-field maps. In this study, the near-field scanning technique provides a reliable and powerful tool for directly mapping plasmonic fields in the immediate proximity of the metamaterial [196–198]. The ability of the metamaterials to concentrate light at a subwavelength scale is not surprising as the energy hot-spots are formed by the near-fields with large wave vectors and determined by the smallest elements of the metamaterial pattern. Nevertheless, the key is that plasmonic excitation patterns can be efficiently controlled by the polarization state and the wavelength of the incident radiation.

2.6 The resonant features of the nanowire fish-scale metamaterial arrays

When discussing the resonant features of the fish-scale metamaterial arrays, the double-periodic nanowire fish-scale nanostructures can be regarded as a sequence of double-strip line waveguide resonators terminated with a short-circuit section. Thus, the origin of the array's resonant features will correlate with the characteristic dimensions of the fish-scale nanowire patterns. Regarding the fish-scale nanostructure with the same structural design as the fabricated metamaterial sample, the full length of the strip, denoted S as described in the schematic diagram Fig. 2.2 (b), is approximately 850 nm within a translational unit cell of 440 $\times$440 nm. According to the previous investigations of fish-scale metamaterials in microwave region [199,200], the wavelength of an array's plasmonic resonant response is linked to the length of the strip resonators. At the main transmission dip, the oscillating electric field is polarized perpendicular to the direction of the strip (X-polarization), generating a standing wave on the strips with a wavelength, λ_s, which is close to $S/2$. This model should also work reasonably for the optical part of the spectrum. Considering the influences of the substrate, the excitation wavelength λ_i of incident radiation for the plasmonic resonance in the strip line waveguide can be roughly estimated as

$$\lambda_i = \lambda_s \sqrt{(\varepsilon + 1)/2}, \tag{2.4}$$

where ε is the permittivity of the substrate [200]. This estimation gives a value of 530 nm for the incident resonant wavelength for a transparent silica substrate with permittivity $\varepsilon = 2.1$, while the simulated resonant dip of the fish-scale nanostructure under X-polarized excitation (shown in Fig. 2.6 (a)) is at 620 nm. Considering the fish-scale nanostructure with an increased length $l = 150$ nm between the upper and lower semicircles, the full length of the strip line waveguide is around $S = 990$ nm in an unit cell of 440 nm^2. According to Equ. 2.4, the excitation resonance is around 615 nm, while the simulated far-field optical spectrum of this fish-scale nanostructure has a resonant dip at 690 nm (the solid blue line shown in Fig. 2.6 (a)). Such differences of the resonant excitation wavelengths may come from the the interactions across the

fish-scale meta-molecules, the finite width and thickness of the metal strips, and the Joule losses of the dielectric substrate. However, the estimated values of the resonant excitation wavelengths still show a qualitative agreement with the simulated and the experimental results above, suggesting the correlation between the resonant features of the fish-scale metamaterial arrays and the characteristic dimensions of the fish-scale nanowire patterns.

For the Y-polarized incident radiation, it is difficult to produce a simple and accurate estimation for the resonant frequencies. However, the resonance seems to appear when the wavelength of excitation in the nanowires is approximately equal to S [199, 200]. Therefore, with the same value of the permittivity of a transparent silica substrate ($\varepsilon = 2.1$), an estimated value for the resonant wavelength 1060 nm is given for the fish-scale metamaterial with the original structural design illuminated with Y polarization, while a resonant wavelength of 1230 nm is given the fish-scale nanostructure with $l = 150$ nm.

The assumption of the fish-scale metamaterials as a resonant waveguide structure suggests that variations of the energy hot-spot localizations caused by changing wavelengths and polarizations, result from a redistribution of the energy in the standing wave. Indeed, when tuning the excitation wavelength away from the plasmonic resonance, the standing wave pattern must redistribute to accommodate for the mismatch between the waveguide wavelength and the length of the strip inside the unit cell.

2.7 Conclusions

To pursue easier and better control of nanoscale light localizations, experiments have been conducted using of aluminium fish-scale metamaterials and have demonstrated rather positive results. It has been proved that subwavelength energy hot-spot distributions in the metamaterial nanowire landscape can be efficiently controlled by the wavelength and polarization of incident radiation. Moreover, subwavelength energy hot-spots as small as 0.23λ are achieved with X-polarized excitation, and their positions are controlled by tuning the wavelength of the incident light beam across the dipole absorption resonance of the fish-scale metamaterial. Although the experimental measurements fail to show a good quantitative agreement with the simulated results, their

qualitative similarity indicates that the influence of the near-field probe is negligible and the experimental data may be interpreted as real near-field intensity distributions. In conclusion, a near-field pattern transition across the plasmonic resonant dip can be quickly and efficiently achieved by tuning the polarization and wavelength of an incident light beam. Also, the positions of the hot-spots show a high correlation with the locations of meta-molecules. Related techniques can be used for tailoring and templating of nanostructured optical fields such as optical trapping, linear and nonlinear molecular spectroscopy, and Raman scattering.

3

Coherent control of nanoscale light localization with metamaterials

3.1 Synopsis

In this chapter, a new approach to precise control of subwavelength light localizations will be investigated. By illuminating an array of interacting meta-molecules with a spatially phase-modulated light beam, isolated nanoscale energy hot-spots can be created in the immediate proximity of a plasmonic metamaterial and moved at will from one meta-molecule of the array to another, thus providing new opportunities for imaging and optical data storage.

In Section 3.2, an introduction to different methods of creating and controlling nanoscale light localizations will be presented, followed by an explanation of our new approach to nanoscale localizing light through the coherent control process. Then, the resonant features of the interacting meta-molecules and a detailed description on the numerical model will be discussed in Section 3.3, while a series of simulation results will be described in Section 3.4. In Section 3.5, a calculation of a simple model which treats current oscillations in individual meta-molecules as point-like dipoles will provide a physical picture of the coherent control system. Also, the feasibility of the modulated field will be considered by decomposing the field into a combination of harmonics. To experimentally demonstrate the idea of coherent control of nanoscale light localization, the details of the experimental setup will be given in Section 3.6, and the experimental results will be described and analyzed in Section 3.7. At the end of this chapter in Section 3.8, the conclusions of this work will be summarized and further applications will be discussed.

3.2 Introduction

3.2.1 Different approaches to control nanoscale light localizations

Precise control and manipulation of optical fields on the nanoscale is an important challenge to conquer in nanophotonics. However, it cannot be overcome by employing conventional focusing methods since the optical wavelength is on a much larger microscale. To achieve the goal of controlling nanoscale light localizations, several approaches have emerged in the last decade [20–31]. For instance, in 2002, a method was suggested based on tailoring phase modulation of ultra-short optical pulses in the time

domain to achieve coherent control of the spatial distribution of energy in designed nanostructures and complex inhomogeneous nanosystems as demonstrated in plates (*i*) and (*ii*) in Fig. 3.1 (a), respectively [26]. In such nanosystems, the localized plasmonic frequencies vary from nanoscale feature to nanoscale feature and thus can be correlated with their positions. The phase modulation of the optical pulses will cause the exciting field to take energy away from surface plasmons localized in those parts of the system where the oscillations are out of phase with the driving pulse. Then, the field localizations will be moved with time to the surface plasmon excitations in other parts where such oscillations occur in phase with the driving pulse as the calculation results show in Fig. 3.1 (b). With phase modulation of the femtosecond optical pulses, the intensity distributions on a designed V shape nanostructure can be controlled and positioned in the time domain. This idea was later experimentally supported by a similar method based on tailoring of ultra-fast pulses in the vicinity of silver nanostructures through adaptive polarization shaping as the schematic representation and experimental results show in Fig. 3.1 (c) and (d) [28].

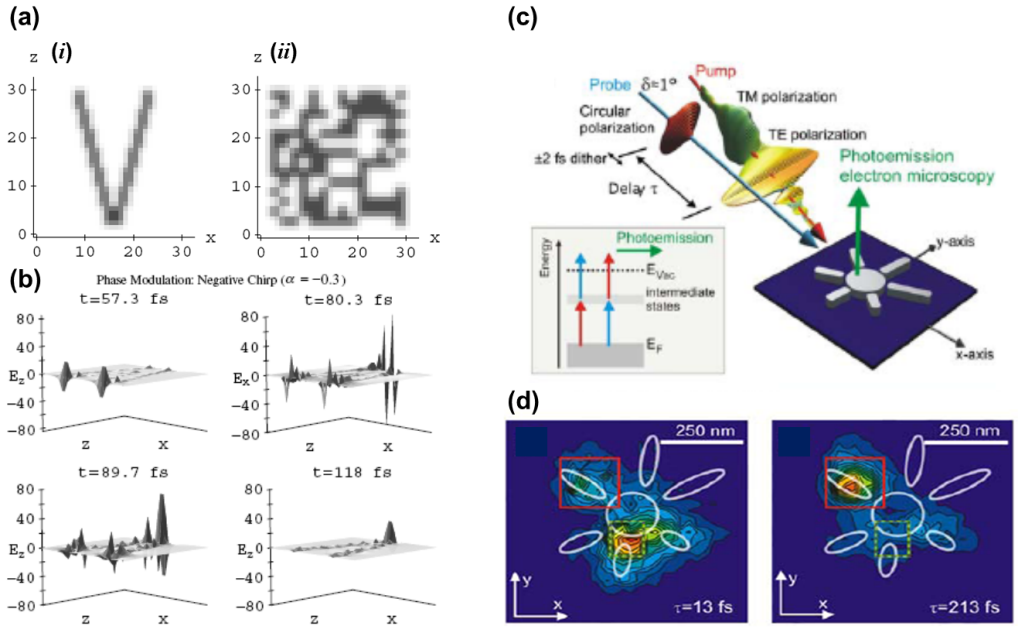

Figure 3.1: ***Spatiotemporal control of nanoscale field excitations.*** *In a designed nanostructure (i) and a complex inhomogeneous nanosystem (ii) shown in plate (a), coherent control of the spatial distribution of energy in nanosystems can be achieved by tailoring the phase modulation of ultra-short optical pulses in the time domain. With this approach, the localized plasmon frequencies vary from nanoscale feature to nanoscale feature and thus can be correlated with their positions [26]. As the calculation results in plate (b) demonstrate, the field localizations on a designed V shape nanostructure can be moved with time by tailoring the phase modulation of femtosecond optical pulses. Regarding experimental demonstrations of coherent control of localized fields in nanosystems, plate (c) schematically shows the experimental configurations with adaptive polarization shaping and modulation of incident ultra-fast optical pulses. By shining the modulated optical pulses onto a star shape silver nanostructure, the energy hot-spot can be repositioned as the experimental results show in plate (d) [28]. Figures are obtained from refs. [26, 28]*

As for other approaches to control nanoscale light localizations in the near-field region, several novel methods have been proposed and investigated recently using different types of nanostructures and manipulating different characteristics of an incident light beam. Some of them will be summarized below.

(a) **Spatially phase-shaped beams illuminating nanoantennas.** By tuning the polarization singularities and subwavelength spatial phase variations at the focus of high-order beams, the near-field distributions on plasmonic nanoantennas can be reconfigured as shown in Fig. 3.2 (a) [21].

(b) **Tailoring plasmon interference by illuminating nanohole arrays with phase modulation.** By actively controlling the light illumination on nanohole

arrays with optimized amplitudes and phases, an energy hot-spot can be created and positioned at an appointed location through plasmon interferences on the metal surface as demonstrated in Fig. 3.2 (b) [29].

(c) **Deterministic optical inversion protocol to achieve required near-field patterns on plasmonic nanostructures.** Based on an exact inversion of the response tensor of a nanosystem, the deterministic optical inversion protocol can provide a physical solution for the incident field leading to generation of a desired near-field pattern on the surface of a nanostructure. Such a result can be expressed in the form of a coherent superposition of high-order beams. Some calculation results are shown in Fig. 3.2 (c) [22].

(d) **Gratings illuminated with incident waves of optimized amplitudes and incident angles.** By optimizing the amplitudes and incident angles of continuous-wave light beams with twelve orientations illuminating on a subwavelength diffraction grating, an isolated light localization can be produced and moved across the grating's surface. The models and calculation results are shown in Fig. 3.2 (d) [20].

These approaches all provide new opportunities for controlling light behavior on the nanoscale; however, they only can be performed through complex nanosystems or the sophisticated manipulation of the incident light beams. Moreover, the nanoscale light localizations can only be moved in a small confined area. As a result, they will increase the costs of nanofabrication and practical realization on the one hand, and will be confined to limited nanosystems on the other. To compensate for these weaknesses, several approaches to nanoscale light localizations control based on the exploitation of metamaterials have been proposed and will be presented below.

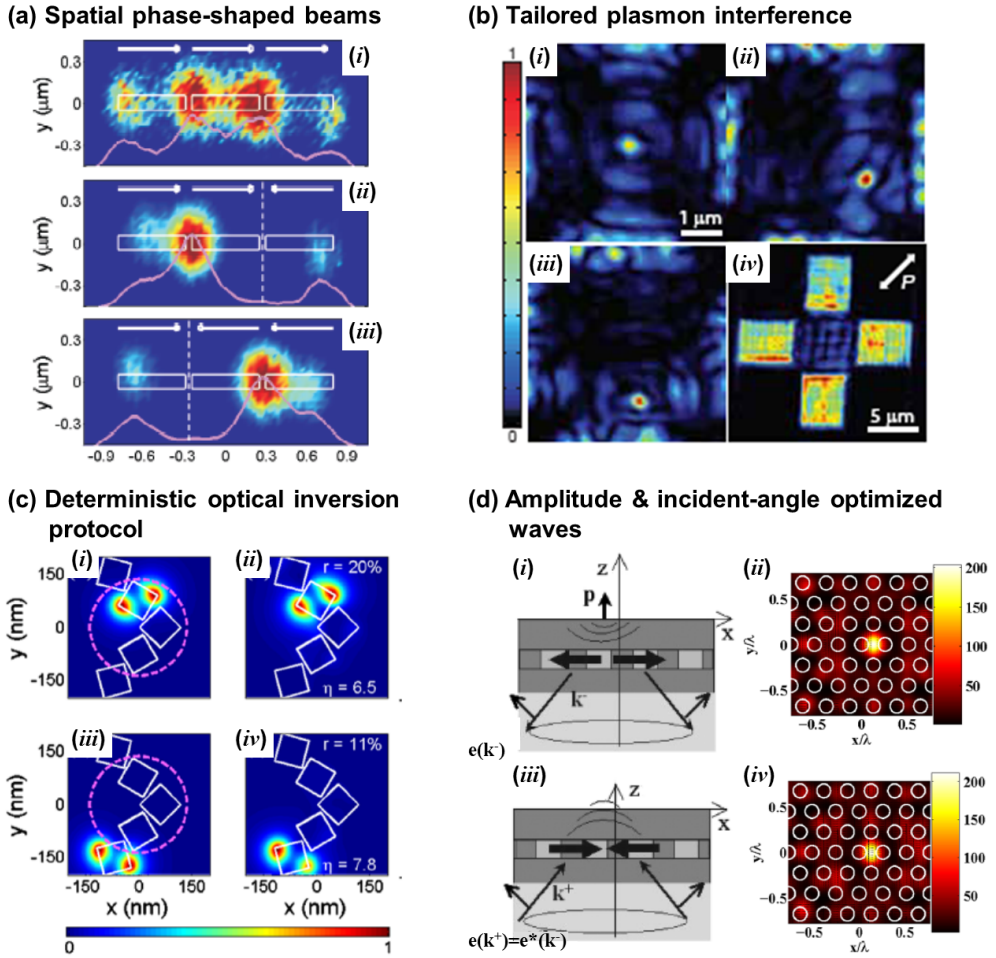

Figure 3.2: ***Different approaches to controlling the nanoscale light localizations in the near-field region.*** *(a) By controlling the polarization singularities and the subwavelength spatial phase variations at the focus of high-order beams, the near-field distributions on plasmonic nanoantennas can be reconfigured [21]; Figure (a) shows the experimental maps recorded for (i) a Gaussian beam and (ii, iii) a HG_{10} beam with a phase shift. (b) By choosing the polarization directions and optimizing the amplitudes and phases of incident light beams applied on four surrounding nanohole arrays, an isolated light localization can be produced and positioned through the tailoring of the plasmon interference waves [29]. (c) With the method of the deterministic optical inversion protocol, required near-fields patterns on nanostructures can be obtained by an exact inversion of the response tensor of a nanosystem [22]. (d) By illuminating the amplitude and incident-angle optimized waves on a subwavelength diffraction grating, an energy localization can be obtained and positioned on the surface of the grating [20]. Figures are obtained from ref. [20–22, 29]*

3.2.2 Controlling nanoscale light localizations through metamaterials

From the discussions of metamaterial research in the previous chapter, it is known that near-field light localizations can be generated and controlled by using a planar metamaterial as a controllable template, illuminated with corresponding resonant frequencies

and polarizations as demonstrated in Fig. 3.3 (a) [30]. Recently, another approach based on the position variations of an array of interacting meta-molecules has been experimentally demonstrated in the microwave region, creating highly concentrated nanoscale energy localizations on the metamaterial landscape [201]. Fig. 3.3 (b), plate (i) shows the image of a metamaterial sample with a little disorder in the arrangement of round asymmetrically split-ring (ASR) meta-molecules, while plate (ii) shows the near-field mapping close to the sample surface. In these results, several energy hot-spots can be created by carefully choosing the resonant frequencies and polarization directions of an incident radiation. From the aspect of design of the meta-molecules and the cost of sample fabrication, it is advantageous to utilize metamaterials with different meta-molecules as a platform to control nanoscale light localizations for different purposes.

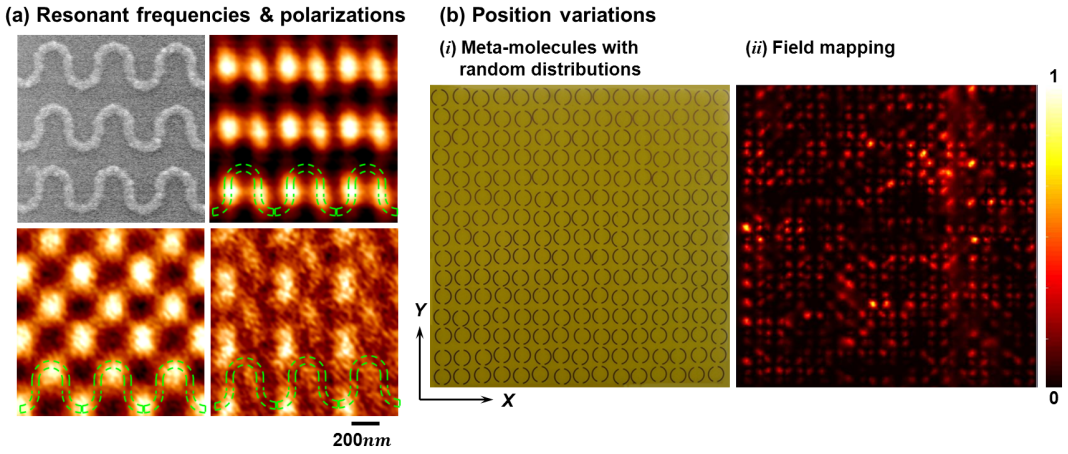

Figure 3.3: ***Controlling near-field light localizations in metamaterial systems.*** *(a) By tuning the excitation wavelengths and polarization states of an incident light beam illuminating a planar metamaterial with fish-scale nanostructure, energy hot-spots can be controlled on the landscape of periodic metamaterial system [30]. (b) By position variation in an array of round ASR meta-molecules, strong light localizations can be produced due to the strong interactions between the interacting meta-molecules [201].*

3.2.3 Coherent control of nanoscale light localizations in an array of interacting meta-molecules

Due to the fact that the size of unit cell in metamaterials is much smaller than the wavelength of excitation, it is very difficult to separate the generated energy hot-spots with a significant distance from each other and form a single, isolated subwavelength

energy hot-spot when a metamaterial system is illuminated with a monochromatic plane wave. This scheme also lacks the flexibility to move the hot-spot arbitrarily on the metamaterial landscape. Thus, in this chapter, we intend to develop a new scheme which only fires a single meta-molecule, generating an isolated subwavelength energy hot-spot in the proximity of a plasmonic metamaterial. This approach can be achieved by modulating the spatial phase of an incident light beam on a much larger scale and with the help of intense interactions and energy exchange between the interacting meta-molecules. Moreover, once an isolated subwavelength energy hot-spot can be created on a single meta-molecule, the nanoscale size of unit cells becomes an advantage in controlling the movement of the energy hot-spot. By shifting the modulated beam, an isolated light localization, or other required pattern, can be moved on the landscape of metamaterials with nanoscale accuracy; that is the same scale as the size of unit cells.

Fig. 3.4 provides a physical picture of this new approach, showing an artistic representation of a metamaterial array excited by a wave with a spatially tailored phase profile. Here, an isolated energy hot-spot can be created on the other side of the array in its immediate proximity. As shown in Fig. 3.4 (a), with a plane wave illuminating a metamaterial system, the interactions of the emitted fields between the meta-molecules are equal and simultaneous. Therefore, the energy will be homogeneously distributed and located on each meta-molecule, forming nanoscale energy hot-spots distributed with the same period as the meta-molecules. However, by allowing spatial phase modulation in the driving fields, as in the schematic in Fig. 3.4 (b), the emitted fields from each meta-molecules will drive in turn the neighboring meta-molecules. In this process, a wave is scattered more than once by the same meta-molecule, resulting in strong interactions between meta-molecules and optical energy concentration onto a single meta-molecule, with a strongly localized peak formed.

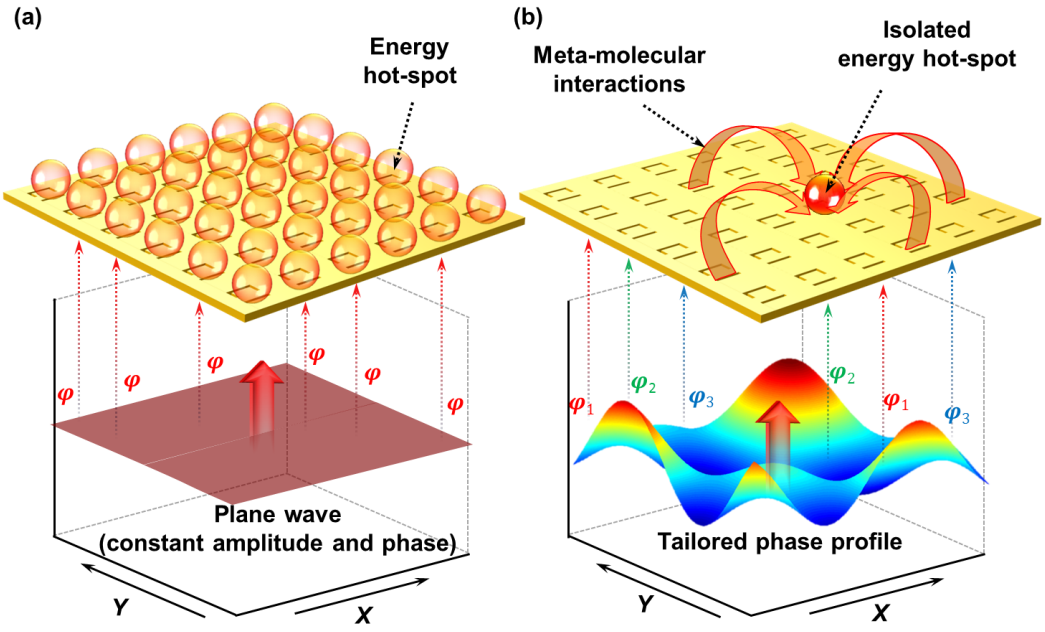

Figure 3.4: ***Plasmonic metamaterials as a near-field focusing device.*** *Artistic impression. (a) With monochromatic plane wave illumination on a planar metamaterial, the interactions between the constituent meta-molecules are equal and simultaneous. Therefore, the optical energy will be homogeneously distributed and located on each meta-molecule, forming periodic energy hot-spots generated on the metamaterial landscape. The separation between the energy hot-spots is equal to or smaller than the size of unit cells. (b) By spatially tailoring the phase profile of an incident light beam, the strong optically-induced interactions between the meta-molecules in a metamaterial system can lead to the formation of a single subwavelength hot-spot located on a certain meta-molecule. This spot may be moved from one metamaterial cell to another by tailoring the phase profile of the incident beam.*

The idea above has a clear mechanical analogue in two coupled identical oscillators (modeling nano-objects) that may be driven to different amplitudes by setting up a phase delay ($\Delta\varphi = \varphi_1 - \varphi_2$) in between the two driving forces (F_1 and F_2). Here, the two driving forces are in sinusoidal form with the same amplitude A as indicated in Fig. 3.5 (a), while the two identical oscillators (blue and red) are connected with a spring with a spring constant of $k_{spring} = 0.25$. Therefore, the dynamics of the two identical oscillators can be obtained from the following simultaneous equations:

$$\begin{cases} \ddot{x_1}(t) + \gamma\dot{x_1}(t) + \omega_0^2 x_1(t) + k_{spring}(x_1(t) - x_2(t)) = Asin(\omega t + \varphi_1) \\ \ddot{x_2}(t) + \gamma\dot{x_2}(t) + \omega_0^2 x_2(t) + k_{spring}(x_2(t) - x_1(t)) = Asin(\omega t + \varphi_2) \end{cases} \tag{3.1}$$

with the initial conditions: $x_1(0) = x_2(0) = 0$; $\dot{x}_1(0) = \dot{x}_2(0) = 0$. Here, to simplify the

simultaneous equations, we assume $\gamma = \omega_0 = A = 1$. Fig. 3.5 (b) shows the calculation results of the amplitude difference ($\Delta A = A_1 - A_2$) between the two identical oscillators in the final steady state. When the driving forces are at the same amplitude and in phase ($\Delta\varphi = 0$), there is no amplitude difference between the two coupled oscillators, which suggests the same energy is stored in each oscillator. When we apply a little phase difference to one of the sinusoidal driving forces, the amplitude difference between the two oscillators indicates that the energy is transferred and stored in one of these two coupled oscillators. The maximum amplitude difference in this specific case is at the phase difference of $\pi/2$ when the driving frequency ω of the driving forces is equal to the resonant frequency ω_0 of individual oscillators. From the result of such a mechanical analogue of the coherent control process, optical energy exchange between the resonant meta-molecules can be expected.

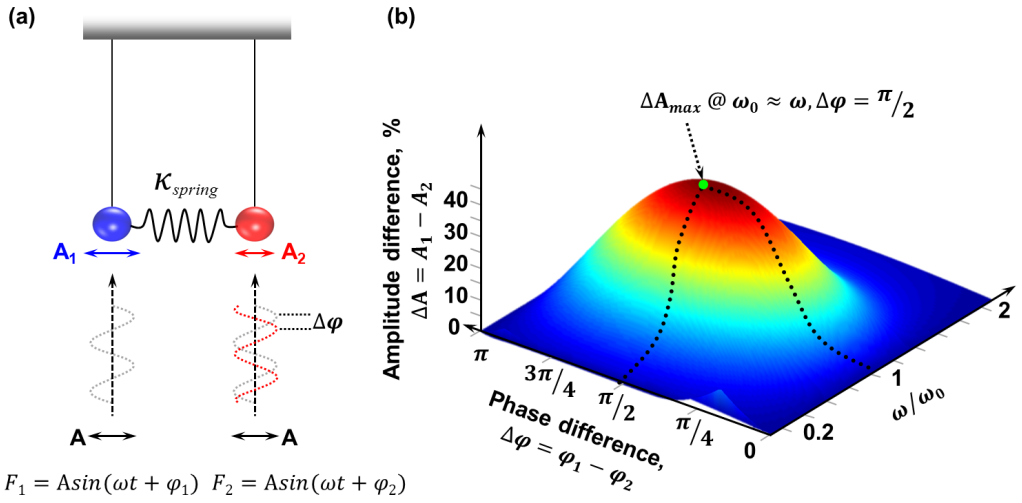

Figure 3.5: ***A mechanical analogue illustrating energy localization by coherent (phase) control of the two driving forces.*** *(a) schematically displays the model of two identical coupled oscillators driven by two sinusoidal driving forces with a phase delay. Identical coupled oscillators driven at the same frequency with the same amplitude will be excited to different levels if they are driven with a phase delay. (a) Here oscillators represent individual meta-molecules of the metamaterials structure. Plate (b) shows the difference between the amplitudes of oscillation as a function of frequency ω and phase difference φ between driving forces. Here ω_0 is the resonant frequency of individual oscillators. The idea of coupled resonators illuminated by a phase modulated beam has a clear mechanical analogue in two coupled identical oscillators (modeling nano-objects) that may be driven to different amplitudes by setting up a phase delay between coherent mechanical forces.*

3.3 The sample descriptions and details of the numerical modeling

To analyze the metamaterial systems under an incident illumination with a spatially tailored phase profile, a direct quantitative numerical simulation using a 3D Maxwell solver (COMSOL) is conducted by qualitatively modelling the plasmonic metamaterial array. In all numerical simulations, we focus on the visible and the near-infrared parts of the spectrum, assuming that metamaterial structures are constructed of gold plasmonic resonators with realistic material parameters and Joule loss factors from well-established data of the dielectric parameters of the metal [194]. An analysis of the design of the plasmonic resonators and the details of the numerical model will be described below.

3.3.1 ASR plasmonic resonators and and the corresponding resonant modes at different frequencies

In the numerical models, meta-molecules with square ASR patterns are used as an array of nanoscale plasmonic resonators in a metamaterial system. The choice of an ASR array is inspired by recent studies that established the key role of inter-meta-molecular interactions in forming the electromagnetic response of the ASR metamaterials [195]. This metamaterial consists of ASR meta-molecules with a lattice period of 440 nm both in the X and Y directions. Considering the illumination wavelengths available in the visible and near-infrared range of the spectrum and restrictions on the sample fabrication, an optimum choice of the ASR meta-molecules' size is 200 $\times$200 nm^2. As shown in the schematic diagrams in Fig. 3.6, two types of ASR meta-molecules are modelled in the numerical simulations. One is the positive ASR meta-molecule composed of gold nanorods whose width is $w_r = 25$ nm arranged in a split square shape (see Fig. 3.6 (a)), while the other is the negative ASR meta-molecule with the same split square shape perforated through a metallic gold thin film (see Fig. 3.6 (b)). The width of the constituent nanoslits is $w_s = 25$ nm. Both the gaps g between the upper and lower parts of the two ASR nanostructures are 75 nm.

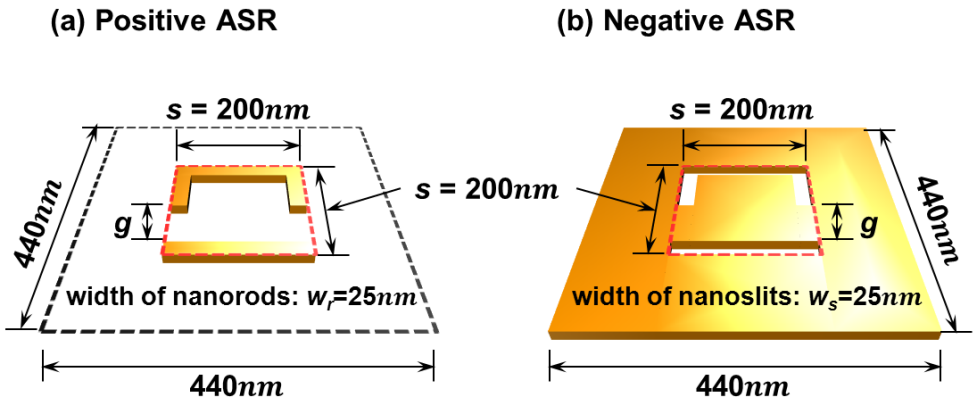

Figure 3.6: ***Asymmetrically split-rings (ASR) meta-molecules as the nanoscale plasmonic resonators in a metamaterial system.*** *Schematic diagrams. In the numerical models, two types of square ASR meta-molecules are used. One is positive ASR meta-molecules with* $w_r = 25$ nm *gold nanorods arranged in a split square shape of* 200×200 nm^2*, while the other is negative ASR meta-molecules perforated with slits* $w_s = 25$ nm *arranged with the same square shape on a metallic gold thin film. The size of unit cells is assumed to be* 440×440 nm^2 *and the gap* g *between the upper and lower nanostructures of the ASR meta-molecules is* 75 nm.

To analyze the resonant modes of the square ASR plasmonic resonators as a function of excitation wavelength, the simulated far-field optical spectra of a free-standing ASR metamaterial are calculated by using a 3D Maxwell solver (COMSOL) and the surface current distributions on the ASR meta-molecules are acquired at different characteristic excitation wavelengths. With the positive ASR meta-molecules and X polarized excitation, the positive square ASR metamaterial with a thickness of 100 nm shows a well-defined plasmonic absorption resonance at $\lambda = 790$ nm corresponding to a local maximum in reflection and a minimum in transmission (Fig. 3.7 (a)). By analyzing the electric field in the Z direction on the surface of the ASR meta-molecules, proportional to the surface charge density [202], the electric charge distributions can be obtained at different excitation wavelengths as the results in Fig. 3.7 (c) to (e) show, and the directions of surface electric currents can be schematically plotted (black arrows). According to V. V. Khardikov *et al.*$'s$ work [203], at the wavelength of 1.05 μm, the closed circulation of electric currents on the surface of ASR meta-molecules represents a magnetic dipole mode perpendicular to the array, while an electric dipole parallel to the surface and an electric quadrupole are the dominant resonant modes at excitation wavelengths of 790 nm and 650 nm, respectively.

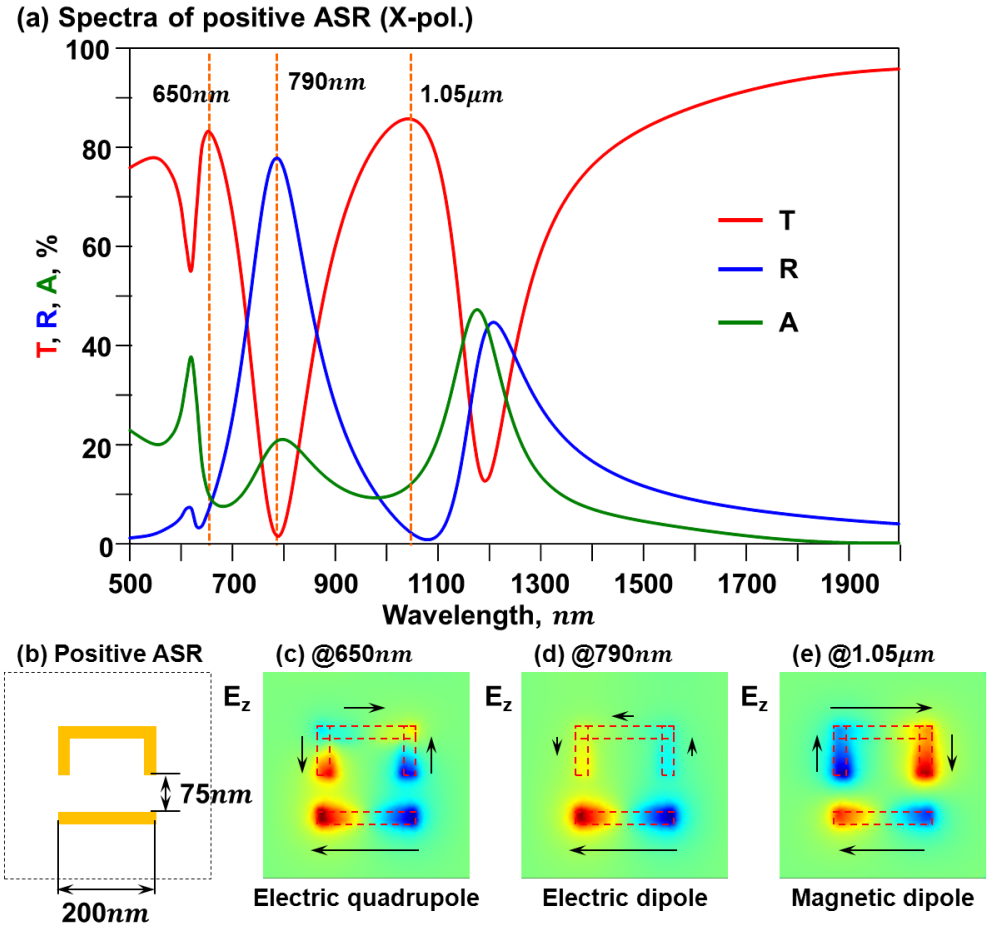

Figure 3.7: ***Simulated far-field optical spectra of an ASR metamaterial array and the surface current distributions at different characteristic wavelengths: Positive ASR nanostructures.*** *Simulation results. With plane wave illumination and X-polarized excitation, the array of positive ASR nanostructures has a well-defined plasmonic resonance at* $\lambda = 790$ nm *corresponding to a local maximum in reflection (blue) and a minimum in transmission (red) (plate (a)). Plate (b) displays the geometry of a positive square ASR arranged in an area of* 200 nm^2 *at the center of an unit cell of* 440 nm^2*. The width and thickness of the constituent gold nanorods are* 25 nm *and* 100 nm*, respectively. Plates (c) to (e) show the simulation results of the electric field along the Z direction on the surface of the ASR meta-molecules (red dashed lines) and the directions of corresponding electric currents are schematically plotted as black arrows. At the wavelength of* $\lambda = 1.05$ μm*, the closed current distribution indicates that a magnetic dipole perpendicular to the array is generated, while at wavelengths of* 790 nm *and* 650 nm*, the electric dipole parallel to the surface and the electric quadrupole are the dominant resonant modes of the ASR plasmonic resonator.*

The simulated far-field optical spectra of a negative ASR metamaterial array can also be obtained through numerical modeling in COMSOL as shown in Fig. 3.8 (a). With Y polarized excitation, the negative square ASR nanostructures perforated on a free-standing 50 nm gold thin film have a well-defined plasmon absorption resonance

at $\lambda = 880$ nm corresponding to a local maximum in transmission and a minimum in reflection. With the help of Babinet's principle for complementary structures such as the positive and negative square ASR meta-molecules [97], the electric near-fields of the structures at the characteristic resonant frequencies of an incident beam correspond to the magnetic near-fields of their complements. Therefore, by analyzing the magnetic field along the Z direction on the surface of the negative ASR meta-molecules, the directions of surface magnetic currents can be schematically plotted as the black arrows indicate in Fig. 3.8 (c) to (e) at the excitation wavelengths of 700 nm, 880 nm and 1.15 μm, respectively. Analogous to the resonant modes of the positive ASR meta-molecules at different wavelengths, the negative ASR plasmonic resonators have an electric dipole mode perpendicular to the array at the excitation wavelength of 1.15 μm, while at wavelengths of 880 nm and 700 nm, the magnetic dipole lying on the surface and magnetic quadrupole modes are the main resonant modes, respectively. We will investigate field localizations in the immediate proximity of the two types of ASR meta-molecules arrays through the coherent control process at the corresponding excitation wavelengths and the polarization directions.

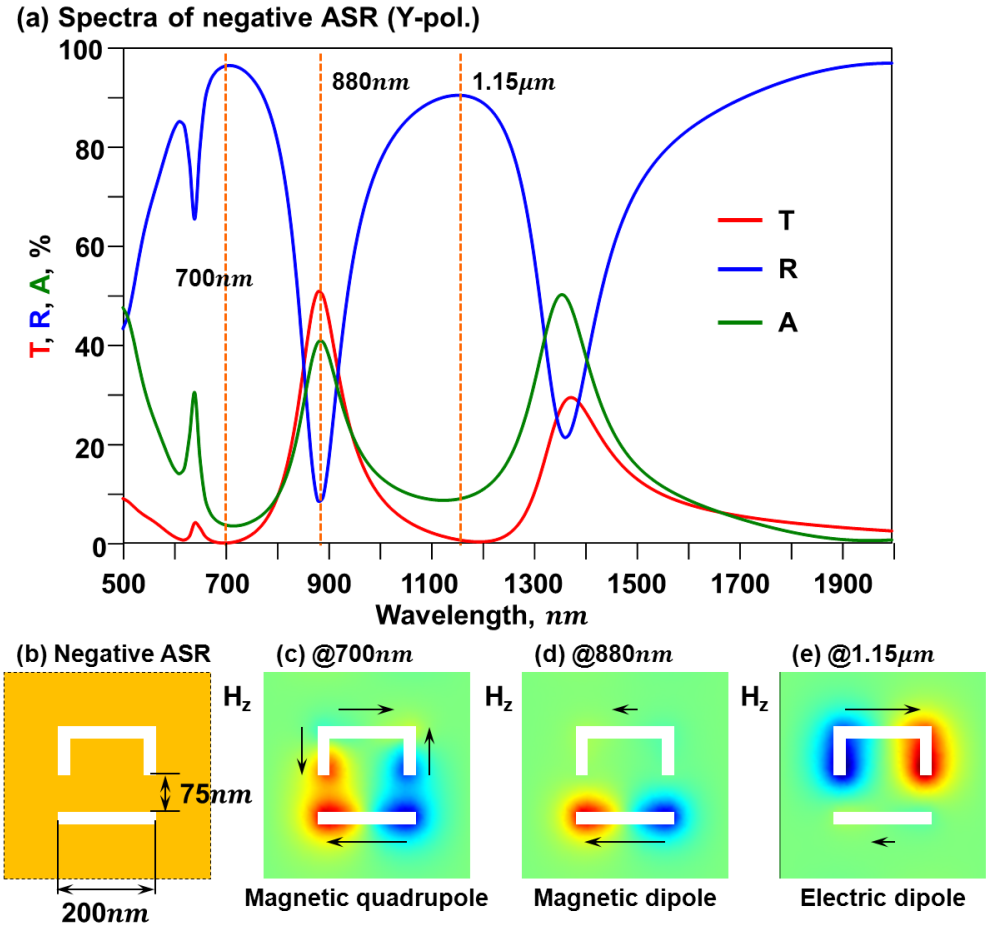

Figure 3.8: ***Simulated far-field optical spectra of an ASR metamaterial array and the surface current distributions at different characteristic wavelengths: Negative ASR nanostructures.*** *Simulation results. With plane wave illumination and Y polarized excitation, the array of negative ASR nanostructures has a well-defined plasmonic resonance at* $\lambda = 880$ nm *corresponding to a local maximum in transmission (red) and a minimum in reflection (blue) (plate (a)). Plate (b) displays the geometry of a negative square ASR meta-molecule arranged in an area of* 200 nm^2 *at the center of a unit cell of* 440 nm^2*. The width of the nanoslits is* 25 nm *and the thickness of the gold thin film is* 50 nm*. Plates (c) to (e) show the simulation results of the magnetic field along the Z direction on the surface of the ASR meta-molecules. According to Babinet's principle, the electric near-fields of structures correspond to the magnetic near-fields of their complements. Therefore, an electric dipole mode of the negative ASR meta-molecules' resonance occurs at the wavelength of* $\lambda = 1.15$ μm*, while a magnetic dipole and a magnetic quadrupole are the dominant resonant modes at* 880 nm *and* 700 nm*, respectively.*

3.3.2 Spatially tailored phase profile of an incident light beam

To demonstrate the idea of controlling nanoscale light localizations on the metamaterial landscape through the coherent control process, first we choose the excitation beam to have a sinusoidal phase profile across its wavefront. With such a simple phase profile,

light can be localized in the array of interacting meta-molecules at certain polarization directions and frequencies of the driving field. In the numerical simulation, as shown in Fig. 3.9, the metamaterial array is driven by manipulating a monochromatic field upon arrival at the metamaterial surface, making the electric field have a constant amplitude, a fixed polarization direction, and a spatially varying phase with sinusoidal profile along the X and Y directions. Considering a continuous modulated phase profile which can be used feasibly in the experiments and the computational ability of our COMSOL server, the period of the sinusoidal phase profile is set to be six unit cells of the metamaterial array, *i.e.* 440 nm $\times$ 6 =2.64 μm in this numerical model. The boundaries in the numerical model are set to periodic boundary conditions, giving a continuity of the phase profile on the boundaries. The modulated phase profile of an incident light beam can be expressed as follows:

$$E(X,Y) = E_0 e^{i\varphi(X,Y)},\ \varphi(X,Y) = (\frac{\Delta\varphi_{max}}{2})\sin((\frac{2\pi}{6a})X)\sin((\frac{2\pi}{6a})Y), \tag{3.2}$$

where a is the pitch of metamaterial and the $\Delta\varphi_{max}$ denotes the maximum difference of the phase angle in the modulated sinusoidal phase profile. The maximum phase difference $\Delta\varphi_{max}$ which can be set in the COMSOL numerical models is 2π. By varying the modulation depth $\Delta\varphi_{max}$ and wavelength of excitation, a series of simulations analysing the energy concentrations, excitation wavelength dependence and the positioning of nanoscale light localizations will be conducted, as described below.

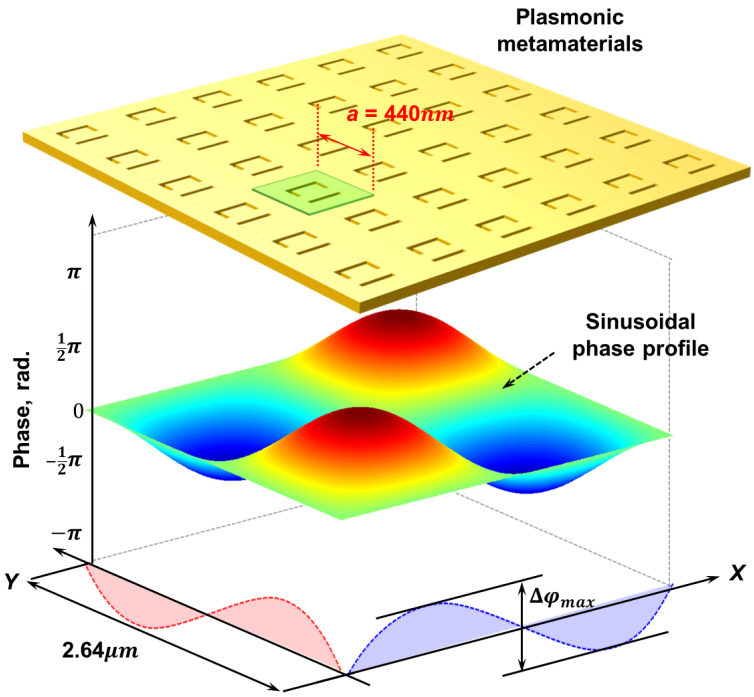

Figure 3.9: ***Coherent control of light localizations with sinusoidal phase profile in*** X ***and*** Y ***directions*** *Artistic impression. A light beam with fixed amplitude and modulated phase profile excites a metamaterial array of interacting plasmonic resonators leading to the formation of the energy hot-spot at the metamaterial. In the simulation, the modulated phase profile can be expressed as* $E(X,Y) = E_0 e^{i\varphi(X,Y)}$*, where* $\varphi(X,Y) = (\Delta\varphi_{max}/2)\sin((2\pi/6a)X)\sin((2\pi/6a)Y)$*. Here,* a *is the size of the unit cells in the metamaterial system and is equal to* 440 nm*. Thus, the spatial period of the sinusoidal phase profile is six unit cells of the metamaterial array (*2.64 μm*). The* $\Delta\varphi_{max}$ *denotes the maximum phase difference in period of the modulated phase profile as indicated in the diagram.*

3.4 Coherent control of nanoscale light localizations in metamaterials: simulation results

3.4.1 Nanoscale energy concentration on a single meta-molecule

With coherent control of an incident excitation beam, the main characteristics of the energy distributions on the landscape of the positive and negative square ASR metamaterials will be illustrated in Fig. 3.10 and Fig. 3.11, respectively. In Fig. 3.10, plates (a) to (d) show the intensity distributions in the immediate proximity of a positive ASR metamaterial array as a function of the amplitude of spatial phase profile modulation. According to the simulated far-field spectra obtained in Fig. 3.7, the excitation wavelength selected here is $\lambda = 790$ nm, while the polarization of the incident light

beam is in the X direction. As expected, with a flat wavefront ($\Delta\varphi_{max} = 0$), all meta-molecules in the metamaterial array are excited equally. The nanoscale energy concentrations are located on the two ends of the bottom bar structures of each square ASR meta-molecule, generating homogeneously distributed intensity peaks with sub-wavelength size as shown in Fig. 3.10 (a). By increasing the modulation depth of the sinusoidal phase modulated light beam, energy tends to concentrate at two opposite quadrants of the 6×6 section of the metamaterial array at a distance of $3\sqrt{2}$ unit cells from one another. When the maximum phase difference in the sinusoidal phase profile modulation reaches $\Delta\varphi_{max} = 2\pi$, only two square ASR meta-molecules are excited and a pair of strong energy localizations are generated at the two opposite quadrants of the 6×6 sub-sections as shown in Fig. 3.10 (d). The pair of the strong intensity peaks has a separation around 200 nm, which is close to the length of the bottom nanorod of the ASR meta-molecule. The full width of the energy hot-spots measured at half of its maximum (FWHM) is around 70 nm (0.089 λ).

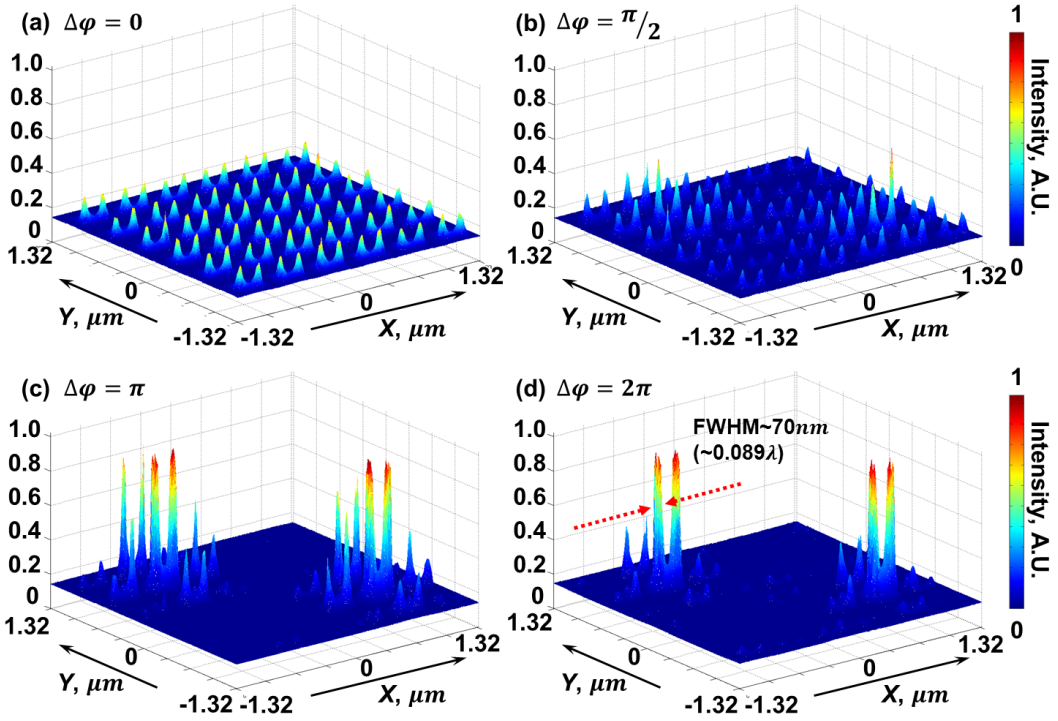

Figure 3.10: ***Coherent control of nanoscale energy localizations on a positive ASR metamaterial array of interacting plasmonic resonators.*** *Simulation results. Color maps (a) to (d) show the buildup of light localizations with increasing modulation depth $\Delta\varphi_{max}$ of the sinusoidal phase modulation in the driving field under X polarization. Note two intensity peaks form at the opposite quadrants of the landscape at resonance conditions at $\lambda = 790$ nm and $\Delta\varphi_{max} = 2\pi$. The size of one of the paired energy hot-spots is around 70 nm (0.089 λ), while there is no excitation on the other quadrant.*

Regarding a negative square ASR meta-molecule array illuminated with a phase modulated excitation beam, the main characteristics of the energy distributions on the metamaterial landscape are represented in Fig. 3.11 (a) to (c) with a modulation depth of the maximum phase difference in the sinusoidal phase profile from 0 to π, respectively. Here, the excitation wavelength is $\lambda = 880$ nm and the polarization is in the Y direction according to the simulated far-field optical spectra of the negative ASR meta-molecules array as shown in Fig. 3.8. As Fig. 3.11 (a) shows, with a flat wavefront ($\Delta\varphi_{max} = 0$), the energy is homogeneously distributed on each negative square ASR meta-molecule and concentrated on the bottom nanoslit of each negative split-ring nanostructure. With increasing of the modulation depth, energy also tends to concentrate at two opposite quadrants of the 6×6 section of the array at a distance of $3\sqrt{2}$ unit cells from one another. With a maximum phase difference of π applied to

the sinusoidal phase profile modulation, two isolated energy peaks will be produced at the two opposite quadrants of the 6×6 section of a metamaterial array as the result in Fig. 3.11 (c) shows. The phase modulation depth of $\Delta\varphi_{max} = \pi$ is the optimum situation while there are only two isolated energy hot-spots generated at the opposite quadrants. With a modulation depth of $\Delta\varphi_{max} = 2\pi$, the localized energy of the two energy hot-spots will decrease and re-distribute to the other meta-molecules. Fig. 3.11 (d) shows the intensity cross-section of the isolated central peak of the resonant hot-spot ($\lambda = 880$ nm), which has a footprint (at half maximum) of only 50 nm $\times$ 152 nm (0.0076 μm^2).

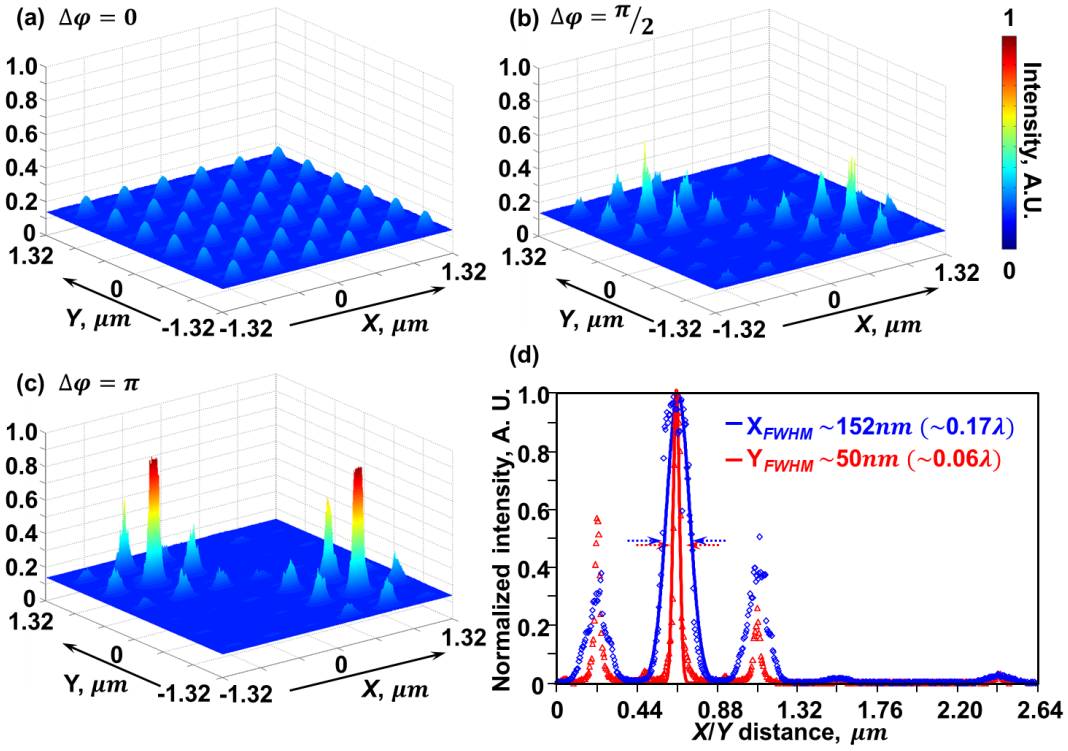

Figure 3.11: ***Coherent control of nanoscale energy localizations on a negative ASR metamaterial array of interacting plasmonic resonators.*** *Simulation results. Color maps (a)-(c) show the buildup of light localization with the increase of sinusoidal phase modulation of the driving field $\Delta\varphi_{max}$ of 0, $\pi/2$ and π, respectively. Note that two intensity peaks form at the opposite quadrants of the landscape at resonance conditions at $\lambda = 880$ nm and $\Delta\varphi_{max} = \pi$. (d) shows the main cross sections of the energy hot-spot created at the metamaterial landscape under the conditions of (c). The subwavelength peak localization has a footprint about 1% of λ^2, and there is no excitation on the other quadrant.*

3.4.2 Light localization effect at different wavelengths of excitation

From the simulation results described above, nanoscale light localizations can be created on certain ASR meta-molecules with phase profile modulation of an incident light beam. Moreover, isolated energy hot-spots can be generated by illuminating a negative ASR metamaterial with a phase modulation depth of π in a sinusoidal phase profile modulation and located at opposite quadrants of a 6×6 meta-molecules array ($\lambda = 880$ nm, Y polarization). To observe the localization effect at different wavelengths of excitation, two wavelengths of 700 nm and 1.15 μm away from the resonant frequency are chosen to examine the coherent control process with a fixed depth of modulation. According to the simulated far-field optical spectra and the surface current distributions, the ASR meta-molecules illuminated with the wavelengths of 700 nm and 1.15 μm are resonant at a magnetic quadrupole mode and an electric dipole mode perpendicular to the surface, respectively. Compared with the results in Fig. 3.11, for a fixed amplitude of the phase modulation ($\Delta\varphi_{max} = \pi$), we found that the energy localization is most pronounced at the plasmonic absorption resonance at 880 nm. Detuning the excitation wavelength away from the resonance will destroy the nanoscale light localizations, as illustrated in Figs. 3.12 (a) and (b) with wavelengths of 700 nm and 1.15 μm, respectively. Well-isolated nanoscale light localizations as seen in Fig. 3.11 (c) cannot be observed.

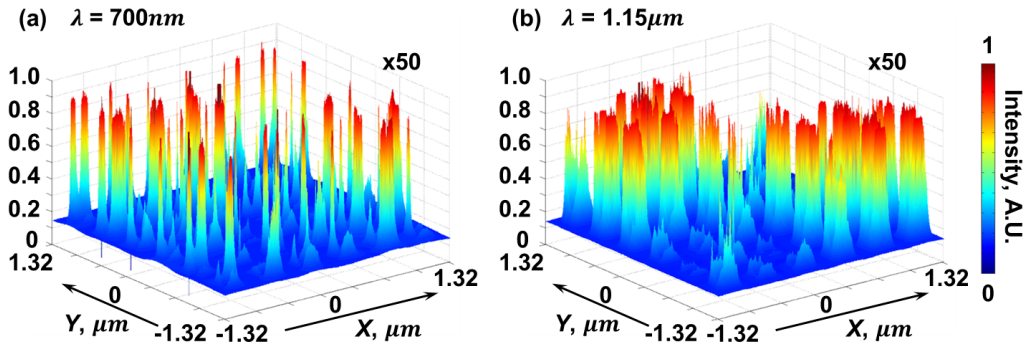

Figure 3.12: ***Detuning the excitation wavelengths away from the plasmonic absorption resonance destroys the energy localizations.*** *Simulation results. Color maps (a) and (b) show the light localization effect at different wavelengths of (a)* 700 nm *and (b)* 1.15 μm *for a fixed phase difference of the modulated field* $\Delta\varphi_{max} = \pi$.

3.4.3 Positioning of nanoscale light localizations with digital fashion

For application of the technique, arbitrarily localizing isolated energy hot-spots at prescribed meta-molecules is appealing. In our simulations, by simply shifting phase profile function of the driving beam $\varphi(X,Y) = (\Delta\varphi_{max}/2)sin((2\pi/6a)(X+\delta X))sin((2\pi/6a)(Y+\delta Y))$ by δX and δY, integer multiples of the lattice period of the metamaterial sample, one can reposition the targeted energy hot-spot across the metamaterial landscape, from one meta-molecule to another. Such an energy hot-spot positioning process is illustrated in Fig. 3.13. With the phase profile shifted by one lattice period along $\hat{X}$ and five periods along -$\hat{Y}$, the meta-molecules are sequentially fired up. Regarding the positioning range of an energy hot-spot, the energy hot-spots are generated simultaneously at two opposite quadrants of the 6×6 section of the array at a distance of $3\sqrt{2}$ unit cells from one another because of the translational symmetry of the modulated phase profile, but actually there is no spatial limitation to moving the targeted energy hot-spot on the landscape of a planar ASR metamaterial. Here, the energy hot-spot may be moved and repositioned in a quantized fashion, from one meta-molecule to another in about $\lambda/2$ steps, the lattice period of the metamaterial array.

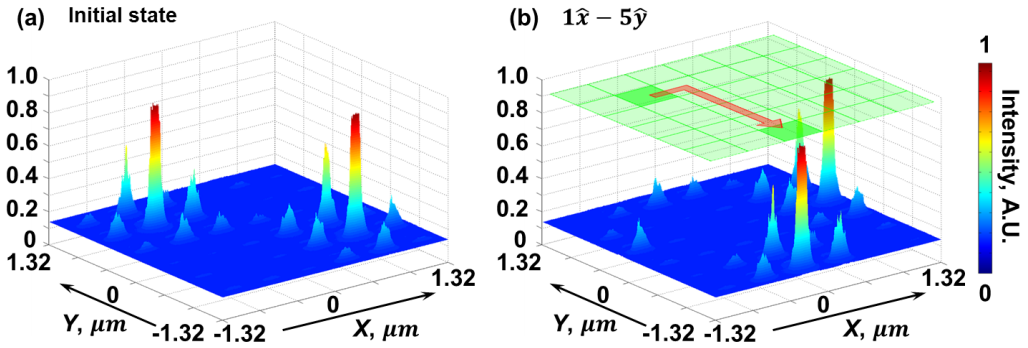

Figure 3.13: ***Positioning of nanoscale light localization with digital fashion.*** *Simulation results. Color maps (a) and (b) show that a targeted energy hot-spot can be moved across the metamaterial plane by shifting the phase profile of the incident beam by ($\delta X = a$, $\delta Y = -5a$).*

3.4.4 Different nanoscale plasmonic resonators and phase profile modulation

• Nanoscale plasmonic resonators with fish-scale nanowire patterns

Besides using the square ASR meta-molecules as an array of discrete nanoscale plas-

monic resonators in the coherent control process, we also examine the coherent control process on continuous nanostructures such as metamaterials with fish-scale nanowires. Through similar procedures, we first conduct simulations of the far-field optical spectra of a gold fish-scale metamaterial array. The unit cell of the fish-scale metamaterial, as the inset in Fig. 3.14 (a) shows, is 440 $\times$440 nm^2, while the width of the nanowires and the thickness of the fish-scale nanowire structure are both 50 nm. By using the 3D Maxwell equation solver (COMSOL), the simulated optical spectra with X-polarized excitation can be obtained and the results are shown in Fig. 3.14 (a). Here, the polarization is selected in the X direction due to the narrow resonant dip occurring in the visible part of the spectrum, while the optical spectra with Y-polarized excitation show a broad resonance in the near-infrared range similar to the results in Chap.2. A plasmonic resonant dip occurs at a local absorption peak at the wavelength of 810 nm with a minimum in transmission (red) and maximum in reflection (blue). To examine the coherent control process, an excitation wavelength is selected at the resonant wavelength of 810 nm, while two other wavelengths are chosen below (660 nm) and above (1 μm) the resonance as the orange dashed lines indicate in Fig. 3.14 (a).

By modulating an incident light beam at different excitation wavelengths with a sinusoidal phase profile as described previously, on a 6 $\times$ 6 section of the fish-scale metamaterial array, only some energy localization at two opposite quadrants can be observed and it is difficult to point out where an energy hot-spot is generated on the metamaterial landscape. Fig. 3.14 (b), (c) and (d) show examples of the intensity field distributions on a fish-scale metamaterial landscape when the array of fish-scale meta-molecules is illuminated by a sinusoidal phase modulated light beam with the modulation depth of $\Delta\varphi_{max} = \pi$. The polarization is in the X direction, while the excitation wavelengths in Fig. 3.14 (b) to (d) are 660 nm, 810 nm and 1 μm, respectively. As the simulation results show, the isolated nanoscale light localizations as shown in Fig. 3.10 (d) and Fig. 3.11 (c) cannot be observed here.

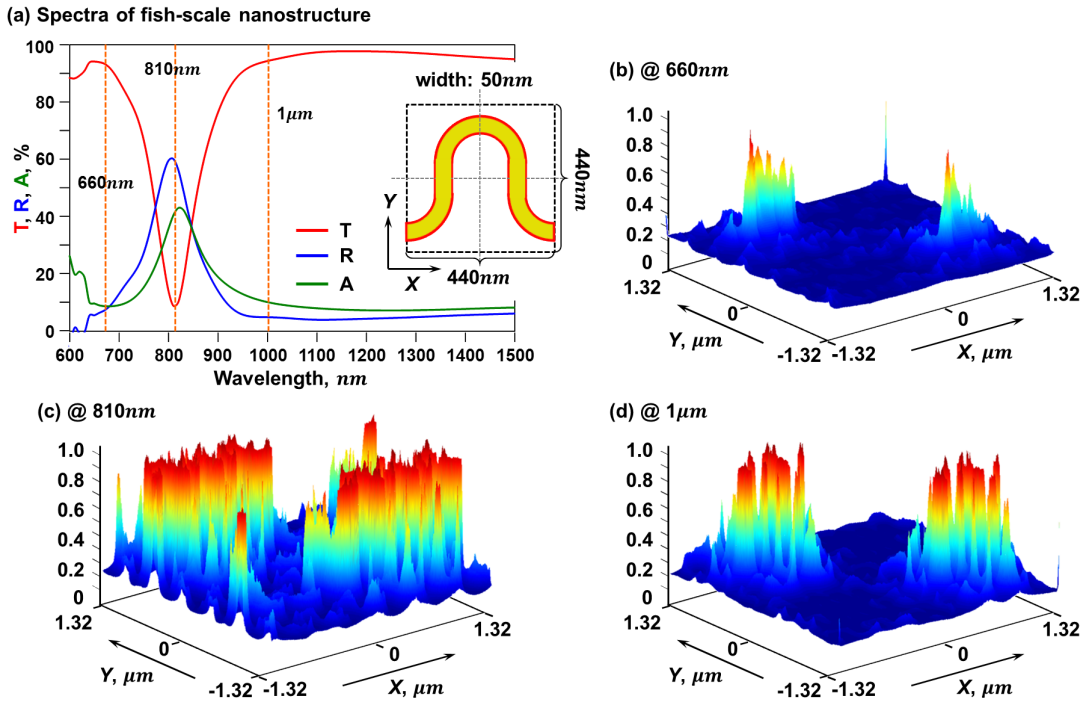

Figure 3.14: ***Coherent control of nanoscale energy localizations in a fish-scale metamaterial.*** *Simulation results. (a) shows the simulated far-field optical spectra of a free-standing fish-scale metamaterial illuminated with a plane wave under X polarization. The unit cell size of the fish-scale meta-molecules is* 440 ×440 nm^2*, while the thickness and the width of the constituent gold nanowires are both* 50 nm *as the inset shows. In the simulation results, a plasmonic resonant dip occurs at the wavelength of* 810 nm *within a local minimum in transmission (red) and maximum in reflection (blue). Color maps (b), (c) and (d) show the field distributions on a fish-scale metamaterial landscape as the array of fish-scale meta-molecules is illuminated with a phase modulated light beam with the X polarization. The phase profile is sinusoidal and the modulation depth is set to be* $\Delta\varphi_{max} = \pi$*. The excitation wavelengths in plates (b) to (d) are* 660 nm, 810 nm *and* 1 μm *respectively as the dashed lines indicate in (a).*

- **Gaussian phase profile modulation**

From the simulation results discussed above, when a negative ASR metamaterial array is illuminated by a Y-polarized light beam with a phase modulation depth of $\Delta\varphi_{max} = \pi$ in the sinusoidal phase profile, there are two isolated energy hot-spots simultaneously generated at opposite quadrants of a 6×6 section of the metamaterial array. The simultaneous generation of the two energy hot-spots is a consequence of the translational symmetry of the modulated phase profile, indicating that the maximum range with an isolated energy hot-spot located is around 1.87 μm in diameter ($3\sqrt{2}$ unit cells). To obtain an isolated energy hot-spot located in an extended field of

view, a sinusoidal phase profile with a longer spatial period should be considered and conducted in simulations. However, such attempts are limited by the computational abilities of the COMSOL server. Thus, to locate the energy hot-spots in a wide area, we try a Gaussian phase profile modulation applied to an incident light beam and examine the energy distributions on the metamaterial landscape as the array is illuminated with such a phase modulation. In the simulation, considering that the isolated energy hot-spots are generated in a section of the array with odd number of unit cells and the computational abilities in the COMSOL server, a 5×5 section of a negative square ASR meta-molecules array is selected and driven by a monochromatic field with the Gaussian phase profile upon arrival at the metamaterial surface. The negative square ASR metamaterial array has the same dimensions as described in Sec. 3.3.1. Therefore, the spatial period of the Gaussian phase profile modulation is 2.2 μm and the Gaussian phase profile can be expressed as

$$E(X,Y) = E_0 e^{i\varphi(X,Y)},\ \varphi(X,Y) = -(\Delta\varphi_{max}) e^{(\frac{X}{5a})} e^{(\frac{Y}{5a})}. \tag{3.3}$$

Fig. 3.15 schematically shows the model of a 5×5 section of a negative square ASR metamaterial array illuminated by an incident light beam with a Gaussian phase profile. The excitation wavelength is selected at $\lambda = 880$ nm, while the polarization is in the Y direction. In the simulation, the boundaries at the X and Y directions are set to have periodic boundary condition and the maximum phase difference in the Gaussian phase profile $\Delta\varphi_{max}$ varies from 0 to 2π.

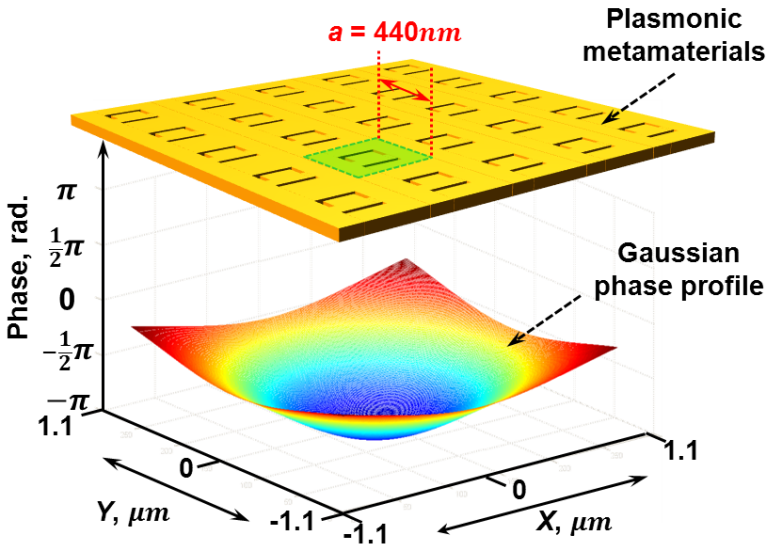

Figure 3.15: ***Coherent control of light localization with Gaussian phase profile in*** X ***and*** Y ***directions*** *Artistic impression. In the simulation model, the modulated phase profile can be expressed as* $E(X,Y) = E_0 e^{i\varphi(X,Y)}$*, where* $\varphi(X,Y) = -(\Delta\varphi_{max})e^{(X/5a)}e^{(Y/5a)}$*. Here, a is the size of the unit cells in the metamaterial system and equal to* 440 nm*. Thus, the spatial period of the Gaussian phase profile is five unit cells of the metamaterial array (*2.2 μm*). The* $\Delta\varphi_{max}$ *denotes the maximum phase difference in period of the modulated phase profile.*

When illuminating an array of negative ASR meta-molecules with an incident light beam with a Gaussian phase profile, Fig. 3.16 (a) and (b) show the field distributions on the metamaterial landscape when the modulation depths $\Delta\varphi_{max}$ are π and 2π, respectively. In the results, it is found that energy is localized in the central area and several energy hot-spots can be created in a 5×5 section of the metamaterial array. However, we cannot see an isolated energy hot-spot on the metamaterial landscape generated within an extended field of view. It is believed that an isolated energy localization could be achieved and arbitrarily positioned on an appointed location by modifying the phase profile modulation of an incident light beam through an iterative optimization process.

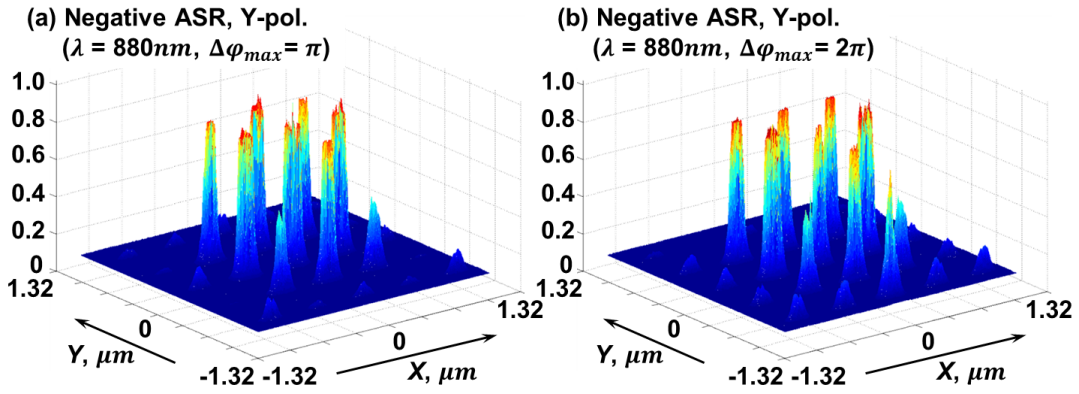

Figure 3.16: ***Coherent control of nanoscale energy localizations on a negative ASR metamaterial array with a Gaussian phase profile modulation.*** *Simulation results. Color maps (a) and (b) show light localization with Gaussian phase modulations of depth π and 2π, respectively. The excitation wavelength is* 880 nm*, while the polarization is in the Y direction. Note that the optical energy can be concentrated on several ASR meta-molecules and create energy hot-spots on the landscape of the metamaterial landscape. However, the aim to create an isolated energy hot-spot located in a wide field of view cannot be achieved.*

3.5 Physical insight into the coherent control process and feasibility of the phase modulated field

After obtaining the simulation results, we will first adopt an approach to gain a physical insight into the energy localization effect through the coherent control process and then examine the feasibility of creating the modulated field $E(X, Y)$ with a sinusoidal phase profile modulation in the far field.

3.5.1 Current oscillations in individual meta-molecules as point-like dipoles

From the above discussions of the energy distributions on the landscape of metamaterials, the strongest localization effect occurs as the positive ASR meta-molecules oscillate in an electric dipole mode at the wavelength of 790 nm, while the negative ASR meta-molecules are resonant in a magnetic dipole mode at $\lambda = 880$ nm. The main feature of such energy localizations can be clarified by a numerical model developed by Dr. S. D. Jenkins and Dr. J. Ruostekoski from the School of Mathematics of the University of Southampton. Their calculation results can help to illustrate how the energy localizations result from a cooperative response of the ASR plasmonic resonator

array, providing a physical insight into the nanoscale energy localization effect. In the numerical model of the nanoscale light localization process, an essential requirement is that individual ASR meta-molecules act as closely spaced discrete scatterers whose strong inter-meta-molecular interactions modify the energy eigen-spectrum of the system. These assumptions will be illustrated below.

In the numerical model, the current oscillations in individual meta-molecules are treated as point-like dipoles. For an incident driving field of a given wavelength exciting the current oscillations, scattered radiation is produced by each meta-molecule. Such emitted fields subsequently drive corresponding oscillations in the neighboring meta-molecules. The system dynamics can be described by Maxwell's wave equations, for instance,

$$(\nabla^2 + k_0^2)\vec{D}^+ = -\nabla \times (\nabla \times \vec{P}^+) - ik_0 \nabla \times \vec{M}^+, \qquad k_0 = \frac{2\pi}{\lambda} \tag{3.4}$$

where $\vec{D}^+(\vec{r},\Omega)$, $\vec{P}^+(\vec{r},\Omega)$, and $\vec{M}^+(\vec{r},\Omega)$ are the positive frequency components of the electric displacement, polarization, and magnetization densities at frequency Ω. Here, $\vec{P}^+(\vec{r},t) = \sum_\Omega \vec{P}^+(\vec{r},\Omega)e^{-i\Omega t}$. In the ASR metamaterial array, constituent meta-molecules are labeled by an index j at position $\vec{r}_j$ and the electric (magnetic) dipole moments of each meta-molecule are $\vec{d}_j$ ($\vec{\mu}_j$). The polarization and magnetization densities are respectively given by

$$\vec{P}(\vec{r},t) = \sum_j \vec{d}_j(t)\delta(\vec{r}-\vec{r}_j) \quad \textit{and} \quad \vec{M}(\vec{r},t) = \sum_j \vec{\mu}_j(t)\delta(\vec{r}-\vec{r}_j). \tag{3.5}$$

where δ denotes the Dirac delta function. Because of dipole-dipole interactions between meta-molecules, the metamaterial displays collective modes of oscillation, each with a distinct resonance frequency and a collective radiative damping rate. The majority of the collective modes do not couple efficiently to the uniform driving field due to the spatial inhomogeneity of the modes. However, by allowing spatial variation in the driving field, one shall be able to excite a superposition of collective modes. A superposition of such modal excitations can lead to the formation of energy hot-spots located only at a few isolated meta-molecules.

The energy localizations result from the effect of strong inter-meta-molecular inter-

actions and can be illustrated by an example of two electric dipoles with a separation much less than the wavelength of light. The collective state of the dipoles exhibits two eigen-modes, super-radiant (enhanced radiative damping rate) and sub-radiant (suppressed radiative damping rate). In the super-radiant eigen-mode, the two electric dipoles are in phase, while they are π out of phase in the sub-radiant eigen-mode. If we prepare an incident field that excites an equal superposition of the two eigen-modes, the energy will then be localized in one of the electric dipoles. Such a result is similar to the mechanical analogue of two identical oscillators described in Fig. 3.5. The sub-radiant and super-radiant states in the two-dipole system are recurrent scattering events − a wave is scattered more than once by the same dipole. This process cannot be described by standard continuous medium electrodynamics, necessitating a discrete scatterer model of the metamaterial system.

Besides the simple system with two electric dipoles as described above, Dr. S. D. Jenkins and Dr. J. Ruostekoski also helped to establish a numerical dipole model which treats the meta-molecules placed in a 6×6 array as point-like dipoles. By illuminating individual dipoles in the array with different phases as indicated in Fig. 3.17 (b), the intensity map in Fig. 3.17 (a) shows a similar distribution to the characteristic field localization features, which have been displayed in Fig. 3.10 (d) and Fig. 3.11 (c), indicating that energy localizations in a metamaterial system result from a cooperative response of the ASR plasmonic resonators. Thus, the numerical dipole model not only provides physical insight into the energy localization effect via the coherent control process, but also calculates the effect of various phase modulations over an area. This area is larger than the one which can be feasibly modelled using COMSOL. A detailed description of the numerical dipole model is given in Appendix A.

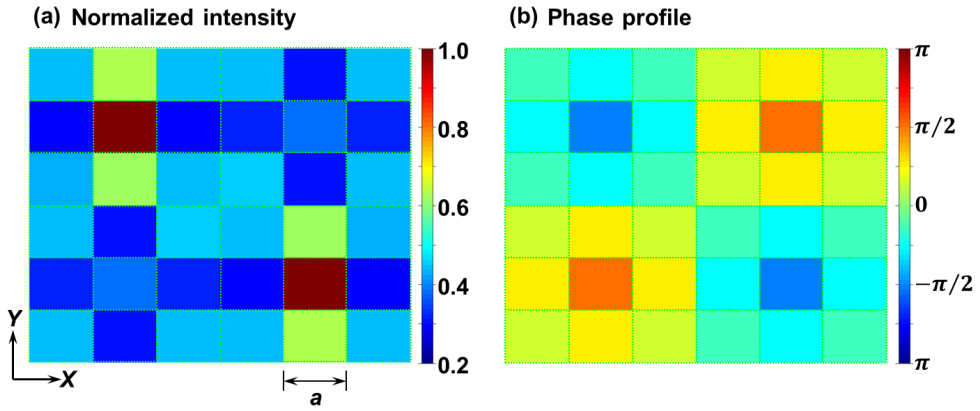

Figure 3.17: ***Simple model of field localization in metamaterial system.*** *Simulation results. Color maps (a) and (b) show the intensity and phase of excitations within the model of individual interacting dipoles representing the meta-molecules of array.*

However, such a numerical model based on the dipolar interactions of an array of nanoscale plasmonic resonators cannot provide information about the surface current distributions to figure out the resonant modes of the meta-molecules at corresponding excitation wavelengths. Thus, before using this novel numerical model to optimize the coherent control process with various phase profile modulations and acquire an isolated energy hot-spot located in a wide field of view, simulations of the far-field optical spectra and the analyses of the surface current distributions on different types of nanoscale plasmonic resonators array need to be conducted first.

3.5.2 The feasibility of the modulated field with a sinusoidal phase profile

To examine the feasibility of the modulated field $E(X,Y)$ with a sinusoidal phase profile modulation in the far-field, a Fourier transform of the modulated field $E(X,Y)$ has been taken to decompose the field into a combination of harmonics as follows.

$$E(X,Y) = E_0 e^{i\varphi(X,Y)} = \sum_{m,n} C(m,n) e^{im\sigma X} e^{in\sigma Y} \tag{3.6}$$

Therefore, the modulated field $E(X,Y)$ can be expanded as follows.

$$E(X,Y) = C(0,0) \tag{3.7}$$

$$+ C(1,0)e^{i\sigma X} + C(0,1)e^{i\sigma Y} + C(-1,0)e^{-i\sigma X} + C(0,-1)e^{-i\sigma Y} \tag{3.8}$$

$$\begin{aligned} &+ C(1,1)e^{i\sigma(X+Y)} + C(1,-1)e^{i\sigma(X-Y)} + C(-1,1)e^{i\sigma(-X+Y)} \\ &+ C(-1,-1)e^{-i\sigma(X+Y)} \end{aligned} \tag{3.9}$$

$$\begin{aligned} &+ C(2,0)e^{i\sigma(2X)} + C(0,2)e^{i\sigma(2Y)} + C(-2,0)e^{i\sigma(-2X)} \\ &+ C(0,-2)e^{i\sigma(-2Y)} \end{aligned} \tag{3.10}$$

$$\begin{aligned} &+ C(2,1)e^{i\sigma(2X+Y)} + C(1,2)e^{i\sigma(X+2Y)} + C(-1,2)e^{i\sigma(-X+2Y)} \\ &+ C(-2,1)e^{i\sigma(-2X+Y)} + C(-2,-1)e^{i\sigma(-2X-Y)} \\ &+ C(-1,-2)e^{i\sigma(-X-2Y)} + C(1,-2)e^{i\sigma(X-2Y)} + C(2,-1)e^{i\sigma(2X-Y)} \end{aligned} \tag{3.11}$$

$$\begin{aligned} &+ C(2,2)e^{i\sigma(2X+2Y)} + C(-2,2)e^{i\sigma(-2X+2Y} \\ &+ C(-2,-2)e^{i\sigma(-2X-2Y)} + C(2,-2)e^{i\sigma(2X-2Y)} \end{aligned} \tag{3.12}$$

$$+ ..... \tag{3.13}$$

Here, $\sigma = 2\pi/(L)$, L is the length of a periodic boundary. Formula (3.7) stands for the constant component, and Formulas (3.8) to (3.12) respectively represent components with absolute (transverse) wavenumber $|\vec{q}|=\sigma$, $|\vec{q}|=\sqrt{2}\sigma$, $|\vec{q}|=2\sigma$, $|\vec{q}|=\sqrt{5}\sigma$, and $|\vec{q}|=2\sqrt{2}\sigma$. Anything beyond (3.12) will have components with transverse wavenumber $|\vec{q}|$ greater than $2\pi/(\lambda)$ and cannot propagate to the far-field region.

Therefore, to confirm that the nanoscale light localizations can still be created on the metamaterial landscape, modulated phase profiles are constructed with the retained propagating components $|m,n| \leq 2$ to ensure that only physically reasonable fields are used in the simulations. As shown in Fig. 3.18, two calculations are conducted to examine the intensity distributions by illuminating a modulated light beam with (a) an ideal sinusoidal phase profile and (b) an approximation using a combination of Fourier components. The good agreement indicates that the modulated field $E(X,Y)$ can be created by a far-field phase modulating device such as an SLM.

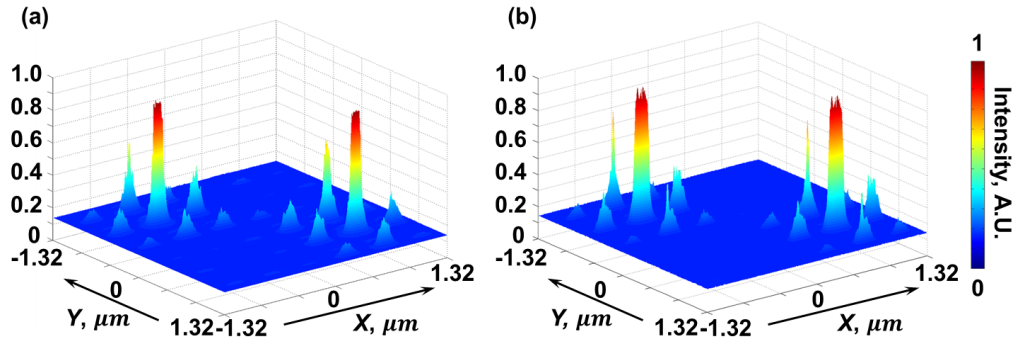

Figure 3.18: ***The feasibility of the sinusoidal modulated field.*** *Simulation results. An array of interacting meta-molecules illuminated by a modulated light beam with (a) sinusoidal phase profile and (b) a combination of Fourier components of the modulated field with the retained components $|m, n| \leq 2$ (first 6 lines in the expanded form). The good agreement between the two calculations indicates that the modulated field $E(X, Y)$ can be created by a far-field phase modulating device such as an SLM.*

Up to this point, we have shown that, through the coherent control process, evanescent field energy can be localized almost entirely at isolated meta-molecules while groups of neighboring meta-molecules remain unexcited. By simply adjusting the spatial phase profile of the incident light beam, the nanoscale hot-spots can be moved from one meta-molecule to another, providing an efficient technique for subwavelength scale optical control and manipulation in a metamaterial system. In contrast with localization techniques relying on laser-pulse excitation [26], our method is based on a continuous-wave source and does not need to depend on a transient redistribution of energy between nano-objects. Therefore, it makes the localization in a meta-material system much simpler to implement. Moreover, it does not require a complex or spatially inhomogeneous nanoscale system; instead it works with periodic, regular planar array of identical nano-objects, opening up opportunities for high-resolution microscopy and data storage applications.

Regarding the subwavelength light localization effect, although our computational capabilities do not allow us to conduct numerical modeling of driving fields modulated at a larger scale which would involve modeling of a larger array of meta-molecules, we argue that in principle a similar nanoscale light localization can take place in larger arrays where individual energy hot-spots are localized in much larger dim areas. Moreover, the nanoscale light localization can be further improved by appropriately selecting nanoscale resonators on metamaterial arrays and the unit cell size or by controlling Joule

losses from the component material. For instance, the nanoscale resonators can be perforated on a silver thin film instead of gold, which enhances the long-range interactions between meta-molecules.

3.6 Experimental configuration

To experimentally demonstrate the idea of the coherent control process of nanoscale light localizations in metamaterials, we use a phase-modulating-only liquid crystal SLM to modulate the phase profile of an incident light beam, illuminating a negative square ASR metamaterial array. The characteristic features of the coherent control process and the nanoscale energy localizations will be examined and measured by a SNOM system. The resonant features of a fabricated negative ASR metamaterial sample and the experimental system with a SNOM and an SLM will be illustrated below.

3.6.1 A negative square ASR metamaterial and its far-field optical spectra

Regarding the metamaterial samples used for the demonstration of the coherent control process, we select the negative square ASR metamaterial array due to convenience of sample fabrication and the obvious isolated intensity peaks obtained in the simulation results. As for the metamaterial sample fabrications, the ASR meta-molecule array has the same dimensions as described in the models and is fabricated with the help from Mr. J. Y. Ou from the Optoelectronics Research Centre in the University of Southampton. As shown in Fig. 3.19 (a), the interacting ASR meta-molecules are fabricated on a gold film of 50 nm thickness deposited on a transparent silica substrate and perforated by focused ion beam (FIB) milling with 25 nm nanoslits arranged in a split square shape of 200 $\times$200 nm^2. The metamaterial sample is composed of a square negative ASR pattern with a lattice period of 440 $\times$440 nm^2 and the overall area of the metamaterial array is 50 $\times$50 μm^2, consisting of 1.2×10^4 meta-molecules. The X- and Y-axis indicate the polarization directions. Fig. 3.19 (b) shows an SEM image of a 6×6 fragment of a fabricated ASR metamaterial sample.

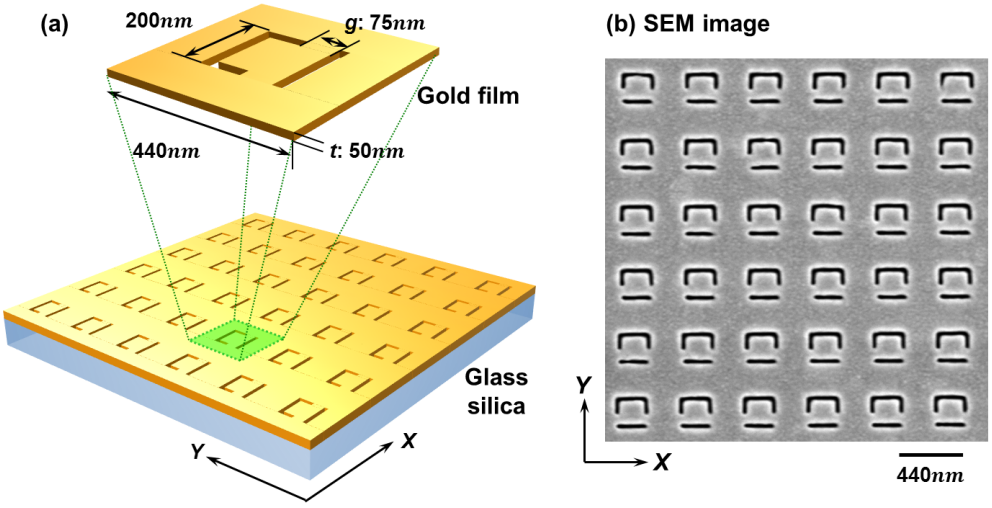

Figure 3.19: ***Negative square ASR meta-molecules as an array of nanoscale plasmonic resonators.*** *An array of negative square ASR meta-molecules is used as the nanoscale plasmonic resonator in the experimental demonstration of the coherent control process. The interacting ASR meta-molecules are fabricated on a gold film of* 50 nm *thickness deposited on a transparent silica substrate and perforated by focused ion beam (FIB) milling with* 25 nm *nanoslits arranged in a split square shape of* 200 ×200 nm^2 *as the schematic diagram in plate (a) shows. The unit cell size of the ASR meta-molecules is* 440 ×440 nm^2*. Plate (b) shows an SEM image of part of a fabricated ASR metamaterial sample, while the X- and Y-axis indicate the polarization directions.*

By using a microspectrophotometer (CRAIC Tech., QDI 2010) with a white light source normally incident on the ASR metamaterial sample, the far-field optical transmission and reflection spectra under the Y-polarized excitation can be acquired as the blue lines in Fig. 3.20 (a) and (b) show, respectively. The absorption spectrum in Fig. 3.20 (c) is determined by subtracting the transmission and reflection spectra from a total amount. The experimental (blue lines) and the simulated (red lines) far-field optical spectra show very a good agreement and a well-defined plasmonic absorption resonance can be found at around the wavelength of 930 nm, corresponding to a local minimum in reflection and maximum in transmission. Here, the resonant wavelength is slightly longer than that in the previous simulation results due to the existence of a silica substrate. According to the surface current distributions and the discussions of the resonant modes, the resonance of the fabricated ASR meta-molecules at the wavelength of 930 nm is a magnetic dipole mode.

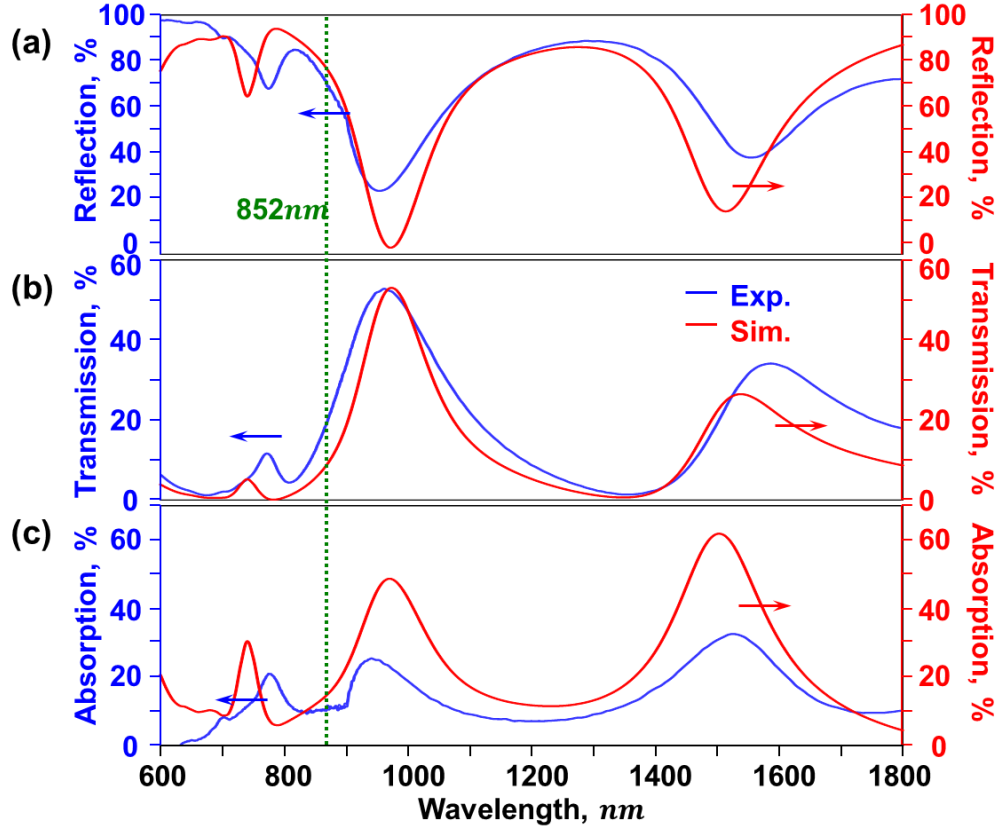

Figure 3.20: ***Comparisons between the experimental measurements and numerical simulations of the far-field optical spectra of a negative square ASR metamaterial array.*** *With normally incident white light illumination on a negative square ASR metamaterial array under Y polarization, the transmission and reflection optical spectra can be acquired as the blue lines shown in plates (a) and (b) respectively, while the absorption spectrum as shown in plate (c) is obtained by subtracting the transmission and reflection from a total amount. The array of the ASR meta-molecules has the same dimension as the fabricated metamaterial sample. Comparison with the simulated far-field optical spectra as the red lines indicate in plates (a) to (c) show good agreement and a well-defined plasmonic absorption resonance can be found at the wavelength of* 930 nm. *The green dashed line shows the excitation wavelength used in the experiments.*

3.6.2 Phase profile modulation

Fig. 3.21 schematically shows the experimental configuration for the coherent control process, including an SLM (Holoeye, PLUTO, 1920×1080 pixels, 8 μm/pixel) for modulating the incident light beam, a set of optics for demagnifying the modulated phase pattern illuminated to the required spatial period on the surface of a metamaterial array and a SNOM system (Omicron Co., Twin-SNOM) for near-field scanning of the nanoscale light localizations with a SNOM probe and far-field observation with a CCD

camera connected to a conventional microscope. The light source we use in the experiments is a laser diode (Thorlabs, Max. power: 100 mW), operating at the wavelength of 852 nm with a bandwidth of 0.5 nm. Such a narrow bandwidth is required to prevent the chromatic aberration from the SLM which we use for the phase modulations.

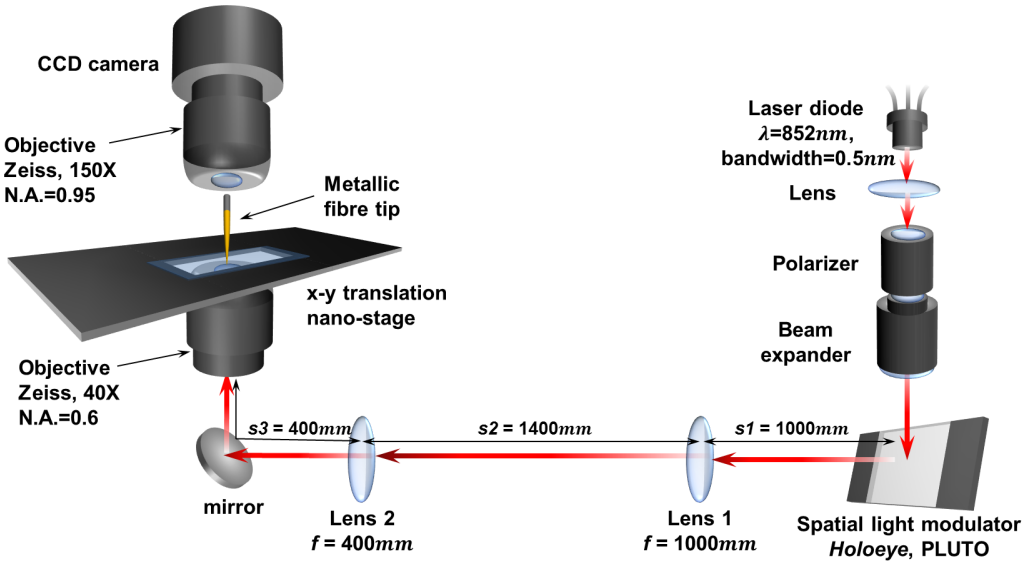

Figure 3.21: ***Mapping nanoscale light localizations of the coherent control process in an array of interacting meta-molecules.*** *Schematic diagram of experimental configurations. An incident monochromatic light beam from a laser diode light source at the wavelength of* 852 nm *is polarized in the Y direction and expanded to homogeneously illuminate an activated SLM through a linear polarizer and a 5X beam expander. The pixels on the SLM are controlled by a computer, giving the required phase modulations to an incident light beam.*

The reason for using the light source with a wavelength of $\lambda = 852$ nm instead of the resonant wavelength of 930 nm obtained in the far-field spectral measurements to excite the interacting ASR meta-molecules array is because of the working wavelengths of a photon multiplier tube (PMT; Hamamatsu Co., H9305-02) employed in the SNOM mapping system. The range of the working wavelengths of this PMT is from 185 nm to 900 nm. Considering that the excitation wavelength has to be close to the plasmonic absorption peak (930 nm) and the generated nanoscale energy distributions must be detected by the PMT for the SNOM mapping, the wavelength of $\lambda = 852$ nm as the green dashed lines indicate in Fig. 3.20 is selected for examining the coherent control process of nanoscale light. Although this excitation wavelength is not exactly at the correct resonant frequency, nanoscale energy concentrations and intensity peaks can still be observed in the experiments.

A sinusoidal phase profile as described in the simulation models is used to demonstrate the coherent control process of nanoscale energy localizations in a metamaterial system. The targeted phase modulation on the metamaterial array is spatially varied along the X and Y directions with a lattice period equal to the size of six unit cells of the metamaterial array and has the following form

$$E(X,Y) = E_0 e^{i\varphi(X,Y)},\ \varphi(X,Y) = (\frac{\Delta\varphi_{max}}{2})\sin(\frac{2\pi}{6a}X)\sin(\frac{2\pi}{6a}Y), \tag{3.14}$$

where $a = 440$ nm is the unit cell of the interacting ASR meta-molecules and thus the spatial period of the modulated sinusoidal phase profile is 2.64 μm both in the X and Y directions. $\Delta\varphi_{max}$ denotes the maximum phase angle difference. The phase profile pattern on the metamaterial array is the Fourier transform of the pattern displayed on the SLM. To calculate the pattern displayed on the SLM, the numerical Fourier transform of Equ. (3.14) is taken. Considering the magnification given by the lenses and the objective, the corresponding amplitude and phase of the pattern on the SLM can be obtained through a computer control of the SLM. To generate the sinusoidal phase profile, 1080×1080 pixels on the SLM are activated and a light beam with a sinusoidal phase profile modulation can be generated.

By passing through a linear polarizer and a 5X beam expander, the incident monochromatic light beam from a laser diode light source is polarized into the correct state to excite the interacting meta-molecules and expanded to homogenously illuminate the operating pixels on SLM. The required spatially-varying phase profile of the light beam with different modulation depths can be routinely achieved by the SLM. After passing through the arranged lenses, lens 1 (focal length: 1000 mm), lens 2 (focal length: 400 mm), and the 40X objective, the modulated light beam is demagnified to the size of the fabricated ASR metamaterial (50×50 μm^2). Thus, a sinusoidal phase profile with a spatial period of 2.64 μm can be obtained as it arrives on the metamaterial sample.

Regarding a considerable concern about such a sinusoidal phase profile modulation, as discussed in Section 3.5.2, only series components with $|m,n| \leq 2$ are retained to propagate to the sample. Nevertheless, the required sinusoidal phase profile can still be formed to excite the nanoscale resonator, generating energy hot-spots on the metamaterial landscape. Fig. 3.22 shows the experimental setup for SNOM mapping.

The plasmonic metamaterial sample is illuminated with the modulated light beam. A quick intensity distribution on the metamaterial surface can be observed by the CCD camera. Also, for the investigation of the nanoscale light localization, a SNOM is used in collection mode and polarization-insensitive metal-coated SNOM tapered fibre probes (Jasco Inc.) with ~ 80 nm aperture are employed to investigate the intensity distribution in the immediate proximity of the interacting meta-molecules array.

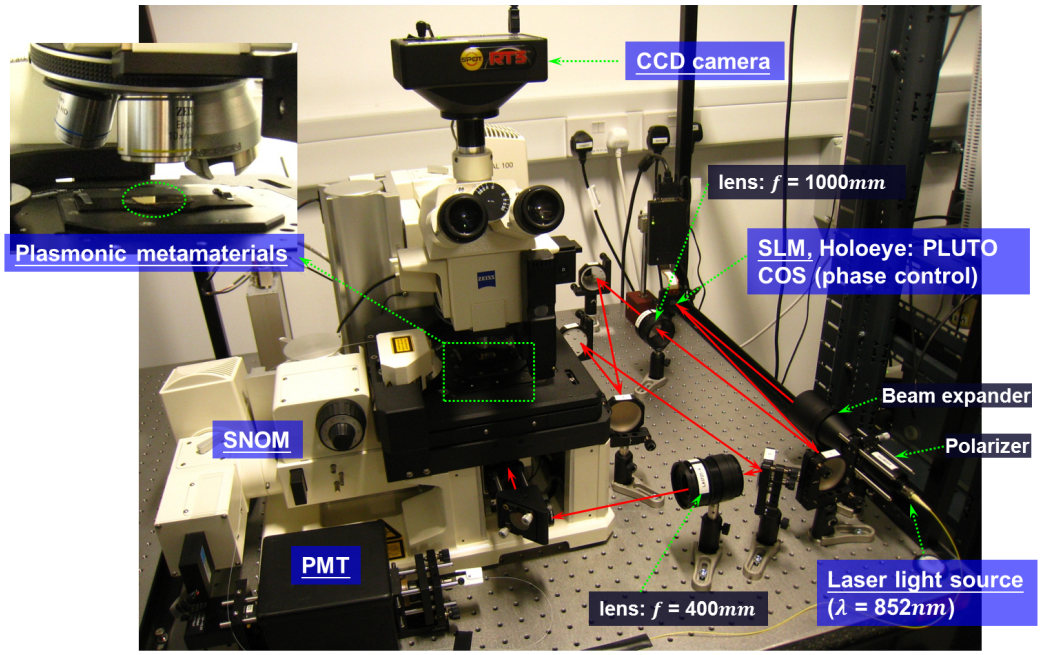

Figure 3.22: ***The existing experimental setup.*** *The wavelength of an incident light beam is* $\lambda = 852$ nm *and the bandwidth of this light source is* 0.5 nm. *The two lenses de-magnify the modulated light beam into the size of the metamaterial sample. A quick observation of the intensity distribution can be obtained by the CCD camera. Also, for the investigation of nanoscale light localization, a SNOM probe can be employed to directly measure the intensity distribution on the metamaterial landscape.*

3.7 Coherent control of nanoscale light localization in metamaterial: experimental demonstration

With the experimental configurations and the fabricated ASR metamaterial sample described above, the main features of the coherent control of nanoscale energy localizations can be experimentally demonstrated as the results in Fig. 3.23 and Fig. 3.24 show. First, regarding the energy concentrations on a few meta-molecules as a function of the modulation depth of the free space spatial phase profile, the CCD images shown in Fig. 3.23 (a) to (c) represent the energy distributions under Y polarized illumination of the ASR metamaterial landscape with maximum phase difference $\Delta\varphi_{max}$ of the modulated sinusoidal phase profile varying from 0 to π. Here, the CCD images are segments which are cut from the original results and have a size corresponding to one spatial period of the modulated sinusoidal phase profile both in the X and Y directions, *i.e.* six unit cells of the ASR meta-molecules or 2.64 μm. The green grids on the images indicate the boundaries of the ASR meta-molecules. From the results, we can know that with a flat wavefront of the incident beam ($\Delta\varphi_{max} = 0$), all meta-molecules in the array are excited equally, showing a nearly homogeneous intensity distribution on the metamaterial landscape as illustrated in Fig. 3.23 (a). By increasing the modulation depth of the sinusoidal phase profile, Fig. 3.23 (b) and (c) show that the energy progressively concentrates at two opposite quadrants of a 6×6 section of the metamaterial array at a distance of $3\sqrt{2}$ unit cells apart. The energy concentrations on a few meta-molecules through the coherent control process can be observed in the CCD images Fig. 3.23 (a) to (c); however, the perceived size of the nanoscale energy hot-spot is limited by the microscope resolution.

To investigate the actual size of the nanoscale energy hot-spots located on a few meta-molecules, near-field optical mappings have been conducted. By approaching a SNOM tip with an aperture of 80 nm to the immediate proximity of the ASR metamaterial and linearly shifting the sample translation stage, the energy hot-spots are revealed and located on certain meta-molecules. The intensity of the energy hot-spots reaches to its maximum as the maximum phase difference of the modulated sinusoidal phase profile is $\Delta\varphi_{max} = \pi$. The result of near-field optical mapping on the excited ASR meta-molecule is shown in Fig. 3.23 (f), while Fig. 3.23 (e) displays the corre-

sponding topographic measurement of the ASR meta-molecule. The size of the energy hot-spot is around 184 nm × 147 nm (0.22 $\lambda \times 0.17\ \lambda$) and thus the near-field is modulated at a scale that is 25 times smaller than the scale at which the incident free space field is modulated. This result conforms to the full 3D Maxwell calculation as the inset in Fig. 3.23 (d) shows, which places the hot-spot at the middle of the short slit of the meta-molecule. As predicted by the theoretical calculations, the localization effect cannot be observed at excitation wavelengths away from the absorption resonance, which has been confirmed by SNOM measurements at a wavelength of $\lambda = 660$ nm.

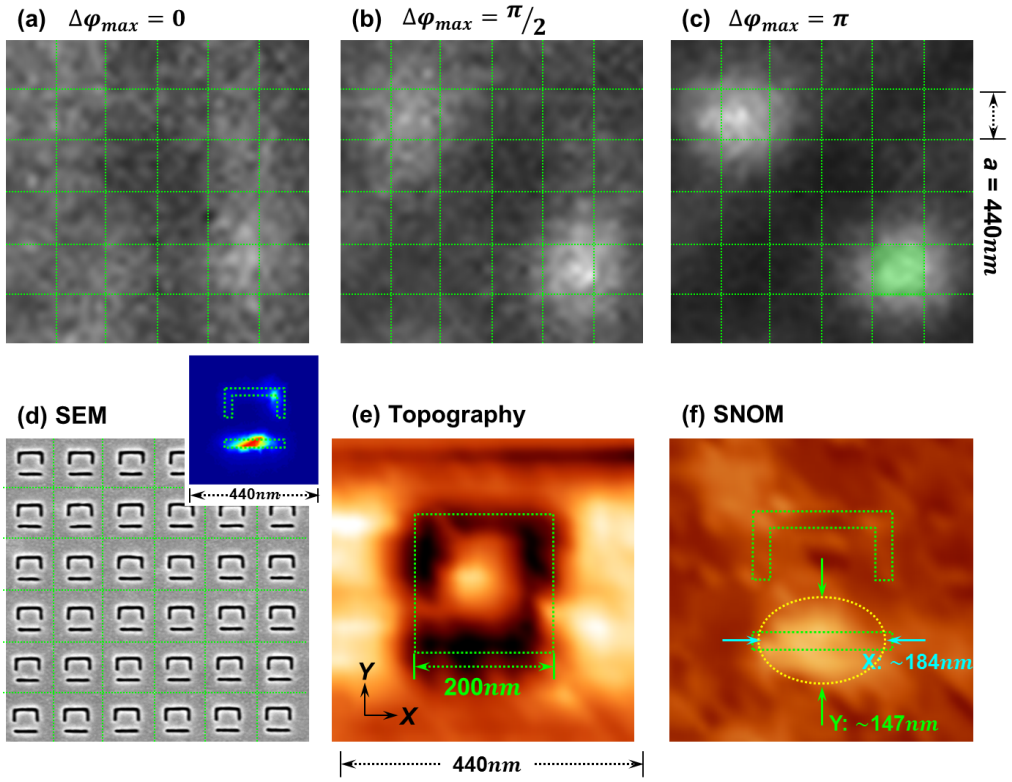

Figure 3.23: ***Experimental demonstration of the coherent control of light localization in a plasmonic mesometrial.*** *Nanoscale light localizations in a plasmonic metamaterial are observed with an optical microscope and a SNOM. Figures (a) to (c) show the transmission optical microscope images of the ASR nanostructures illuminated with coherent laser radiation at* $\lambda = 852$ nm *at different wavefront distortions: (a) plane wave illumination, (b) harmonic phase modulation with period of six lattice cells (*2.64 µm*) and* $\Delta\varphi_{max} = \pi/2$*, and (c) for* $\Delta\varphi_{max} = \pi$*, when the maximum localization is achieved. Note that the optical microscope does not reveal the actual size of the energy hot-spots. Figures (d) and (e) represent the SEM image of the plasmonic metamaterial array and topographic image of the individual unit cell (*440 ×440 nm*), respectively. (f) shows the intensity distribution measured by the SNOM, as predicted by full 3D Maxwell calculations in the inset to figure (d).*

In terms of controlling the subwavelength light localizations with a nanoscale footprint, Fig. 3.24 illustrates how the energy hot-spot can be repositioned on the "metamaterial chessboard". By simply shifting the modulated sinusoidal phase profile of the driving beam $\varphi(X,Y) = (\Delta\varphi_{max}/2)sin((2\pi/6a)(X+\delta X))sin((2\pi/6a)(Y+\delta Y))$ with digital steps δX and δY, *i.e.* integer multiples of the lattice period of the metamaterial sample, the targeted energy hot-spot (the red dot in Fig. 3.24 (a)) is repositioned across the metamaterial landscape, from one meta-molecule to another. The results demonstrated in Fig. 3.24 (a) to (f) show a sequence of translations, two steps along $\hat{x}$ and then three steps along -$\hat{y}$.

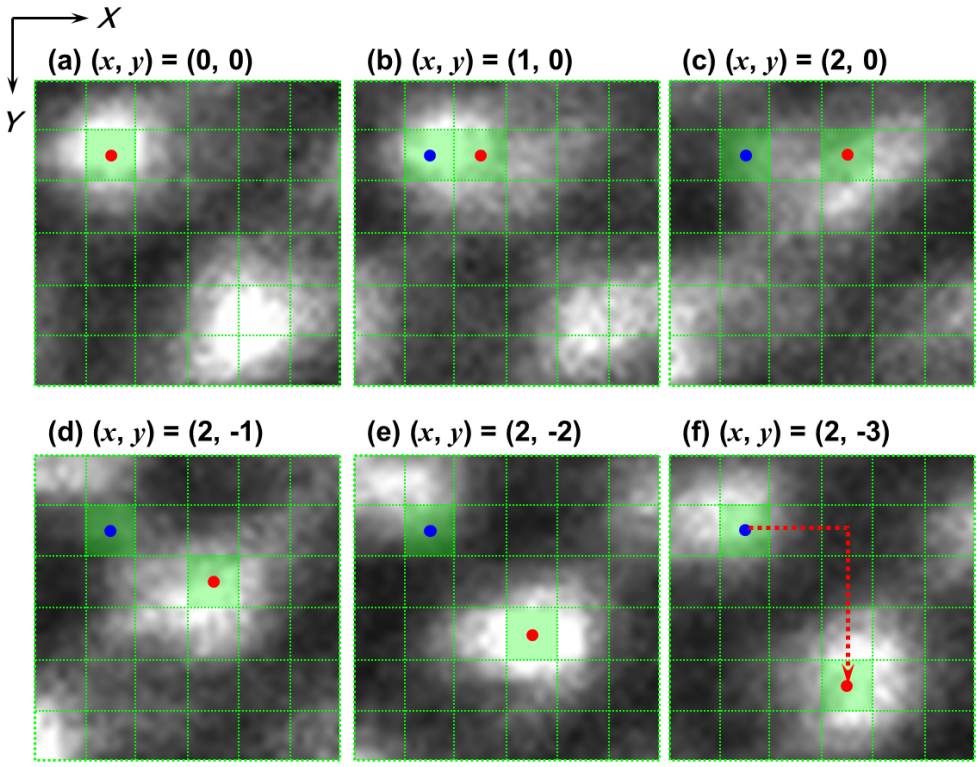

Figure 3.24: ***Repositioning the energy hot-spot across the metamaterial landscape with digital fashion.*** *Repositioning the energy hot-spot across each meta-molecules on the metamaterial landscape by shifting the phase profile of the driving beam along x and y directions. CCD image (a) shows the energy hot-spots can be positioned $3a\hat{x} + 3a\hat{y}$ apart at the resonant conditions of $\lambda = 852$ nm and $\Delta\varphi_{max} = \pi$. The red dot indicates the initial location of the targeted energy hot-spot. CCD images (b) to (f) show the process of moving the targeted hot-spot at chosen meta-molecules in this space by simply shifting the phase profile of the driving beam. (f) shows that the energy hot-spot has been moved from (0,0) to (2,-3) step by step.*

The experiments reported above confirm the viability of nano-focusing through coherent control on a 6×6 fragment of the metamaterial array. We suggest that meta-molecular interactions can help localize light at a much smaller scale than the required wavefront modulation. Using this approach, localization can be controlled in the neighborhood of meta-molecules that is covered by the extent of the interactions. Previous measurements conducted with arrays of ASR of different size [204] indicated that the interaction neighborhood would increase with the reduction of Joule losses in the system. Therefore one can expect that the nano-focusing mechanism will work even better with lower loss plasmonic materials such as silver or in the near-infrared part of the spectrum where plasmonic Joule losses are smaller. These improvements will offer a much bigger photonic chessboard for manipulation of the near-field.

Although the repositioning of the targeted energy hot-spot in a digital fashion can be performed by simply adjusting the phase profile of an incident light beam, a slight intensity difference still can be observed in Fig. 3.24, where the targeted hot-spot is located on different meta-molecules. Such a difference may result from a little dislocation of the interacting meta-molecules' position, which causes a variation of the inter-meta-molecular interactions. Furthermore, considering the fact that interaction between meta-molecules is a complex process to generate a nanoscale light localization, the spectral selection of an excitation wavelength by a normal incident wave illumination on a planar metamaterial may not be the most applicable way to obtain the strongest subwavelength energy hot-spot. A spectral investigation on an array of interacting meta-molecules with a modulated light beam illumination may give further information on the choice of excitation wavelength.

3.8 Conclusions

In conclusion, through studies above, we have both theoretically and experimentally demonstrated the coherent control of light localization in photonic metamaterial. By illuminating an array of interacting plasmonic resonators with a coherent continuous light beam with a tailored spatial variation of the phase profile, well-isolated energy hot-spots can be created and positioned at chosen meta-molecules on the metamaterial landscape.

In contrast with other recent plasmon interference technique that offered diffraction-limited hot-spots [29], our method generates subwavelength hot-spots that are substantially smaller with a footprint reported $\sim 0.04\ \lambda^2$ here, which can be beneficial not only for imaging but also for nonlinear and switching applications. Another distinct feature of our approach is that the hot-spot can be moved and repositioned in a quantized fashion, from one meta-molecule to another, in steps of the lattice period (about $\lambda/2$). Such quantization of the hot-spot location makes this method rather attractive for digital applications. We also expect that an increase of the positioning resolution may occur with further progress in photonic metamaterials. However, even though an SLM can synthesize complex wavefront of the free space beam at will, there remains a challenge to develop algorithms that will allow arbitrary patterns of near-field hot-spots to be written on the metamaterial array. In this way, substantial opportunities can be created for optical data storage, nanophotonic circuits addressing, and nanoluminescent bio-assay labelling.

4

Subwavelength light localization beyond the near field

4.1 Synopsis

After discussing nanoscale light localizations created and controlled in the near-field region, this chapter will report on the use of nanohole arrays as super-oscillating binary masks to generate subwavelength focused spots beyond the near field. Moreover, to generate an isolated energy hot-spot within a wide field of view, nanoholes with different arrangements will be considered and the generated diffraction patterns above the nanohole arrays will be systematically analysed.

In Section 4.2, a brief introduction of optical super-oscillation will be given and preceding investigations of using a 5-fold symmetry quasi-periodic nanohole array as a super-oscillating binary mask will be summarized. In Section 4.3, the diffraction patterns generated above periodic, quasi-periodic and radially quasi-periodic nanohole arrays will be discussed and compared. In Section 4.4, two kinds of radially quasi-periodic nanohole arrays − 20-fold and 27-fold symmetry − will be designed to test and compare their focusing abilities both experimentally and theoretically. To extensively investigate the use of a quasi-periodic nanohole array as a light concentrator, discussions on design parameters and illumination wavelengths will be included in Section 4.5. In Section 4.6, conclusions to this chapter will be presented.

4.2 Light focusing by a super-oscillating binary mask

While trying to recover or enhance the evanescent fields to achieve subwavelength field localizations in the optical domain, all experiments must take place in a range very close to the sample surface, consequently restricting their practical uses. To remove the limit, here we will adopt the idea of optical super-oscillation, which can achieve subwavelength concentrations of light beyond the near field [8–10, 146]. According to M. V. Berry *et al.* 's work, the super-oscillating field can be created by a proper combination of the Fourier components in an optical system and in principle the size of the generated super-oscillating energy hot-spots can be arbitrarily small [9]. Such an idea was experimentally accomplished by F. M. Huang *et al.* through the use of a nanohole array on a metal screen with a quasi-periodic arrangement as a super-oscillating binary mask [10,146]. Following their studies, in this thesis, we will mainly test nanohole arrays with different quasi-periodic arrangements and observe the corresponding diffrac-

tion patterns generated above the arrays. Related techniques used in the investigations of the super-oscillating binary masks and several major findings will be summarized below.

4.2.1 Algorithms for generating quasi-periodic patterns on a 2D plane

In this thesis, two ways are employed to acquire the nanoholes' positions in quasi-periodic patterns on a 2D plane. One is the multigrid method and the other is based on the projection of a hypercubic lattice [205–208]. In the multigrid method, quasi-periodic nanohole arrays with N-fold rotational symmetry can be obtained by converting the voids and vertices which are constructed from N sets of parallel lines. The N sets of parallel lines are arranged overlapped and each set is rotated by $2\pi/N$ radians. Fig. 4.1 (a) shows a schematic diagram of an example for $N = 5$. The 5 parallel lines sets are arranged overlapped and the angle between neighboring lines sets is $2\pi/5 = 72°$. Two basic types of constituent tilings, (i) and (ii), with 5 different orientations ($\boldsymbol{e}_i$, $i = 1, 2, .., 5$) are formed by the overlapped lines sets. By converting the vertices and their related tilings, a quasi-periodic sequence can be obtained and a 5-fold symmetry quasi-periodic tiling can be generated as displayed in Fig. 4.1 (b). As for the cut and projection method, a hypercubic lattice in N-dimensions is projected onto a 2D plane by slicing the lattice at an arbitrary angle. If the plane is selected to pass through one of the points in the N-dimensional hypercubic lattice, the resulting quasi-periodic pattern will have N-fold rotational symmetry around that point. This idea is illustrated by a schematic diagram of the projection of a cubic lattice onto a sliced plane in Fig. 4.1 (c) and the inset in Fig. 4.1 (c) shows the result of the projection of a 5-dimensional hypercubic lattice onto a 2D plane. Both the methods above can generate the same coordinates of nanoholes on a quasi-periodic pattern, while Fig. 4.2 (a) to (c) show several examples of generated quasi-periodic patterns with different orders of rotational symmetry.

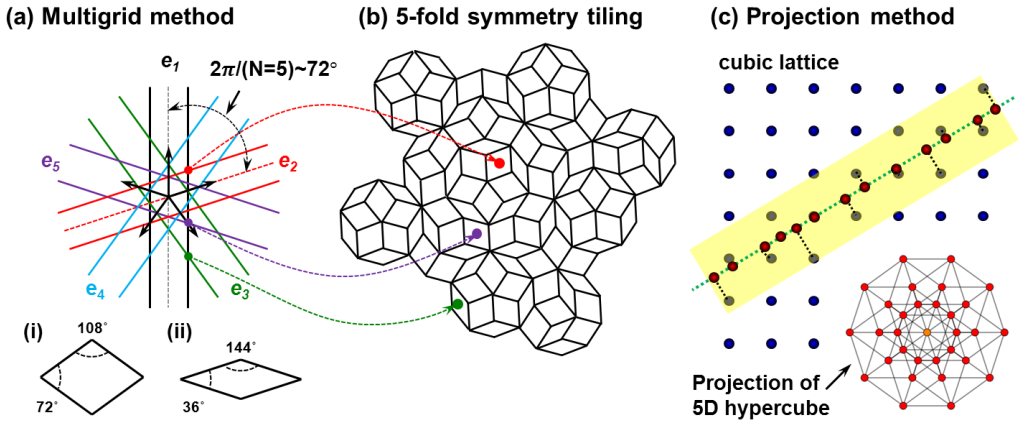

Figure 4.1: ***Algorithms for generating quasi-periodic patterns on a 2D plane.*** *Schematic diagrams. (a) shows a 5-fold symmetry quasi-periodic pattern generated by the multigrid method. 5 sets of parallel lines are arranged overlapped with equal angle of $2\pi/5$ radian and two types of constituent tilings, (i) and (ii), with five different orientations ($\boldsymbol{e}_i$) can be obtained by the intersection of any two of the parallel line sets. By converting the vertices and their related tilings, a quasi-periodic sequence can be obtained and a 5-fold symmetry quasi-periodic pattern can be generated on a 2D plane as shown in (b). (c) schematically illustrates the projection method which can be used to generate quasi-periodic patterns as well. The inset obtained from Ref. [209] shows a projection of a 5-dimensional hypercubic lattice onto a 2D plane.*

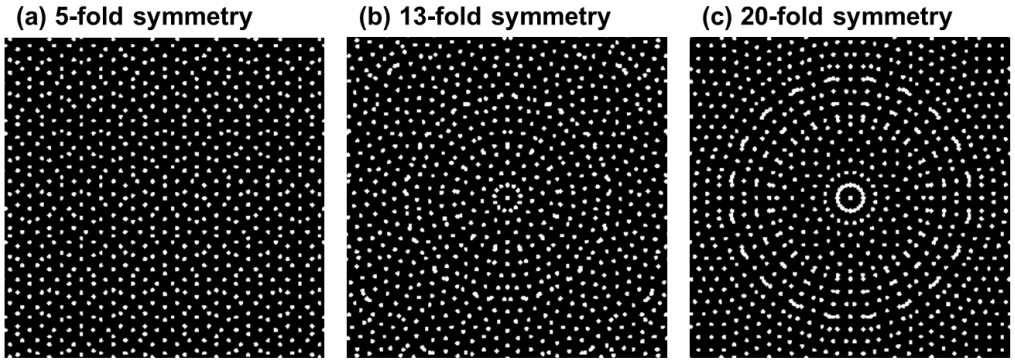

Figure 4.2: ***Patterns of quasi-periodic nanohole arrays with different orders of rotational symmetry.*** *Schematic diagrams. Plates (a) to (c) schematically show the fragments of generated quasi-periodic nanohole arrays' patterns with 5-fold, 13-fold and 20-fold rotational symmetry, respectively. The coordinates of nanoholes (white dots) are obtained by the multigrid method using JcrystalSoft Nanotube Modeler [210].*

4.2.2 Experimental setup for mapping diffraction patterns

To map the field distributions created by a nanohole array, two experimental arrangements are designed to obtain the diffraction patterns at different distances away from the array's surface. Fig. 4.3 shows the schematic diagram, including (a) a conventional

optical microscope equipped with a CCD device with Z control of 1 µm resolution, and (b) a SNOM fibre tip equipped with a nanoscale Z control between the tip and the array's surface. In our SNOM setup, the maximum distance SNOM probe can be lifted from the array's surface is 16 µm. Regarding the optical sources, illumination wavelengths can be selected by using a super-continuum laser with several band-pass filters or diode lasers with different optical frequencies. By passing light through a set of mirrors and collimators, the nanohole array samples can be illuminated homogeneously.

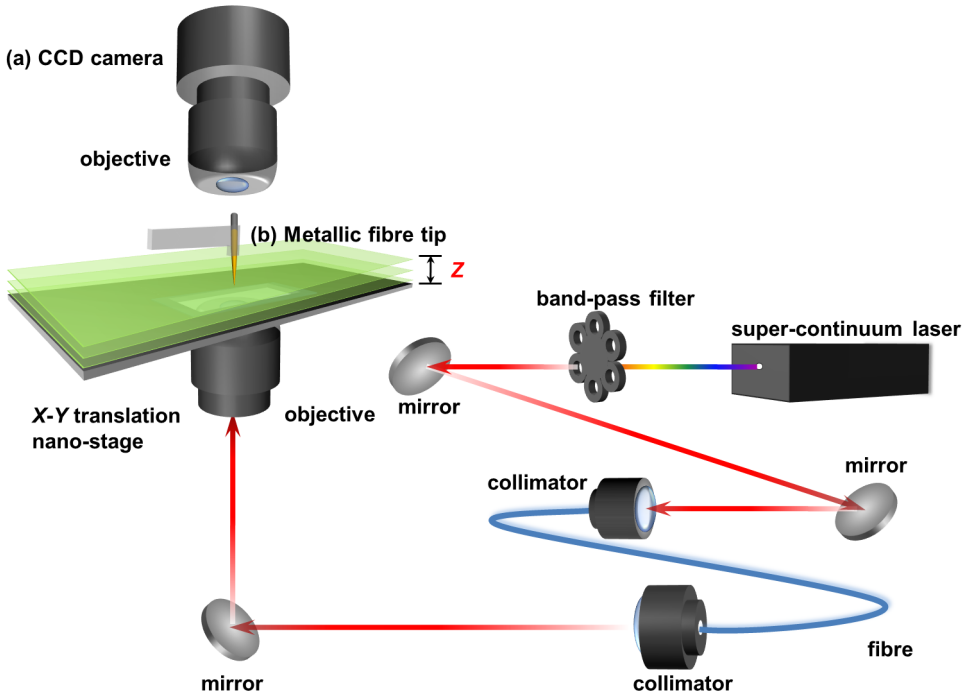

Figure 4.3: ***Schematic representation of the experimental configuration for diffracted field distribution mapping.*** *Schematic diagram. To map the field distributions above nanohole arrays, two approaches are available in our experimental setup. One is the use of a conventional optical microscope equipped with a CCD device; the other is the exploitation on a SNOM with a precise distance Z control between a SNOM scanning probe and the array's surface.*

4.2.3 Theoretical calculations of field distribution maps through the scalar angular spectrum method

The scalar angular spectrum method is used to calculate field intensity maps at different distances away from the array's surface [97, 105]. The calculations are based on the diffraction theory employing the angular spectrum representation of the diffracted field.

The diffracted field distribution at a distance Z away from the nanohole array's surface can be expressed as

$$E(X,Y,Z) = \iint F(\kappa_x,\kappa_y)e^{-i(\kappa_x X+\kappa_y Y)}e^{-iZ\sqrt{\kappa^2-{\kappa_x}^2-{\kappa_y}^2}}d\kappa_x d\kappa_y, \tag{4.1}$$

where κ is the wavevector of light and $F(\kappa_x,\kappa_y)$ is the Fourier components of the electromagnetic field at the plane of the nanohole array, $Z = 0$.

The calculation results shown in Fig. 4.4 are compared with F. M. Huang's experimental results [10] in Fig. 4.5. As we can see, the calculated field maps at different characteristic distances correspond well to the experimental measurements. Such consistency suggests that the field distribution maps are reconstructed by the light diffraction from the related nanohole array, and that the field maps above different types of nanohole arrays can be reliably obtained through the scalar angular spectrum method.

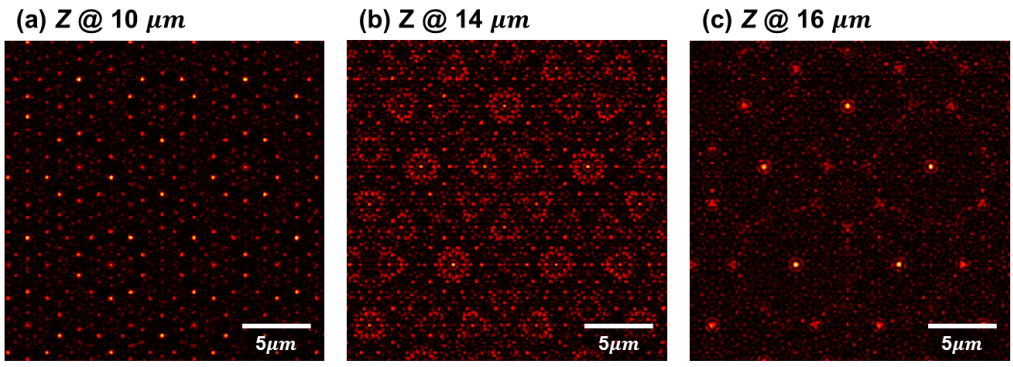

Figure 4.4: ***Calculated field maps at different heights Z above a 5-fold symmetry quasi-periodic nanohole array.*** *Calculation results. Field maps (a), (b) and (c) are obtained by the scalar angular spectrum method with calculations at distances of* 10 μm, 14 μm *and* 16 μm *away from the array's surface, respectively. Each field map is* 30 ×30 μm^2 *and the illumination wavelength is* 500 nm. *Note the theoretical calculations of the diffraction patterns are in line with the experimental results, which are shown in Fig. 4.5.*

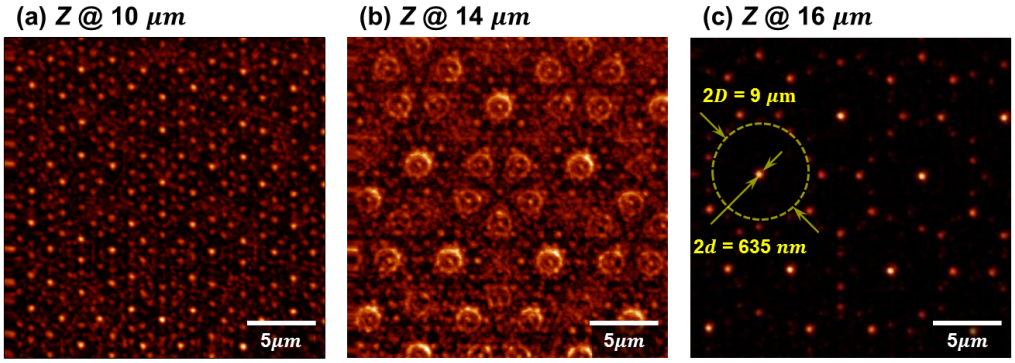

Figure 4.5: ***Field distribution mappings at different heights Z above a 5-fold symmetry quasi-periodic nanohole array.*** *The maps are obtained from Ref. [10]. Maps (a), (b) and (c) were measured at height Z of* 10 μm, 14 μm *and* 16 μm, *respectively. Each scanning area was* 30 ×30 μm^2. *The images were obtained by a SNOM using illumination wavelength of* 500 nm. *Note that highly sparse hot-spots were observed at $Z = 16$ μm and the distance between adjacent hot-spots was around* 9 μm.

4.2.4 Rich spectral components in the reciprocal plane of a quasi-periodic arrangement

The reasons for using a quasi-periodic nanohole array instead of a periodic one are explained as follows.

The diffracted field distributions above a nanohole array originate from a reconstruction of spatial frequencies contained in the array's field. Furthermore, according to W. D. Montgomery's work [211], a diffracted field distribution will show a full reconstruction of the array's pattern at a height Z if its spatial frequencies are discrete and located in the reciprocal plane at rings of radii ρ,

$$\rho^2 = 1/\lambda^2 - (m/Z)^2, \tag{4.2}$$

where m is an integer and $0 \leq m \leq (Z/\lambda)$. λ is the wavelength of an incident wave. A periodic nanohole array is an example of a self-imaging object. As shown in Fig. 4.6 (a), the spectral components of a regular nanohole array in the reciprocal plane are sets of equidistant dots and have equal magnitude. Montgomery's condition is fulfilled for all spectral maxima and a self-imaging pattern can be generated at distance Z away from the array's surface. In contrast to the periodic case, a 5-fold symmetry quasi-periodic nanohole array displays a rich spatial frequency spectrum as shown in Fig. 4.6 (b), which lies between the dotted and ring spectra of regular and circular grating,

respectively. Several significant spectral components are located on Montgomery's rings in the reciprocal plane of the array's field, indicating that the Montgomery's condition can be fulfilled, **but not all of spectral components simultaneously contribute to reconstruct the array's field**. Moreover, the difference on the color depth in the reciprocal plane indicates the different magnitude of spectral components. Such a difference means that the weights of the spectral components, which are used to reconstruct a diffraction pattern, are varied at different heights Z. Thus, reconstruction of a quasi-periodic nanohole array is a complex diffraction process because it involves a superposition of a large number of partial reconstructions happening at different heights from the array. Despite its sophistication, as distance Z varies from the array, a continuous evolution of partially reconstructed images of the array can be observed and well-defined sparsely distributed foci as energy hot-spots can be seen at some proper distances and wavelengths as shown in Fig. 4.5 (c). The subwavelength nature of these hot-spots is due to the effect of achieving rapid changes of a field known as optical super-oscillation.

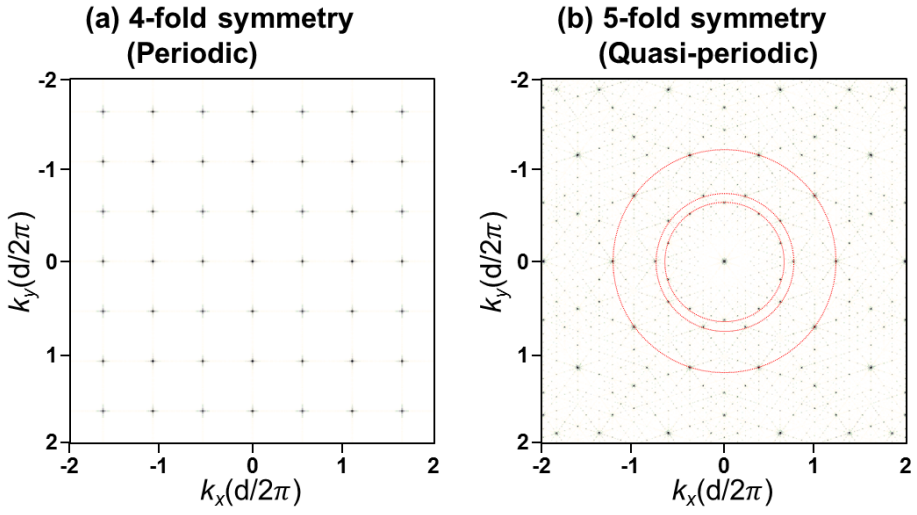

Figure 4.6: ***Comparison of the reciprocal plane between a periodic and a quasi-periodic nanohole array's field.*** *Reciprocal planes of the (a) periodic (4-fold) and (b) 5-fold symmetry quasi-periodic nanohole array. Red dashed circles in (b) show several Montgomery's rings. Note that the spectral components on a reciprocal plane of a regular nanohole array's field (a) have the equidistance and the same magnitude between the spectral maxima. However, the spectral maxima on a reciprocal plane in a quasi-periodic case (b) exhibit a rotationally symmetric distribution and the distances between the spectral maxima are not the same. The difference on the color depth of the spectral maxima also indicates that weights of the spectral components are different at different heights Z.*

The key reasons for using a quasi-periodic nanohole array as a super-oscillating binary mask are as follows:

- A quasi-periodic nanohole array can be used as a super-oscillating binary mask for its rich spatial frequency spectrum in the reciprocal plane.
- At a certain distance away from the array, sparsely distributed energy hot-spots can be created and separated by few micrometers.
- By using the algorithms for generating quasi-periodic patterns and the scalar angular spectrum method, a new quasi-periodic nanohole array can be designed and the field distribution above the arrays can be obtained without the need to manufacture the array.

With these well-developed techniques, a series of studies of different types of nanohole arrays will be conducted theoretically and experimentally as described in Section 4.3 and Section 4.4, with the aim of achieving a smaller energy hot-spot located in a much wider field of view for practical applications.

4.3 Different types of nanohole arrays

There are two primary objectives in the study of using nanohole arrays to obtain sub-wavelength light localizations in the far-field region. One is to understand the relation between the arrangements of nanoholes and the generated diffraction patterns above the nanohole arrays; the other is to achieve a subwavelength energy hot-spot within a wide field of view generated by a properly designed super-oscillating binary mask. To realise both of the above goals, different types of nanohole arrays are considered and will be systematically studied based on the categories including periodic, quasi-periodic and radially quasi-periodic nanohole arrays.

4.3.1 Nanohole arrays with periodic arrangements and the Talbot effect

The nanohole arrays with arrangements of 4-fold (periodic translation in the X and Y directions) and 6-fold (hexagonal) symmetry are regarded as periodic nanohole arrays,

whose patterns are partially shown in schematic diagrams in Fig. 4.7 (a) and (b) respectively. In the calculations, each of the nanohole arrays is designed to be included in an area of 50 ×50 μm^2 and the diameter of nanoholes is 200 nm. With plane wave illumination, several diffracted field distributions will show reconstructions of the array's pattern and repeatedly occur at regular distances away from the nanohole array. This phenomenon is called the Talbot effect and the regular distance between repeated diffracted images is defined as the Talbot distance Z_T, which can be found by the following formula,

$$Z_T = \frac{a^2}{\lambda}, \tag{4.3}$$

where a is the period of the nanoholes and λ is the wavelength of light incident on the nanohole array.

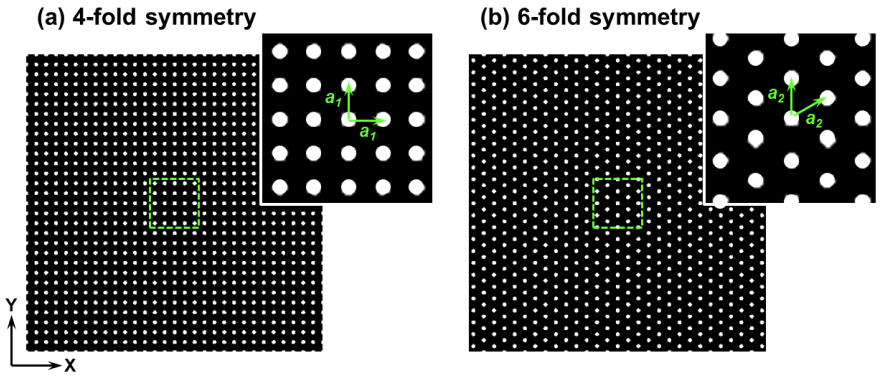

Figure 4.7: ***Patterns of nanohole arrays with periodic arrangements.*** *(a) shows the pattern of a nanohole array with periodically translational symmetry both in the X and Y directions (4-fold) with the period of a_1, while (b) shows a hexagonal arrangement (6-fold) with the equal distance a_2 to the neighboring nanoholes. The green dashed squares indicate a zoom-in area as shown in the insets on both figures.*

A series of calculations based on the use of a 4-fold symmetry nanohole array as an example will be conducted to demonstrate the Talbot effect. Such a nanohole array has a laterally periodic distribution in the nanohole arrangement and the period of the nanoholes a_1 is 1 μm as the fragment shown in Fig. 4.8 (a). In the calculations, all the nanoholes of 200 nm in diameter are included in an area of 50 ×50 μm^2 and the wavelength of the incident plane wave is selected at $\lambda = 660$ nm. Therefore, according to the formula of the Talbot effect, the array's field will be repeated at the Talbot distance of 1.515 μm. A calculated result of the diffracted field distribution on the XZ

plane at $Y = 0$ is shown in Fig. 4.8 (d), while Fig. 4.8 (b) and (c) display the diffraction patterns on the XY plane at the distance of 1.52 μm and 3.03 μm away from the array's surface, respectively. The period between the bright spots on the diffracted images is the same as the distance between the nanoholes a_1. From the results, it is found that the self-imaged diffraction patterns are repeated every Talbot distance Z_T.

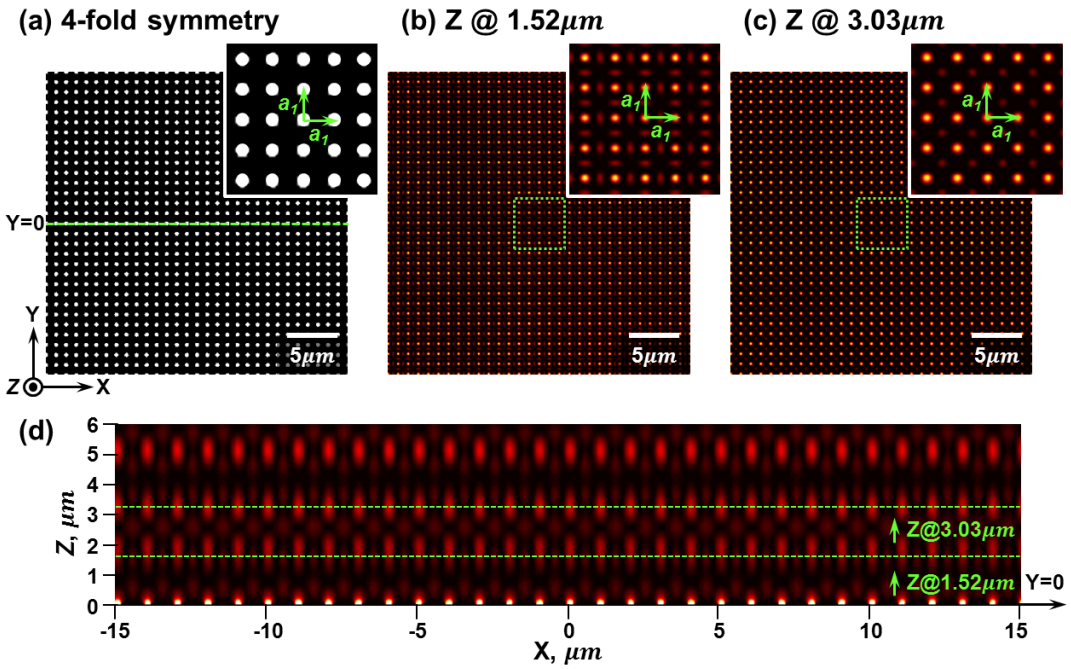

Figure 4.8: ***Self-imaging of a periodic nanohole array: Talbot effect.*** *(a) schematically shows the fragment of a 4-fold symmetry quasi-periodic nanohole array and the overall area of the array in calculations is* 50 ×50 μm^2 *with the nanohole size of* 200 nm. *The array is illuminated by a plane wave at a wavelength of* 660 nm *and the period between nanoholes is* $a_1 = 1$ μm. *Note that the self-imaging occurs at multiples of the Talbot distance* $Z_T = a^2/\lambda$ *(*∼ 1.515 μm*). (d) shows a calculated diffracted field distribution along the Z direction on XZ plane at* $Y = 0$ *of a 4-fold symmetry nanohole array. (b) and (c) show the reconstruction of the periodic array's field on the XY plane at the distance of* 1.52 μm *and* 3.03 μm *away from the array. The reconstructed pattern repeats every Talbot distance and the period between the bright spots* a_1 *is the same as the period of nanoholes. The insets in (b) and (c) are the zoom-in images with the same area of* 5 ×5 μm^2 *as the green dashed squares indicate.*

According to the Talbot effect, an image of a periodic nanohole array's pattern can be re-produced at the Talbot distance, forming numerous optical spots in the image plane. The size of such generated spots is unlikely to be beyond the diffraction limit due to the limited number of spatial frequencies in the reciprocal plane. In addition, Fig. 4.8 (b), (c) and (d) indicate that the evolution of reconstructed field intensities changes

periodically and continuously in both the transverse and axial directions. Thus, it is very difficult to employ a periodic nanohole array as a super-oscillating mask to generate hot-spots for practical applications. Unlike the periodic cases, nanohole arrays with a quasi-periodic arrangement display complex diffraction patterns above the arrays due to the large number of spatial frequencies in the reciprocal plane. We find that the higher the rotational symmetry is within quasi-periodic nanohole arrays, the more nanoholes will be arranged on concentric rings with different sizes surrounding a central nanohole, making a radially symmetric quasi-periodic arrangement of the nanoholes. Therefore, in our studies, we classify the nanohole arrays with quasi-periodic arrangements into two categories. One is the quasi-periodic nanohole arrays with lower order rotational symmetry; the other is the radially symmetric quasi-periodic nanohole arrays. Both will be discussed below.

4.3.2 Quasi-periodic nanohole arrays and super-oscillating hot-spots

In our studies, we consider the quasi-periodic nanohole arrays with 5-fold, 7-fold and 9-fold symmetry as quasi-periodic nanohole arrays with lower order of rotational symmetry, which are schematically shown in Fig. 4.9 (a), (b) and (c), respectively. Unlike the periodic nanohole arrays, which show translational symmetry, quasi-periodic cases display a rotational symmetry instead. Such arrangements of nanoholes exhibit rich spectral components of the array's field, which generate a super-oscillating field at a certain distance away from the array.

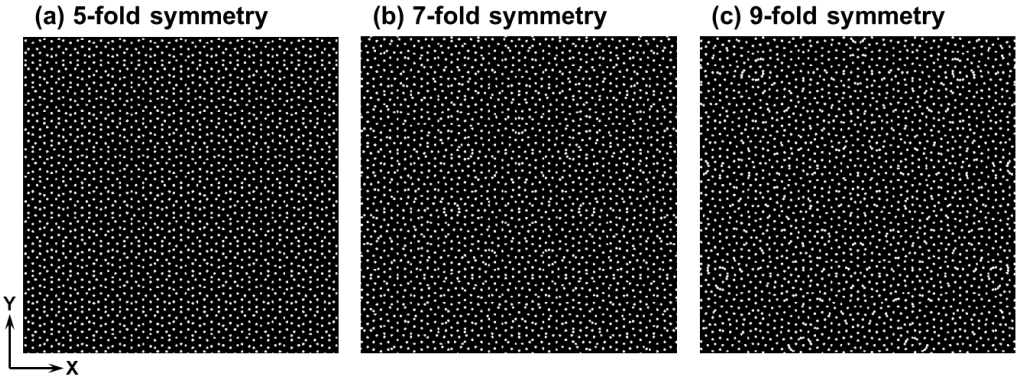

Figure 4.9: ***Patterns of nanohole arrays with quasi-periodic arrangements.*** *Plates (a) to (c) schematically show the patterns of 5-fold, 7-fold and 9-fold symmetry quasi-periodic nanohole arrays, respectively.*

To examine the behaviour of light diffraction in the diffraction zone, a 5-fold symmetry quasi-periodic nanohole array with nanoholes of 200 nm in diameter is again used as an example to observe the field distributions above the array. A calculated field distribution on the XZ plane at $Y = 0$ is shown in Fig. 4.10 (d) with a wavelength of the incident plane wave of 500 nm. Here, several significant energy hot-spots can be found at different distances away from the array's surface as the green arrows indicate. At the distance of 10 μm and 16 μm from the array, the energy hot-spots will be sparsely distributed on the XY plane as shown in Fig. 4.10 (b) and (c), respectively. Unlike the light diffraction from periodic nanohole arrays, the patterns of field distributions with quasi-periodic nanohole arrays do not show duplicate images of the array's geometry, but produces bright foci of energy concentration. The foci are sparsely distributed in the focal plane. In Fig. 4.11, we see that sparsely distributed energy hot-spots can also be generated by using 7-fold and 9-fold symmetry quasi-periodic nanohole arrays.

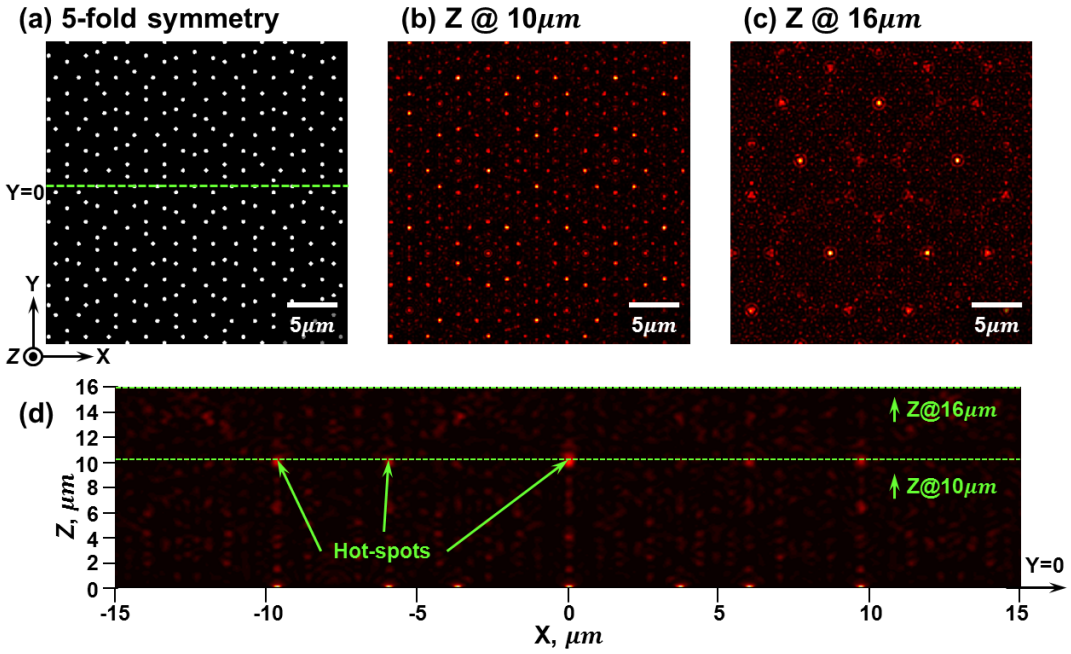

Figure 4.10: ***Sparsely distributed energy hot-spots above a 5-fold symmetry quasi-periodic nanohole array.*** *(a) schematically shows the pattern of a fragment of a 5-fold symmetry quasi-periodic nanohole array and the overall area of the array in calculations is* 50 ×50 μm^2 *with a nanohole size of* 200 nm. *(d) shows a calculated diffraction pattern along the Z direction on the XZ plane at $Y = 0$ with a 5-fold symmetry quasi-periodic nanohole array illuminated by a plane wave at wavelength of* 500 nm. *Note that several significant energy hot-spots can be produced on the XY plane at certain distances away from the array's surface as the calculation results shown in (b) and (c) at the distance of* 10 μm *and* 16 μm, *respectively. The image size of (a), (b) and (c) is* 30 ×30 μm^2.

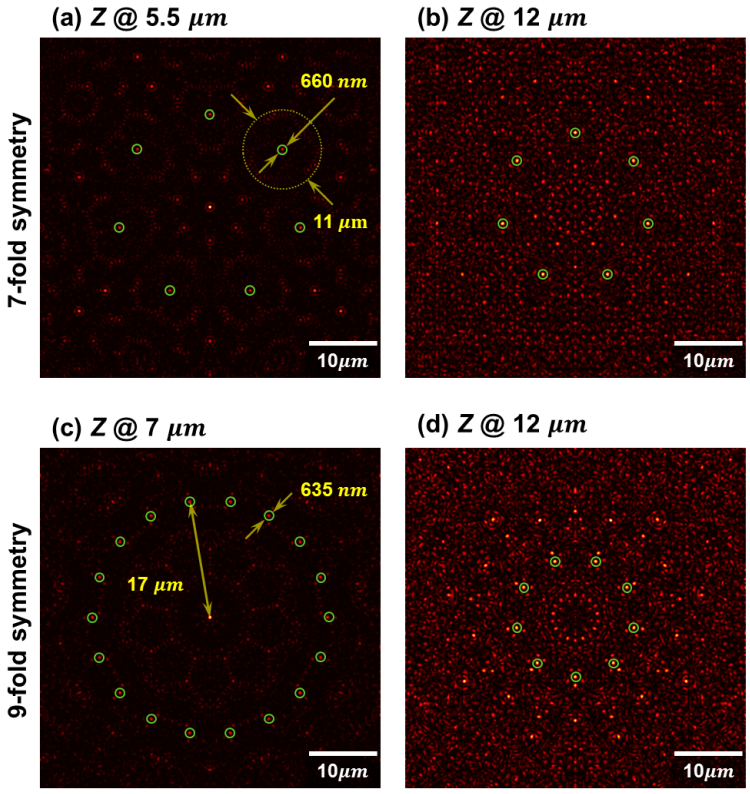

Figure 4.11: ***Sparsely distributed energy hot-spots above quasi-periodic nanohole arrays.*** *Plates (a) to (d) shows the calculated field maps above a 7-fold (upper row) and 9-fold (bottom row) symmetry quasi-periodic nanohole array at the height Z indicated in the figure. In all the cases, the nanohole arrays are illuminated with a wavelength of* 660 nm *and the image size is* 50×50 μm^2. *Note that the number of the generated energy hot-spots is correlated to the order of rotational symmetry in the quasi-periodic nanohole arrays.*

The results displayed in Fig. 4.11 show that the number and locations of energy hot-spots are highly correlated with the order of rotational symmetry of the quasi-periodic nanohole arrays. More specifically, the number of energy hot-spots will be identical to the order of rotational symmetry or its multiples. Also, it is worth mentioning that such energy hot-spots' distribution has the same rotational symmetry as the nanoholes' arrangement on the array, *i.e.* hot-spots are rotated around a central energy hot-spot by $2\pi/N$ radians, where N is the order of the rotational symmetry. This result may be explained by the distribution of spectral maxima in the reciprocal plane of a quasi-periodic nanohole array's field. As we have mentioned above, diffracted field distributions at various distances Z above a nanohole array are reconstructed from the superposition of spectral maxima, which correspond to Montgomery's condition and

are located on different concentric rings. Regarding the nanoholes with quasi-periodic arrangements, the distribution of spectral maxima on Montgomery's rings has the same order of rotational symmetry with the nanoholes' arrangement. Therefore, once an energy hot-spot is generated at distance Z above the array's surface and at distance D away from the array's central axis, N energy hot-spots with distance D to the central axis will be displayed on the image plane (XY plane) and rotated around the centre by $2\pi/N$ radians. However, it is difficult to predict and explain why the hot-spots will be generated at particular Z distances since the diffraction process above the quasi-periodic nanohole arrays is complex. According to the calculation results, it is possible to separate the surrounding hot-spots from the central light localization by careful choice of the distances, wavelengths or the order of rotational symmetry of the quasi-periodic nanohole arrays; however, such results are still not good enough to meet our requirement − to generate a single isolated energy hot-spot within in a wide field of view. A solution can be found by using a radially symmetric quasi-periodic nanohole array as an isolated super-oscillating field generator.

4.3.3 Radially symmetric quasi-periodic nanohole arrays and an isolated super-oscillating energy hot-spot

While viewing the nanohole arrangements with higher order of rotational symmetry, it is found that the nanoholes are arranged on concentric rings with different sizes, forming a radially symmetric pattern on a 2D plane. Fig. 4.12 (a), (b) and (c) represent the schematic diagrams of radially symmetric quasi-periodic nanohole arrays with 13-fold, 20-fold and 27-fold rotational symmetry respectively. To examine the behaviour of light diffraction along the wave propagation direction Z, a 20-fold symmetry quasi-periodic nanohole array is used as an example to observe the diffracted field distributions above the array. The designed 20-fold symmetry quasi-periodic pattern contains about 4,000 nanoholes of 200 nm in diameter and is contained in an area of 50 $\times$50 μm^2 as shown in Fig. 4.13 (a). The wavelength for light illumination on the array is $\lambda = 660$ nm. Through the central point, a calculated result of field distribution on the XZ plane at fixed $Y = 0$ (green dashed line on Fig. 4.13 (a)) is shown in Fig. 4.13 (b). Here, most of the light diffraction is concentrated in the centre ($X, Y = 0$) and contributes to create several highly-isolated energy hot-spots along the Z direction as the green

arrows indicate in Fig. 4.13 (b). Therefore, by using a radially symmetric quasi-periodic nanohole array as a super-oscillating binary mask, it is possible to find that an isolated subwavelength energy hot-spot can be generated on the XY plane several micrometers away from the array and located within a wide field of view. Such a result helps to realize more practical and promising applications, especially in scanning microscope systems or nanolithography.

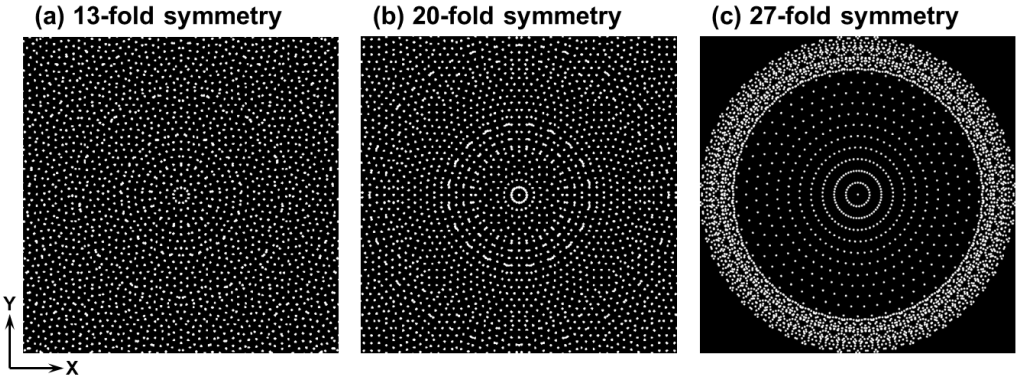

Figure 4.12: ***Patterns of nanohole arrays with radially symmetric quasi-periodic arrangements.*** *Plates (a) to (c) schematically represent the 13-fold, 20-fold and 27-fold symmetry quasi-periodic nanohole arrays respectively.*

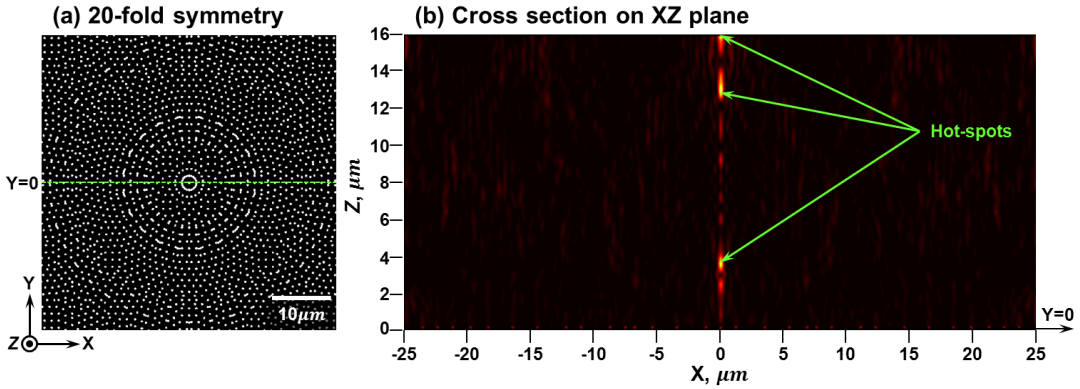

Figure 4.13: ***Light diffraction above a radially quasi-periodic nanohole array.*** *Plate (a) schematically represents the pattern of a 20-fold symmetry quasi-periodic nanohole array. The quasi-periodic pattern is in an area of* $50 \times 50\ \mu\text{m}^2$ *and contains about 4,000 nanoholes of* 200 nm *diameter. (b) shows a calculated diffraction pattern along the* Z *direction on* XZ *plane at* $Y = 0$ *with the nanohole array illuminated by a plane wave of* $\lambda = 660$ nm*. Note that an isolated energy hot-spot can be produced along the* Z *direction as the green arrows indicate, meaning that the radially symmetric quasi-periodic nanohole array can be used as an isolated hot-spot generator.*

As the comparison of the reciprocal plane shows (Fig. 4.6), the more spectral components with varying magnitudes available in the reciprocal plane of an array's field, the

more super-oscillating fields are likely to be generated in the reconstructed diffraction patterns. Therefore, as well as the quasi-periodic nanohole arrays, other nanostructures arranged with different algorithms such as the Fibonacci sequence, mid-temp coulomb gas and the Poisson process, might also generate super-oscillating fields above the array's surface. Taking a 2D Fibonacci lattice shown in Fig. 4.14 (a) as an example, the different magnitude of the corresponding spatial frequencies (Fig. 4.14 (b)) may provide the possibility of generating super-oscillating fields above the array, though the spectral components are distributed regularly [212] in the reciprocal plane. These types of array, therefore, might work and would also be interesting to investigate; however, they have not been tested in this thesis. Here, we focused on the quasi-periodic nanohole arrays with different rotational symmetry because the coordinates of the nanoholes can be easily obtained using commercial software [210]. It is also based on the previous study using a 5-fold quasi-periodic nanohole array as a super-oscillating binary mask [8, 10, 146, 157].

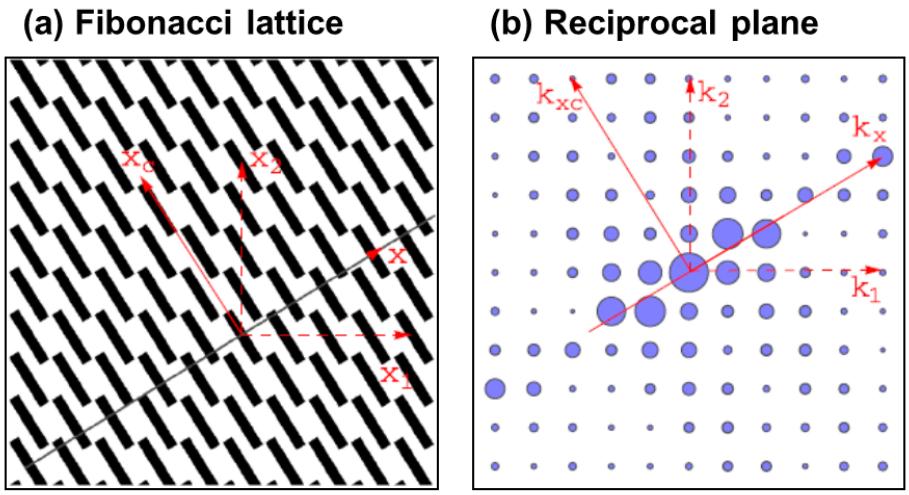

Figure 4.14: ***The 2D Fibonacci lattice and its corresponding reciprocal plane of the spectral components.*** *(a) The geometric diagram of a Fibonacci sequence on a 2D plane which is derived from the cut and project method. (b) The corresponding spectral components in the reciprocal space and the size of the bubbles represents the magnitude of the spatial frequencies. Images are taken from Ref. [212].*

4.4 Radially symmetric quasi-periodic nanohole arrays

To evaluate whether radially symmetric quasi-periodic nanohole arrays can be used as a super-oscillating binary mask to generate subwavelength energy hot-spots in the far-field region, two kinds of radially symmetric quasi-periodic nanohole arrays with different rotational symmetry − 20-fold and 27-fold symmetry − will be designed to test and compare their focusing abilities.

4.4.1 20-fold symmetry quasi-periodic nanohole array

• Sample description

Fig. 4.15 (a) schematically shows the pattern of a 20-fold symmetry quasi-periodic nanohole array whose coordinates are obtained by the multigrid method using JcrystalSoft Nanotube Modeler [210]. In this nanohole array design, there are about 4,000 nanoholes of 200 nm diameter included in the array within an area of 50 $\times$50 μm^2 and arranged on concentric rings with different sizes. Fig. 4.15 (b) shows the reciprocal plane of the 20-fold symmetry quasi-periodic nanohole array's field. It is found that the rich spectral components of the quasi-periodic nanohole array are discrete and located on different circles in the reciprocal plane with a 20-fold rotational symmetry, making it possible to generate super-oscillating energy hot-spots at different distances away from the array.

Fig. 4.15 (c) shows the SEM image of a fabricated 20-fold symmetry quasi-periodic nanohole array sample. The pattern of the sample is constructed in accordance with the algorithm described above and manufactured by Dr. Y. Chen at Rutherford Appleton Laboratory in the U.K. by e-beam lithography (EBL). All the nanoholes of 200 nm are fabricated on a 50 nm thick aluminium film. This selection of material and film thickness is sufficient to make the array act as an ideal binary mask. A diode laser is used for illumination at a wavelength of $\lambda = 660$ nm.

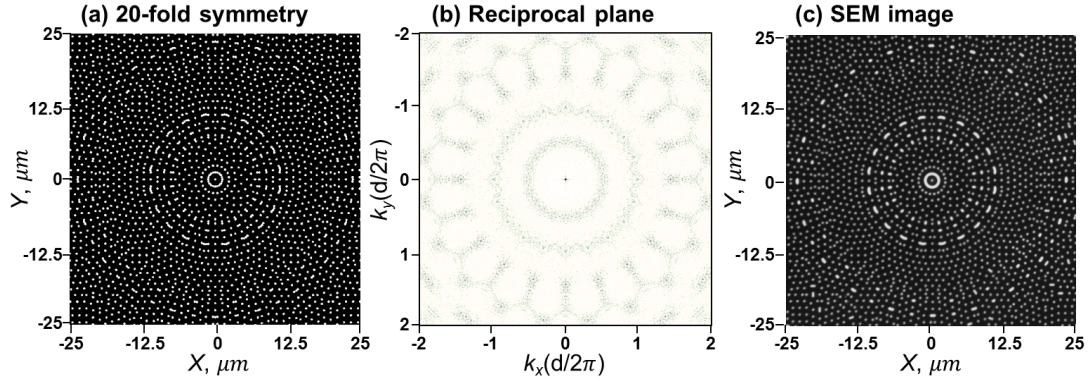

Figure 4.15: ***Super-oscillating binary mask: a radially symmetric quasi-periodic nanohole array with 20-fold rotational symmetry.*** *(a) Schematic diagram of a 20-fold symmetry quasi-periodic nanohole array. The white dots indicate the positions of the nanoholes. In the design, all the nanoholes of* 200 nm *in diameter are included in an area of* 50 ×50 μm^2 *and arranged on concentric rings with different sizes. (b) Reciprocal plane of the radially symmetric quasi-periodic nanohole array's field. A 20-fold rotational symmetry in the distribution of spectral components can be observed. (c) The SEM image of a fabricated 20-fold symmetry quasi-periodic nanohole array, whose pattern shows accordance with the schematic diagram (a). The SEM image is obtained from Dr. Y. Chen at Rutherford Appleton Laboratory in the U.K. and the nanohole array is fabricated on a* 50 nm *thick aluminium film.*

• Theoretical calculations of diffraction patterns above the array

In order to obtain the theoretical diffraction patterns above a 20-fold symmetry quasi-periodic nanohole array, the scalar angular spectrum method is used to calculate field intensity maps at different distances Z away from the array's surface. As shown in Fig. 4.16, the calculated field maps in plates (a) to (i) represent the field distributions at different distances Z from the sample surface (at $Z = 0$ μm) up to the distance of $Z = 8$ μm away from the quasi-periodic nanohole array. The size of the calculated area is the same as the area of the nanohole array (50 ×50 μm^2) and the array is under plane wave illumination at a wavelength of 660 nm in accordance with the experimental light source. The calculated results show that a significant isolated energy hot-spot can be generated at the distance of 4 μm away from the nanohole array. As shown in Fig. 4.16 (e), most of the transmitted energy is concentrated at the centre of the image plane, forming an energy hot-spot, while the rest of the area is dim. Thus, a highly isolated energy hot-spot can be theoretically generated by using a 20-fold symmetry quasi-periodic nanohole array and located in a wide field of view of around 50 μm.

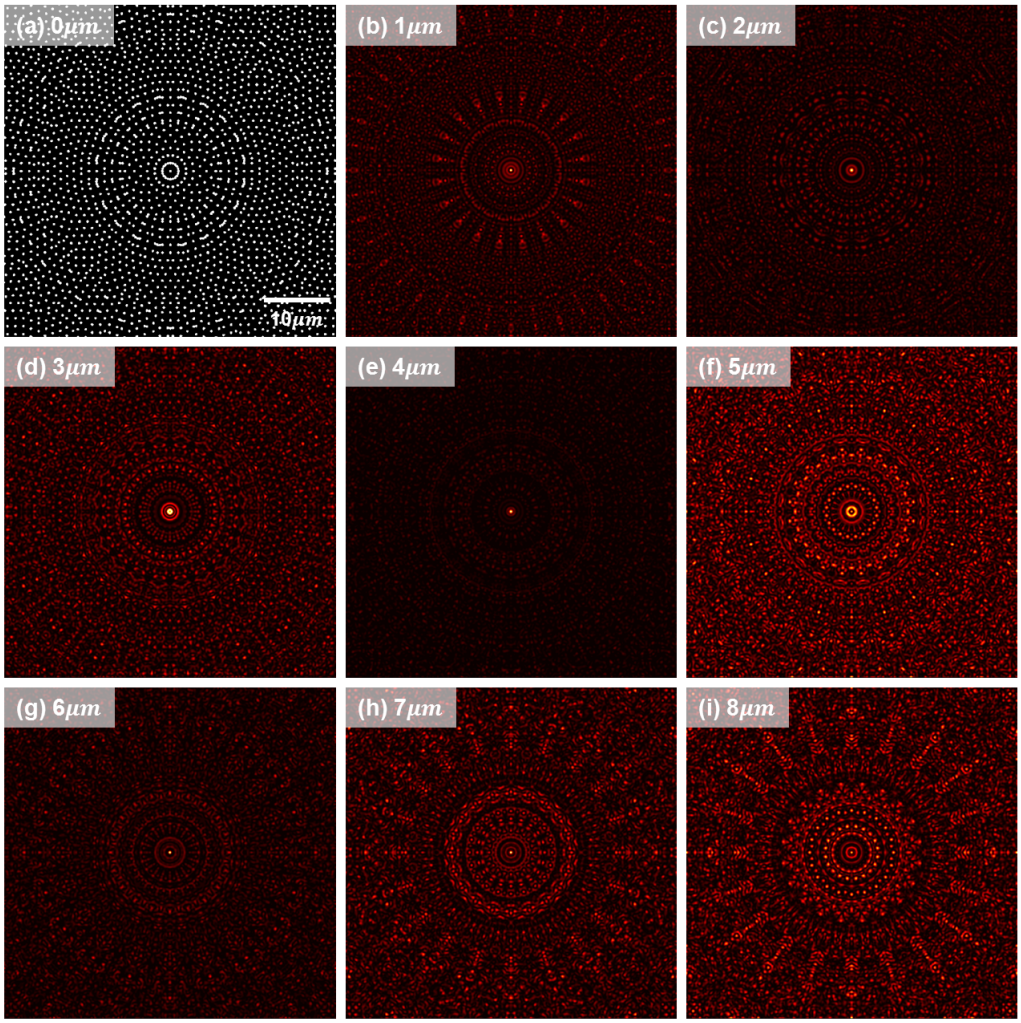

Figure 4.16: ***Calculated field maps at different heights Z above a 20-fold symmetry quasi-periodic nanohole array.*** *Calculation results. Field distribution maps (a) to (i) represent the field distributions at different distances away from the sample surface (a) to the height of $Z = 8$ μm (i). The 20-fold symmetry quasi-periodic nanohole array is under plane wave illumination with a wavelength of* 660 nm. *Note an isolated energy hot-spot can be produced at the distance of* 4 μm *away from the array's surface as shown in (e). All the size of image planes is* 50×50 μm^2.

As mentioned in Sec. 4.3.3 and the calculation result shown in Fig. 4.13 (b), several energy hot-spots can be produced along the Z direction by using a 20-fold symmetry quasi-periodic nanohole array as a super-oscillating binary mask. To precisely determine how far the isolated energy hot-spot is away from the array and to carefully examine the possibility of other isolated hot-spots, a finer and more extensive distance interval is taken into account. In Fig. 4.17, several isolated energy hot-spots are obtained at different distances from the surface of a 20-fold symmetry quasi-periodic

nanohole array. The distances presented in Fig. 4.17 (a), (b) and (c) are 3.5 μm, 13.5 μm and 16 μm, respectively. It should be noted that a subwavelength energy hot-spot of 320 nm (0.48 λ) can be obtained beyond the diffraction limit at the distance of 3.5 μm, that is, beyond the evanescent field region. The light focusing ability of the array can be estimated by the formula of diffraction limit, $\Delta = 0.61\ \lambda/N.A.$ where the Δ is the size of a focused spot. Therefore, the effective N.A. of the 20-fold symmetry quasi-periodic nanohole array is around 1.25 at the wavelength of 660 nm. This significant finding of an isolated energy hot-spot generation has demonstrated that a 20-fold symmetry quasi-periodic nanohole array can be used as a high N.A. lens to concentrate light into a focused spot.

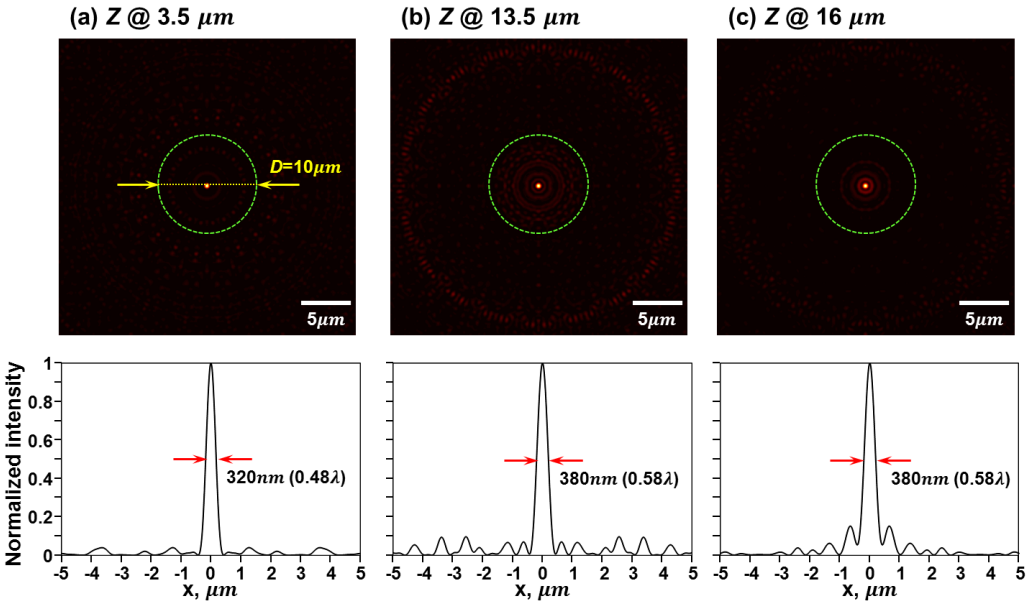

Figure 4.17: ***Several isolated energy hot-spots generated along the*** Z ***direction.*** *Calculation results. With illumination of* 660 nm *on a 20-fold symmetry quasi-periodic nanohole array, several isolated energy hot-spots can be generated at the distance* Z *of* 3.5 μm, 13.5 μm *and* 16 μm, *which are presented in plates (a) to (c), respectively. Here, the size of images is a zoom-in area of* 30 ×30 μm^2. *Note that a subwavelength energy hot-spot can be obtained beyond the diffraction limit at the distance of* 3.5 μm.

• Experimental results and discussions

To experimentally verify the theoretical calculations described above and map the field intensity distributions, experiments both on a conventional optical microscope equipped with a CCD device and a SNOM with a nanoscale Z control have been conducted. First,

in the setup with a conventional microscope, optical images are captured by a digital camera (Canon, EOS) through a 150X objective (Zeiss, N.A.=0.95) with the resolution of the optical images around 200 nm per pixel. With a coarse height tunning of 1 μm, the optical images of the diffracted field distributions at distances away from the array's surface can be acquired. In our experiments, a diode laser with a collimator is used as a plane wave light source to illuminate the array and the wavelength is at 660 nm. Plates (a) to (i) in Fig. 4.18 show the transmission optical microscope images of the field distribution maps at different distances from the sample surface (at $Z = 0$ μm) to the distance of $Z = 8$ μm away from the quasi-periodic nanohole array, respectively. All the images in Fig. 4.18 have a size of 50 ×50 μm^2. These optical microscope images of the diffracted field distributions show a qualitative agreement with the calculated results illustrated in Fig. 4.16. Some of them show clear patterns with a 20-fold rotational symmetry. Due to the limited image resolution and the coarse height tunning in the optical microscope setup, detailed field distribution maps and exact focal distance of an isolated energy hot-spot cannot be obtained. To solve these problems, a SNOM with a subwavelength aperture fibre probe and nanoscale step control is used to acquire detailed information about the field intensity distributions.

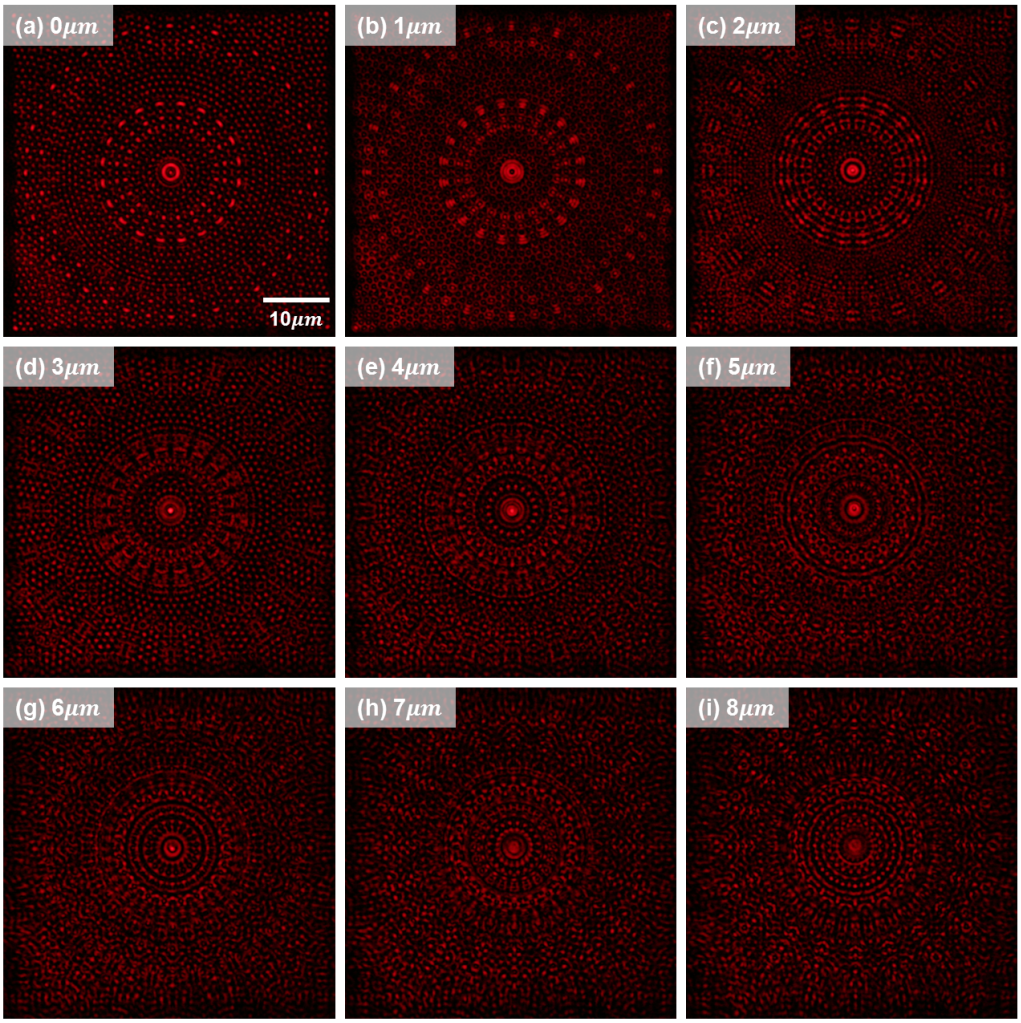

Figure 4.18: ***Transmission optical microscope images of field distributions above a 20-fold symmetry quasi-periodic nanohole array.*** *Transmission optical images. Maps (a) to (i) represent the field distributions at different distances from the sample surface (a) to the height of* $Z = 8$ μm *(i), respectively. The illumination wavelength is* 660 nm. *Note these results qualitatively correspond well with the theoretical calculations as shown in Fig. 4.16, but lack detailed information on the field distributions. The size of the images is* 50×50 μm^2.

By using a SNOM probe scanning at a certain distance away from the array's surface, details of the field distribution maps can be revealed. Fig. 4.19 shows the SNOM mappings at different distances away from a 20-fold symmetry quasi-periodic nanohole array. The scanning area is 30×30 μm^2 and aperture size of the SNOM probe is around 60 nm. Here, the resolution of the SNOM images is 150 nm per pixel. In Fig. 4.19, plates (a) to (f) display the field distributions at different distances from 1 μm to 6 μm away from the quasi-periodic nanohole array's surface, respectively. Among

these scanning results, well isolated energy hot-spots can be found at both distances of 2 μm and 3 μm away from the sample. However, their patterns do not perfectly resemble the previous calculation results of the image planes at 2 μm and 3 μm as shown in Fig. 4.16 (c) and (d). These differences may result from the inhomogeneous light illumination on the sample (a slight tilting of an incident light beam or the sample arrangement), the flatness and thickness variation on the sample surface in the thin film fabrication process or topographic defects on the surface of scanning probes. The reasons will be discussed further below.

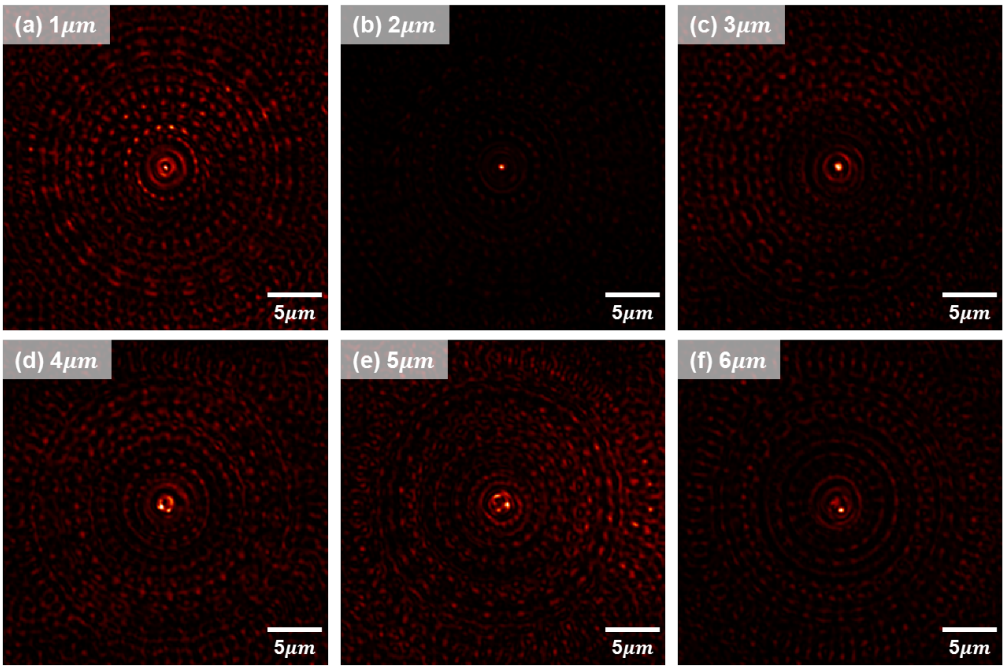

Figure 4.19: ***SNOM mappings at different heights Z above a 20-fold symmetry quasi-periodic nanohole array.*** *Maps (a) to (f) represent the field distributions at the distances from* 1 μm *to* 6 μm*, respectively. The illumination wavelength is* $\lambda = 660$ nm *and the scanning area is* 30×30 μm^2*. Note that well isolated energy hot-spots are produced at the height of* 2 μm *and* 3 μm*.*

Fig. 4.20 (a) and (b) schematically illustrate the impact of an uneven sample surface and the scanning probe's topographic defects on the diffracted field measurements, respectively. In Fig. 4.20 (a), some inhomogeneous defects protrude from the sample surface, which might come from the thin film coating process or environmental temperature change. When approaching a scanning probe to the sample, these defects will cause a false zero level measurement of the sample surface. Therefore, when a scanning probe is lifted up and set to scan at height of Z away from the sample, it actually scans

the diffracted field at the height of $Z+\Delta Z$ with an unintended increase of distance ΔZ. The same reasoning can be used for the situation of topographic defects on a scanning probe as shown in Fig. 4.20 (b). Such diffracted field measurements with an unintended height difference will cause inconsistency between the experimental and calculation results. Therefore, another set of calculations with an imaging distance correction are conducted. In the calculation results shown in Fig. 4.21, with an increase of height difference by 0.4 µm, the calculated field distributions show a very good agreement with the SNOM scanning results demonstrated in Fig. 4.19.

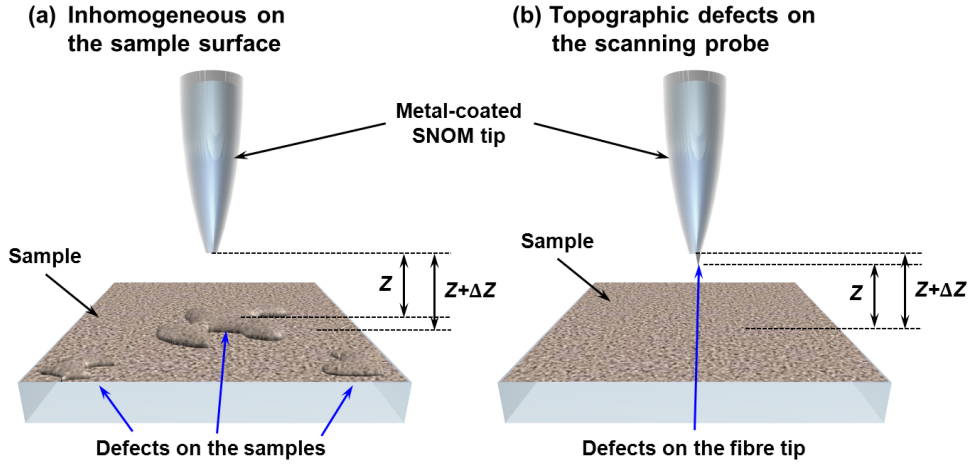

Figure 4.20: ***Impact of an uneven sample surface and the scanning probe's topographic defects on the diffracted field measurements at different heights.*** *Schematic diagrams. Inhomogeneity on the sample surface (a) and topographic defects on a scanning probe will cause a false zero level measurement of the sample surface, which might make the fibre tip scan at the height of $Z+\Delta Z$ with an unintended distant increase ΔZ.*

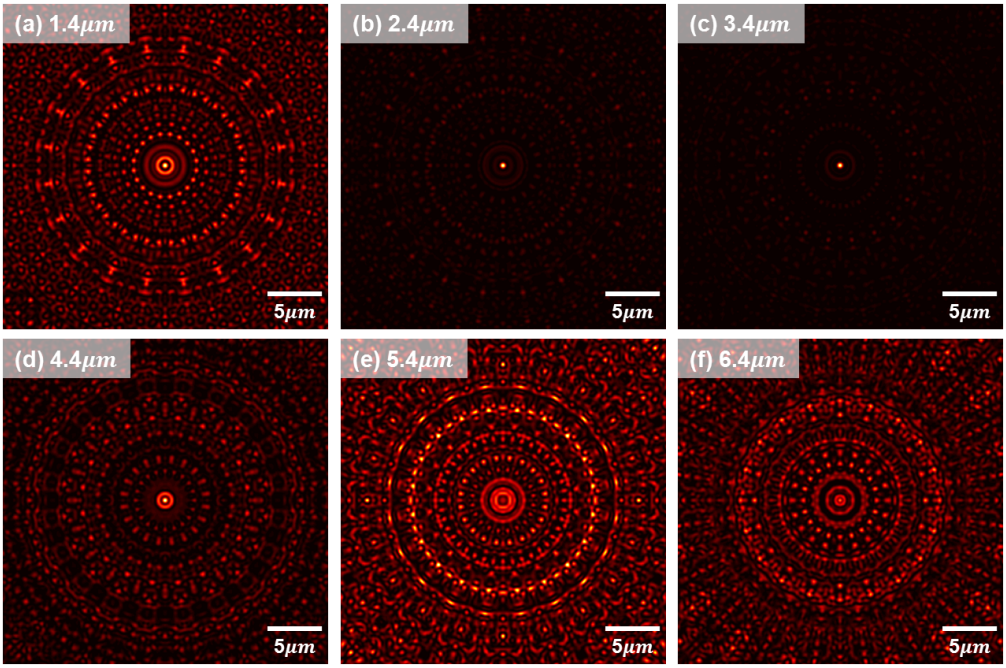

Figure 4.21: ***Calculated field maps above a 20-fold symmetry quasi-periodic nanohole array with an imaging distance correction.*** *Calculation results. Maps (a) to (f) represent the calculated field distributions at the distances from* 1.4 μm *to* 6.4 μm*, respectively. Note the calculated patterns correspond well with the SNOM scanning measurements shown in Fig. 4.19 with a height difference of* 0.4 μm*, which might be from the topographic defects on the sample surface and the fibre tip. The size of all the images is* 30 ×30 μm^2.

To determine the exact focal length and the size of an isolated energy hot-spot, a finer height interval of 100 nm in the Z direction and a finer scanning step of 50 nm in the X and Y directions are adopted in the intensity field mapping. The experimental results are shown in the first row of Fig. 4.22 from the distances of 3 μm to 3.9 μm. All the scanning areas are 9 ×9 μm^2. Compared with the theoretical calculations shown in the second row in Fig. 4.22, a strong agreement between the experimental and calculation results can be found, but an imaging distance correction of 0.4 μm still occurs. Regarding the size of the energy hot-spots, Fig. 4.22 (c) shows that the cross-section profile of the energy hot-spot at the scanning height of 3 μm, with the size of the isolated hot-spot around 320 nm (0.48 λ), which corresponds well to the calculation result at $Z = 3.4$ μm. In Fig. 4.22 (d), the cross-section suggests that a smaller localized spot of 250 nm (0.38 λ) can be produced at a height of 3.7 μm, but surrounded by a larger side band. Unlike the cross-section profile of the calculation result at $Z = 4.1$ μm,

the asymmetrical energy distribution on the side band may result from inhomogeneous light illumination or a slight tilt of the nanohole array in the experiments.

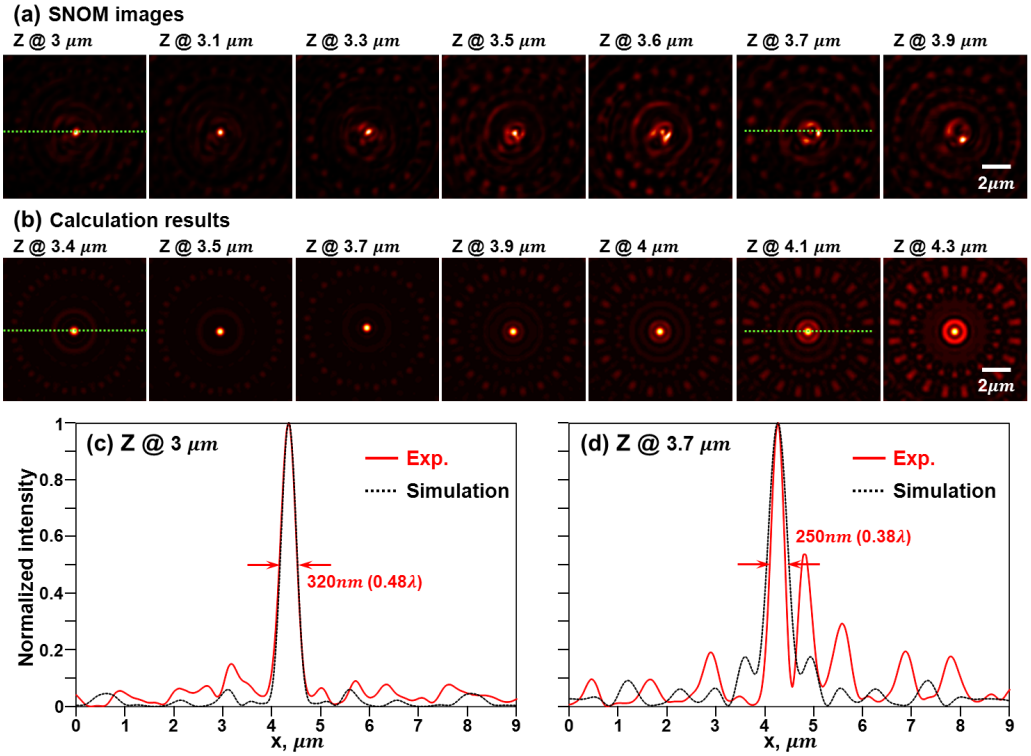

Figure 4.22: ***Finer SNOM mapping at different heights Z above a 20-fold symmetry quasi-periodic nanohole array and the corresponding calculation results.*** *Upper row: SNOM mappings; Bottom: Calculated field distributions with an imaging distance correction* $\Delta Z = 0.4$ μm. *The size of all the images is of* 9×9 μm^2. *(c) and (d) display the comparison of cross-section profiles both on the experimental and calculation results, which correspond to the green dashed lines in row (a) and (b). Note that an isolated subwavelength energy hot-spot of* 320 nm *(*0.48 λ*) can be obtained at the scanning distance of* 3 μm, *while a smaller localized spot of* 250 nm *(*0.38 λ*) is produced at distance of* 3.7 μm *with a surrounding bright halo. The asymmetrical intensity cross-section profile in the SNOM mapping result at distance of* 3.7 μm *may result from the slight tilting of the light source illumination or the nanohole array sample arrangement.*

4.4.2 27-fold symmetry quasi-periodic nanohole array

• Sample descriptions

The other type of radially symmetric quasi-periodic nanohole arrays used as an isolated energy hot-spot generator is a nanohole array with a 27-fold symmetry quasi-periodic arrangement, whose schematic diagram is shown in Fig. 4.23 (a). In this nanohole array design, there are about 4,000 nanoholes of 200 nm included in an range of 80 μm in diameter. The coordinates of nanoholes are obtained by the cut and project method

with assistance from Mr. V. Savinov in Optoelectronics Research Centre, University of Southampton [206]. In the nanoholes' arrangement, as shown in Fig. 4.23 (a), all the nanoholes are located on concentric rings with different sizes and some of them may overlap the others. The nanohole array sample is also fabricated on a 50 nm thick aluminum thin film by Dr. Y. Chen at Rutherford Appleton Laboratory in the U.K. using the EBL technique. Fig. 4.23 (b) shows the SEM image of a fabricated sample in accordance with the designed 27-fold symmetry quasi-periodic pattern.

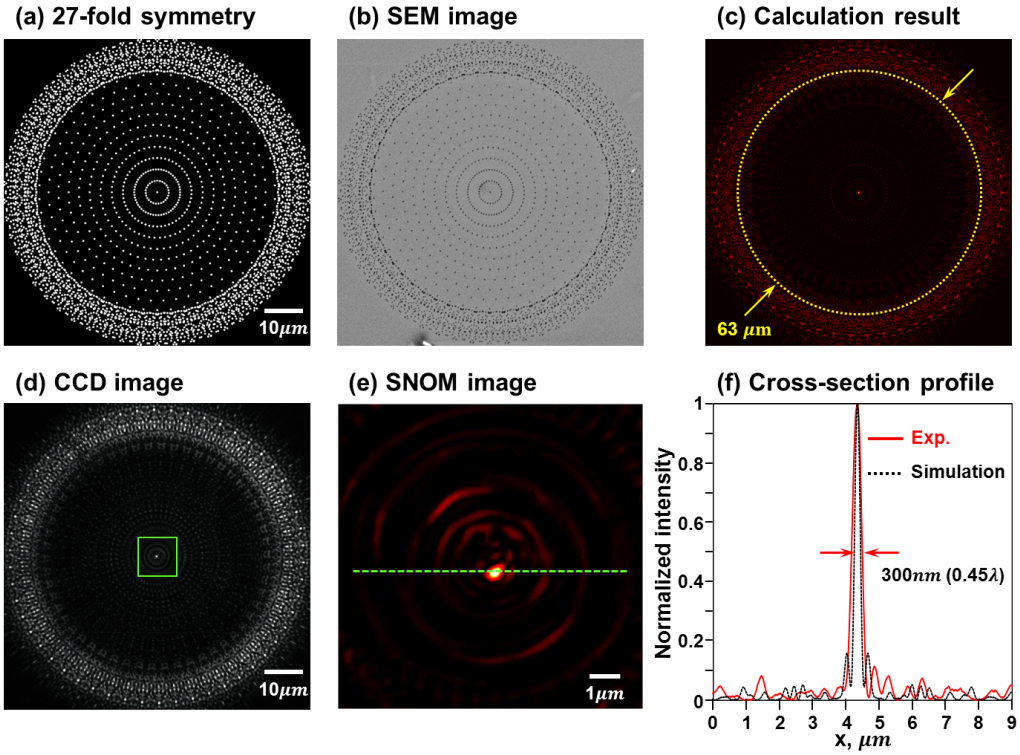

Figure 4.23: ***27-fold symmetry quasi-periodic nanohole array as an isolated energy hot-spot generator.*** *(a) shows a schematic diagram of a 27-fold symmetry quasi-periodic nanohole array. The nanohole array is* 80 μm *in diameter and the size of nanoholes is* 200 nm*. The nanoholes are positioned on different concentric rings and some of them may overlap the others. (b) displays the SEM image of a fabricated sample on a* 50 nm *aluminum thin film. (c) Calculated diffraction pattern above the nanohole array at the distance of* $Z = 4.4$ μm*. A well isolated energy hot-spot is located at centre in a wide view field of* 63 μm *in diameter. (d) shows a corresponding CCD image of the field distribution at the distance around* 4 μm *away from the sample surface. The image size is* 80 ×80 μm^2*. (e) A SNOM mapping on a zoom-in area of* 10 ×10 μm^2 *around the central bright spot as the green indicates in (d). The scanning distance is* 4.4 μm *away from the array's surface. (f) The cross-section profiles show a good agreement between experimental and calculation results and the size of the isolated energy hot-spot is around* 300 nm *(*0.45 λ*). The CCD image (d) is obtained from Dr. E. T. F. Rogers at Optoelectronics Research Centre, University of Southampton.*

• **Subwavelength energy hot-spot in the far-field region**

Among the calculated field distributions, the best isolated energy hot-spot can be found at the distance of 4.4 μm away from the surface of a 27-fold symmetry quasi-periodic nanohole array when the array is illuminated with plane wave at a wavelength of 660 nm. The calculated intensity map is shown in Fig. 4.23 (c). An isolated energy hot-spot is located within a wide view field of 63 μm in diameter and the size of the hot-spot is around 280 nm. In the experimental confirmations, a diode laser operated at the wavelength of 660 nm is used as an optical source and an optical microscope with a CCD device (SPOT, RT3) is employed to capture the field distribution images through a 150X objective at different distances away from the array's surface. Here, the resolution of the acquired optical images is around 50 nm per pixel. As the CCD image in Fig. 4.23 (d) shows, a corresponding diffraction pattern to the theoretical calculation can be found at around 4 μm away from the sample surface. By SNOM mapping of a zoom-in area of 10 $\times$10 μm^2 as the green square indicates in Fig. 4.23 (d), the well isolated energy hot-spot can be found at the height of 4.4 μm. The zoom-in SNOM scanning result in Fig. 4.23 (e) displays the detailed field distribution around the central hot-spot. To obtain the size of the energy hot-spot and compare with the theoretical calculations, cross-section profiles of the hot-spot on the SNOM experiments and theoretical calculation are presented in Fig. 4.23 (f). A very good agreement between the results can be found, and the size of the isolated energy hot-spot from the experimental measurement is around 300 nm (0.45 λ). Therefore, the focusing ability of a 27-fold symmetry quasi-periodic nanohole array can be estimated by the formula of diffraction limit and the effective N.A. is about 1.34 when the operating wavelength is 660 nm.

4.4.3 Axial resolution of the generated energy hot-spot

From the above theoretical calculations and experimental results, both types of radially symmetric quasi-periodic nanohole arrays − 20-fold and 27-fold rotational symmetry − can both be used as a light concentrator to generate an isolated super-oscillating energy hot-spot on the XY image plane beyond the evanescent field region. Besides the subwavelength lateral resolution, another important issue is the axial resolution

of the generated energy hot-spot in the Z direction. A series of calculations on the evolution of the super-oscillating field along the Z direction have been conducted to estimate the axial resolution of the generated energy hot-spot. The calculation results shown in Fig. 4.24 (a) and (b) display the diffracted field distributions on the XZ plane of a 20-fold and a 27-fold symmetry quasi-periodic nanohole array illuminated with plane wave of 660 nm, respectively. The two radially quasi-periodic nanohole arrays have the same design parameters as described previously. In Fig. 4.24 (a), the field distribution shows an energy hot-spot generated on the XZ plane at $Y = 0$ along the central axis of a 20-fold symmetry quasi-periodic nanohole array in a range from 2 μm to 5 μm away from the sample surface. At the distance of $Z = 3.6$ μm, the energy hot-spot exhibits the maximum intensity and the minimum spot size on the XY plane. The lateral resolution here is around 320 nm (0.48 λ), while the axial resolution of the energy hot-spot in the Z direction is around 750 nm. According to the formula of axial resolution,

$$\triangle = \frac{2\lambda}{(N.A.)^2}, \tag{4.4}$$

$\triangle$ is the size (FWHM) of the generated spot in the Z direction. The effective N.A. of a 20-fold symmetry quasi-periodic nanohole array can be estimated as around 1.32 when the illumination wavelength is at $\lambda = 660$ nm. In addition, when using a 27-fold symmetry quasi-periodic nanohole array as an isolated energy hot-spot generator, the energy hot-spot is generated in a range of 3 μm to 6 μm away from the array's surface and the calculated field distribution on the XZ plane is shown in Fig. 4.24 (b). The best lateral resolution of the spot is around 250 nm (0.38 λ) at the height of $Z = 4.8$ μm, while the axial resolution is about 750 nm, giving an effective N.A. of 1.32. These results are similar to the use of a high N.A. conventional lens of 1.34 operated in oil at $\lambda = 500$ nm. These results can lead to further applications like scanning microscopy, bio-sensors or detectors and high density data storage.

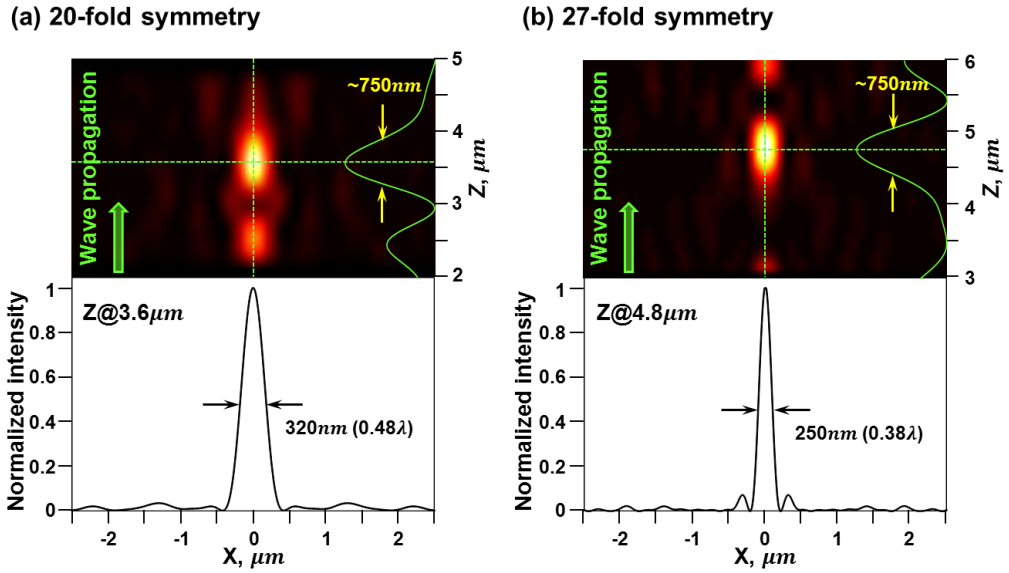

Figure 4.24: ***Axial resolution of the generated energy hot-spots.*** *Calculated field distributions along the Z direction on XZ plane at* $Y = 0$ *of (a) a 20-fold and (b) a 27-fold symmetry quasi-periodic nanohole array illuminated by a plane wave of* $\lambda = 660$ nm. *In (a), the optical energy is concentrated at centre, forming an energy hot-spot in the Z direction along the central axis of the array. Energy hot-spot with the maximum intensity and the minimum size is generated at the height of* 3.6 μm *away from the array's surface. The lateral resolution is around* 320 μm *(*0.48 λ*), while the axial resolution is around* 750 μm. *In (b), the size of the generated hot-spot is around* 250 μm *(*0.38 λ*) and the axial resolution is around* 750 μm. *Note that both results show that radially quasi-periodic nanohole arrays with 20-fold and 27-fold rotational symmetry can be used as an isolated hot-spot generator and the effective N.A. is around 1.32.*

Regarding the size of the super-oscillating energy hot-spots, an energy hot-spot can be arbitrarily small based on the theory of optical super-oscillation. In fact, when a super-oscillating field is generated as a very small concentrated energy hot-spot at certain place, a rapidly increasing side band of optical energy will surround the energy hot-spot as Fig. 4.22 (a) at distance of 3.7 μm shows. Although the size of the focused spot can be very small, it is complicated to make the use of super-oscillations practically with the presence of high intensity halos surrounding the hot-spot. Therefore, it will be a challenge to obtain a well isolated subwavelength energy hot-spot within in a much wider field of view. Based on our studies so far, the best result can only be achieved by using a radially symmetric quasi-periodic nanohole array as a super-oscillating binary mask to generate an isolated hot-spot whose size is slightly beyond the diffraction limit. For example, the size of an energy hot-spot generated by the use of a 20-fold symmetry quasi-periodic nanohole array in Fig. 4.19 (a) at $Z = 3$ μm is 320 nm (0.48 λ), while in

Fig. 4.23 (e), a subwavelength energy hot-spot of 300 nm (0.45 λ) occurs at $Z = 4.4$ μm with the use of a 27-fold symmetry quasi-periodic nanohole array.

To make a use of the super-oscillating energy hot-spots in an optical imaging system, the spot energy is an important issue and has to be considered. In our cases, an isolated energy hot-spot is generated at $Z = 3$ μm by a 20-fold symmetry quasi-periodic nanohole array and the ratios of the spot energy to the total incident energy (R_i) and the total transmitted energy behind the array (R_t) are around 0.002% and 0.04%, respectively. A 27-fold symmetry quasi-periodic nanohole array generates a subwavelength energy hot-spot at $Z = 4.4$ μm and the energy ratios R_i and R_t are around 0.00025% and 0.01%, respectively. The low energy ratio R_i of the two super-oscillating binary masks results from the limited number of nanaholes (around 4,000 nanoholes for each nanohole array) distributed on a much wider area. The fraction of the 20-fold and 27-fold symmetry quasi-periodic nanohole arrays that is transparent is around 5% and 2.5%, respectively. Thus, most of the incident energy is reflected by the binary masks. Regarding the ratio R_t between the spot energy and the transmitted energy behind the arrays, it is found that the energy of the focused spot generated by using the 27-fold symmetry quasi-periodic nanohole array is much less than the one generated by the use of a nanohole array with 20-fold symmetry, although the spot size is slightly smaller. From the calculation result and the CCD image shown in Fig. 4.23 (c) and (d), it is found that most of the energy is located in the outer sidebands while a subwavelength focus is generated at the centre. It is expected that by further investigation, subwavelength light localization with significantly higher efficiency can be achieved.

4.5 Discussions

In the results above, we focused on the relationship between nanohole arrangement and the diffraction patterns generated above the nanohole arrays. Through theoretical calculations and experimental examinations, an isolated energy hot-spot within a wide field of view can be produced by using radially symmetric quasi-periodic nanohole arrays (we have used quasi-periodic nanohole arrays with 20-fold and 27-fold rotational symmetry as examples). Besides the nanoholes' arrangements, other parameters which also affect the generated diffraction patterns are also interesting to investigate, for instance, the nanoholes' size, the overall area of nanoholes and the illumination wavelengths. In this section, the impact of different parameters on the generated diffraction patterns will be extensively discussed and a 7-fold symmetry quasi-periodic nanohole array will be used to demonstrate the differences, chosen for its rich distributions of energy hot-spots.

4.5.1 Different sizes of nanoholes

Regarding the nanoholes diameter ϕ, we have previously fixed the nanoholes' size at $\phi = 200$ nm. The pattern of a 7-fold symmetry quasi-periodic nanohole array with the nanoholes' size of 200 nm in an overall area of 50 $\times$50 μm^2 is shown in Fig. 4.25 (a). All the nanoholes are distributed on a 2D plane. With plane wave illumination at wavelength of $\lambda = 660$ nm, energy hot-spots can be generated on a plane 4 μm from the array's surface and form a field distribution with 7-fold rotationally symmetric arrangement as shown in Fig. 4.25 (b). As the green dashed lines indicate, the angle between neighboring energy hot-spots which have equal distance from the central spot is $2\pi/7$.

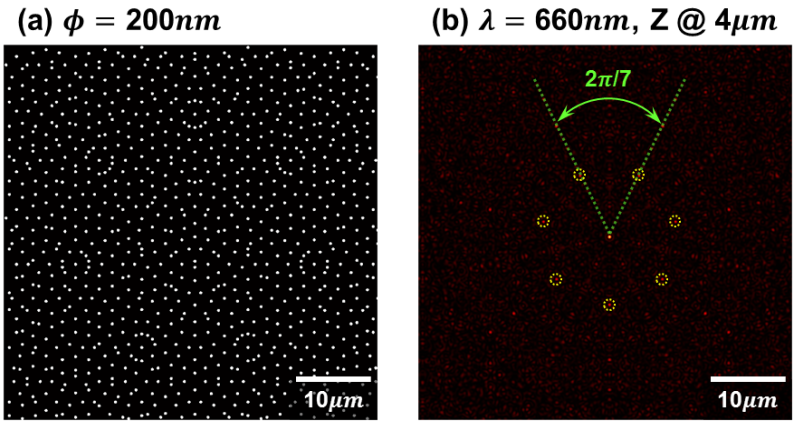

Figure 4.25: ***Energy hot-spots generated above a 7-fold symmetry quasi-periodic nanohole array.*** *Calculated field distributions. (a) shows the pattern of a 7-fold symmetry quasi-periodic nanohole array with nanoholes size of* 200 nm*. The pattern is contained in an overall area of* 50 ×50 μm^2*. With plane wave illumination of* 660 nm *on the nanohole array, energy hot-spots with 7-fold rotational symmetry can be produced on an image plane* 4 μm *away from the array's surface. The yellow dashed circles show the positions of energy hot-spots which are located on the same concentric ring, while the green dashed lines indicate the angle of* $2\pi/7$ *between the neighboring hot-spots.*

To consider the impact of nanohole diameter ϕ on the generated patterns above the array, we change the nanohole's diameter from 400 nm to 1 μm. The patterns with different nanohole sizes are shown in Fig. 4.27 (a) to (d), respectively. All the nanohole array patterns are included in an overall area of 50 ×50 μm^2 and the 7-fold rotational symmetry of the nanoholes' distribution can still be observed. With an increase in the nanoholes' size, some of nanoholes may overlap neighboring nanoholes, forming some ring patterns on the binary masks as shown in plate (d).

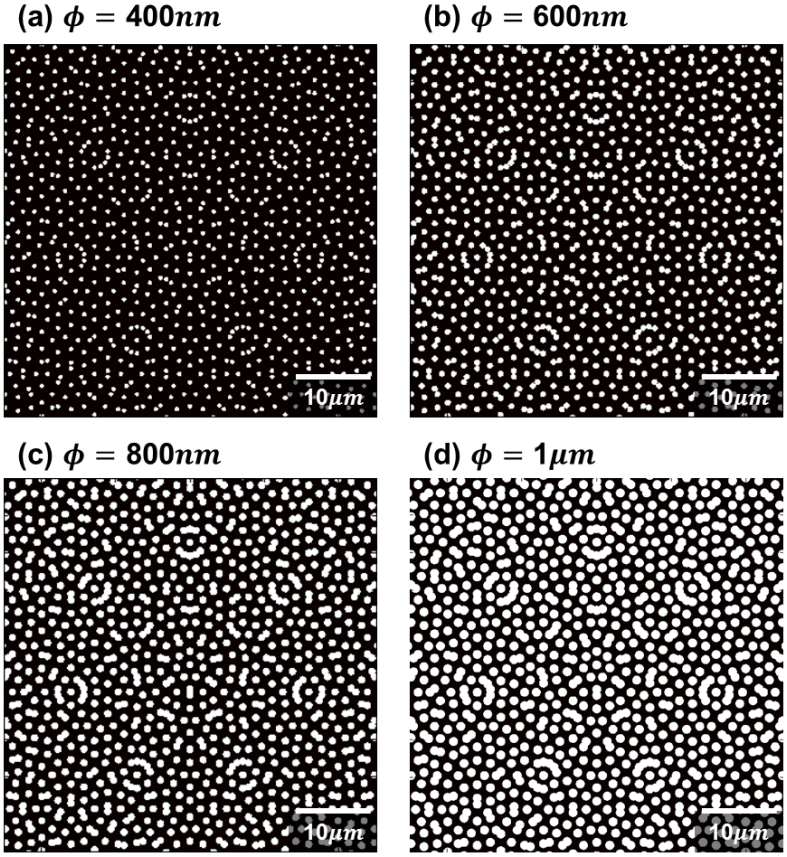

Figure 4.26: ***Patterns of a 7-fold symmetry quasi-periodic nanohole array with different nanoholes' size*** ϕ**.** *Schematic diagrams. Plates (a) to (d) show the patterns of a 7-fold symmetry quasi-periodic nanohole array with the size of nanoholes changed from* 400 nm *to* 1 μm *in diameter. The overall area of each array pattern is* 50 ×50 μm^2*. Note that some of nanoholes may overlap with the neighboring nanoholes as the size of nanoholes increases.*

Fig. 4.27 shows the diffracted field distributions from the arrays at a height of 4 μm (λ = 660 nm). In the results, all the maps exhibit a 7-fold rotationally symmetric arrangement which are similar to the diffraction pattern shown in Fig. 4.25 (b), indicating the positions of nanoholes are significant to the pattern generation above the array.

With an increase in the nanoholes' size, though energy hot-spots with higher intensity can be created due to more optical energy passing through the binary mask in the same overall area, the energy side lobes around the hot-spots will rapidly increase, making the field distributions complicated. As Fig. 4.27 (d) shows, many subwavelength energy hot-spots at local centers surrounded by bright halos occur on the image plane. The size of the energy hot-spots can be arbitrarily small, but the energy of the spots will be much lower compared to the surrounding side lobes. This is the expense

of subwavelength hot-spot generation. Such a complicated field distribution makes the use of the subwavelength hot-spots more difficult. Therefore, an equilibrium choice on the size of nanoholes with different nanohole arrangements is required, depending on the intended application.

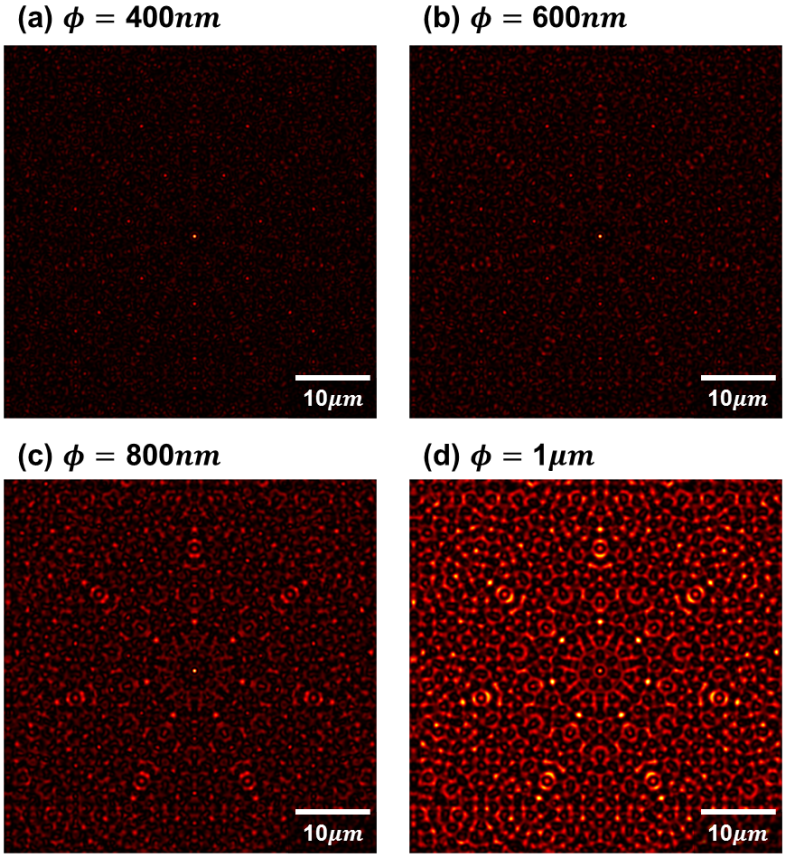

Figure 4.27: ***Diffraction patterns generated above 7-fold symmetry quasi-periodic nanohole arrays with different nanoholes' size.*** *Calculation results. Plates (a) to (d) display the calculated field distributions above 7-fold symmetry quasi-periodic nanohole arrays with nanoholes' diameter changed from* 400 nm *to* 1 µm. *The illumination wavelength is* $\lambda = 660$ nm *and the patterns are on a plane* 4 µm *from the arrays' surface. Note that the patterns have similar 7-fold rotational symmetry. With an increase in the nanoholes' size, more subwavelength optical localizations with increased energy side lobes surrounded can be observed on the image plane. The size of all the images is* 50×50 µm^2.

4.5.2 Selection of illumination wavelengths

Regarding the wavelength of illumination on nanohole arrays, it is not necessary to use $\lambda = 660$ nm as in the previous discussions. The reason for choosing this illumination wavelength is that the optical source could be easily acquired in our lab to conduct the experiments. Actually, with different wavelength illumination of the same nanohole array, a similar diffraction pattern can be created at different distance from the array's surface. Here, we use the 7-fold symmetry quasi-periodic nanohole array illuminated with two different wavelengths of 550 nm and 660 nm as an example. As the calculation results in Fig. 4.28 (a) and (b) show, similar diffraction patterns can be created by the array illuminated with the two wavelengths at height of 16 μm and 14.8 μm, respectively. In fact, in the designs of nanohole arrays to achieve an isolated energy hot-spot generation within a wide field of view, we have also tested radially symmetric quasi-periodic nanohole arrays with different orders of rotational symmetry and different illumination wavelengths. Fig. 4.29 shows some calculation results, indicating that an isolated energy hot-spot can be created at different distance above different types of nanohole arrays with differing illumination wavelengths.

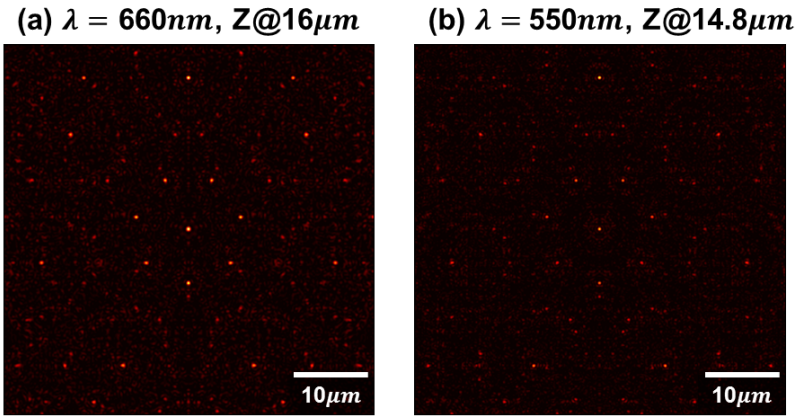

Figure 4.28: ***Similar diffraction patterns generated above a 7-fold symmetry quasi-periodic nanohole array with different illumination wavelengths.*** *Calculation results. (a) shows a significant field distribution above a 7-fold symmetry quasi-periodic nanohole array created by an illumination of* $\lambda = 660$ nm *at height of* 16 μm*, while a similar diffraction pattern (b) can be revealed at different height of* 14.8 μm *when the array is illuminated by* $\lambda = 550$ nm*. The size of the image plane is* 50×50 μm^2*.*

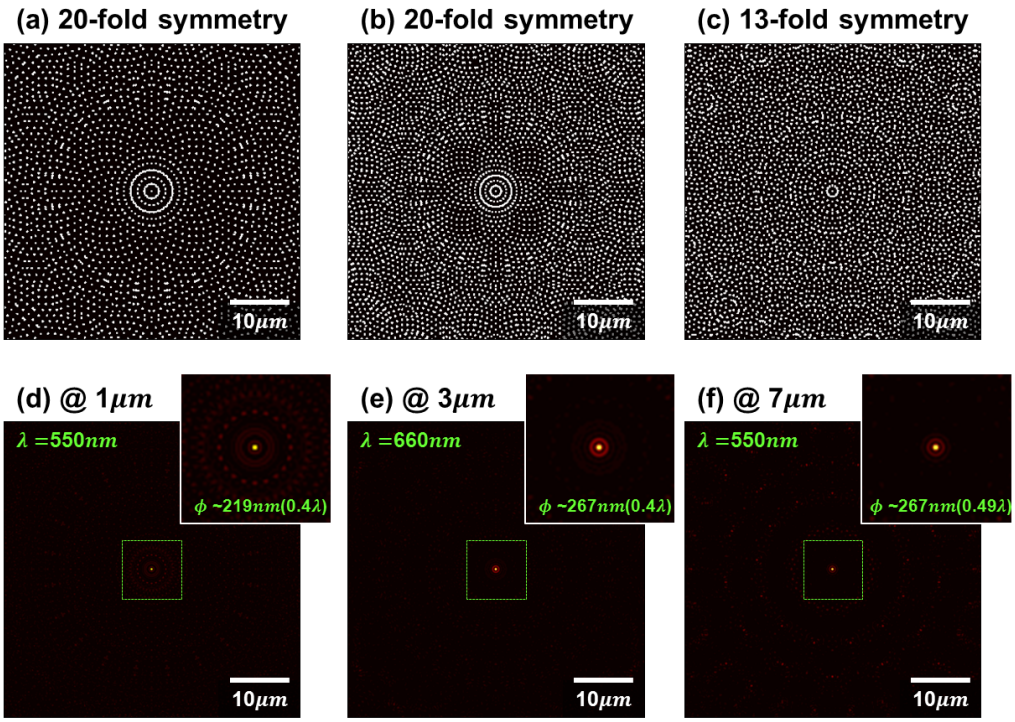

Figure 4.29: ***Isolated energy hot-spots generated by radially symmetric quasi-periodic nanohole arrays with different rotational symmetry and different illumination wavelengths.*** *Calculated field distributions. Plates (a) to (c) schematically show the patterns of nanohole arrays with different rotational symmetry. The patterns are included in an overall area of* 50 ×50 μm^2 *and the diameter of the nanoholes is* 200 nm. *Plates (d) to (f) display the corresponding field distributions of an energy hot-spot generated on planes at different heights Z with different illumination wavelengths as indicated in the figures. The insets show the detailed field distributions in a zoom-in area of* 10 ×10 μm^2.

4.5.3 Scaling of the nanohole arrays

Another interesting issue is the impact of the scaling on the nanohole arrays' design on the diffraction patterns generated above it. According to the algorithms for generating quasi-periodic pattern on a 2D plane, there is no boundary limitation on the quasi-periodic sequence. That is to say, the positions of nanoholes can be obtained anywhere on an infinite plane and the distance between nanoholes can be arbitrarily changed using different scales. Here, we use the 7-fold symmetry quasi-periodic nanohole arrays with different scaling sizes as an example. As shown at the top of Fig. 4.30, the nanohole array pattern **a** is included in an area of 50 ×50 μm^2 as shown in the plate (i) of Fig. 4.30 (a), while the other array **b** with a scale factor of 2 is included within an area of 100 ×100 μm^2 as shown in the plate (i) of Fig. 4.30 (b). The diameter of the nanoholes in both nanohole arrays is fixed at 200 nm. With plane wave illumination of

$\lambda = 660$ nm on the nanohole array **a**, diffraction patterns within 50 μm^2 at $Z = 4$ μm and $Z = 16$ μm away from the array are shown in plates (*ii*) and (*iii*) in Fig. 4.30 (a). By using an illumination wavelength with scale factor of 2 on the scaled nanohole array **b**, identical field distributions will be produced at twice the imaging distance Z. As shown, plates (*ii*) and (*iii*) in Fig. 4.30 (b) show the same calculated diffraction patterns as the plates (*ii*) and (*iii*) in Fig. 4.30 (a). The illumination wavelength is 1.32 μm and the patterns are on scaled image planes of 100 μm^2 at $Z = 8$ μm and 32 μm. The ratio of energy hot-spots to the overall area is the same in both cases.

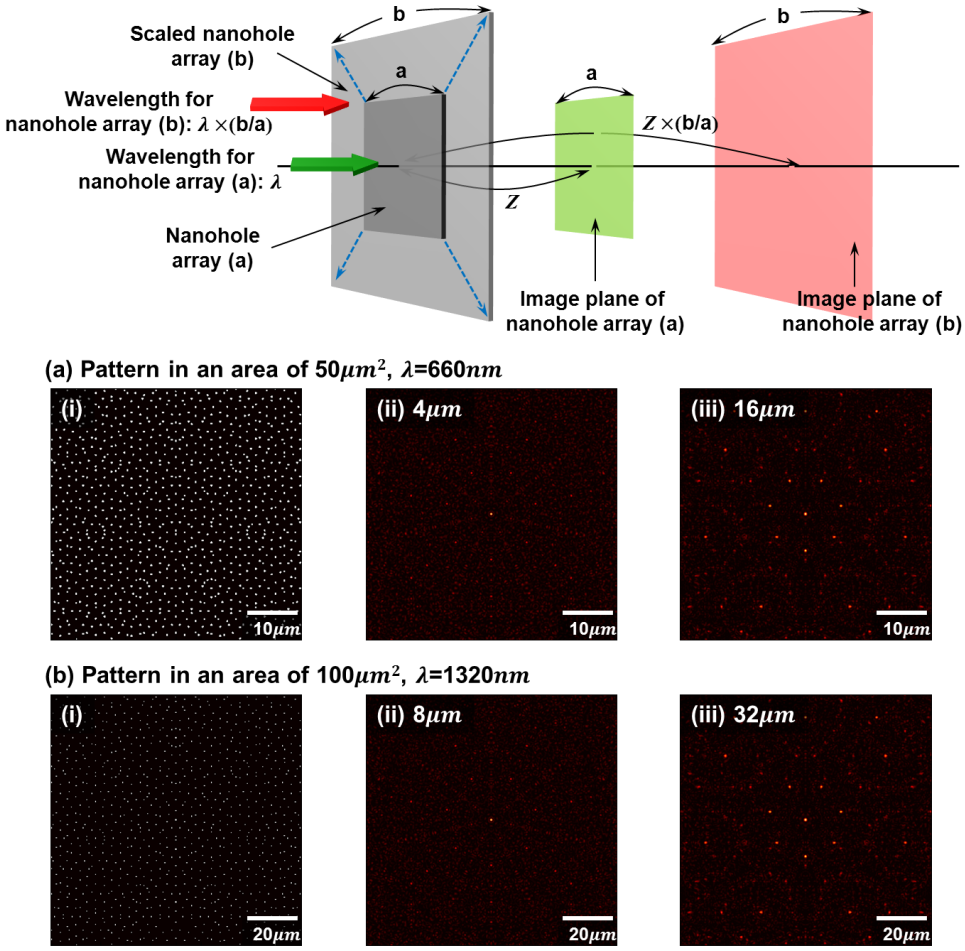

Figure 4.30: ***Field distributions generated above different scaled nanohole arrays.*** *At the top of the figure, the schematic diagram shows an arrangement of illuminations on different scaled nanohole arrays and identical field distributions generated at scaled imaging distances. Plate (i) in (a) shows the pattern of a 7-fold symmetry quasi-periodic nanohole array in an area of* 50 μm^2*, while (ii) and (iii) display the diffraction patterns at* $Z = 4$ μm *and* 16 μm *respectively as the array illuminated with* $\lambda = 660$ nm*. (b) shows the plane wave illumination of* 1.32 μm *on a scaled nanohole array of* 100 μm^2*. Plates (ii) and (iii) in (b) display the same field distributions at scaled imaging distance of* 8 μm *and* 32 μm*.*

Since the same field distributions can be created further away from an expanded nanohole array's surface, it is of interest to re-examine and compare the transverse and axial focusing ability of the 20-fold and 27-fold symmetry quasi-periodic nanohole arrays within the same overall area. By fixing the area of the two nanohole arrays in a size of 50 ×50 μm^2 and illuminating with a plane wave of $\lambda = 660$ nm, the calculated field distributions of a 20-fold and a 27-fold symmetry quasi-periodic nanohole array on XZ plane at $Y = 0$ are shown in Fig. 4.31 (a) and (b), respectively. As seen

from the results, both nanohole arrays can be used as super-oscillating binary masks to concentrate diffracted light along the central axis of the arrays and generate isolated energy hot-spots on planes at various heights. Regarding the Z-extent of the focusing, the optical energy can be propagated further away from the array's surface by using a 27-fold symmetry quasi-periodic nanohole array, activating a "light channel" along the central axis of the array. Along the light channel, several subwavelength energy hot-spots can be produced at various distances away from the array's surface. This result can lead to further applications like scanning microscopy, bio-sensors or detectors and high density data storage.

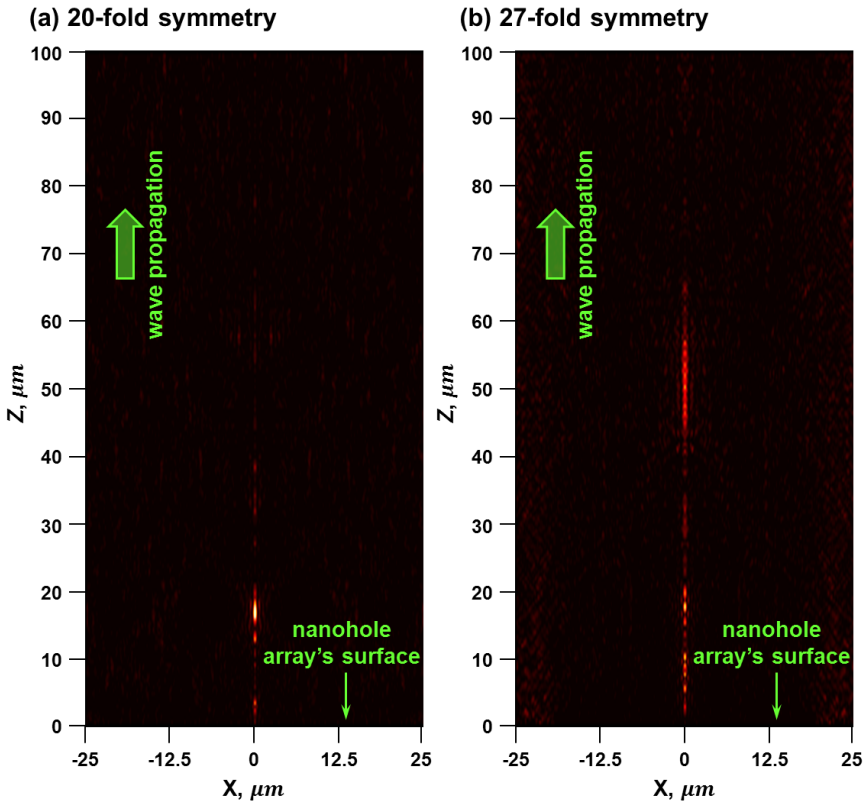

Figure 4.31: ***Light channel activation.*** *Calculated field distributions along the Z direction on XZ plane at $Y = 0$. Radially symmetric quasi-periodic nanohole arrays with (a) 20-fold and (b) 27-fold rotational symmetry are included in an overall area of* $50 \times 50\ \mu m^2$ *and illuminated by a plane wave of* $\lambda = 660$ nm. *In both cases, the optical energy can be concentrated at centre of the array and several energy hot-spots can be produced along the Z direction, making it an isolated hot-spot generator. By using a 27-fold symmetry quasi-periodic nanohole array, a light channel is activated and the optical energy can be propagated further away from the array's surface than with the use of a 20-fold symmetry quasi-periodic nanohole array.*

To sum up, the field distributions generated above nanohole arrays are highly correlated with nanohole arrangements, the parameters of the nanohole array design and the illumination wavelengths. An isolated energy hot-spot can be created within a wide field of view by using a quasi-periodic nanohole array with radially symmetric arrangement as an isolated energy hot-spot generator. The optimum hot-spot size and intensity can be obtained through an optimization process of various parameters in the nanohole arrays' design such as the size of nanoholes, the scaling of the nanohole array's pattern and the illumination wavelengths. Regarding the patterns of nanohole arrays' design, in this thesis, we only considered and discussed the quasi-periodic nanohole arrays with different rotational symmetry to be used as a super-oscillating binary mask to generate energy hot-spots beyond the evanescent region. In fact, it is also interesting to explore other nanoholes' arrangements which can be obtained from different algorithms such as Fibonacci lattice, mid-temp coulomb gas and the Poisson process. Besides the binary masks composed of discrete nanoholes, recently a super-oscillating binary mask with multiple concentric rings also shows a subwavelength hot-spot created at few wavelengths away from the array's surface, which can be used for subwavelength imaging [152].

4.6 Conclusions

Through theoretical and experimental analyses of the generated diffraction patterns above nanohole arrays with different nanohole arrangements, it has been demonstrated that a well-defined, isolated subwavelength energy hot-spot can be created in a wide field of view by illuminating a super-oscillating binary mask of a radially symmetric quasi-periodic nanohole array. Such an isolated energy hot-spot has been observed at distances ranging from a few microns to a few tens of microns away from the surface of the array. With the existence of such highly-concentrated energy hot-spots, a quasi-periodic nanohole array can mimic the function of a high N.A. lens to collect light into a very small volume. It is believed that this technology can be applied in a wide range of areas. For instance, it can be used as a light pen for subwavelength imaging or lithography by scanning the object under investigation across the focal spot. In addition, its advantage over near-field scanning probes is the large distance between the nanohole

array and the object, of the order of a few microns. This feature allows the array to be used for focusing inside cells and other microscale objects. Also, the considerable gap between the array and the object will lead to much faster scanning and more rapid image acquisition than near-field optical microscopy. With such high localization of optical energy and subwavelength resolution, other applications can also be envisaged, such as high resolution photolithography, high-density optical data storage, and optical trapping.

5

Nanohole array as a lens

5.1 Synopsis

In this chapter, the lensing functions and imaging abilities of a quasi-periodic nanohole array in a metal screen will be investigated and demonstrated. First, a brief introduction on how to use a nanohole array as an imaging lens will be illustrated in Section 5.2. Then Section 5.3 will show a comparison of the imaging of a point light source between using periodic and quasi-periodic nanohole arrays and include a description of how an imaged pattern can be generated on the other side of a nanohole array based on the self-imaging mechanism. In Section 5.4, the lensing functions of a quasi-periodic nanohole array will be theoretically and experimentally verified by (1) one-to-one imaging of a point light source and (2) linear displacement of an imaged spot. Furthermore, in Section 5.5, imaging of two separated point light sources with coherent and incoherent light illumination will be considered to evaluate the effective numerical aperture (N.A.) of a quasi-periodic and a radially quasi-periodic nanohole array lens. Before proceeding to the conclusions in Section 5.7, Section 5.6 will present the calculation results of the imaging of single nanoslits with different lengths and their combinations with different separations, such as double nanoslits and gratings.

5.2 Lensing functions of a quasi-periodic nanohole array

The mechanism of how a nanohole array can work like a conventional lens for imaging will be illustrated below.

As mentioned in Chapter 4, a quasi-periodic nanohole array in a metal screen can be used as a light concentrator, converting optical energy into energy hot-spot foci [10, 146]. Our studies have shown that such focusing ability enables subwavelength energy hot-spots to be created at distances a few tens of wavelengths away from the array. Moreover, through careful selection of nanohole array patterns and the wavelength of incident radiation, an isolated focused hot-spot can be created within a wide field of view by illuminating a radially symmetric quasi-periodic nanohole array, making the nanohole array perform as a high N.A. lens.

The focusing ability of a quasi-periodic nanohole array mentioned above is manifested by illuminating the nanohole arrays with a plane wave. However, a focused spot can also be created on the other side of a quasi-periodic nanohole array by point source

illumination [157]. As long as the focused spot moves correctly as light source moves, this focusing ability with a point source illumination gives another exploitation of a quasi-periodic nanohole array to mimic the one-to-one imaging function of a conventional lens − the ability to image a point light source a few tens of wavelengths from the array into an imaged spot on the other side of the array. As Fig. 5.1 (a) illustrates, an imaged spot will be formed on the other side of a lens. When linearly shifting the point light source from Y to $Y + \delta Y$, the imaged spot will move in the opposite direction from y to $y + \delta y$ on the image plane. Similarly, based on the one-to-one imaging ability of a quasi-periodic nanohole array, Fig. 5.1 (b) schematically illustrates the imaging mechanism and how a quasi-periodic nanohole array functions as a conventional lens to image different objects. As shown, the point light source is placed on an object plane at a distance of Z_{obj} away from the array, while an imaged spot is generated on the other side of the array at Z_{img}. A small movement of the point light source leads to a linear displacement of the imaged spot; therefore, such a correlation implies that a nanohole array performs the one-to-one imaging function of a conventional lens. Furthermore, complex structures which are composed of multiple point light sources can be imaged with resolutions comparable to the imaging with conventional lenses with high N.A.. By using a quasi-periodic nanohole array as a lens, important applications such as X-ray imaging and nano-optical circuits may be found in circumstances where conventional optical lenses cannot readily be applied. To demonstrate the use of a nanohole array as a lens, a discussion on the selection of nanohole array patterns will be presented below. Then, the lensing functions and imaging abilities will be discussed for different types of quasi-periodic nanohole arrays, coherent and incoherent light sources, and various imaged objects.

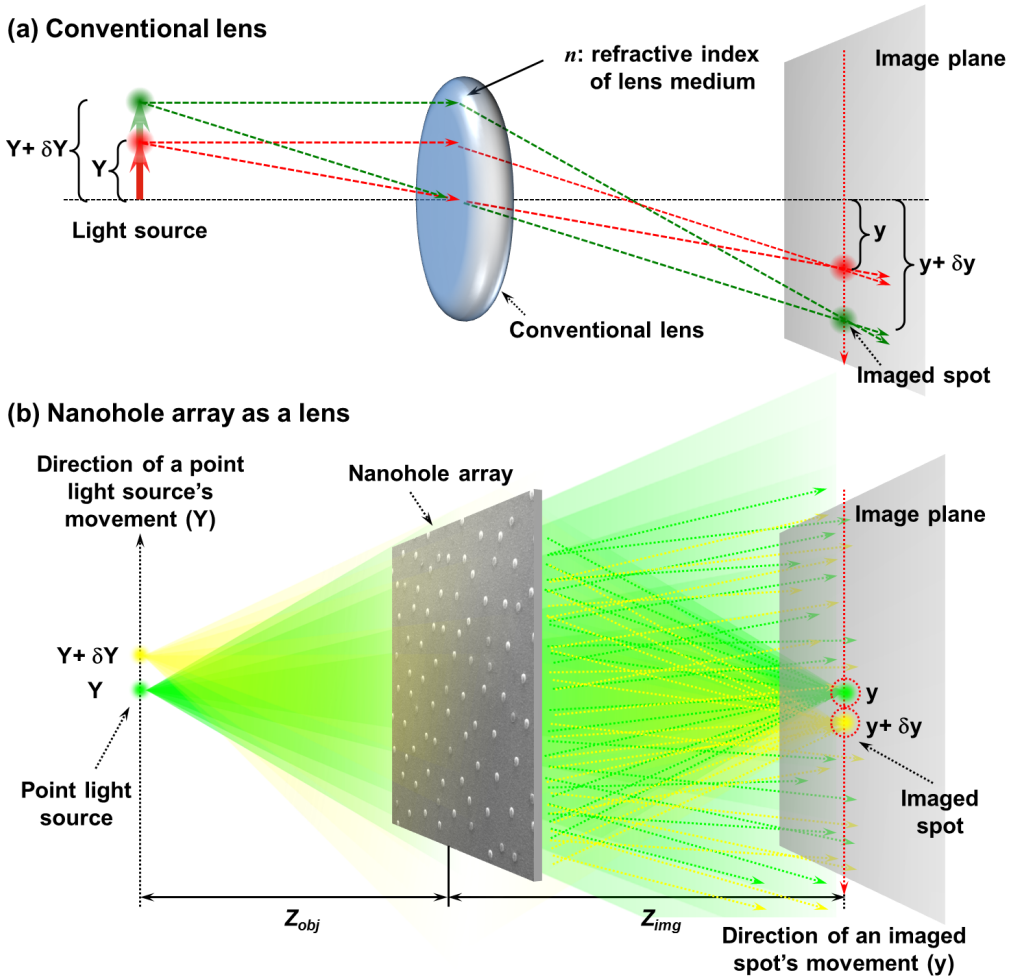

Figure 5.1: ***A quasi-periodic nanohole array can be used as a conventional lens for the imaging.*** *Schematic diagrams illustrate that a quasi-periodic nanohole array (b) can be used as a conventional lens (a) to image two closely spaced optical point sources (Y and $Y+\delta Y$) into two imaged spots (y and $y+\delta y$) on the other side of the array. Compared to the imaging of point light sources with a conventional lens, a quasi-periodic nanohole array with a point light source illumination also shows the ability to generate a focused spot on the other side of the array which can be considered as an imaged spot of the point light source.*

The displacement of imaged spots is opposite to the direction of light sources' movement which mimics the imaging function of a conventional lens. The image plane is at distance Z_{img} away from the nanohole array, while the point light sources are placed on an object plane at distance Z_{obj} to the array. Both of the distances are in a range of few tens of wavelength.

5.3 Selection of nanohole array patterns

Although nearly any array with small holes can create a diffraction pattern of foci when illuminated by a point light source, a careful choice of nanohole arrays' pattern is still required since the patterns are highly related to the lensing performance of a nanohole

array. Here, we use a periodic and a quasi-periodic nanohole array as examples. For consistency, in both cases, nanoholes of each array are included in an area of 50 $\times$50 μm^2 and the diameter of the nanoholes is 200 nm. In theoretical calculations, a point light source illumination of $\lambda = 660$ nm is placed on the central axis of each array and at a distance of $Z_{obj} = 11.4$ μm to the arrays' surface. First, for the periodic case, a regular 51×51 nanohole array with translational symmetry is used and a segment of the array is shown in Fig. 5.2 (a). The pitch of the nanoholes is 1 μm. With a point light source illumination, a calculated result of the field distribution above the array on the XZ plane at $Y = 0$ is shown in Fig. 5.2 (b), while Fig. 5.2 (c) and (d) display the diffraction patterns on the XY plane at the distance of $Z_{img} = 5.8$ μm and $Z_{img} = 11$ μm away from the array's surface as the green dashed lines indicated in Fig. 5.2 (b), respectively. From the calculation results, it is found that the regular nanohole array with a point light source illumination will be self-imaged into a pattern of dense focused hot-spots and the generated diffraction patterns above the array fail to reveal an imaged pattern of the point light source, suggesting that a periodic nanohole array is not suitable to be used as a lensing device for the imaging.

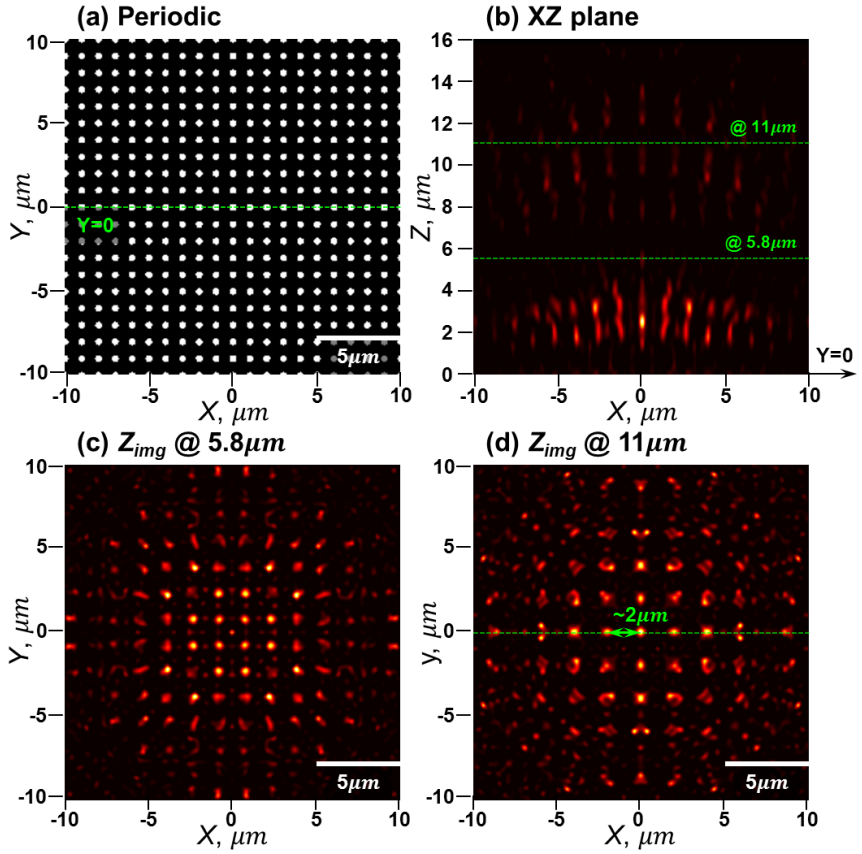

Figure 5.2: ***Lensing performance of a periodic nanohole array.*** *Calculation results. Plate (a) schematically shows a fraction of a* 51×51 *periodic nanohole array. The diameter of the nanoholes is* 200 nm *and the period between the nanoholes is* 1 µm*. The nanohole array is illuminated with a point light source which is on the central axis of the designed array and placed on an object plane at* $Z_{obj} = 11.4$ µm *away from the array's surface. The wavelength is* $\lambda = 660$ nm*. (b) shows a calculated result of field distributions above the array on the* XZ *plane at* $Y = 0$*, while plates (c) and (d) display the diffraction patterns on the* XY *plane at the distance of* $Z_{img} = 5.8$ µm *and* $Z_{img} = 11$ µm *as the green dashed lines indicated in (b). Note that the generated diffraction patterns show dense hot-spot foci with a magnified period as the green arrow indicates in (d). The diffraction patterns above a periodic nanohole array fail to reveal an image of the point light source.*

On the other hand, by illuminating a quasi-periodic nanohole array with a point light source, a very different result can be produced. Here, we use a 5-fold symmetry quasi-periodic nanohole array as an example and a segment of the array's pattern is schematically shown in Fig. 5.3 (a). By illuminating with a point light source of 660 nm placed at $Z_{obj} = 11.4$ µm away from the array, a calculated field distribution above the quasi-periodic nanohole array on the XZ plane at $Y = 0$ is shown in Fig. 5.3 (b), while Fig. 5.3 (c) and (d) display the diffraction patterns at distances of $Z_{img} = 8.1$ µm and $Z_{img} = 11$ µm away from the array's surface, respectively. In the results, it is found

that most of the optical energy from a point light source illumination is concentrated on the central axis of the designed array and forms an isolated hot-spot at some distance on the other side of the array. As Fig. 5.3 (d) at $Z_{img} = 11$ μm shows, an isolated focused spot, which can be interpreted as an imaged spot of the point light source, is generated on the other side of the array, mimicking the imaging function of a lens.

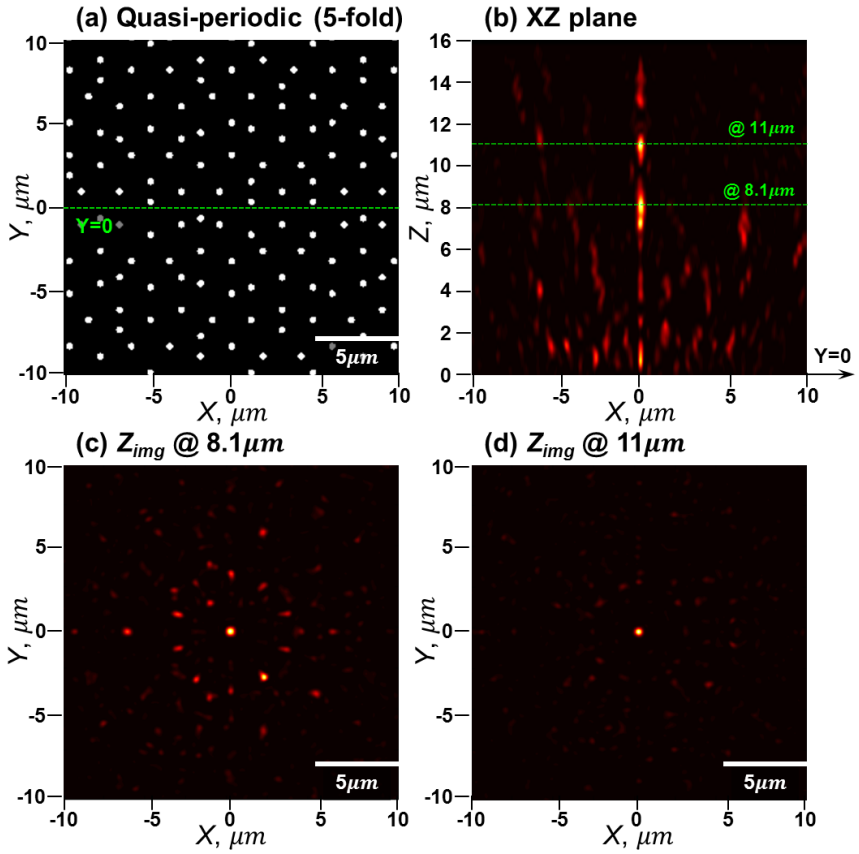

Figure 5.3: ***Lensing performance of a quasi-periodic nanohole array.*** *Calculation results. Plate (a) schematically shows a fraction of a 5-fold symmetry quasi-periodic nanohole array and the diameter of the nanoholes is* 200 nm. *A point light source of* $\lambda = 660$ nm *is placed on an object plane at* $Z_{obj} = 11.4$ μm *away from the array's surface and located on the central axis of the array. (b) shows the calculated field distribution above the array on the* XZ *plane at* $Y = 0$, *while plates (c) and (d) display the diffraction patterns on the* XY *plane at the distance of* $Z_{img} = 8.1$ μm *and* $Z_{img} = 11$ μm *as the green dashed lines indicated in (b). Note that a focused spot is generated as an image of the source on the other side of the quasi-periodic nanohole array at* $Z_{img} = 11$ μm *as shown in plate (d).*

As mentioned in Section 4.2, the diffraction patterns generated above nanohole arrays result from the partial reconstruction of the array's field. With plane wave illumination on a regular nanohole array with a period a, the diffracted field distributions will show reconstruction of the array's field at periodic distances from the array. This phenomenon is called the Talbot effect and the foci in the reconstructed patterns have the same period a as the period between the nanoholes in the array. Furthermore, if a periodic nanohole array is illuminated with a divergent light beam which can be created by a point-like light source illumination, the reconstructed image of the array's field will be magnified. Therefore, the reconstructed field distributions of hot-spot foci do not necessarily have the same period as the original patterns, as demonstrated in Fig. 5.2 (d) with a increased period of 2 μm.

The lensing functions of a quasi-periodic nanohole array can also be compared to the partial reconstruction of the array's field in the diffraction zone. As noted, reconstruction of a quasi-periodic nanohole array's field above the array is a complex diffraction process and the weight of the spectral maxima is varied at different distances away from the array's surface. Therefore, with divergent light beam illumination, partial reconstruction of the array's field will take place and the pattern of reconstructed field distributions will have the appearance of a scaled partial image of the array. **What is worth mentioning is that at some distances an imaged pattern representing the point light source will occur.** In other words, the pattern results from a constructive interference of waves emanated from a large number of nanoholes in the array as the focused spot of a conventional lens depends on the available wave vectors of the interfering waves.

When a quasi-periodic nanohole array is illuminated with a plane wave, well-defined sparsely distributed foci will be generated in the diffraction patterns. In contrast, in the case of a point-like source, a bright imaged spot will emerge in the area on the other side of the array which is immediately opposite to the point source. If there is a relative movement between the array and the point-like source along the direction perpendicular to the axis Z, the bright imaged spot in the diffraction pattern will move accordingly to maintain the constructive interference necessary for the formation of foci. This is how a quasi-periodic nanohole array mimics the imaging function of a conventional lens.

Since the light diffraction above a quasi-periodic nanohole array is complex, the lensing functions and the imaging abilities of different types of nanohole array lenses need more in depth investigation. According to the order of rotational symmetry in the quasi-periodic nanohole arrays, as categorised in Chapter 4, there are two types of the quasi-periodic nanohole arrangement with different orders of rotational symmetry − quasi-periodicity and radially symmetric quasi-periodicity. To demonstrate and compare the lensing functions of these two types of quasi-periodic nanohole arrays, one-to-one imaging of a point light source and linear displacement of an imaged spot will be used to verify the lensing functions of a nanohole array lens. In addition, in terms of the imaging abilities of nanohole array lenses, different types of objects with coherent and incoherent illumination will be investigated. The results will be described and discussed below.

5.4 Lensing functions of a nanohole array lens with quasi-periodic arrangement

5.4.1 One-to-one imaging of a point light source

To demonstrate that a nanohole array can function as a lens and compare the lensing functions of quasi-periodic nanohole arrays with different rotational symmetry, we first use a 5-fold symmetry quasi-periodic nanohole array to acquire one-to-one imaging of a point light source and test the linear displacement of an imaged spot. The array has a 5-fold rotational symmetry quasi-periodic pattern and the positions of nanoholes are obtained by the cut and project method. There are about 14,000 nanoholes contained in an area of 200 $\times$200 μm^2 and the array is identical to the schematic diagram as shown in Fig. 5.3 (a). The diameter of nanoholes is 200 nm and the minimum separation between the neighbouring nanoholes is 1.2 μm. This quasi-periodic nanohole array sample is fabricated by Dr. Y. Chen at Rutherford Appleton Laboratory in the U.K. and manufactured by the e-beam lithography (EBL) technique in a 100 nm aluminium film deposited on a silica substrate. To theoretically calculate diffracted field distributions above the array, the scalar angular spectrum method is employed and a point light source with a wavelength of 660 nm is used to illuminate the quasi-periodic nanohole array. In the model, a point light source is located on the central axis of the

array and placed on an object plane at $Z_{obj} = 11.4$ µm away from the array's surface. The distance of $Z_{obj} = 11.4$ µm chosen here is corresponding to the focal distance of the array under a plane wave illumination at $\lambda = 660$ nm.

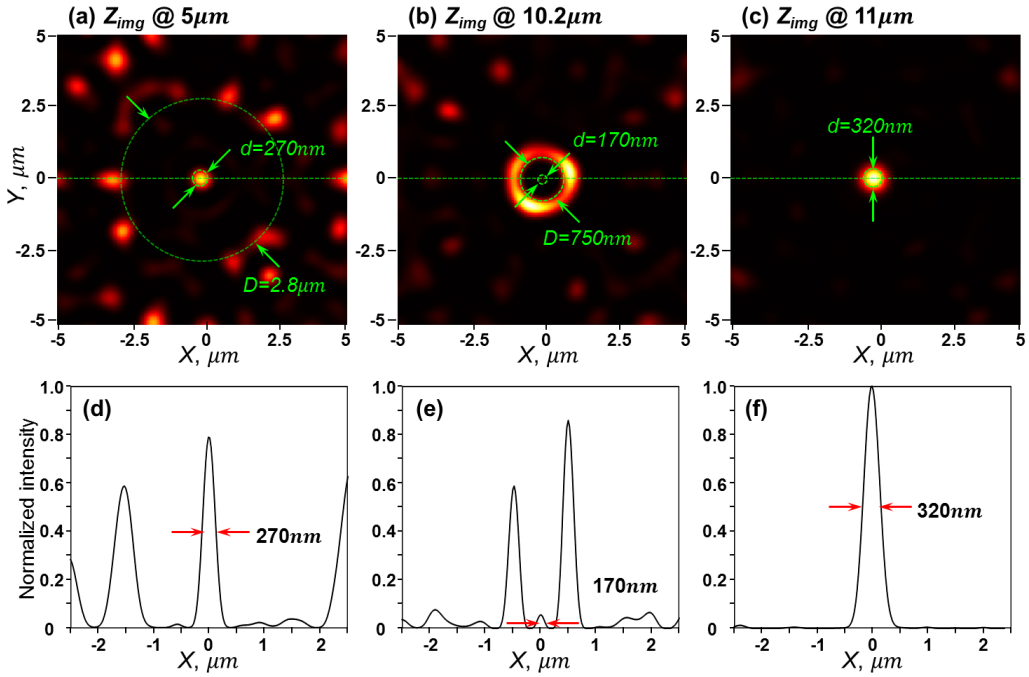

Figure 5.4: ***Lensing functions of a 5-fold symmetry quasi-periodic nanohole array lens: One-to-one imaging of a point light source.*** *Plates (a) to (c) display the calculated field distributions of foci at different distances Z_{img} of* 5 µm, 10.2 µm *and* 11 µm *away from a 5-fold symmetry quasi-periodic nanohole array lens, respectively. The array is under point light source illumination at a wavelength of* $\lambda = 660$ nm, *while the point light source is placed on an object plane at* $Z_{obj} = 11.4$ µm *away from the array's surface. The green dashed lines indicate the field of view D and the size of foci d in diameter. Note that a representative imaged spot is selected at* $Z_{img} = 11$ µm *where the field of view D is maximum, exceeding the image size of* 10 ×10 µm^2.

With point light source illumination, the calculated diffraction patterns can be obtained on the other side of the array theoretically. As described in Fig. 5.3 (b), most of the optical energy from the point light source illumination is concentrated on the central axis and several diffraction patterns with bright spots at centre can be seen at the distances Z_{img} of 5 µm, 10.2 µm and 11 µm above the array as shown in Fig. 5.4 (a) to (c), respectively. Such a bright spot is analogous to the focus of a conventional lens. In this sense, there are two important parameters to be considered − the diameter d of the imaged spot size at full width half maximum (FWHM) and the diameter D of the field of view defined as the dark area around the central bright spot. To use a nanohole

array as a lens feasibly, minimization of the focused spot size d and maximization of the field of view D have to be taken into consideration. In Fig. 5.4 (a), at $Z_{img} = 5$ μm, a focused spot with a diameter of $d = 270$ nm is generated within a field of view of $D = 2.8$ μm. Fig. 5.4 (b) shows a smaller focused spot of $d = 170$ nm presented in a halo of optical energy within a smaller field of view of $D = 0.75$ μm at $Z_{img} = 10.2$ μm, reconfirming that subwavelength optical fields can be created in the far field without the evanescent waves [8, 10, 146]. In respect of the largest field of view, exceeding the image size of 10 ×10 μm^2, it is found at $Z_{img} = 11$ μm, where the diameter of the focused spot size is around 320 nm. Such a bright focused spot can be considered as an imaged spot representing the original point light source and the distance Z_{img} between the image plane and the array is the focal length. An experiment to verify the one-to-one imaging ability of a 5-fold symmetry quasi-periodic nanohole array will be conducted as follows.

To experimentally demonstrate the one-to-one imaging using the lensing functions of a 5-fold symmetry quasi-periodic nanohole array, a metal coated tapered fibre tip is used as a point-like light source to illuminate the quasi-periodic nanohole array sample. The schematic diagram of the experimental setup is shown in Fig. 5.5 (a). A SNOM probe is positioned above the nanohole array at a distance of $Z_{obj} = 11.5$ μm with the aperture size of the probe around 100 nm. As for the optical source, a diode laser operating at $\lambda = 635$ nm is launched into the fibre and thus creates a point-like light source above the nanohole array's surface. The pattern of an imaged focused spot is formed on the other side of the array and is imaged onto the CCD array of a digital camera (SPOT, RT3) through an objective lens (N.A.=0.65) and a magnifying lens in front of the camera. With a coarse position tunning of the CCD camera, images of the generated diffraction patterns can be obtained in 1 μm steps away from the array's surface. To confirm the feasibility of imaging in this experimental setup, Fig. 5.5 (b) shows a fragment (20 ×20 μm^2) of a CCD image of the quasi-periodic nanohole array's surface when the array is illuminated with an normally incident white light source. Here, a clear 5-fold rotational symmetry quasi-periodic pattern on the sample surface can be seen. By using a fibre tip as a point-like light source to illuminate the nanohole array, a diffraction pattern with a focused spot located at centre can be observed at distance of $Z_{img} = 11$ μm from the array's surface as shown in Fig. 5.5 (c). Such a

focused spot resembles the imaging of the point light source and the size of the imaged spot is around 500 nm.

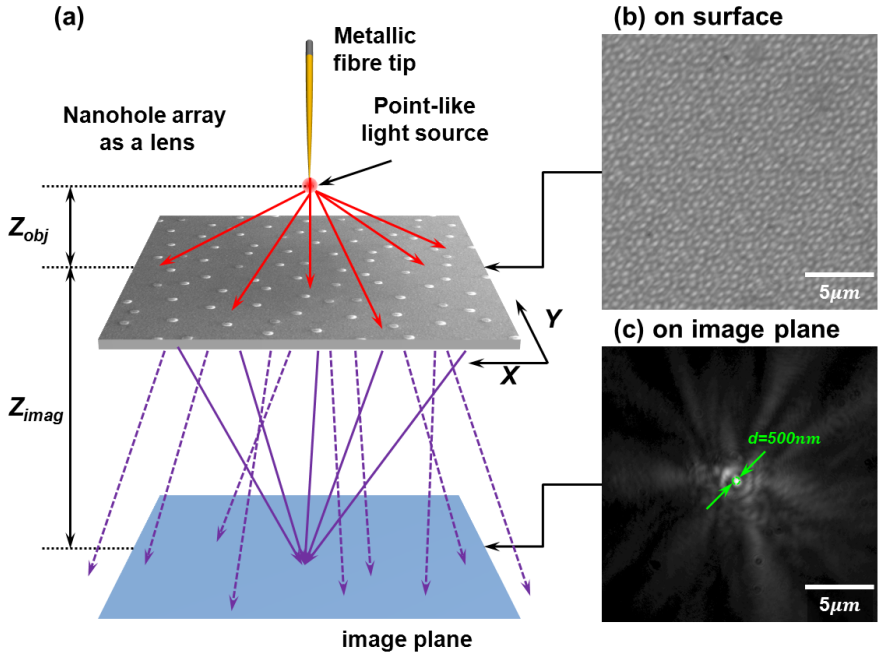

Figure 5.5: ***Schematic diagram of the experimental setup for the one-to-one imaging of a quasi-periodic nanohole array and the results.*** *(a) A tapered metallic fibre tip is used as a point-like light source to illuminate the quasi-periodic nanohole array and positioned above the array at a distance of* Z_{obj}*. The diffraction patterns at different distances away from the array are imaged by a CCD camera with a coarse position tunning of* 1 μm*. (b) shows a CCD image of the quasi-periodic nanohole array's surface when the array is illuminated with normally incident white light. A distinguished 5-fold symmetry quasi-periodic pattern can be observed here. By positioning a fibre tip at* $Z_{obj} = 11.5$ μm *above the array, (c) shows an imaged focused spot which represents the point light source formed on an image plane at distance of* $Z_{img} = 11$ μm *away from the array and the size of the imaged spot is around* 500 nm*. Here, the wavelength of the light launched into fibre is* 635 nm*. The size of both CCD images is* 20×20 μm^2*.*

5.4.2 Linear displacement of an imaged spot

Besides one-to-one imaging of a point light source, another essential property of a lens is the ability to image a moving point light source, showing an imaged spot with a linear displacement opposite to the direction movement of the light source. With the same experimental setup as mentioned above, by fixing the SNOM probe on the same object plane at a distance of $Z_{obj} = 11.5$ μm away from the sample surface and moving it from a starting point at $Y = 0$ nm to $Y+\delta Y = 600$ nm with a nanoscale step of $\delta Y = 100$ nm, an imaged focused spot on the image plane at $Z_{img} = 11$ μm will be formed and moved

linearly in the opposite direction from $y = 0$ nm to $y + \delta y = 600$ nm. As Fig. 5.6 (a) shows, the step between the imaged spots is around $\delta y = 100$ nm, corresponding to the movement of the light source. Fig. 5.6 (b) shows the corresponding calculated results for imaged spot movement with shift of the point light source. Such a linear displacement of an imaged focused spot in this small range is analogous to a conventional lens with approximately unitary magnification.

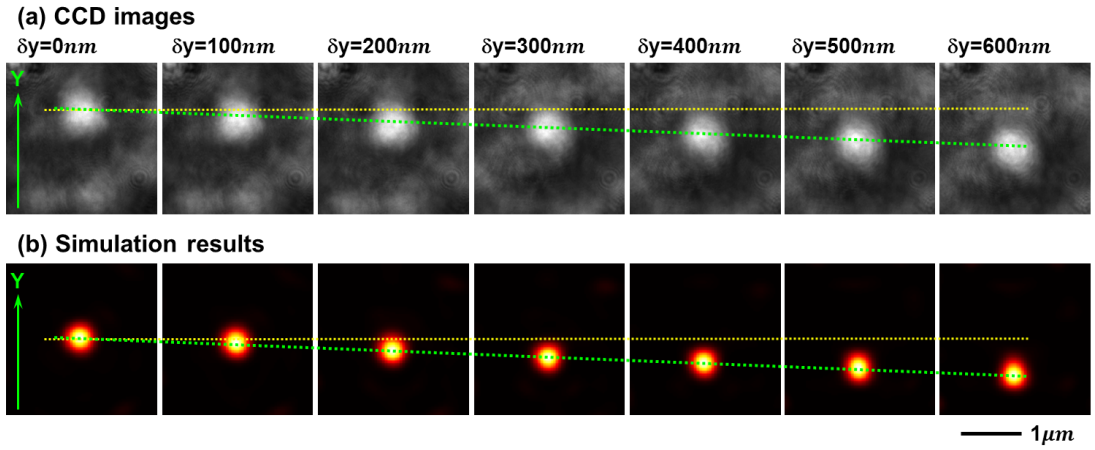

Figure 5.6: ***Lensing functions of a 5-fold symmetry quasi-periodic nanohole array lens: linear displacement of an imaged spot.*** *Lensing function of a 5-fold symmetry quasi-periodic nanohole array lens: when a point light source moves in the Y direction as the green arrows indicate, an imaged spot moves linearly in the opposite direction y. By fixing a SNOM probe on an object plane at* $Z_{obj} = 11.5$ μm *away from the array's surface and moving it linearly with a nanoscale step of* 100 nm*, (a) shows CCD images of the imaged spot with a linear displacement in the opposite direction y. The moving step of the imaged spot is around* 100 nm*, showing an approximately unitary magnification of the moving point light source. (b) shows the corresponding calculation results. All the images have a size of* 2.5×2.5 μm^2.

5.4.3 Effective imaging area of a nanohole array lens

From the theoretical and experimental results discussed above, the imaging properties of a nanohole array conform to the lensing functions of a conventional lens in a small range. However, regarding large imaging area with a nanohole array lens, there are two possibilities which might affect the image quality and the position of an imaged spot.

(1) Light from a point light source illumination is divergent and the distances from the point light source to each nanohole are different. Therefore, when a nanohole array is illuminated with a point light source, the intensities on each nanohole will

be different, depending on the positions of light sources.

(2) Regarding nanoholes' distribution on a quasi-periodic nanohole array, there is no translational symmetry on the nanoholes' arrangement. Namely, when a point light source on an object plane moves in the direction parallel to the array's surface, the number and arrangement of nanoholes which exhibit high intensity may change slightly.

In such circumstances, when a point light source is moved arbitrarily far away from a pre-set starting point, the linear displacement of a represented imaged spot and the correlation between point light sources and imaged spots may be affected. Thus, it is of interest to estimate the effective imaging area, where a point light source can still be imaged on the other side of a quasi-periodic nanohole array lens, showing the correlation between point light sources and imaged spots. To determine the size of the effective imaging area, here we will theoretically calculate the diffraction patterns with a point light source illumination moved further away from a pre-set starting point on an object plane. Moreover, for those positions of a point light source which exceed the effective imaging range, a series of calculations will be conducted to find a new imaged spot to represent the point light source at different imaging distances and positions.

In Fig. 5.7, the two rows of images (a) and (b) show the calculation results of diffraction patterns with a point light source of $\lambda = 660$ nm moved away from a pre-set starting point to ± 3 μm in the X and Y direction, respectively. Both the calculated maps in the middle of the two sequences display an imaged spot generated at $Z_{img} =$ 11 μm away from a 5-fold symmetry quasi-periodic nanohole array, when a point light source is placed on the central axis of the array at $Z_{obj} = 11.4$ μm. The images have an area of 10×10 μm^2. The white dots in each image show the positions of a point light source in calculations and the green triangles display the expected location of a corresponding imaged spot. As the results show, an imaged spot which represents the original point light source cannot be clearly distinguished in the blurred images when the point light source is moved to ± 3 μm away from the pre-set starting point both in the X and Y direction, while it still can be seen if the movement of the point light source is less than ± 2 μm. Therefore, the effective imaging area of a 5-fold symmetry quasi-periodic nanohole array lens can be estimated to have a diameter of 4 μm to

6 μm. In the effective imaging area, an imaged spot can be seen on the other side of the nanohole array lens which represents the point light source and shows a correlated displacement with the point light source. For those positions of a point light source outside the effective imaging area, calculations in which we carefully choose the imaging distance to find an imaged spot will be conducted and demonstrated below.

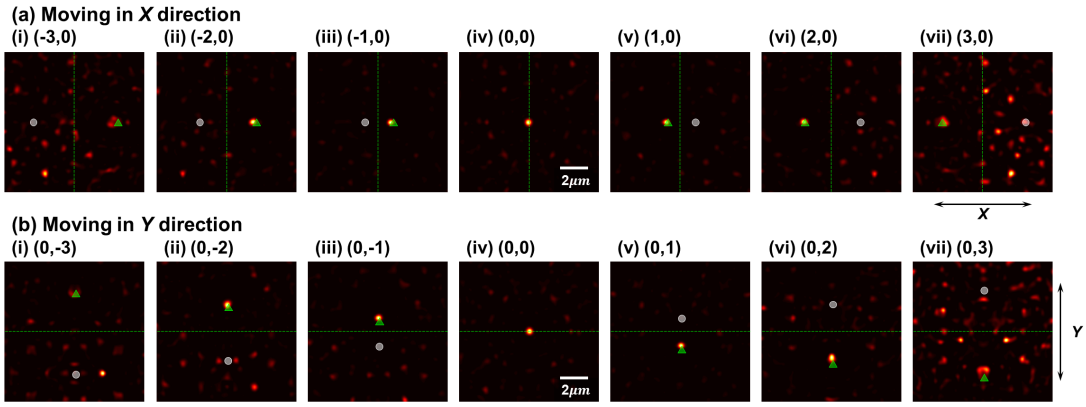

Figure 5.7: ***Imaging of a point light source moved away from a pre-set starting point.*** *Calculation results. The two rows of images (a) and (b) show the calculated field distributions with a point light source moved away from a pre-set starting point to* ± 3 μm *in the* X *and* Y *directions, respectively. Both the images in the middle of the two rows display an imaged spot generated on an image plane at* $Z_{img} = 11$ μm *away from a 5-fold quasi-periodic nanohole array lens, when a point light source of* $\lambda = 660$ nm *is positioned on an object plane at* $Z_{obj} = 11.4$ μm. *From the results, an imaged spot which represents the original point light source cannot be clearly distinguished in the blurred images as the light source is moved to* ± 3 μm *away from the pre-set starting point both in the* X *and* Y *direction, suggesting an estimated effective imaging area is around* 4 μm *to* 6 μm *in diameter. Here, the size of images is* 10×10 μm^2.

As the nanoholes are distributed in a quasi-periodic array, there is no defined centre in the nanoholes' arrangement. That is to say, there is no particular position which is the "best" starting point to place the point light source above the array. Thus, to demonstrate that any place above a quasi-periodic nanohole array lens can be a suitable starting point, a point light source is positioned at 6 μm in the X direction and -2.5 μm in the Y direction away from the former starting point (outside the effective imaging area) as the white dot indicates in Fig. 5.8 (a). The point light source of $\lambda = 660$ nm is placed on an object plane at the same object distance of $Z_{obj} = 11.4$ μm away from the 5-fold symmetry quasi-periodic nanohole array's surface. An imaged spot of the point light source can be found immediately opposite to the point source at a different imaging distance of $Z_{img} = 11.2$ μm. This location of the point light source can be

used as a new starting point and the effective imaging range of the imaged spot can be shown to have a similar size.

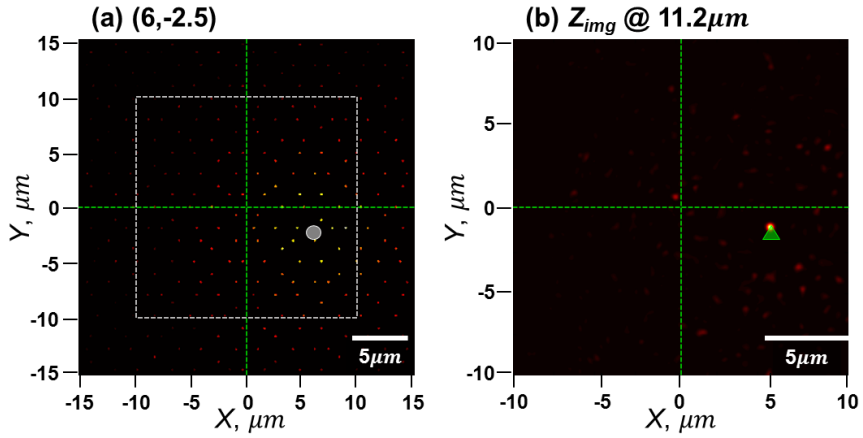

Figure 5.8: ***A new starting point to place a point light source above a quasi-periodic nanohole array lens.*** *Calculation results. With a new location of a point light source of* $\lambda = 660$ nm *placed at* 6 μm *in the* X *direction and* -2.5 μm *in the* Y *direction as the white dot indicates in plate (a), an imaged spot can be found immediately opposite to the point light source on an image plane at* $Z_{img} = 11.2$ μm *away from a nanohole array lens, while the point light source is placed on an object plane at* $Z_{obj} = 11.4$ μm.

From the discussions above, the object distance Z_{obj} between an object plane and the surface of a nanohole array lens is only selected at $Z_{obj} = 11.4$ μm. This is because when a 5-fold symmetry quasi-periodic nanohole array is illuminated with a plane wave of $\lambda = 660$ nm, optical energy concentrations as energy hot-spot foci will be generated on an image plane at a distance of 11.4 μm away from the array's surface. However, there is not any specific reason to limit ourselves to only position a point light source on an object plane at an object distance with a fixed value. Therefore, it is interesting to examine the lensing functions of a nanohole array lens with a point light source located at different distances Z_{obj} away from the array lens' surface. Here, we choose the location of a point light source at a distance of $Z_{obj} = 16$ μm as an example. From the calculation results, an imaged focused spot which can represent the point light source and demonstrate the one-to-one imaging abilities of a nanohole array lens is generated at the distance of $Z_{img} = 15.1$ μm on the other side of the array as shown in Fig. 5.9 (d). The imaged spot has a smaller size of 300 nm. By moving the point light source on the object plane at a distance of $Z_{obj} = 16$ μm, linear displacement of the imaged spot can be obtained within an effective imaging area with a similar size of

4 μm to 6 μm in diameter as the calculation results indicate in Fig. 5.10.

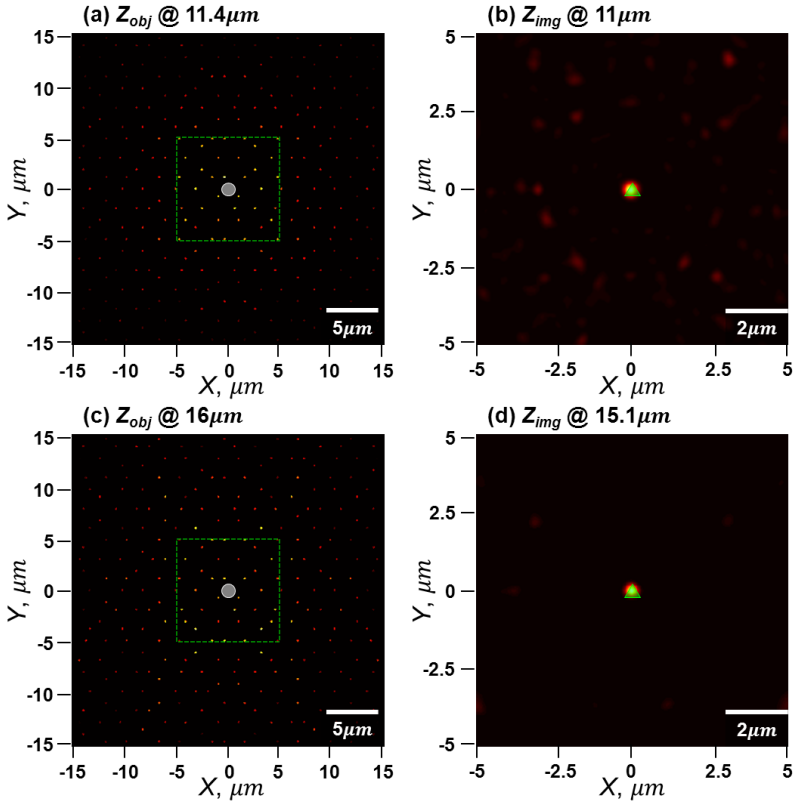

Figure 5.9: ***A point light source placed on an object plane with different object distances*** Z_{obj}. *Calculation results. By using a 5-fold symmetry quasi-periodic nanohole array as a nanohole array lens, a represented imaged spot as shown in plate (b) is generated on an image plane at* $Z_{img} = 11$ μm *away from the nanohole array lens, while a point light source of* $\lambda = 660$ nm *is placed on an object plane at object distance of* $Z_{obj} = 11$ μm. *When a point light source is moved along the central axis of the array to a distance of* $Z_{obj} = 16$ μm, *an imaged spot will be produced on another image plane at* $Z_{img} = 15.1$ μm *which is demonstrated in plate (d).*

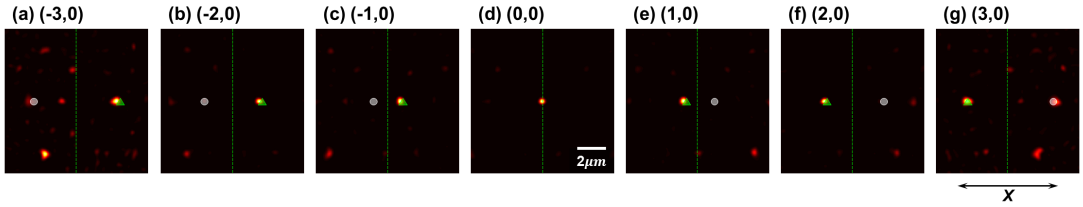

Figure 5.10: ***Imaging of a point light source moved away from a starting point.*** *Calculation results. Plate (d) shows an imaged focused spot generated on the other side of a 5-fold symmetry quasi-periodic nanohole array lens at a distance of* $Z_{img} = 15.1$ μm*, while a point light source of* $\lambda = 660$ nm *is placed on an object plane at* $Z_{obj} = 16$ μm *away from the nanohole array lens. By moving the point light source away from the starting point to* ±3 μm *in the X direction on the object plane, plates (a) to (g) show the calculation results of the diffraction patterns with the imaged spot. From the results, an imaged spot which represents the original point light source cannot be clearly distinguished in the blurred images when a point light source is moved to* ±3 μm *away from the starting point in the X direction, suggesting an estimated effective imaging area is around* 4 μm *to* 6 μm *in diameter. Here, the size of images is* 10 ×10 μm^2.

5.4.4 Lensing functions of a nanohole array lens with radially symmetric quasi-periodic arrangements

Besides the nanohole array lens with a 5-fold symmetry quasi-periodic arrangement, we have also studied the one-to-one imaging of an optical source using a 20-fold symmetry quasi-periodic nanohole array, which exhibits a radially symmetric arrangement of nanoholes. This array contains about 4,000 nanoholes, whose diameter is 200 nm and all the nanoholes are contained in an overall area of 50 ×50 μm^2. A segment of a 20-fold symmetry quasi-periodic nanohole array is schematically shown in Fig. 5.11 (a). The coordinates of the nanoholes in the array are obtained from the multigrid method using JcrystalSoft Nanotube Modeler. In the model, a point light source of $\lambda = 660$ nm is located on the central axis of the 20-fold symmetry quasi-periodic nanohole array and placed at a distance of $Z_{obj} = 13.5$ μm away from the array's surface. Again, the distance of Z_{obj} chosen here is that at which an isolated focused energy hot-spot is created when a 20-fold symmetry quasi-periodic nanohole array is illuminated with a plane wave of $\lambda = 660$ nm. Compared to point light source illumination on a 5-fold symmetry quasi-periodic nanohole array, optical energy from a point light source is more concentrated on the central axis of a 20-fold symmetry quasi-periodic nanohole array as the calculated field distributions on the XZ plane at $Y = 0$ show in Fig. 5.11 (b). From the calculated field distributions, several focused spots to represent as an image of the point light source are obtained on the other side of the nanohole array

lens at different imaging distances.

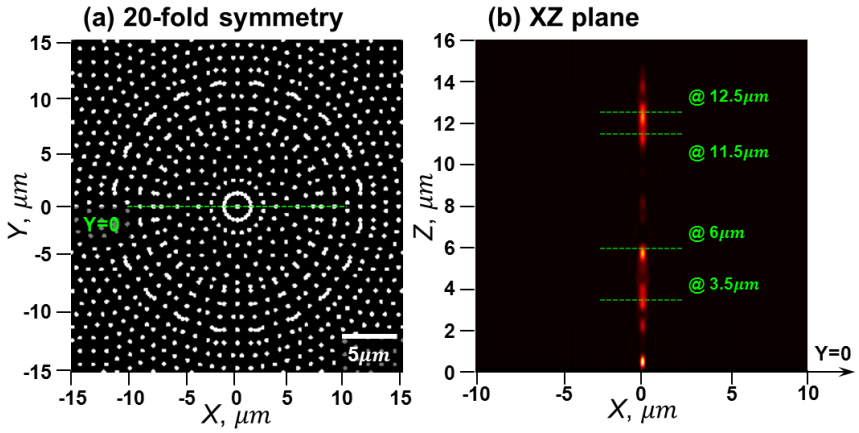

Figure 5.11: ***Lensing performance of a radially symmetric quasi-periodic nanohole array.*** *Calculation results. Plate (a) schematically shows a fragment of a 20-fold symmetry quasi-periodic nanohole array and the size of nanoholes is* 200 nm *in diameter. With a point light source illumination of* 660 nm *placed on an object plane at* Z_{obj} = 13.5 μm *away from the array's surface and located on the central axis of the designed array, plate (b) shows the calculation results of field distributions above the array on the* XZ *plane at* $Y = 0$. *Note that several imaged spots can be generated on the central axis of the array to represent the point light source on the other side of the nanohole array lens.*

In Fig. 5.12, plates (a) to (d) show different characteristic diffraction patterns with a focused imaged spot created on the central axis at the imaging distance Z_{img} of 3.5 μm, 6 μm, 11.5 μm and 12.5 μm from the array as the green dashed lines indicate in Fig. 5.11 (b), respectively. Among the results, the focused spots have similar spot size d and exist in nearly the same range of view field D. By linearly moving the point light source illumination, the linear displacement of an imaged spot occurs at every characteristic imaging distance as in the results summarized in Fig. 5.13. These similarities of imaged spots' size d, field of view D and the linear displacement of an imaged spot make it very difficult to determine the focal plane, which can be used as a true image of the original optical source. Considering the magnification $M = Z_{img}/Z_{obj}$, at the characteristic distance of 12.5 μm away from the array's surface, the magnification of an imaged spot is largest and is approximately unitary, similar to the imaging of a conventional lens when the test object is placed at twice the focal length. With this largest magnification, complex objects with small separations are more likely to be resolved on the other side of the nanohole array lens.

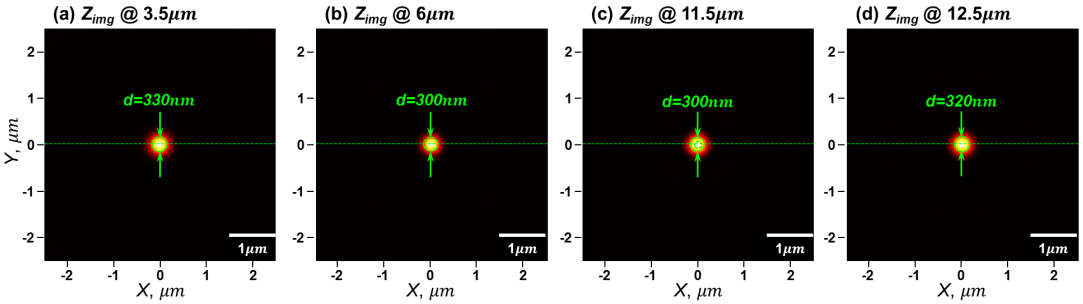

Figure 5.12: ***Energy hot-spot foci as imaged spots created at different distances*** Z_{img} ***from a 20-fold symmetry quasi-periodic nanohole array.*** *Calculation results. With a point light source at a wavelength of* 660 nm*, several focused spots are generated at different distances* Z_{img} *of* 3.5 μm, 6 μm, 11.5 μm *and* 12.5 μm *from the array as shown in plates (a) to (d), respectively. All the images have a size of* 10 ×10 μm^2*. Note that these focused spots have similar spot size d and exist in nearly the same range of view field D.*

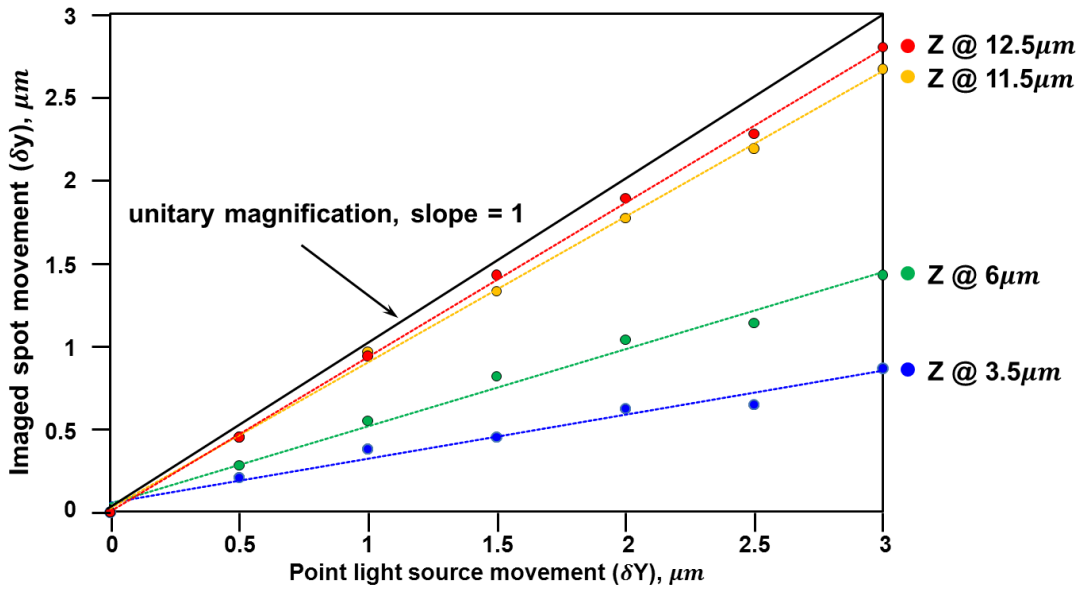

Figure 5.13: ***Linear displacement of imaged spots at different characteristic imaging distances*** Z_{img}*. Calculation results. Comparison of the linear displacement of several focused spots generated at different characteristic distances* Z_{img} *of* 3.5 μm, 6 μm, 11.5 μm *and* 12.5 μm *with a point light source's movement in the Y direction. The point light source is placed at* 13.5 μm *away from a 20-fold symmetry quasi-periodic nanohole array and the illumination wavelength is at* λ = 660 nm*. Note that the focused spot at* Z_{img} = 12.5 μm *is selected to be a represented imaged spot because of the approximately unitary magnification.*

To examine the size of the effective imaging area of a 20-fold symmetry quasi-periodic nanohole array lens, Fig. 5.14 (a) to (g) show the calculated diffraction patterns with a point light source moved away from a pre-set starting point to ±3 μm in the X direction. In the middle of the image sequence, plate (d) shows an imaged spot

generated on an image plane at $Z_{img} = 12.5$ μm, while the point light source as a starting point is placed on the central axis of the array and at $Z_{obj} = 13.5$ μm away the array. By moving the point light source away from the pre-set starting point, as the results show in Fig. 5.14, the linear displacement of the imaged spot and the position correlation with the point light source are maintained as the point light source is moved to 3 μm away from the starting point, indicating that the effective imaging area of a 20-fold symmetry quasi-periodic nanohole array lens is larger than that of a 5-fold symmetry quasi-periodic nanohole array. From the results in Fig. 5.13, at $Z_{img} = 12.5$ μm, the range of the effective imaging area is maximum and has a diameter of around 5.4 μm.

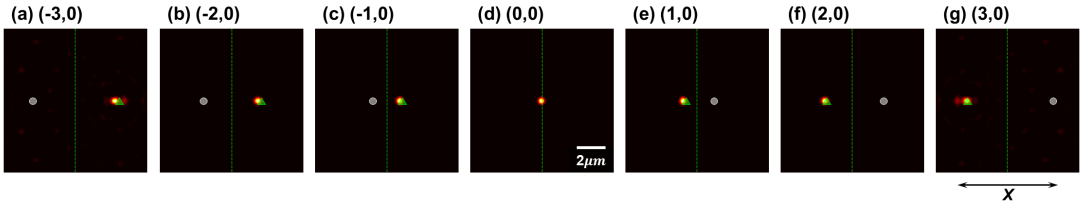

Figure 5.14: ***Imaging of a point light source moved away from a pre-set starting point by a radially symmetric quasi-periodic nanohole array lens.*** *Calculation results. Plate (d) shows an imaged spot generated on the other side of a 20-fold symmetry quasi-periodic nanohole array lens at a distance of* $Z_{img} = 12.5$ μm*, while a point light source of* $\lambda = 660$ nm *is placed on an object plane at* $Z_{obj} = 13.5$ μm *away from the array. By moving the point light source away from the starting point, the linear displacement of the imaged spot and the position correlation with the point light source are maintained as the point light source is moved to* 3 μm *away from the starting point as shown in plates (a) and (g). Note that the effective imaging area of a 20-fold symmetry quasi-periodic nanohole array lens is larger than that of a 5-fold symmetry quasi-periodic nanohole array.*

Before testing the imaging abilities of a nanohole array lens, a discussion on the effective imaging area of the two types of nanhole array lenses will be presented. By moving a point light source and carefully choosing the image plane, both the 5-fold and 20-fold symmetry quasi-periodic nanohole arrays show approximately unitary magnification of an imaged spot as summarized in Fig. 5.15 (a). However, if a point light source of 660 nm is moved to 2.5 μm away from a pre-set starting point, no distinguished imaged spot will be found on an image plane at the same imaging distance Z_{img} when using a 5-fold symmetry quasi-periodic nanohole array as a lens. As shown in Fig. 5.15 (b), the imaged spot representing the original point source is vague. In contrast, under the same condition, using a 20-fold symmetry quasi-periodic nanohole

array, a distinguished imaged spot can be observed as Fig. 5.15 (c) indicates. Here the effective imaging area can be extended to a range of about 6 µm in diameter. Such a larger field of view results from the high radial symmetry of the nanohole arrangement and provides the advantage of observing objects over a larger area.

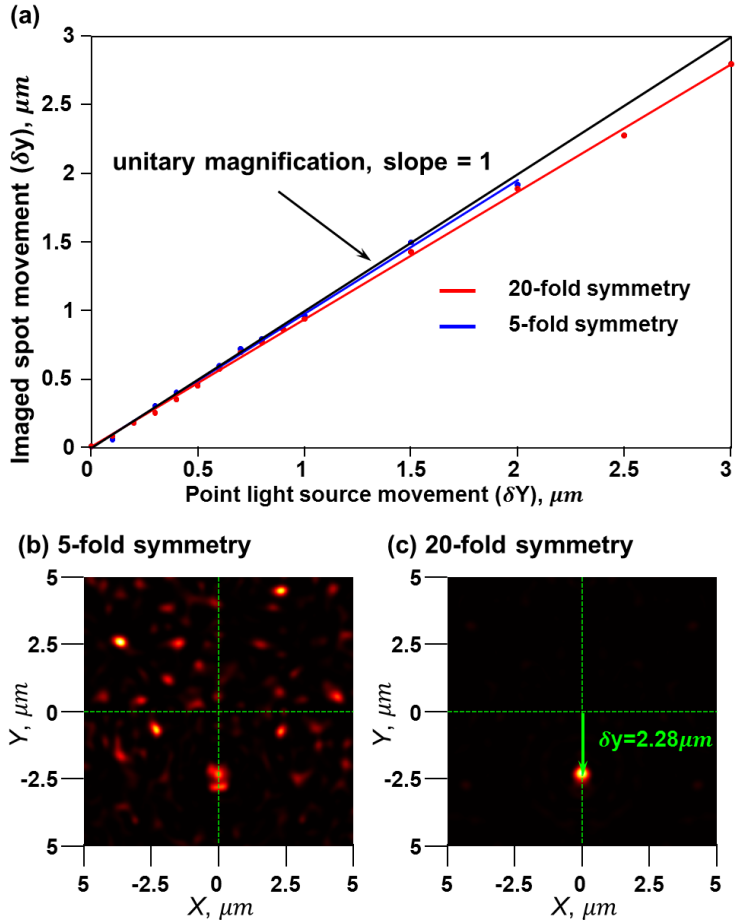

Figure 5.15: ***Comparison of the effective imaging area of a 5-fold and a 20-fold symmetry quasi-periodic nanohole array lenses.*** *Calculation results. Plate (a) summarizes the relationship between the movement of a point light source and a correlated imaged spot. Both 5-fold and 20-fold symmetry quasi-periodic nanohole array lenses show approximately unitary magnification. By moving a point light source to* 2.5 µm *away from a pre-set starting point, a distinguished imaged spot can still be observed by using a 20-fold symmetry quasi-periodic nanohole array as a lens as shown in plate (c), while a chaotic field distribution and a blurred imaged pattern are acquired as shown in (b) by the use of a 5-fold symmetry quasi-periodic nanohole array lens.*

5.5 Imaging abilities of a nanohole array lens: point light source illumination

From the results above, we found that the essential lensing functions of (1) the one-to-one imaging of a point light source and (2) the linear correlation of movement between a point light source and its corresponding imaged spot make a quasi-periodic nanohole array perform as a conventional lens in a local imaging area. In this section, we will further examine and evaluate the imaging abilities of a quasi-periodic nanohole array by distinguishing two adjacent point light sources with different separations through a series of calculations.

5.5.1 Imaging abilities of a quasi-periodic nanohole array lens: 5-fold symmetry quasi-periodic nanohole array lens

In the model, as shown in the schematic diagram in Fig. 5.16, optical sources with a separation S are placed on an object plane at a distance of Z_{obj} away from a nanohole array lens. The size of nanohole array lenses in the calculations is 50 $\times$50 μm^2 and the illumination wavelength is $\lambda = 660$ nm. By theoretical calculations with the scalar angular spectrum method, field distributions on the other side of the array will be obtained at different imaging distances Z_{img}. One of them may reveal an imaged pattern of the adjacent point light sources with two imaged spots separated by a distance of S'. Furthermore, two types of illumination − coherent and incoherent − will be taken into account in a series of calculations.

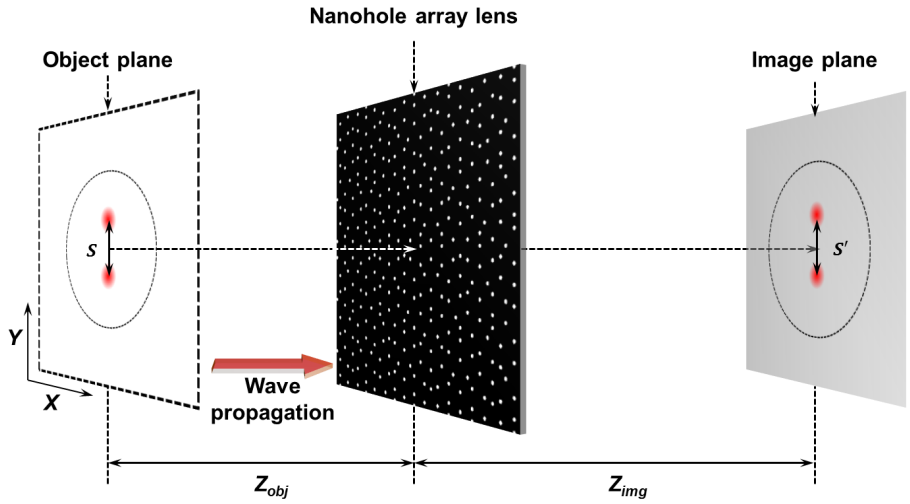

Figure 5.16: ***Imaging of two adjacent point light sources with a nanohole array lens.*** *Schematic diagram. In the model, two point light sources with a separation S are placed on an object plane at a distance of Z_{obj} away from a nanohole array lens. In calculations, the size of nanohole array lenses is 50 ×50 μm^2 and the illumination wavelength of the optical sources is $\lambda = 660$ nm. Field distributions on the other side of the nanohole array lens will be obtained at different imaging distances Z_{img}. Note that one of the field maps may reveal an imaged pattern with two imaged spots separated with a distance S' which can be seen as an image of the two light sources.*

First, a 5-fold symmetry quasi-periodic nanohole array is used as a nanohole array lens to image two close point light sources with different separation distances S. The 5-fold symmetry quasi-periodic nanohole array contains about 4,000 nanoholes of 200 nm in diameter and covers an area of 50 ×50 μm^2. The two adjacent point light sources are placed on an object plane 11.4 μm away from the array's surface and the mid-point of the sources is on the central axis of the designed nanohole array. By using the 5-fold symmetry quasi-periodic nanohole array lens to image two separated point light sources, calculated imaged patterns with coherent and incoherent light sources are generated on an image plane at $Z_{img} = 11$ μm as shown in Fig. 5.17 and Fig. 5.18, respectively. In Fig. 5.17, plates (a) to (d) display the calculation results of imaging two coherent light sources with a separation of 550 nm, 600 nm, 650 nm and 700 nm, while plates (a) to (d) in Fig. 5.18 show calculation results with incoherent light sources separated by 400 nm, 450 nm, 500 nm and 550 nm, respectively. All the calculated imaged patterns are in a size of 5 ×5 μm^2 and the yellow dashed circles indicate the estimated size of an effective imaging area of a 5-fold symmetry quasi-periodic nanohole array lens which is around 4 μm in diameter.

To determine whether the two optical sources can be resolved on the image plane or not, the Abbe-Rayleigh rule is applied − the two point light sources can be resolved when the central maximum of one imaged spot falls outside the location of the first minimum of the other [94]. Therefore, due to the cross-section profiles of imaged spots in the imaged patterns shown in Fig. 5.17 (e), two coherent point light source illuminations with wavelength of 660 nm are resolved when they are separated by $S = 600$ nm, while a distance between the two imaged spots is around $S' = 750$ nm. Regarding the incoherent illumination, as the cross-section profiles indicate in Fig. 5.18 (e), the imaged spots of the two separated point light sources are resolved when the sources are separated by a distance of $S = 450$ nm and the separation of the two imaged spots is $S' = 460$ nm. It appears that a 5-fold symmetry quasi-periodic nanohole array lens shows better resolving power under incoherent illumination than coherent illumination, just as a conventional lens does. By analogy with the resolving power of a conventional lens under coherent illumination, the effective N.A. of a nanohole array lens can be given by

$$N.A. = \frac{0.77\lambda}{S'}, \tag{5.1}$$

where S' is the resolving distance between the two imaged spots. Therefore, the 5-fold symmetry quasi-periodic nanohole array shows a resolving ability analogous to a conventional lens of N.A.=0.85 under coherent illumination. Similarly, the resolving power of a conventional lens under incoherent illumination is given by

$$N.A. = \frac{0.61\lambda}{S'}. \tag{5.2}$$

In this case, the quasi-periodic nanohole array lens can function as a conventional lens with an effective N.A.=0.89 under incoherent illumination.

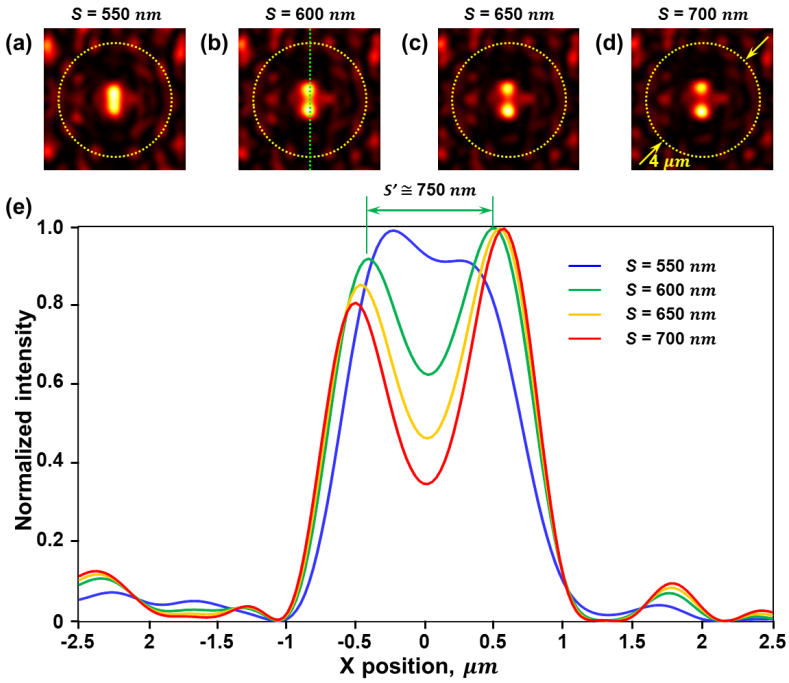

Figure 5.17: ***Imaging of two separated coherent point light sources by a quasi-periodic nanohole array lens.*** *Plates (a) to (d) show the calculated patterns of imaging two coherent light sources with a separation of* 550 nm, 600 nm, 650 nm *and* 700 nm, *respectively. The two point light sources of* $\lambda = 660$ nm *are placed at* $Z_{obj} = 11.4$ μm *away from a 5-fold symmetry quasi-periodic nanohole array lens, while the imaged patterns are generated at* $Z_{img} = 11$ μm. *The size of the images is* 5×5 μm^2 *and the yellow dashed circles indicate the effective imaging area of the quasi-periodic nanohole array lens. Plate (e) shows the cross-section profiles of the imaged spots. Note that two coherent point light sources are resolved when they are separated by* $S = 600$ nm, *while the distance between the two imaged spots is around* $S' = 750$ nm, *giving an effective N.A. of 0.85.*

~

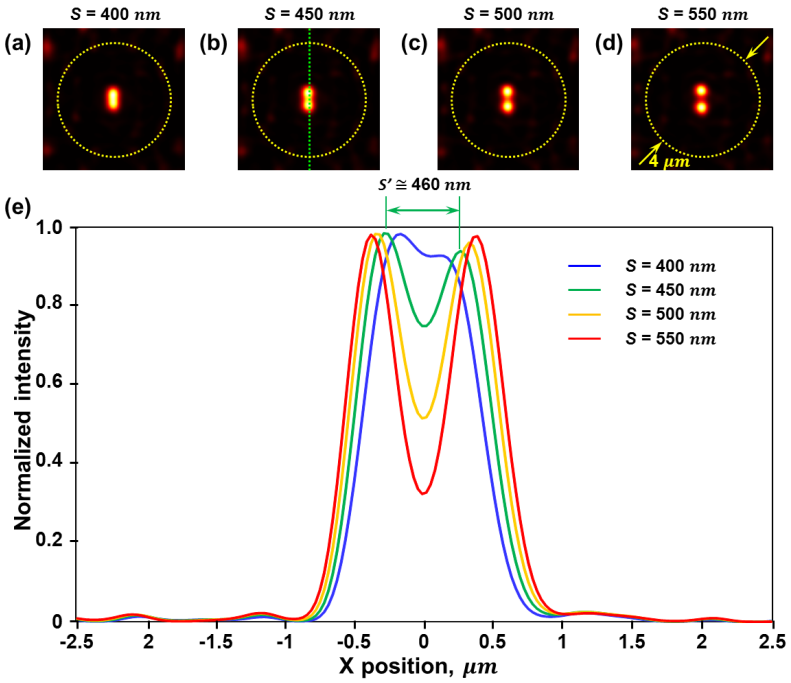

Figure 5.18: ***Imaging of two separated incoherent point light sources by a quasi-periodic nanohole array lens.*** *Plates (a) to (d) show the calculated patterns of imaging two incoherent light sources with a separation of* 400 nm, 450 nm, 500 nm *and* 550 nm, *respectively. The two point light sources of* $\lambda = 660$ nm *are placed at* $Z_{obj} = 11.4$ μm *away from a 5-fold symmetry quasi-periodic nanohole array lens, while the imaged patterns are generated at* $Z_{img} = 11$ μm. *The size of the images is* 5×5 μm^2 *and the yellow dashed circles indicate the effective imaging area of the quasi-periodic nanohole array lens. Plate (e) shows the cross-section profiles of the two imaged spots in the imaged patterns. Note that two coherent point light sources are resolved when they are separated by* $S = 450$ nm, *while the distance between the two imaged spots is around* $S' = 460$ nm, *giving an effective N.A. of 0.89.*

5.5.2 Imaging abilities of a radially symmetric quasi-periodic nanohole array lens: 20-fold symmetry quasi-periodic nanohole array lens

In addition, the imaging abilities of a 20-fold symmetry quasi-periodic nanohole array are also investigated through a series of calculations of the imaging of two separated point light sources. The 20-fold symmetry quasi-periodic nanohole array contains about 4,000 nanoholes in an area of 50×50 μm^2 and the size of the nanoholes is 200 nm. As in the schematic diagram of the model shown in Fig. 5.16, the two separated point light sources with incoherent illumination are positioned on an object plane at $Z_{obj} =$ 13.5 μm away from the radially symmetric quasi-periodic nanohole array lens, while imaged spots will be generated on an image plane at $Z_{img} = 12.5$ μm. The mid-point of the two incoherent point light sources is aligned with the central axis of the radially

symmetric quasi-periodic nanohole array lens. In Fig. 5.19, plates (a) to (d) display the calculation results of imaging two incoherent light source illuminations with different separations of 500 nm, 550 nm, 600 nm and 650 nm, respectively. All the calculated imaged patterns are in a zoom-in area of 5 $\times$5 μm^2. The imaged patterns show that the two point light sources can be resolved when the separation between the point light sources is $S = 600$ nm, while the separation between the imaged spots is about $S' = 510$ nm. The effective N.A. of the 20-fold symmetry quasi-periodic nanohole array lens can be estimated as around 0.67 under incoherent light illumination. Such a result indicates that the resolving power of a 20-fold symmetry quasi-periodic nanohole array lens may not be as good as that in a quasi-periodic nanohole array lens with 5-fold rotational symmetry. This may be explained by the magnification ($M = Z_{img}/Z_{obj}$) of the 5-fold symmetry nanohole array lens in its effective imaging area. As shown in Fig. 5.14 (a), it is found that the magnification of a 5-fold symmetry nanohole array lens is closer to the unitary magnification than that in a nanohole array with 20-fold rotational symmetry. Thus, with the same separation S, a 5-fold symmetry quasi-periodic nanohole array lens can separate the imaged spots with a longer displacement S'.

However, regarding the effective imaging area of a nanohole array lens, a larger imaging range can be obtained by a 20-fold symmetry quasi-periodic nanohole array. By separating two incoherent point light sources to 6 μm away from each other, as shown in Fig. 5.20, the imaged spots are still clearly seen because of the larger imaging area of a 20-fold symmetry quasi-periodic nanohole array lens, while a chaotic imaged pattern is obtained when a 5-fold symmetry quasi-periodic nanohole array is used. In summary, the resolving abilities of a 20-fold symmetry quasi-periodic nanohole array are not as good as that of a 5-fold symmetry quasi-periodic nanohole array lens. However, with a wide imaging area, structures such as objects composed of multiple point light sources, slits with different lengths or grating structures can be imaged by a 20-fold symmetry quasi-periodic nanohole array lens. A series of calculations on the imaging of different features by a 20-fold symmetry quasi-periodic nanohole array lens will be conducted and discussed in the following sections.

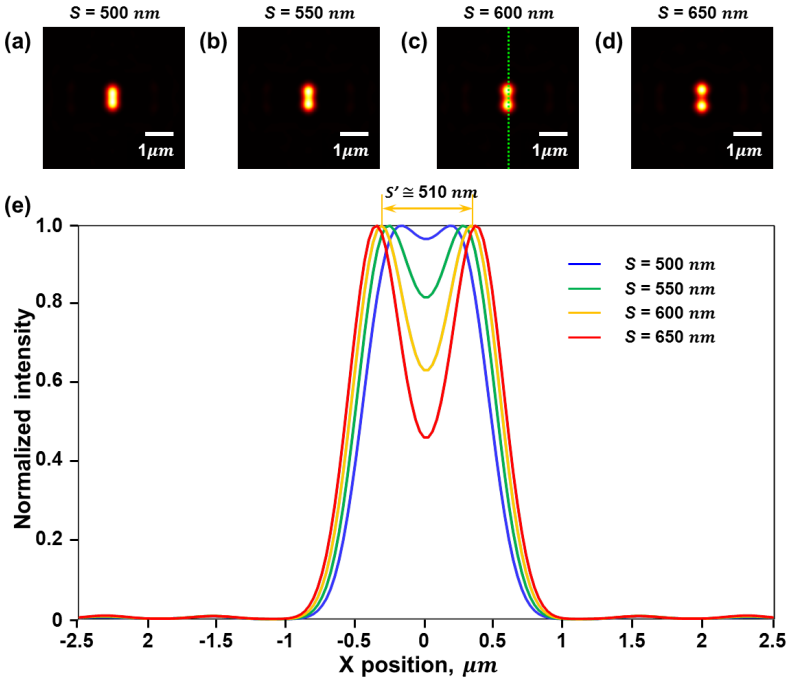

Figure 5.19: ***Imaging of two separated incoherent point light sources by a radially symmetric quasi-periodic nanohole array lens.*** *Plates (a) to (d) show the calculated patterns of imaging two incoherent light sources with the separation of* 500 nm, 550 nm, 600 nm *and* 650 nm, *respectively. Plate (e) shows the cross-section profiles of the two imaged spots in the imaged patterns. Note that two incoherent point light sources are resolved when they are separated by* $S = 600$ nm, *while a distance between the two imaged spots is around* $S' = 510$ nm, *giving an effective N.A. of 0.67.*

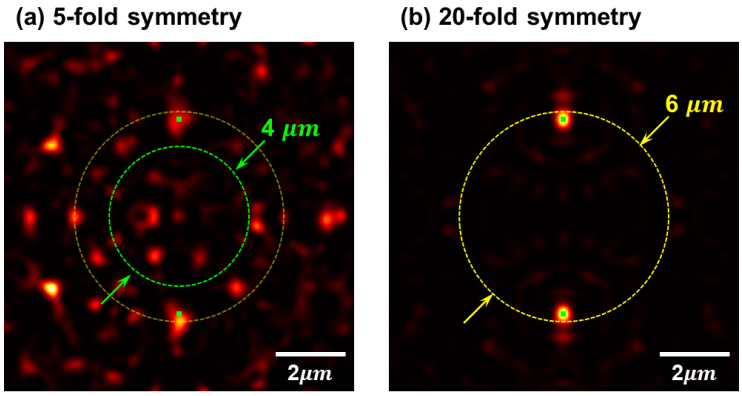

Figure 5.20: ***Comparison of an effective imaging area of nanohole array lenses: imaging of two separated incoherent point light sources.*** *Calculation results. Plates (a) and (b) show a comparison of the effective imaging area using a 5-fold (a) and a 20-fold (b) symmetry quasi-periodic nanohole array lens, respectively. By separating the two incoherent point light sources with a separation of* 6 μm, *two imaged spots can still be revealed by using a 20-fold symmetry quasi-periodic nanohole array lens, indicating that a larger effective imaging area than that of a 5-fold symmetry quasi-periodic nanohole array lens.*

5.5.3 Structures composed of multiple point light sources

In order to test the imaging quality with realistic objects and determine the effective imaging area of a nanohole array lens, several structures composed of multiple incoherent point light sources of $\lambda = 660$ nm are designed and placed on an object plane at $Z_{obj} = 13.5$ μm away from a 20-fold symmetry quasi-periodic nanohole array lens. The structures are characters of **M**, **E**, **T** and **A** as shown in Fig. 5.21 (a) to (d), respectively. The characters are included in an area of 2.5 ×2.5 μm^2 and the central point of each character is aligned with the central axis of the array. The smallest separation distance between the light sources is 500 nm.

By using a 20-fold symmetry quasi-periodic nanohole array as a lens to image the designed structures, calculated imaged patterns which reveal the designed characters are generated on an image plane at an optimum imaging distance of $Z_{img} = 12.5$ μm and the results are shown in Fig. 5.21 (i) to (iv), corresponding to the designed characters as shown in the plates (a) to (d) but rotated by 180°. In the results, the appearance of the characters can be recognized but some details of the imaged spots are not distinguished. Also, the inhomogeneous intensity distributions on the imaged patterns indicate that the nanoholes' distribution on the 20-fold symmetry quasi-periodic nanohole array lens is not exactly the same in all the orientations.

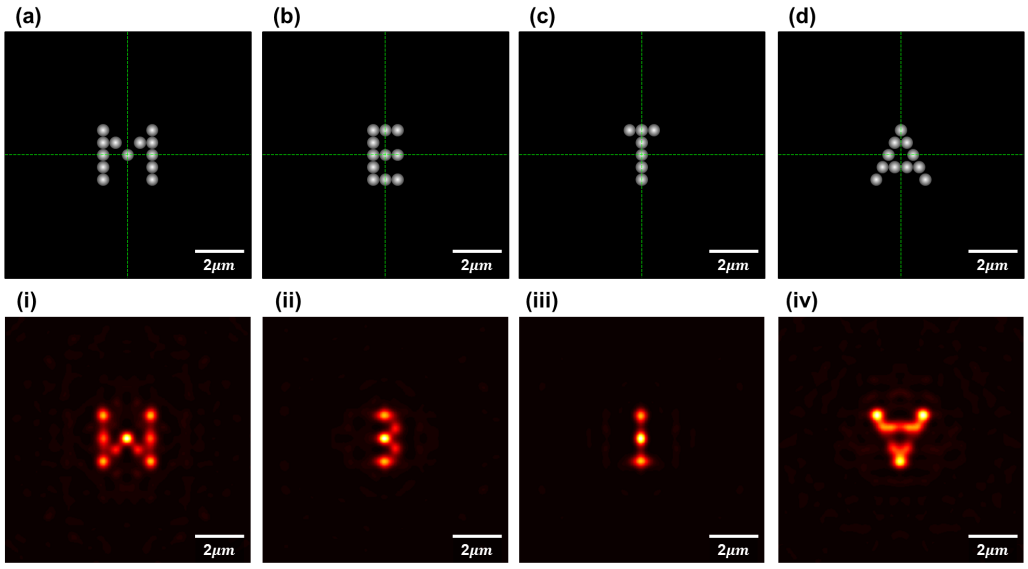

Figure 5.21: ***Imaging of designed structures which are composed of multiple incoherent point light sources.*** *Calculation results. Plates (a) to (d) display the designed structures which are composed of multiple incoherent point light sources of* $\lambda = 660$ nm *as characters of* ***M****,* ***E****,* ***T*** *and* ***A****, respectively. The smallest distance between the point light sources is* 500 nm*. The designed characters are placed on an object plane at* $Z_{obj} = 13.5$ μm *away from a 20-fold symmetry quasi-periodic nanohole array lens and the size of the structures is* 2.5 ×2.5 μm^2 *whose central point is aligned with the central axis of the array lens. Plates (i) to (iv) show the corresponding imaged patterns but with a rotation of* 180°*. All the images are* 10 ×10 μm^2*.*

Furthermore, we combined the above designed characters together to create a structure over a larger area, such as the combined characters of **ET** and **META** which are schematically shown in Fig. 5.22 (a) and (c), respectively. The combined characters are placed on an object plane at $Z_{obj} = 13.5$ μm and the central point of the structures is on the central axis of the quasi-periodic nanohole array. The size of the combined characters of **ET** is 6.5 ×2.5 μm^2, while **META** is 10 ×2.5 μm^2. By imaging with a 20-fold symmetry quasi-periodic nanohole array lens, the calculated imaged patterns which correspond to the structures shown in Fig. 5.22 (a) and (c) are displayed in Fig. 5.22 (b) and (d), respectively. In the results, the imaged pattern of combined characters **ET** is still clearly distinguished, though some blurred patterns are generated on the edge of the pattern. In the imaged pattern of **META** shown in Fig. 5.22 (d), in the range of effective imaging area, part of the combined characters can be imaged on the other side of the nanohole array lens. However, the imaging quality is also affected by the point light sources outside the effective imaging area and is not as good as the imaged

pattern shown in plate (b).

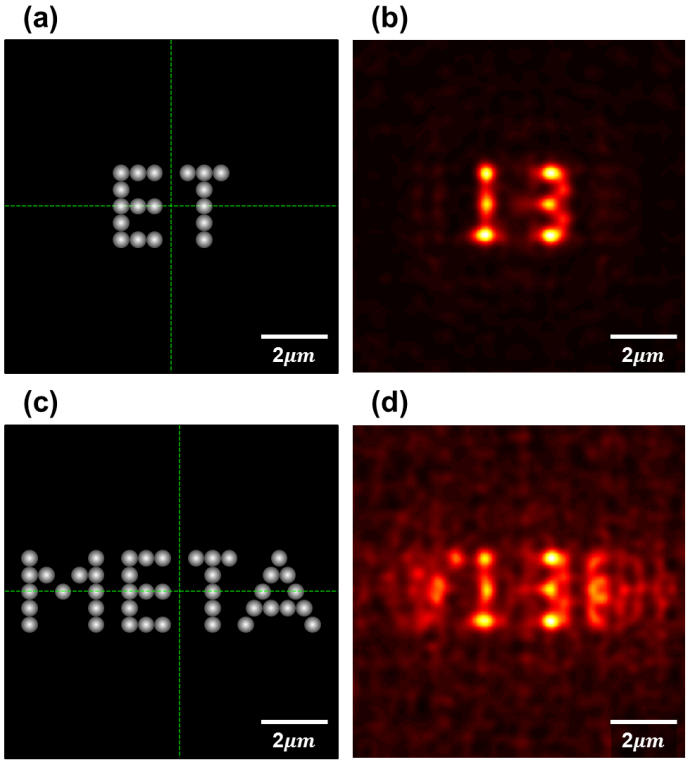

Figure 5.22: ***Imaging of large structures composed of multiple incoherent point light sources.*** *Calculation results. The designed structures of combined characters composed of multiple incoherent point light sources are placed on an object plane at* $Z_{obj} = 13.5$ μm *away from a 20-fold symmetry quasi-periodic nanohole array lens. The combined characters of* ***ET*** *as shown in plate (a) are included in an area of* 6.5×2.5 μm^2*, while the characters of* ***META*** *are in an area of* 10×2.5 μm^2 *as in plate (c). Plates (b) and (d) display corresponding images to the combined characters on an image plane at* $Z_{img} = 12.5$ μm.

5.6 Imaging abilities of a nanohole array lens: light illumination from nanoslits and their combinations

In addition to examining the imaging of point light sources and their various arrangements, we also tried to image other objects such as nanoslits and their combinations with different separations. First we tested the imaging of single nanoslits with different lengths by using a 20-fold symmetry quasi-periodic nanohole array as a lens. Imaged patterns with corresponding lengths to the objects are seen on the other side of the nanohole array lens. Then, with a fixed length of the constituent nanoslits, objects of

double nanoslits with different separations were investigated and the imaging abilities of using a 20-fold symmetry quasi-periodic nanohole array lens can be estimated. At the end of this section, imaging of grating structures with different periods will be tested and the effective imaging field of a nanohole array lens will be verified.

As in the model schematically displayed in Fig. 5.23 (a), objects such as single nanoslits (b), double nanoslits (c) and grating structures (d) are positioned on an object plane at Z_{obj} away from a 20-fold symmetry quasi-periodic nanohole array lens, while corresponding images of the test objects will be generated on the other side of the array at an optimum imaging distance of Z_{img}. In the calculations, the illumination wavelength is assumed to be $\lambda = 660$ nm and the central point of each object is on the central axis of the nanohole array lens. The test object parameters are as follows: l denotes the length of nanoslits and w is the width, separation S is the edge-to-edge distance between two adjacent nanoslits and the period $P = w+S$ of a grating structure is the center-to-center distance of the constituent nanoslits as indicated in Fig. 5.23 (c) and (d). A series of theoretical calculations on the imaging of single nanoslits with different lengths l, objects of double nanoslits with different separations S and grating structures with different period P will be conducted and discussed below.

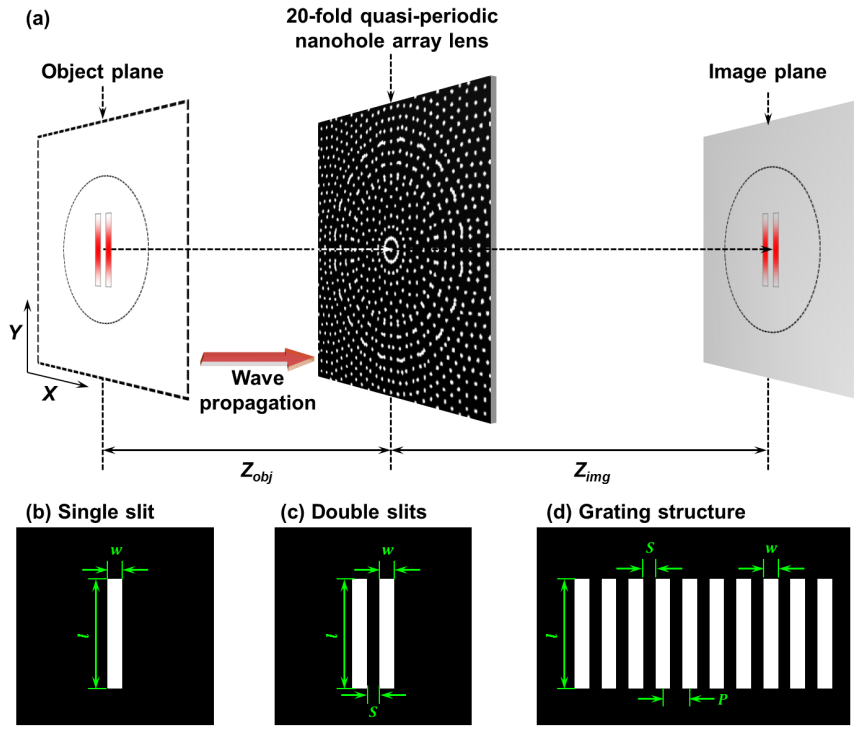

Figure 5.23: ***Imaging of single nanoslits, double nanoslits and grating structures.*** *(a) schematically displays the model of the imaging of nanoslits and their different combinations. In calculations, objects composed of different numbers of nanoslits are located on an object plane at Z_{obj} away from a 20-fold symmetry quasi-periodic nanohole array lens, while the corresponding imaged patterns are generated at an optimum imaging distance Z_{img}. The illumination wavelength is assumed to be $\lambda = 660$ nm. Schematic diagrams (b) to (d) show the testing objects: a single nanoslit, double nanoslits and grating structures, respectively. l denotes the length of nanoslits and w is the width. Separation S is the edge-to-edge distance between two adjacent nanoslits and the grating period P is the center-to-center distance of constituent nanoslits. The centre of all the testing objects is aligned with the central axis of the nanohole array lens.*

5.6.1 Single nanoslits with different lengths

Fig. 5.24 displays the calculation results of imaging of single nanoslits with different lengths. The nanoslits are set to have a fixed width $w = 200$ nm and various lengths l changed from 1 μm to 4 μm as shown in Fig. 5.24 (a) to (g). The test objects are placed on an object plane at $Z_{obj} = 13.5$ μm away from a 20-fold symmetry quasi-periodic nanohole array lens and plates (i) to (vii) in Fig. 5.24 show the corresponding imaged patterns of each single nanoslit objects which can be clearly generated on an image plane at an imaging distance of $Z_{img} = 13.5$ μm. All the images displayed here are in a zoom-in area of 10 ×10 μm^2. The images demonstrate that imaged patterns of the single nanoslit objects can be created with correct lengths. Regarding the intensity

distributions of the imaged patterns, more unwanted energy in the region of the imaged nanoslits and larger energy side lobes are seen with an increase in the length of the nanoslits. This may result from the different diffraction patterns generated by the illumination of single nanoslits with different lengths, causing various energy distributions on the nanoholes of the array lens. With an increase of the length, more nanoholes with higher energy are included to construct the imaged pattern. However, the diffraction pattern of a single nanoslit and the arrangement of nanoholes are not identical in all orientations, generating some unwanted energy distribution on the corresponding images. Considering the correspondence to the testing objects and lower energy distribution around an imaged nanoslit pattern, we chose the single nanoslit with a length of 1.5 μm as a unit element to form the objects of double nanoslits and grating structures. The calculations of the imaging of double nanoslits and grating structures will be conducted in the next sections.

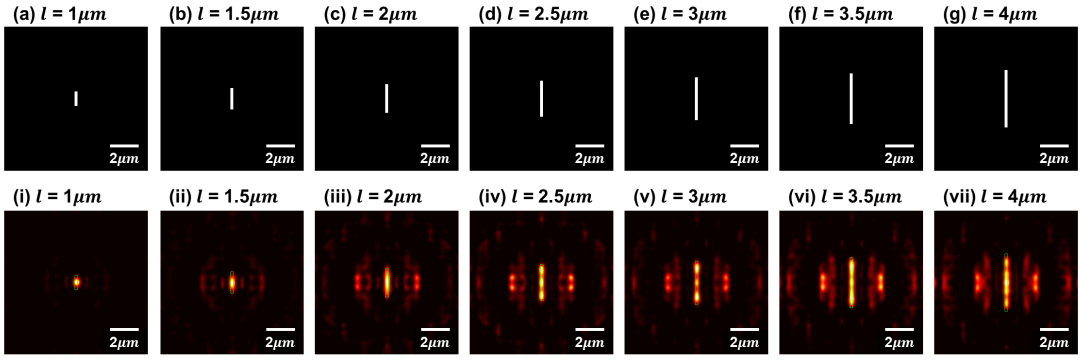

Figure 5.24: ***Imaging of single nanoslits with different lengths.*** *Calculation results. The objects are placed on an object plane at* $Z_{obj} = 13.5$ μm *away from a 20-fold symmetry quasi-periodic nanohole array lens. The width of the nanoslits is fixed at* 200 nm *and the length is varied from* 1 μm *to* 4 μm *as plates (a) to (g), respectively. By imaging with the nanohole array lens, plates (i) to (vii) show the corresponding imaged patterns to the single nanoslit objects generated on an image plane at* $Z_{img} = 13.5$ μm *and the green dashed rectangles indicate the geometry of the single nanoslit objects. Note that the lengths of imaged nanoslits correspond to the length of the test objects. All the images have an area of* 10×10 μm^2.

5.6.2 Double nanoslits with different separations

For imaging of double nanoslits by a 20-fold symmetry quasi-periodic nanohole array lens, the objects are placed on an object plane at $Z_{obj} = 13.5$ μm and the separation S between the constituent nanoslits is changed from 200 nm to 500 nm as shown in

Fig. 5.25 (a) to (f). In calculations, the width and length of each nanoslit is fixed at $w = 200$ nm and $l = 1.5$ μm. Light from the two nanoslits is incoherent and the wavelength is set to be $\lambda = 660$ nm. Plates (i) to (vi) in Fig. 5.25 display the images with corresponding imaged double nanoslits patterns generated on an image plane at $Z_{img} = 13.5$ μm. The imaging ability of a 20-fold symmetry quasi-periodic nanohole array lens can be estimated by comparing the cross-section profiles of the imaged nanoslits shown in Fig. 5.26. According to the Abbe-Rayleigh rule, the cross-section profiles show that a double nanoslit with incoherent light illumination can be distinguished when the separation of two constituent nanoslits is $S = 250$ nm, suggesting that the effective N.A. of a 20-fold symmetry quasi-periodic nanohole array lens is around 0.89.

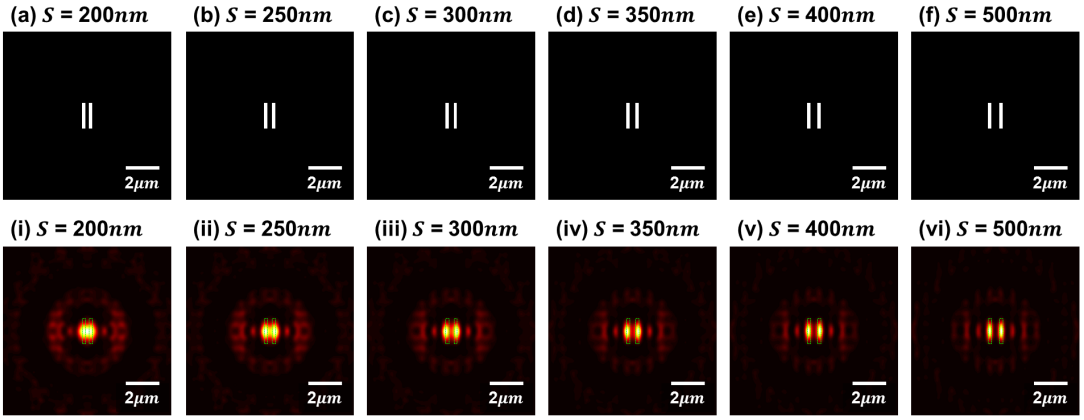

Figure 5.25: ***Imaging of double nanoslits with different separations*** S**.** *Calculation results. The double nanoslits with varied separations* S *are placed on an object plane at* $Z_{obj} = 13.5$ μm *away from a 20-fold symmetry quasi-periodic nanohole array lens. The width and length of each nanoslit are fixed at* 200 nm *and* 1.5 μm *respectively, while the separation* S *between the two nanoslits is varied from* 200 nm *to* 500 nm *as the schematic diagrams show (plates (a) to (f)). Plates (i) to (vi) show the corresponding imaged patterns generated on an image plane at* $Z_{img} = 13.5$ μm *and the green dashed lines display the expected location and size of the double nanoslit objects. All the images have an area of* 10×10 μm^2.

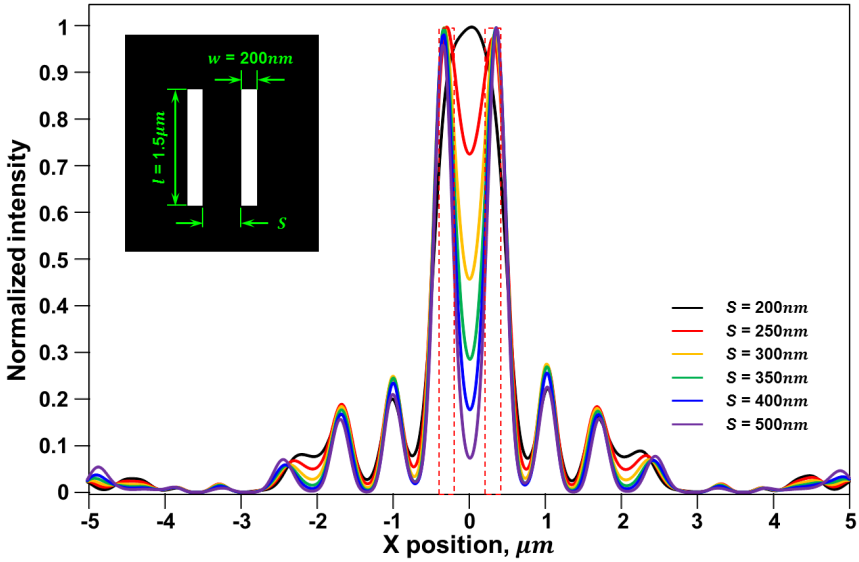

Figure 5.26: ***Comparison of cross-section profiles on the imaged double nanoslits patterns.*** *Cross-section profiles on the imaged double nanoslits patterns when shown in Fig. 5.26 (i) to (vi). Note that the double nanoslits can be distinguished when the separation between the two nanoslits is* 250 nm*, giving an effective N.A. of a 20-fold symmetry quasi-periodic nanohole array lens analogue to a conventional lens around 0.89. The red dashed lines show an original double nanoslit with* $S = 250$ nm*.*

5.6.3 Gratings with different periods

The imaging of grating structures by a 20-fold symmetry quasi-periodic nanohole array lens is schematically shown in Fig. 5.27. The grating structures contain 12 nanoslits with incoherent illumination of 660 nm and are placed on an object plane at 13.5 μm away from the quasi-periodic nanohole array lens. The length and width of each nanoslit are fixed at $l = 1.5$ μm and $w = 200$ nm, respectively. The grating periods P between the constituent nanoslits are 600 nm and 650 nm, indicating that the overall areas of the two designed gratings are 6.8 $\times$1.5 μm^2 and 7.35 $\times$1.5 μm^2. The geometric center of the grating structures is aligned with the central axis of the nanohole array lens.

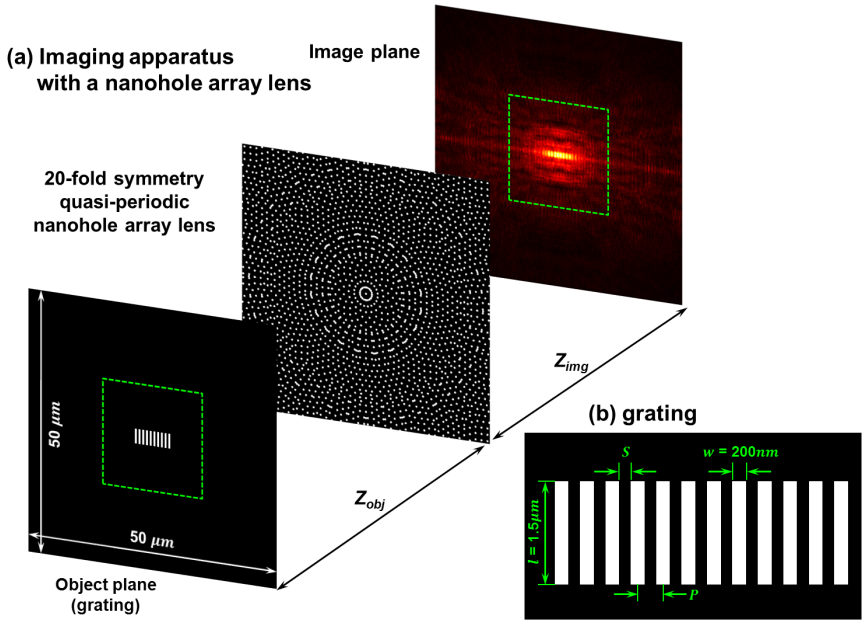

Figure 5.27: ***Imaging of gratings by a 20-fold symmetry quasi-periodic nanohole array lens.*** *Schematic diagrams. (a) shows the imaging of grating structures by using a 20-fold symmetry quasi-periodic nanohole array, while (b) schematically displays the grating structures. The grating structures are placed on an object plane at* Z_{obj} = 13.5 μm. *The length and width of each nanoslit are fixed at* l = 1.5 μm *and* w = 200 nm, *respectively. The grating periods* P *between the constituent nanoslits are* 600 nm *and* 650 nm, *indicating that the overall areas of the two designed gratings are* 6.8 ×1.5 μm^2 *and* 7.35 ×1.5 μm^2. *The geometric centre of the grating structures is aligned with the central axis of the nanohole array lens.*

By using the 20-fold symmetry quasi-periodic nanohole array as a lens to image the gratings, Fig. 5.28 (a) and (b) show the imaged patterns of different gratings with period P of 600 nm and 650 nm, respectively. The gratings consist of 12 nanoslits whose width is 200 nm and length is 1.5 μm. The total width of each grating is 5.7 μm and 6.15 μm. By varying the imaging distance from the array, the best resolved images are produced at 13.5 μm. As shown, at the centre of the effective imaging area of around 6 μm in diameter, the nanoslits in gratings can be resolved. The smallest resolving distance is around 300 nm, equal to the edge-to-edge distance between the nanoslits. However, slits are not imaged clearly at the two ends of the grating. Such results again demonstrate the effective imaging area when using a quasi-periodic nanohole array as a lens.

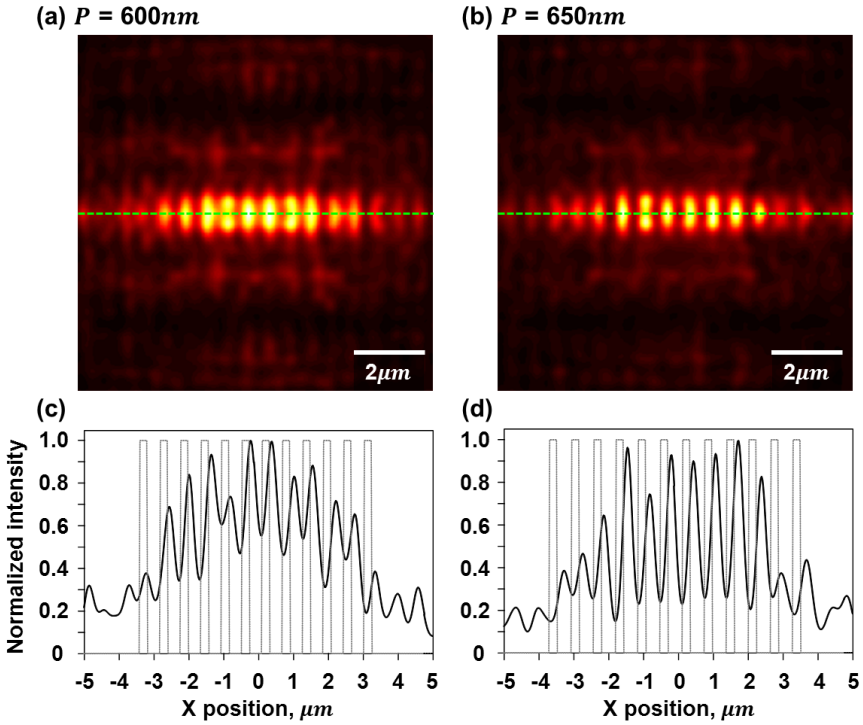

Figure 5.28: ***Imaging of grating structures with different periods.*** *Calculation results. A 20-fold symmetry quasi-periodic nanohole array is used for the imaging of grating structures with different periods P. The grating structures consist of 12 nanoslits whose width is $w = 200$ nm and length is $l = 1.5$ μm. In the calculations, the periods of adjacent nanoslits are* 600 nm *and* 650 nm*, indicating the overall areas of the two designed gratings are* 5.7×1.5 μm^2 *and* 6.15×1.5 μm^2*. By positioning the gratings on an object plane at* $Z_{obj} = 13.5$ μm*, optimum imaged patterns are revealed on an image plane at* $Z_{img} = 13.5$ μm *as shown in plates (a) and (b), respectively.*

In the calculation results discussed above, it is shown that structures composed of incoherent light sources can be imaged by a nanohole array lens. Within the effective imaging area, objects with a separation below the diffraction limit can be resolved and displayed on an image plane by carefully choosing the imaging distance Z_{img}. In the calculations, the imaging of incoherent light sources is the superposition of intensities from each imaged pattern of the component light source, while the imaging of the coherent light sources is the superposition of the amplitudes. Therefore, as long as the one-to-one imaging function and the corresponding linear displacement of a point source can be found using a nanohole array lens, then structures composed of incoherent light sources should be imaged by the nanohole array lens in the calculations. However, in an experimental realization, samples of incoherent light sources are not easy to prepare. One possible sample preparation is test objects composed of quantum dots

or fluorescent nanoparticles. In this approach, the size and the shape of component fluorescent light-emitting objects have to be considered. Fluorescent objects with large size and irregular shape may not be successfully imaged on the other side of a nanohole array lens.

5.7 Conclusions

In conclusion, by theoretical calculations and experimental investigations, we have demonstrated that a quasi-periodic nanohole array can perform the function of a conventional lens, that is, the one-to-one imaging of a point light source to an imaged focused spot on the other side of the array. Moreover, the linear displacement of an imaged focused spot representing the original point light source shows the approximately unitary magnification with the movement of original source. Such a result implies the possibility of directly imaging the objects of multiple light sources by using a quasi-periodic nanohole array as a lens. Through the imaging of two separated point light sources, a 5-fold symmetry quasi-periodic nanohole array shows an imaging ability analogous to a conventional lens with high N.A.; however, the imaging field of view is not large enough for practical imaging applications. By examining the imaging ability of nanohole arrays with different nanohole arrangements, a larger effective imaging area can be produced when a radially symmetry quasi-periodic nanohole array is used as a lens. In this chapter, we use a 20-fold symmetry quasi-periodic nanohole array as an example to demonstrate that complex structures composed of multiple point sources can be imaged with resolutions comparable to a high N.A. lens.

Despite the complicated light diffraction behaviour above nanohole arrays, according to the optical super-oscillation theory, there is no limitation in the size of hot-spots or in the field of view. Thus, a nanohole array lens with higher N.A. can be achieved by more sophisticated arrangement on the nanoholes, generating small subwavelength hot-spots within a large field of view and mimicking the functions of real lenses. However, there lies another challenge. As energy losses are inevitable in pursuit of high resolution in a large field of view via super-oscillation, here the price to pay will be a decrease in the power concentrated in the hot-spot and an increase in the power of the unfocused side-bands located outside the field of view. This will require experiments

with increasingly sensitive detectors.

6

Conclusions

6.1 Summary

This thesis represents a study of nanoscale light control with different types of nanophotonic metamaterials. Two main research topics of manipulating subwavelength light localizations have been investigated. One is the precise control of light localizations in the near-field with planar plasmonic metamaterials; the other is the generation of a subwavelength light localization beyond the near-field by using super-oscillating binary masks with different arrangements of nanoholes.

Prior to the work presented here, several ideas of controlling near-field light localizations have been suggested. However, they can only be conducted in complex nanosystems or lack nanoscale accuracy in hot-spot positioning. To improve these weaknesses, this thesis has made a number of theoretical and experimental advances.

- It has been experimentally demonstrated that a planar metamaterial can be used as a controllable template for nanoscale light localizations. Subwavelength energy hot-spots in the near-field of a fish-scale metamaterial can be efficiently controlled by tuning the polarization and wavelength of an incident light beam.

- It was shown that the positions of near-field light localizations are highly correlated to the nanostructure, unit cell size and the dipole absorption resonance of an array of meta-molecules.

- Through coherent control of a monochromatic continuous light beam with a spatially tailored phase profile, it has been theoretically and experimentally demonstrated for the first time that well-isolated energy hot-spots of a fraction of a wavelength can be created and positioned on the landscape of a metamaterial.

- A new experimental configuration for the coherent control of nanoscale light localization has been established by an integration of a SNOM and a phase-only SLM.

- By simply modulating the input phase profile, the hot-spot position on the metamaterial can be prescribed and moved at will from one meta-molecule of the array to another in a digital fashion. The accuracy of hot-spot movement depends on the size of the meta-molecules, which can be much smaller than the wavelength of the incident light.

Regarding subwavelength light localizations generated beyond the near-field, previous studies used a quasi-periodic nanohole array as a super-oscillating binary mask. However, the distance between adjacent energy hot-spots is too small, which restricts the practical uses of this technique. Therefore, this thesis has made further exploration of hot-spot generation and new exploitation of nanohole arrays.

- It has been demonstrated for the first time that an isolated subwavelength hot-spot can be created beyond the near-field and can be located in a wide field of view by using a radially symmetric quasi-periodic nanohole array.
- The lensing functions of quasi-periodic nanohole arrays have been discovered. It was shown that the imaging ability of a nanohole array lens is similar to a conventional lens with high N.A. With the use of a radially symmetric quasi-periodic nanohole array, the effective imaging field can be extended and complex objects composed of multiple light sources can be resolved.

6.2 Outlook

This research has proposed informative approaches to and demonstrated new techniques for the precise control of nanoscale light localizations. However, there still remain a few challenges and some room for further studies. Here, a brief outlook is given on future work and potential applications, hopefully making the most use of the findings yielded by the present study.

Advanced apparatus for controlling near-field light localizations

Regarding control of light localization in the near-field, it has been demonstrated in this thesis that well-isolated energy hot-spots can be created and positioned by modulating the phase profile of an incident light beam. It would be interesting to extend this technique to generate arbitrary patterns with subwavelength resolution on the landscape of metamaterials. This can be realized by developing new algorithms to modulate the amplitude and phase profiles of an incident light beam, and by an arrangement of optics for individually controlling each meta-molecule. Furthermore, due to strong optically induced interactions between meta-molecules, new designs for the

nanostructure, the unit cell size, and the arrangement of meta-molecule arrays will be required. It is believed that these efforts will make great contributions to applications such as the development of high-definition imaging devices, data storage with phase-change nanoparticles, and nanoluminescent bio-assay labelling with quantum dots.

Imaging devices with super-oscillating masks

In this thesis, it has been demonstrated that a quasi-periodic nanohole array can be used as a lens to generate an isolated subwavelength focused spot beyond the near-field and to image objects on the other side of the array. Therefore, it will be of interest to develop new types of imaging devices such as a scanning type microscope and coverglasses with nanoholes for direct imaging. However, issues to be considered include the energy expense, the stability, and the contrast with background noise in pursuit of high resolution imaging. As a result, more sophisticated arrangements of nanoholes for super-oscillating binary masks are required. Meanwhile, a new type of super-oscillating dynamic lens can be created by using an SLM to control the amplitude and phase of a light beam.

A

Collective excitations in an ensemble of identical meta-molecules

The following numerical model of the collective excitations in an ensemble of identical meta-molecules was provided Dr. S. D. Jenkins and Dr. J. Ruostekoski from the School of Mathematics at the University of Southampton.

A.1 Theoretical Model

We consider an ensemble of N meta-molecules placed at positions $\vec{r}_j$ ($j = 1, \ldots, N$) arranged in a 2D rectangular lattice. This lattice is driven by an external, phase modulated, beam with electric field $\vec{E}_{in}(\vec{r}, t)$ as described in the text. In general, the charge and current densities for the single-molecule oscillatory modes are described by a polarization density $\vec{P}_j(\vec{r}, t)$ and magnetization density $\vec{M}_j(\vec{r}, t)$. For simplicity, we assume that the spatial extent of a meta-molecule is much smaller than the wavelength of light and that the electric quadrupole moment of the meta-molecule vanishes. Each meta-molecule is described by a single mode of current oscillation whose contribution to the scattering of electromagnetic wave we then approximate by its electric and magnetic dipole moments. The state of the meta-molecule j is represented by the dynamic variable $Q_j(t)$ with units of charge and whose spatial characteristics have been separated out into time independent functions $\vec{\psi}(\vec{r})$ and $\vec{\varpi}(\vec{r})$. Explicitly,

$$\vec{P}_j = Q_j(t)\vec{\psi}(\vec{r}-\vec{r}_j) \simeq \vec{d}_j\delta(\vec{r}-\vec{r}_j) \tag{A.1}$$

$$\vec{M}_j = I_j(t)\vec{\varpi}(\vec{r}-\vec{r}_j) \simeq \vec{\mu}_j\delta(\vec{r}-\vec{r}_j) \tag{A.2}$$

where $I_j(t) = dQ_j/dt$ is the current. In this work, we assume the electric dipoles are aligned with the incident electric field and that the magnetic dipoles are oriented along the driving field's propagation direction so that only the electric dipoles are driven by the incident beam.

In our dynamical model, in the absence of radiation losses, each current oscillation behaves as a simple LC circuit with self capacitance C and self inductance L. The emitted radiation results in a damping of the current oscillation, which we treat here using the phenomenological line-widths Γ_E and Γ_M associated with electric and magnetic dipole radiation respectively. In the multi-molecule system, however, the radiated fields couple to the dipole moments of all other molecules in the system. It is convenient to represent the current oscillations in terms the dimensionless normal variables

$$b_j(t) = \frac{e^{i\omega_0 t}}{\sqrt{2\omega_0}}\left(\frac{Q_j}{\sqrt{C}} + i\frac{\Phi_j}{\sqrt{L}}\right), \tag{A.3}$$

where $\Phi_j = \int d^3r\vec{B}\cdot\vec{\varpi}$ describes the effective magnetic flux through the meta-molecule j, C and L are the effective self capacitance and self inductance of a single meta-molecule, and $\omega_0 = 1/\sqrt{LC}$ denotes the resonance frequency. By ignoring the frequency dependence of spontaneous emission rates and coupling coefficients, and after making the rotating wave approximation, the equations of motion read

$$\dot{\mathrm{b}}(t) = \mathfrak{C}\mathrm{b}(t) + \mathrm{F}(t), \tag{A.4}$$

where $\mathrm{b} = (b_1, \ldots, b_N)^T$, the coupling matrix

$$\mathcal{C} = -\frac{\Gamma_E + \Gamma_M}{2}\mathbf{1} + i\frac{3}{4}\left(\Gamma_E \mathcal{G}_E + \Gamma_M \mathcal{G}_M\right) + \frac{3}{4}\sqrt{\Gamma_E \Gamma_M}\left(\mathcal{G}_\times + \mathcal{G}_\times^T\right), \tag{A.5}$$

the driving field contribution is given by

$$\mathrm{F} = i\frac{e^{i\omega_0 t}}{\sqrt{2\omega_0}}\frac{\mathcal{E}_{in}(t)}{\sqrt{L}}, \tag{A.6}$$

and $\mathcal{E}_{in}$ is the electromotive force induced by the driving field $\mathcal{E}_j = \int d^3r\, \vec{E}_{in}(\vec{r}, \Omega) \cdot \vec{\psi}(\vec{r} - \vec{r}_j)$,The dimensionless coupling matrices $\mathcal{G}_E$, and $\mathcal{G}_M$ result from interactions with the electric or magnetic fields scattered from the electric or magnetic dipoles respectively, while the matrix $\mathcal{G}_\times$ accounts for the electric (magnetic) fields produced by the magnetic (electric) dipoles.

Equation (A.4) corresponds to the integral representation of Maxwell's wave equations, as described by Eq.(1) in the text, and can be efficiently solved as a linear system. In the limits we've considered, there exist as many distinct collective eigenmodes of oscillation as there are meta-molecules in the system. Each collective mode corresponds to an eigenvector of the matrix $\mathcal{C}$ and has a distinct resonance frequency and decay rate, determined by the imaginary and real parts respectively of the corresponding eigenvalue. In the context of this simplified model, the scheme we proposed in this manuscript boils down to choosing a spatial profile and detuning of the driving field so as to excite a linear combination of these eigenmodes such that the steady state solution is localized on the meta-molecular crystal.

A.2 Effect of collective modes

The effect of strong interactions between different meta-molecules and the resulting collective radiative modes can be illustrated by a simple example of a 2×2 metamaterial array. If the inter-dipole separation is much smaller than the wavelength of light, the resonance frequencies and the radiative damping rates are very different from the ones

of an isolated dipole and they are affected by recurrent scattering processes in which the wave is scattered several times by the same dipole. The four energy eigenmodes of the system can be represented as shown in Fig. A.1. Here the positive (negative) amplitude of the current oscillation mode is displayed as + (−) sign.

If an incident field can be prepared in such a way that it excites an equal superposition of the four eigenmodes $\Phi = \sum_j \frac{1}{2}\phi_j$, then one can immediately observe the approximate cancelation of the optical excitation energy in three of the four dipoles in the 2×2 metamaterial array. Due to the different eigenmode energies, the field profile in general is time-dependent. In large systems, however, there can be several modes with almost identical energies. This simple example illustrates the localization in one of the dipoles.

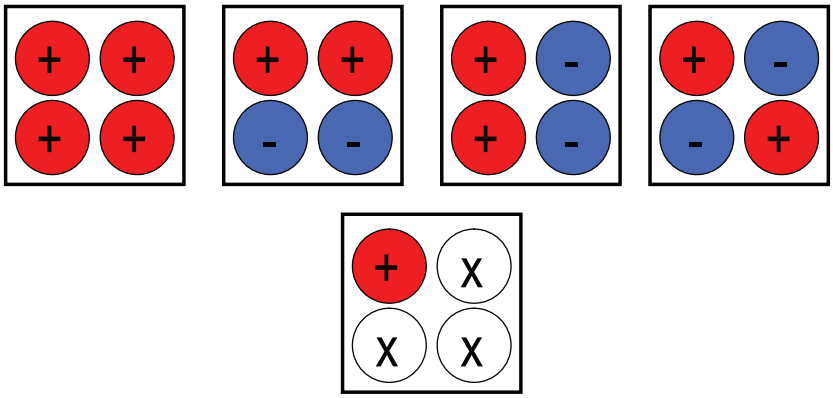

Figure A.1: ***Four eigenstates of a*** 2×2 ***metamaterial system.*** *First row: The four eigenstates of a* 2×2 *metamaterial system* ϕ_j $(j = 1, \ldots, 4)$*, respectively. The + (−) sign refers to the positive (negative) amplitude of the current oscillation mode. The second row: a superposition state* $\Phi = \sum_j \frac{1}{2}\phi_j$ *dominantly exciting one of the dipoles. Here the sites marked by x are not excited.*

B

Experimental setup for coherent control process

B.1 Experimental configuration

The coherent control of nanoscale light localization was demonstrated with a scanning near-field optical microscope (SNOM; Omicron) integrated with a phase-modulating-only liquid crystal spatial light modulator (SLM; Holoeye, PLUTO, 1920 × 1080 pixels, 8 μm/pixel). A schematic diagram of the experimental configuration is shown in Fig. B.1. The light source was a laser diode (Thorlabs, Max. power: 100 mW), operating at a wavelength of 852 nm and bandwidth of 0.5 nm.

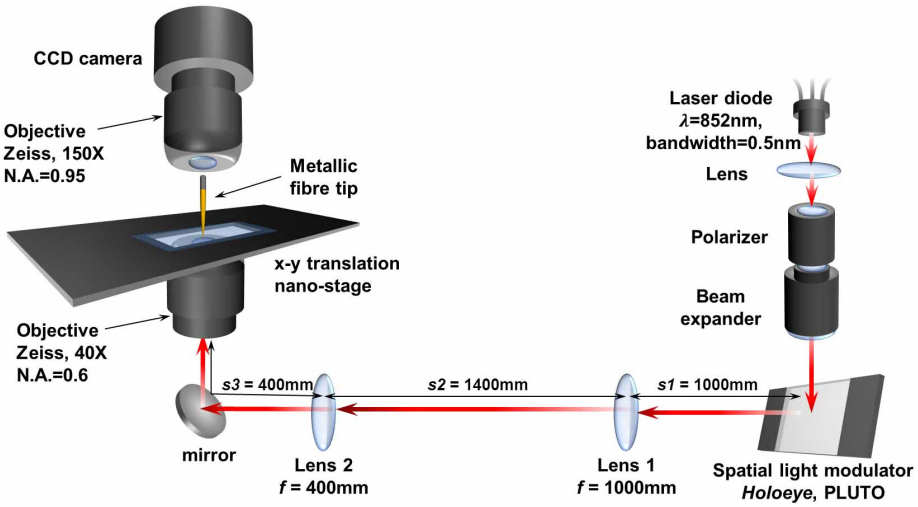

Figure B.1: ***Schematic experimental setup for coherent control of nanoscale light localization.*** *An incident monochromatic light beam with spatially-modulated phase profile impinging on an interacting meta-molecules array was tailored by a phase-only SLM. Demagnification by the optical setup (Lens 1, Lens 2 and the microscope objective) shrinks the size of the modulated light beam to illuminate a metamaterial sample. The near-field intensity distributions of the metamaterial array under the resonant conditions were directly measured by a SNOM.*

B.2 Phase profile modulation

In the experiments, the wavefront of an incident modulated light beam had a sinusoidal form which can be formulated as below. The modulated wavefront is spatially varied along the x and y direction with a period of six unit cells of the metamaterial array.

$$E(x,y) = E_0 e^{i\phi(x,y)}, \quad \phi(x,y) = \frac{\phi_{max}}{2}\sin(\kappa x)\sin(\kappa y) \tag{B.1}$$

where $\kappa = 2\pi/(6a)$, a is the unit cell of the interacting meta-molecules. According to the formula, the required sinusoidal phase profile for illuminating the metamaterial sample can be displayed as shown in Fig. B.2(b), while the amplitude remains nearly the same everywhere (see Fig. B.2(a)). By taking the Fourier transform of the modulated field and considering the magnification which is given by the optics setup (Lens 1: f=1000 mm, Lens 2: f=400 mm and microscope objective: 40×), a transformation of the modulated field can be interpreted in Fourier space as shown in Fig. B.3. The corresponding amplitude and phase in a free space can be obtained through computer control of pixels of the SLM. In our cases, an array of 1080×1080 pixels was activated to generate a light beam with a sinusoidal phase profile modulation. Fortunately, as shown in Fig. B.3(a), the approximately homogeneous amplitude indicates that such a sinusoidal phase profile can be performed by the phase-only SLM.

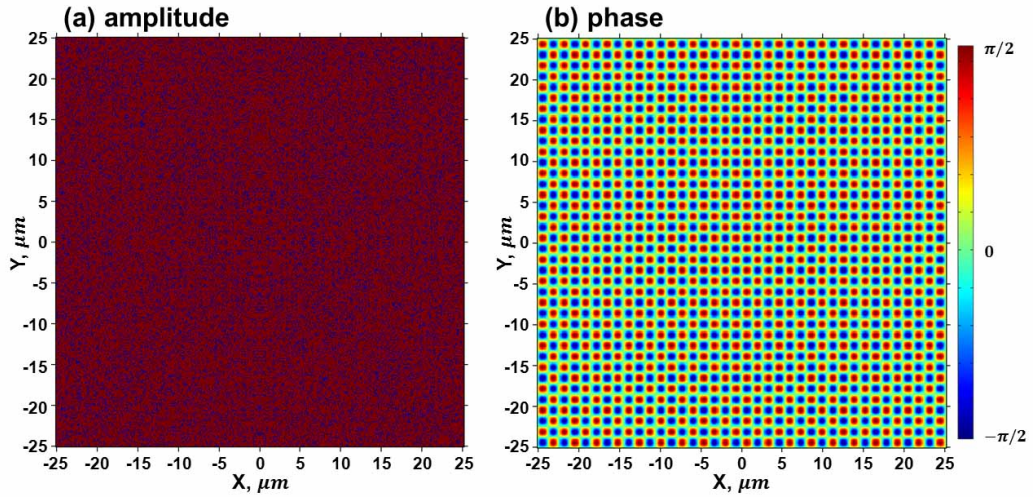

Figure B.2: ***Required amplitude and modulated phase profile*** *The expected (a) amplitude and (b) modulated phase profile illuminated on the surface of a metamaterial sample. The amplitude is expected to be homogeneous distributed on the metamaterial landscape, while the phase profile has a sinusoidal phase modulation.*

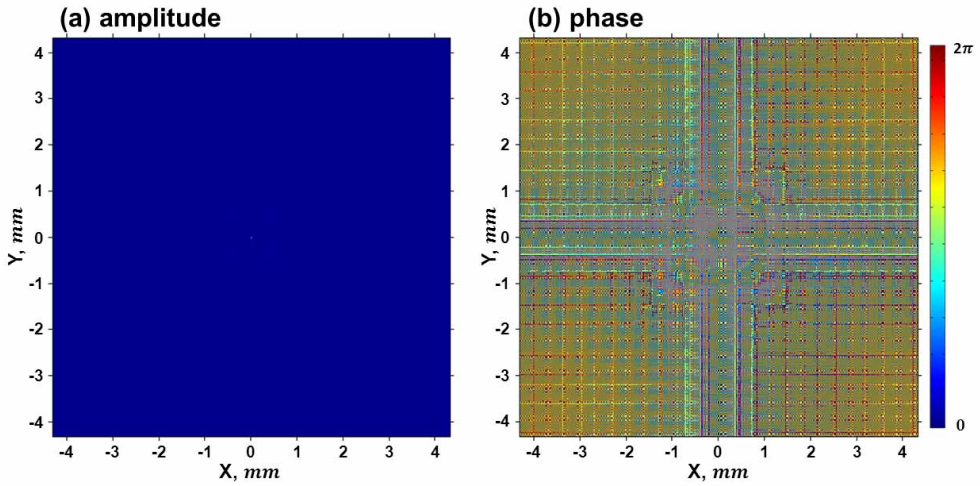

Figure B.3: ***Transformation of the modulated field in Fourier space.*** *The corresponding amplitude and phase in a free space can be obtained through a computer control on pixels of the SLM.*

C Publications

C.1 Journal Publications

- T. S. Kao, E. T. F. Rogers, J. Y. Ou, and N. I. Zheludev. "Digitally addressable focusing of light into a subwavelength hot-spot". Nano Lett., 12(6):2728 (2012).
- T. S. Kao, S. D. Jenkins, J. Ruostekoski, and N. I. Zheludev. "Coherent control of nanoscale light localization in metamaterial: creating and positioning isolated sub-wavelength energy hot-spots". Phys. Rev. Lett., 106:085501 (2011)
- T. S. Kao, F. M. Huang, Y. Chen, E. T. F. Rogers, and N. I. Zheludev. "Metamaterial as a controllable template for nanoscale field localization". Appl. Phys. Lett., 96:041103 (2010)
- B. -R. Lu, Y. Chen, S. -W. Wang, E. Huq, E. Rogers, T. S. Kao, X. -P. Qu, Ran Liub, N. I. Zheludev, "A novel 3D nanolens for sub-wavelength focusing by self-aligned nanolithography". Microelectronic Eng., 87:1506 (2010)
- F. M. Huang, T. S. Kao, V. A. Fedotov, Y. Chen, and N. I. Zheludev. "Nanohole array as a lens". Nano Lett., 8(8):2469 (2008)

C.2 Conference Contributions

- (invited) J. Y. Ou, T. S. Kao, J. Zhang, E. Plum, K. F. MacDonald, and N. I. Zheludev. "Manipulating light with photonic metamaterials". *SPIE Optics and Photonics 2011*, San Diego, CA, USA, 21-25 Aug. (2011)

- (oral) T. S. Kao, S. Jenkins, J. Ruostekoski, and N. Zheludev. "Coherent control of nanoscale light localization: creating and positioning isolated sub-wavelength energy hot-spots". *CLEO/Europe-EQEC*, Munich, Germany, 22-26 May (2011)

- (oral) T. S. Kao, S. Jenkins, J. Ruostekoski, and N. I. Zheludev. "Coherent control of nanoscale light localization: positioning a hot-spot at will". *NANOMETA 2011*, Seefeld, Austria, 3-6 Jan. (2011)

- (poster) E. T. F. Rogers, T. Roy, T. S. Kao, J. Y. Ou, V. Savinov, S. Sano, J. Lindberg, M. R. Dennis, and N. I. Zheludev. "The Super-oscillating Superlens". *NANOMETA 2011*, Seefeld, Austria, 3-6 Jan. (2011)

- (invited) J. Baumgartl, M. Malizu, S. Kosemier, K. Dohlakia, N. Shapira, A. Szameit, M. Segev, E. T. F. Rogers, T. S. Kao, V. Savinov, and N. I. Zheludev. "Manipulating light with photonic metamaterials". *Metamaterials'2010*, Karlsruhe, Germany, 13-16 Sep. (2010)

- (oral) E. T. F. Rogers, T. S. Kao, V. Savinov, Y. Chen, and N. I. Zheludev. "Super-resolution imaging beyond the near-field". *Photon 10*, Southampton, UK, 23-26 Aug. (2010)

- (oral) T. S. Kao, E. T. F. Rogers, V. Savinov, and N. I. Zheludev. "Optical super-resolution imaging beyond the near-field using a nanohole array". *5th EOS Topical Meeting on Advanced Imaging Techniques*, Engelberg, Switzerland, 29 June-2 July (2010)

- (invited) E. T. F. Rogers, T. S. Kao, J. Baumgartl, M. Mazilu, S. Kosmeier, K. Dholakia, and N. I. Zheludev. "Super-resolution through super-oscillations". *CIMTEC 2010*, Montecatini Terme, Italy, 06-18 Jun. (2010)

- (oral) J. Baumgartl, M. Mazilu, S. Kosmeier, E. T. F. Rogers, T. S. Kao, V. Savinov, K. Dholakia, and N. I. Zheludev. "Optical super-resolution through super-oscillations". *SPIE Photonics Europe 2010*, Brussels, Belgium, 12-16 Apr. (2010)

- (poster) T. S. Kao, E. T. F. Rogers, Y. Chen, and N. I. Zheludev. "Plasmonic metamaterial as a controllable template for nanoscale light localization". *SPIE*

Photonics Europe 2010, Brussels, Belgium, 12-16 Apr. (2010)

- (oral) F. M. Huang, T. S. Kao, and N. I. Zheludev. "Superresolution without evanescent fields". *CLEO/Europe-EQEC*, Munich, Germany, 14-19 Jun. (2009)

- (oral) Z. Wang, T. S. Kao, and N. I. Zheludev. "Talbot Effect in a Dielectric Microspheres Array: Foci Self-imaging". *CLEO/Europe-EQEC*, Munich, Germany, 14-19 Jun. (2009)

- (poster) T. S. Kao, F. M. Huang, V. A. Fedotov, and N. I. Zheludev. "Subwavelength localization of light on double-periodic nanowire metamaterials". *NANOMETA 2009*, Seefeld, Austria, 5-8 Jan. (2009)

- (poster) T. S. Kao, F. M. Huang, V. A. Fedotov, and N. I. Zheludev. "Subwavelength far-field focusing and localization of light in nanostructures". *CFN summer school on Nano-Phtonics 2008*, Bad Herrenalb, Germany, 21-26 Aug. (2008)

- (invited) F. M. Huang, T. S. Kao, V. A. Fedotov, and N. I. Zheludev. "Imaging with a nanohole array". *SPIE Plasmonics: Nanoimaging, Nanofabrication, and Their Applications IV*, San Diego, CA, USA, 10-14 Aug. (2008)

References

[1] E. H. Synge. "A suggested model for extending microscopic resolution into the ultra-microscopic region". *Phil. Mag.*, 6:356, 1928.

[2] D. W. Pohl, W. Denk, and M. Lanz. "Optical stethoscopy: image recording with resolution $\lambda/20$". *Appl. Phys. Lett.*, 44:651, 1984.

[3] S. W. Hell and J. Wichmann. "Breaking the diffraction resolution limit by stimulated emission: stimulated-emission-depletion fluorescence microscopy". *Opt. Lett.*, 19:780, 1994.

[4] S. W. Hell. "Toward fluorescence nanoscopy". *Nature Biotechnol.*, 21:1347, 2003.

[5] X. Zhuang. "Nano-imaging with STORM". *Nature Photon.*, 3:365, 2009.

[6] J. B. Pendry. "Negative refraction makes a perfect lens". *Phys. Rev. Lett.*, 85:3966, 2000.

[7] X. Zhang and Z. Liu. "Superlenses to overcome the diffraction limit". *Nature Mater.*, 7:435, 2008.

[8] N. I. Zheludev. "What diffraction limit?". *Nature Mater.*, 7:420, 2008.

[9] M. V. Berry and S. Popescu. "Evolution of quantum superoscillations and optical superresolution without evanescent waves". *J. Phys. A*, 39:6965, 2006.

[10] F. M. Huang, N. I. Zheludev, Y. Chen, and F. J. G. de Abajo. "Focusing of light by a nanohole array". *Appl. Phys. Lett.*, 90:091119, 2007.

[11] T. Taubner, D. Korobkin, Y. Urzhumov, G. Shvets, and R. Hillenbrand. "Near-field microscopy through a SiC superlens". *Science*, 313:1595, 2006.

[12] Y. Xiong, Z. Liu, C. Sun, and X. Zhang. "wo-dimensional imaging by far-field superlens at visible wavelengths". *Nano Lett.*, page 3360, 2007.

[13] Z. Liu, H. Lee, Y. Xiong, C. Sun, and X. Zhang. "Far-field optical hyperlens magnifying sub-diffraction-limited objects". *Science*, 315:1686, 2007.

[14] W. Srituravanich, N. Fang, C. Sun, Q. Luo, and X. Zhang. "Plasmonic nanolithography". *Nano Lett.*, 4:1085, 2004.

[15] W. Srituravanich, S. Durant, H. Lee, C. Sun, and X. Zhang. "Deep subwavelength nanolithography using localized surface plasmon modes on planar silver mask". *J. Vac. Sci. Technol. B*, 23:2636, 2005.

[16] D. B. Shao and S. C. Chen. "Numerical simulation of surface-plasmon-assisted nanolithography". *Opt. Exp.*, 13:6964, 2005.

[17] E. Ozbay. "Plasmonics: Merging photonics and electronics at nanoscale dimensions". *Science*, 311:189, 2006.

[18] K. S. Johnson, J. H. Thywissen, N. H. Dekker, K. K. Berggren, A. P. Chu, R. Younkin, and M. Prentiss. "Localization of metastable atom beams with optical standing waves: Nanolithography at the Heisenberg limit". *Rev. Sci. Instrum.*, 280:1583, 1998.

[19] X. Luo and T. Ishihara. "Surface plasmon resonant interference nanolithography technique". *Appl. Phys. Lett.*, 84:4780, 2004.

[20] A. Sentenac and P. C. Chaumet. "Subdiffraction light focusing on a grating substrate". *Phys. Rev. Lett.*, 101:013901, 2008.

[21] G. Volpe, S. Cherukulappurath, R. J. Parramon, G. Molina-Terriza, and R. Quidant. "Controlling the optical near field of nanoantennas with spatial phase-shaped beams". *Nano Lett.*, 9:3608, 2009.

[22] G. Volpe, G. Molina-Terriza, and R. Quidant. "Deterministic subwavelength control of light confinement in nanostructures". *Phys. Rev. Lett.*, 105:216802, 2010.

[23] M. I. Stockman. "Nanofocusing of optical energy in tapered plasmonic waveguides". *Phys. Rev. Lett.*, 93:137404, 2004.

[24] C. G. Schroer and B. Lengeler. "Focusing hard X-rays to nanometer dimensions by adiabatically focusing lenses". *Phys. Rev. Lett.*, 94:054802, 2005.

[25] D. K. Gramotnev and S. I. Bozhevolnyi. "Plasmonics beyond the diffraction limit". *Nature Photon.*, 4:83, 2010.

[26] M. I. Stockman, S. V. Faleev, and D. J. Bergman. "Coherent control of femtosecond energy localization in nanosystems". *Phys. Rev. Lett.*, 88:067402, 2002.

[27] M. Schnell, A. Garcia-Etxarri, A. J. Huber, K. Crozier, J. Aizpurua, and R. Hillenbrand. "Controlling the near-field oscillations of loaded plasmonic nanoantennas". *Nature Photon.*, 3:287, 2009.

[28] M. Aeschlimanna, M. Bauerb, D. Bayera, T. Brixnerc, S. Cunovicd, F. Dimlerc, A. Fischera, W. Pfeifferd, M. Rohmera, C. Schneidera, F. Steeba, C. Strberd, and D. V. Voroninec. "Spatiotemporal control of nanooptical excitations". *Proc. Natl. Acad. Sci. USA*, 107:5329, 2010.

[29] B. Gjonaj, J. Aulbach, P. M. Johnson, A. P. Mosk, L. Kuipers, and Ad Lagendijk. "Active spatial control of plasmonic fields". *Nature Photon.*, 5:360, 2011.

[30] T. S. Kao, F. M. Huang, Y. Chen, E. T. F. Rogers, and N. I. Zheludev. "Metamaterial as a controllable template for nanoscale field localization". *Appl. Phys. Lett.*, 96:041103, 2010.

[31] T. S. Kao, S. D. Jenkins, J. Ruostekoski, and N. I. Zheludev. "Coherent control of nanoscale light localization in metamaterial: creating and positioning isolated subwavelength energy hot-spots". *Phys. Rev. Lett.*, 106:085501, 2011.

[32] J. A. O'Keefe. "Resolving power of visible light". *J. Opt. Soc. Am.*, 46:359, 1956.

[33] E. A. Ash and G. Nicholls. "Super-resolution aperture scanning microscope". *Nature*, 237:510, 1972.

[34] A. Lewis, M. Isaacson, A. Harootunian, and A. Muray. "Development of a 500$\mathring{A}$ spatial resolution light microscope". *Ultramicroscopy*, 13:227, 1984.

[35] E. Betzig, M. Isaacson, and A. Lewis. "Collection mode near-field scanning optical microscopy". *Appl. Phys. Lett.*, 61:2088, 1987.

[36] E. Betzig and J. K. Trautman. "Near-field optics: Microscopy, spectroscopy, and surface modification beyond the diffraction limit". *Science*, 257:189, 1992.

[37] E. Betzig and R. J. Chichester. "Single molecules observed by near-field scanning optical microscopy". *Science*, 262:1422, 1993.

[38] D. P. Tsai, H. E. Jackson, R. C. Reddick, S. H. Sharp, and R. J. Warmack. "hoton scanning tunneling microscope study of optical waveguides". *Appl. Phys. Lett.*, 56:1515, 1990.

[39] D. P. Tsai, J. Kovacs, Z. Wang, M. Moskovits, V. M. Shalaev, J. S. Suh, and R. Botet. "Photon scanning tunneling microscopy images of optical excitations of fractal metal colloid clusters". *Phys. Rev. Lett.*, 72:4149, 1994.

[40] L. Novotny and S. J. Stranick. "Near-field optical microscopy and spectroscopy with pointed probes". *Annu. Rev. Phys. Chem.*, 57:303, 2006.

[41] L. Novotny and B. Hecht. *Principle of nano-optics.* Cambridge university press, 2006.

[42] S. Kawata, editor. *Near-field optics and surface plasmon polariton.* Springer, 2001.

[43] R. Vogelgesang and A. Dmitriev. "Real-space imaging of nanoplasmonic resonances". *Analyst*, 135:1175, 2010.

[44] L. Schermelleh, R. Heintzmann, and H. Leonhard. "A guide to super-resolution fluorescence microscopy". *J. Cell Biol.*, 190:165, 2010.

[45] M. Fernandez-Suarez and A. Y. Ting. "Fluorescent probes for super-resolution imaging in living cells". *Nature Reviews: Molecular Cell Biology*, 9:929, 2008.

[46] D. A. Rothenfluh, H. Bermudez, C. P. Oneil, and J. A. Hubbell. "Biofunctional polymer nanoparticles for intra-articular targeting and retention in cartilage". *Nature Mater.*, 7:248, 2008.

[47] V. Guarani, G. Deflorian, C. A. Franco, M. Kruger, L. K. Phng, K. Bentley, L. Toussaint, F. Dequiedt, R. Mostoslavsky, M. H. H. Schmidt, B. Zimmermann, R. P. Brandes, M. Mione, C. H. Westphal, T. Braun, A. M. Zeiher, H. Gerhardt, S. Dimmeler, and M. Potente. "Acetylation-dependent regulation of endothelial notch signalling by the SIRT1 deacetylase". *Nature*, 473:234, 2011.

[48] M. G. L. Gustafsson, D. A. Agard, and J. W. Sedat. "I^5M: 3D widefield light microscopy with better than 100nm axial resolution". *J. Micro.*, 195:10, 1999.

[49] L. Shao, B. Isaac, S. Uzawa, D. A. Agard, J. W. Sedat, and M. G. L. Gustafsson. "I^5S: wide-field light microscopy with 100-nm-scale resolution in three dimensions". *Biophys.*, 94:4971, 2008.

[50] B. Rothenhausler and W. Knoll. "Surface-plasmon microscopy". *Nature*, 332:615, 1988.

[51] S. Kawata, Y. Inouye, and P. Verma. "Plasmonics for near-field nano-imaging and superlensing". *Nature Photon.*, 3:388, 2009.

[52] F. Wei and Z. Liu. "Plasmonic structured illumination microscopy". *Nano Lett.*, 10:2531, 2010.

[53] T. A. Klar and S. W. Hell. "Subdiffraction resolution in far-field fluorescence microscopy". *Opt. Lett.*, 24:954, 1999.

[54] E. Rittweger, K. Y. Han, S. E. Irvine, C. Eggeling, and S. W. Hell. "STED microscopy reveals crystal colour centres with nanometric resolution". *Nature Photon.*, 3:144, 2009.

[55] T. A. Klar, S. Jakobs, M. Dyba, A. Egner, and S. W. Hell. "Fluorescence microscopy with diffraction resolution limit broken by simulated emission". *Proc. Natl. Acad. Sci. USA*, 97:8206, 2000.

[56] R. Schmidt, C. A. Wurm, S. Jakobs, J. Engelhardt, A. Egner, and S. W. Hell. "Spherical nanosized focal spot unravels the interior of cells". *Nature Methods*, 5:539, 2008.

[57] K. I. Willig, S. O. Rizzoli, V. Westphal, R. Jahn, and S. W. Hell. "STED-microscopy reveals that synaptotagmin remains clustered after synaptic vesicle exocytosis". *Nature*, 440:935, 2006.

[58] S. W. Hell, S. Jakob, and L. Kastrup. "Imaging and writing at the nanoscale with focused visible light through saturable optical transitions". *Appl. Phys. A*, 77:859, 2003.

[59] S. W. Hell. "Strategy for far-field optical imaging and writing without diffraction limit". *Phys. Lett. A*, 326:140, 2004.

[60] S. W. Hell, M. dyba, and S. Jakobs. "Concepts for nanoscale resolution in fluorescence microscopy". *Curr. Opin. Neurobiol.*, 14:599, 2004.

[61] S. Jakobs M. Hofmann, C. Eggeling and S. W. Hell. "Breaking the diffraction barrier in fluorescence microscopy at low light intensities by using reversibly photoswitchable proteins". *Proc. Natl. Acad. Sci. USA*, 102:17565, 2005.

[62] P. C. Maurer, J. R. Maze, P. L. Stanwix, L. Jiang, A. V. Gorshkov, A. A. Zibrov, B. Harke, J. S. Hodges, A. S. Zibrov, A. Yacoby, D. Twitchen, S. W. Hell, R. L. Walsworth, and M. D. Lukin. "Far-field optical imaging and manipulation of individual spins with nanoscale resolution". *Nature Phys.*, 6:912, 2010.

[63] H. Shroff, C. G. Galbraith, J. A. Galbraith, and E. Betzig. "Live-cell photoactivated localization microscopy of nanoscale adhesion dynamics". *Nature Methods*, 5:417, 2008.

[64] S. T. Hess, T. P. K. Giriragan, and M. D. Mason. "Ultra-high resolution imaging by fluorescence photoactivation localization microscopy". *Biophys, J.*, 91:4258, 2006.

[65] E. Betzig, G. H. Patterson, R. Sougrat, O. W. Lindwasser, S. Olenych, J. S. Bonifacino, M. W. Davidson, J. Lippincott-Schwartz, and H. F. Hess. "Imaging intercellular fluorescent proteins at nanometer resolution". *Science*, 313:1642, 2006.

[66] M. J. Rust, M. Bates, and X. Zhuang. "Sub-diffraction-limit imaging by stochastic optical reconstruction microscopy (STORM)". *Nature Methods*, 3:793, 2006.

[67] S. W. Hell and M. Kroug. "Ground-state-depletion fluorescence microscopy: a concept for breaking the diffraction resolution limit". *Appl. Phys. B*, 60:495, 1995.

[68] S. Bretschneider, C. Eggeling, and S. W. Hell. "Breaking the diffraction barrier in fluorescence microscopy by optical shelving". *Phys. Rev. Lett.*, 98:218103, 2007.

[69] E. Rittweger, D. Wildanger, and S. W. Hell. "Far-field fluorescence nanoscopy of diamond color centers by ground state depletion". *EPL*, 86:14001, 2009.

[70] J. Renger, R. Quidant, N. van Hulst, and L. Novotny. "Surface-enhanced nonlinear four-wave mixing". *Phys. Rev. Lett.,*, 104(331):046803, 2010.

[71] H. Harutyunyan, S. Palomba, J. Renger, R. Quidant, and L. Novotny. "Nonlinear dark-field microscopy". *Nano Lett.*, 10:5076, 2010.

[72] P. Ghenuche, S. Cherukulappurath, T. H. Taminiau, N. F. van Hulst, and R. Quidant. "Spectroscopic mode mapping of resonant plasmon nanoantennas". *Phys. Rev. Lett.*, 101:116805, 2008.

[73] R. Chenuche, S. Cherukulappurath, and R. Quidant. "Mode mapping of plasmonic stars using TPL microscopy". *New J. Phys.*, 10:105013, 2008.

[74] M. Breit, S. Malkmus, J. Feldmann, and H. U. Danzebrink. "Near-field second harmonic generation by using uncoated silicon tips". *Appl. Phys. Lett.*, 90:093114, 2007.

[75] M. Zavelani-Rossi, M. Celebrano, P. Biagioni, D. Polli, M. Finazzi, L. Duo, G. Cerullo, M. Labardi, M. Allegrini, J. Grand, and P. M. Adam. "Near-field second-harmonic generation in single gold nanoparticles". *Appl. Phys. Lett.*, 92:093119, 2008.

[76] R. Heintzmann, T. M. Jovin, and C. Cremer. "Saturated patterned excitation microscopy - a concept for optical resolution improvement". *J. Opt. Soc. Am. A*, 19:1599, 2002.

[77] M. G. L. Gustafsson. "Nonlinear structured-illumination microscopy: wide-field fluorescence imaging with theoretically unlimited resolution". *Proc. Natl. Acad. Sci. USA*, 102:13081, 2005.

[78] N. Fang, H. Lee, C. Sun, and X. Zhang. "Sub-diffraction-limited optical imaging with a silver superlens". *Science*, 308:534, 2005.

[79] E. Betzig, J. K. Trautman, R. Wolfe, E. M. Gyorgy, P. L. Finn, M. H. Kryder, and C. H. Chang. "Near-field magneto optics and high density data storage". *Appl. Phys. Lett.*, 61:142, 1992.

[80] B. D. Terris, H. J. Mamin, D. Rugar, W. R. Studenmund, and G. S. Kino. "Near-field optical data storage using a solid immersion lens". *Appl. Phys. Lett.*, 3765:388, 1994.

[81] B. D. Terris, H. J. Mamin, and D. Rugar. "Near-field optical data storage". *Appl. Phys. Lett.*, 68:141, 1996.

[82] D. P. Tsai and W. C. Lin. "robing the near fields of the super-resolution near-field optical structure". *Appl. Phys. Lett.*, 77:1413, 2000.

[83] W. C. Liu, C. Y. Wen, K. H. Chen, W. C. Lin, and D. P. Tsai. "Near-field images of the AgO_x-type super-resolution near-field structure". *Appl. Phys. Lett.*, 78:685, 2001.

[84] T. Kikukawa, T. Nakano, T. Shima, and J. Tominaga. "Rigid bubble pit formation and huge signal enhancement in super-resolution near-field structure disk with platinum-oxide layer". *Appl. Phys. Lett.*, 81:4697, 2002.

[85] M. Wuttig and N. Yamada. "Phase-change materials for rewriteable data storage". *Nature Mater.*, 6:824, 2007.

[86] B. F. Soares, F. Jonsson, and N. I. Zheludev. "All optical phase-change memory in a single gallium nanoparticle". *Phys. Rev. Lett.*, 98:153905, 2007.

[87] T. S. Kao, Y. H. Fu, H. W. Hsu, and D. P. Tsai. "Study of the optical response of phase-change recording layer with zinc oxide nanostructured thin film". *J. Micro.*, 229:561, 2008.

[88] S.-C. Kong, A. V. Sahakian, A. Heifetz, A. Taflove, and V. Backman. "Robust detection of deeply subwavelength pits in simulated optical data-storage disks using photonic jets". *Appl. Phys. Lett.*, 92:211102, 2008.

[89] W. Srituravanich, L. Pan, Y. Wang, C. Sun, D. B. Bogy, and X. Zhang. "Flying plasmonic lens in the near field for high-speed nanolithography". *Nature Nanotech.*, 3:733, 2008.

[90] T. L. Andrew, H.-Y. Tsai, and R. Menon. "Confining light to deep subwavelength dimensions to enable optical nanopatterning". *Science*, 324:917, 2009.

[91] R. Yan, D. Gargas, and P. Yang. "Nanowire Photonics". *Nature Photon.*, 3:569, 2009.

[92] R. A. McMillan, C. D. Paavola, J. Howard, S. L. Chan, N. J. Zaluzec, and J. D. Trent. "Ordered nanoparticle arrays formed on engineered chaperonin protein templates". *Nature Mater.*, 1:247, 2002.

[93] I. L. Medintz, H. T. Uyeda, E. R. Goldman, and H. Mattoussi. "Quantum dot bioconjugates for imaging, labelling and sensing". *Nature Mater.*, 4:435, 2005.

[94] E. Abbe. "Beitrage zur theorie des mikroskops und der mikroskopischen wahrnehmung". *Arch. Mikr. Anat.*, 9:413, 1873.

[95] J. D. Jackson. *Classical Electrodynamics.* John Wiley & Sons, 1999.

[96] M. Born and E. Wolf. *Principle of Optics, 7th.* Cambridge University Press, 1999.

[97] E. Hecht. *Optics.* Addison-Wesley, 1998.

[98] R. H. Ritchie. "Plasma losses by fast electrons in thin films". *Phys. Rev.*, 106:874, 1957.

[99] H. Raether. *Surface plasmons on smooth and rough surfaces and on gratings.* Springer, 1988.

[100] G. A. Truskey, J. S. Burmeister, E. Grapa, and W. M. Reichert. "Total internal reflection fluorescence microscopy (TIRFM) II. Topographical mapping of relative cell/substratum separation distances". *J. Cell Sci.*, 103:491, 1992.

[101] J. Dominguez-Escobar, A. Chastanet, A. H. Crevenna, V. Fromion, R. Wedlich-Soldner, and R. Carballido-Lopez. "Processive movement of MreB-Associated cell wall biosynthetic complexes in bacteria". *Science*, 333:225, 2011.

[102] S. Blair and Y. Chen. "Resonant-enhanced evanescent-wave fluorescence biosensing with cylindrical optical cavities". *Appl. Opt.*, 40:570, 2001.

[103] X. Wei and S. M. Weiss. "Guided mode biosensor based on grating coupled porous silicon waveguide". *Opt. Exp.*, 19:11330, 2011.

[104] C. Heine and R. H. Morf. "Submicrometer gratings for solar energy applications". *Appl. Opt.*, 34:2476, 1995.

[105] J. W. Goodman. *Introduction to Fourier optics 3rd.* Roberts & company, 2004.

[106] G. Binnig, H. Rohrer, Ch. Gerber, and E. Weibel. "Tunneling through a controllable vacuum gap". *Appl. Phys. Lett.*, 40:178, 1982.

[107] V. A. Markel and T. F. George, editors. *Optics of nanostructured materials.* John Wiley & Sons, Inc., 2001.

[108] P. J. Valle, J. J. Greffet, and R. Carminati. "Optical contrast, topographic contrast and artifacts in illumination-mode scanning near-field optical microscopy". *J. Appl. Phys.*, 86:648, 1999.

[109] J. S. Bouillard, S. Vilain, W. Dickson, and A. V. Zayats. "Hyperspectral imaging with scanning near-field optical microscopy: applications in plasmonics". *Opt. Exp.*, 18:16513, 2010.

[110] L. Aigouy, P. Prieto, A. Vitrey, J. Anguita, A. Cebollada, M. U. Gonzalez, A. Garcia-Martin, J. Labeguerie-Egea, and M. Mortier. "Strong near-field optical localization on an array of gold nanodisks". *J. Appl. Phys.*, 110:044308, 2011.

[111] M. Garcia-Parajo, E. Cambril, and Y. Chen. "Simultaneous scanning tunneling microscope and collection mode scanning near?field optical microscope using gold coated optical fiber probes". *Appl. Phys. Lett.*, 65:1498, 1994.

[112] R. Carminati, A. Madrazo, M. Nieto-Vesperinas, and J. J. Greffet. "Optical content and resolution of near-field optical images: Influence of the operating mode". *J. Appl. Phys.*, 82:501, 1997.

[113] Z. Fang, Q. Peng, W. Song, F. Hao, J. Wang, P. Nordlander, and X. Zhu. "Plasmonic focusing in symmetry broken nanocorrals". *Nano Lett.*, 11:893, 2011.

[114] F. Zenhausern and H. K. Wickramasinghe M. P. OBoyle. "Apertureless near-field optical microscope". *Appl. Phys. Lett.*, 65:1623, 1994.

[115] R. Bachelot, P. Gleyzes, and A. C. Boccara. "Reflection-mode scanning near-field optical microscopy using an apertureless metallic tip". *Appl. Opt.*, 36:2160, 1997.

[116] H. G. Frey, F. Keilmann, A. Kriele, and R. Guckenberger. "Enhancing the resolution of scanning near-field optical microscopy by a metal tip grown on an aperture probe". *Appl. Phys. Lett.*, 81:5030, 2002.

[117] W. E. Kock. "Metallic delay lenses". *Bell Sys. Tech. J.*, 27:58, 1948.

[118] J. C. Bose. "On the rotation of plane of polarisation of electric waves by a twisted structure". *Proc. Roy. Soc.*, 63:146, 1898.

[119] I. V. Lindell, A. H. Sihvola, and J. Kurkijarvi. "Karl F. Lindman: The last Hertzian and a Harbinger of electromagnetic chirality". *IEEE Antennas Propag. Mag.*, 34:24, 1992.

[120] V. G. Veselago. "The electrodynamics of substances with simultaneously negative values of ε and μ". *Sov. Phys. Uspekhi*, 10:509, 1968.

[121] D. R. Smith, W. J. Padilla, D. C. Vier, S. C. Nemat-Nasser, and S. Schultz. "Composite medium with simultaneously negative permeability and permittivity". *Phys. Rev. Lett.*, 84:4184, 2000.

[122] R. A. Shelby, D. R. Smith, and S. Schultz. "Experimental verification of a negative index of refraction". *Science*, 292:77, 2001.

[123] W. H. Escovitz, T. R. Fox, and R. Levi-Setti. "Scanning transmission ion microscope with a field ion source". *Proc. Natl. Acad. Sci. USA*, 72:1826, 1975.

[124] J. Orloff and L. Swanson. "Study of a field-ionization source for microprobe applications". *J. Vac. Sci. Tech.*, 12:1209, 1975.

[125] R. Seliger, J. W. Ward, V. Wang, and R. L. Kubena. "A high-intensity scanning ion probe with submicrometer spot size". *Appl. Phys. Lett.*, 34:310, 1979.

[126] C. R. K. Marrian, E. A. Dobisz, and J. A. Dagata. "Electron?beam lithography with the scanning tunneling microscope". *J. Vac. Sci. Tech.*, 10:2877, 1992.

[127] C. Vieu, F. Carcenac, A. Pepin, Y. Chen, M. Mejias, A. Lebib, L. Manin-Ferlazzo, L. Couraoud, and H. Launois. "Electron beam lithography: resolution limits and applications". *Appl. Surf. Sci.*, 164:111, 2000.

[128] G. M. Whitesides and M. Boncheva. "Beyond molecules: Self-assembly of mesoscopic and macroscopic components". *Proc. Natl. Acad. Sci. USA*, 99:4769, 2002.

[129] J. F. Galisteo, F. Garcia-Santamaria, D. Golmayo, B. H. Juarez, C. Lopez, and E. Palacios. "Self-assembly approach to optical metamaterials". *J. Opt. A: Pure Appl. Opt.*, 7:S244, 2005.

[130] J. H. Lee, Q. Wu, and W. Park. "Metal nanocluster metamaterial fabricated by the colloidal self-assembly". *Opt. Lett.*, 34:443, 2009.

[131] J. Valentine, S. Zhang, T. Zentgra, E. Ulin-Avila, D. A. Genov, G. Bartal, and X. Zhang. "Three-dimensional optical metamaterial with a negative refractive index". *Nature*, 455:376, 2008.

[132] N. Engheta and R. W. Ziolkowski. *Metamaterials: Physics and engineering explorations*. John Wiley & Sons & IEEE Press, 2006.

[133] S. Zouhdi, A. Sihvola, and A. P. Vinogradov. *Metamaterials and plasmonics: fundamentals, modelling, applications*. Springer, 2009.

[134] N. I. Zheludev. "The Road Ahead for Metamaterials". *Science*, 328:582, 2010.

[135] M. L. Povinelli, S. G. Johnson, J. D. Joannopoulos, and J. B. Pendry. "Toward photonic-crystal metamaterials: Creating magnetic emitters in photonic crystals". *Appl. Phys. Lett.*, 82:1069, 2003.

[136] X. Liu, T. Tyler, T. Starr, A. F. Starr, N. M. Jokerst, and W. J. Padilla. "Taming the blackbody with infrared metamaterials as selective thermal emitters". *Physical Review Letters*, 107:045901, 2011.

[137] H. Chen, C. T. Chan, and P. Sheng. "Transformation optics and metamaterials". *Nature Mater.*, 9:387, 2010.

[138] A. Vakil and N. Engheta. "Transformation optics using grapheme". *Science*, 332:1291, 2011.

[139] D. Schurig, J. J. Mock, B. J. Justice, S. A. Cummer, J. B. Pendry, A. F. Starr, and D. R. Smith. "Metamaterial electromagnetic cloak at microwave frequencies". *Science*, 314:977, 2006.

[140] W. Cai, U. K. Chettiar, A. V. Kildishev, and V. M. Shalaev. "Optical cloaking with metamaterials". *Nature Photon.*, 1:224, 2007.

[141] J. Valentine, J. Li, T. Zentgraf, G. Bartal, and X. Zhang. "An optical cloak made of dielectrics". *Nature. Mater.*, 8:568, 2009.

[142] T. Ergin, N. Stenger, P. Brenner, J. B. Pendry, and M. Wegener. "Three-dimensional invisibility cloak at optical wavelengths". *Science*, 328:337, 2010.

[143] P. J. S. G. Ferreira and A. Kempf. "Super-oscillations: Faster than the Nyquist rate". *IEEE Trans. Signal Proces.*, 54:3732, 2006.

[144] A. Kempf. "Black hoes, bandwidths and Beethoven". *J. Math. Phys.*, 41:2360, 2000.

[145] D. A. Yakir Aharonov and L. Vaidman. "How the result of a measurement of a component of the spin of a spin -1/2 particle can turn out to be 100". *Phys. Rev. L*, 60:1351, 1988.

[146] F. M. Huang, Y. Chen, F. J. Garcia de Abajo, and N. I. Zheludev. "Optical super-resolution through super-oscillations". *J. Opt. A, Pure Appl. Opt.*, 9:S285, 2007.

[147] L. Levi. "Fitting a band-lmited signal to given points". *IEEE Trans. Info. Theo.*, 11:372, 1965.

[148] M. S. Calder and A. Kempf. "Analysis of super-oscillatory wave functions". *J. Ma*, 46:012101, 2005.

[149] G. Toraldo Di Francia. "Super-gain antennas and optical resolving power". *Il Nuovo Cimento*, 9:1943, 1952.

[150] Z. S. Hegedus and V. Sarafis. "Superresolving filters in confocally scanned imaging systems". *J. Opt. Soc. Am. A*, 3:1892, 1986.

[151] T. R. M. Sales and G. M. Morris. "Fundamental limits of optical superresolution". *Opt. Lett.*, 22:582, 1997.

[152] E. T. F. Rogers, J. Lindberg, T. Roy, S. Savo, J. E. Chad, M. R. Dennis, and N. I. Zheludev. "A super-oscillatory lens optical microscope for subwavelength imaging". *Nature Mater.*, 2012.

[153] S. A. Schelkunoff. "A mathematical theory of linear arrays". *Bell Sys. Tech. J.*, 22:80, 1943.

[154] C. J. Bouwkamp and N. G. de Bruijn. "The problem of optimum antenna current distribution". *Philips. Res. Rep.*, 1:135, 1946.

[155] F. M. Huang and N. I. Zheludev. "Super-resolution without evanescent waves". *Nano Lett.*, 9:1249, 2009.

[156] D. Slepian and H. O. Pollak. "Prolate spheroidal wave functions, Fourier analysis and uncertainty II". *Bell System Tech. J.*, 40:44, 1961.

[157] F. M. Huang, T. S. Kao, V. A. Fedotov, Y. Chen, and N. I. Zheludev. "Nanohole array as a lens". *Nano Lett.*, 8:2469, 2008.

[158] X. Qu, D. Wu, L. Mets, and N. F. Scherer. “Nano-meter-localized multiple single-molecule fluorescence micriscopy”. *Proc. Natl. Acad. Sci. USA*, 101:11298, 2004.

[159] R. J. Ober, S. Ram, and S. E. Ward. “Localization accuracy in single-molecule mi”. *Biophys, J.*, 86:1185, 2004.

[160] R. Heintzmann and G. Ficz. “Breaking the resolution limit in light micriscopy”. *Brief. Func. Geno. Prote.*, 5:289, 2010.

[161] T. D. Lacoste, X. Michalet, F. Pinaud, D. S. Chemla, A. P. Alivisatos, and S. Weiss. “Ultrahigh-resolution multicolor colocalization of single fluorescence probes”. *Proc. Natl. Acad. Sci. USA*, 97:9461, 2000.

[162] N. L. Mahy, P. E. Perry, and S. Gilchrist. “Spatial organization of active and inactive genes and noncoding DNA within chromosome territories”. *J. Cell Biol.*, 157:579, 2002.

[163] K. Bystricky, P. Heun, and L. Gehlen. “Long-range compaction and flexibility of interphase chromatin in budding yeast analyzed by high-resolution imaging techniques”. *Proc. Natl. Acad. Sci. USA*, 101:16495, 2004.

[164] nd A. D. Schmidt P. J. Keller, A. Santella, K. Khairy, Z. Bao, J. Wittbrodt, and E. H. K. Stelze. “Fast, high-contrast imaging of animal development with scanned light sheet-based structured-illumination microscopy”. *Nature Methods*, 7:637, 2010.

[165] P. Kner, B. B. Chhun, E. R. Griffis, L. Winoto, and M. G. L. Gustafsson. “Super-resolution video microscopy of live cells by structured illumination”. *Nature Methods*, 6:339, 2009.

[166] R. Heintzmann and M. G. L. Gustafsson. “Subdiffraction resolution in continuous samples”. *Nature Photon.*, 3:362, 2009.

[167] K. Strehl. “Aplanatische und fehlerhafte Abbildung im Fernrohr”. *Zeitschrift fr Instrumentenkunde*, 15:362, 1895.

[168] K. Strehl. “ber Luftschlieren und Zonenfehler”. *Zeitschrift fr Instrumentenkunde*, 22:213, 1902.

[169] Y. J. Zhang, H. C. Xiao, and C. W. Zheng. "Diffractive super-resolution elements applied to near-field optical data storage with solid immersion lens". *New J. Phys.*, 6:75, 2004.

[170] Y. Zhang. "Multiple reflection effect inside a hemispherical solid immersion lens". *Opt. Comm.*, 266:94, 2006.

[171] Y. Zhang and X. Ye. "Three-zone phase-only filter increasing the focal depth of optical storage systems with a solid immersion lens". *Appl. Phys. B*, 86:97, 2007.

[172] Q. Wu, F. D. Feke, R. D. Grober, and L. P. Chislain. "Realization of numerical aperture 2.0 using a gallium phosphide solid immersion lens". *Appl. Phys. Lett.*, 75:4064, 1999.

[173] K. Koyama, M. Yoshita, M. Baba, T. Suemoto, and H. Akiyama. "High collection efficiency in fluorescence microscopy with a solid immersion lens". *Appl. Phys. Lett.*, 75:1667, 1999.

[174] T. R. M. Sales and G. M. Morris. "Axial superresolution with phase-only pupil filters". *Opt. Comm.*, 156:227, 1998.

[175] M. A. A. Neil, R. Juskaitis, T. Wilson, and Z. J. Laczik. "Optimized pupil-plane filters for confocal microscope point-spread function engineering". *Opt. Lett.*, 25:245, 2000.

[176] H. Luo and Zhou C. "Comparison of superresolution effects with annular phase and amplitude filters". *Appl. Opt.*, 43:6242, 2004.

[177] H. Ding, Q. Li, and W. Zou. "Design and comparison of amplitude-type and phase-only transverse super-resolving pupil filters". *Opt. Comm.*, 229:117, 2004.

[178] P. N. Gundu, E. Hack, and P. Rastogi. "'Apodized superresolution' - concept and simulations". *Opt. Comm.*, 249:101, 2005.

[179] D. M. de Juana, J. E. Oti, V. F. Canales, and M. P. Cagigal. "Transverse or axial superresolution in a 4Pi confocal microscope by phase-only filters". *J. Opt. Soc. Am. A*, 20:2172, 2003.

[180] R. Mercatelli, S. Soria, G. Molesini, F. Bianco, G. Righini, and F. Quercioli. "Supercontinuum source tuned by an on-axis monochromator for fluorescence lifetime imaging". *Opt. Exp.*, 18:20505, 2010.

[181] X. Tao, B. Fernandez, O. Azucena, M. Fu, D. Garcia, Y. Zuo, D. C. Chen, and J. Kubby. "Adaptive optics confocal microscopy using direct wavefront sensing". *Opt. Lett.*, 36:1062, 2011.

[182] D. A. Rothenfluh, H. Bermudez, C. P. O'neil, and J. A. Hubbell. "Biofunctional polymer nanoparticles for intra-articular targeting and retention in cartilage". *Nature Mater.*, 7:248, 2008.

[183] H. Yoo, I. Song, and D. G. Gweon. "Aberration corrected beam scanning stimulated emission depletion microscopy". *International J. of Optomechatronics*, 2:401, 2008.

[184] T. W. Ebbesen, H. J. Lezec, H. F. Ghaemi, T. Thio, and P. A. Wolff. "Extraordinary optical transmission through sub-wavelength hole arrays". *Nature*, 391:667, 1998.

[185] N. Papasimakis, V. A. Fedotov, A. S. Schwanecke, N. I. Zheludev, and F. J. Garcia de Abajo. "Enhanced microwave transmission through quasicrystal hole arrays". *Appl. Phys. Lett.*, 91:081503, 2007.

[186] V. M. Shalaev, W. Cai, U. K. Chettiar, H.-K. Yuan, A. K. Sarychev, V. P. Drachev, and A. V. Kildishev. "Negative index of refraction in optical metamaterials". *Opt. Lett.*, 30:3356, 2005.

[187] G. Dolling, C. Enkrich, M. Wegener, C. M. Soukoulis, and S. Linden. "Simultaneous negative phase and group velocity of light in a metamaterial". *Science*, 312:892, 2006.

[188] V. A. Fedotov, A. V. Rogacheva, N. I. Zheludev, P. L. Mladyonov, and S. L. Prosvirnin. "Mirror that does not change the phase of reflected wave". *Appl. Phys. Lett.*, 88:091119, 2006.

[189] A. S. Schwanecke, V. A. Fedotov, V. V. Khardikov, S. L. Prosvirnin, Y. Chen, and N. I. Zheludev. "Optical magnetic mirrors". *J. Opt. A, Pure Appl. Opt.*, 9:L1, 2007.

[190] A. S. Schwanecke, V. A. Fedotov, V. V. Khardikov, S. L. Prosvirnin, Y. Chen, and N. I. Zheludev. "Nanostructured metal film with asymmetric optical transmission". *Nano Lett.*, 8:2940, 2008.

[191] V. A. Fedotov, A. S. Schwanecke, N. I. Zheludev, V. V. Khardikov, and S. L. Prosvirnin. "Asymmetric transmission of light and enantiomerically sensitive plasmon resonance in planar chiral nanostructures". *Nano Lett.*, 7:1996, 2007.

[192] B. Hecht, H. Bielefeldt, Y. Inouye, and D. W. Pohl. "Facts and artifacts in near-field optical microscopy". *J. Appl. Phys.*, 81:2492, 1997.

[193] A. Garcia-Etxarri, I. Romero, F. J. Garcia de Abajo, R. Hillenbrand, and J. Aizpurua. "Influence of the tip in near-field imaging of nanoparticle plasmon modes: Weak and strong coupling regimes". *Phys. Rev. B*, 79:125439, 2009.

[194] P. B. Johnson and R.W. Christy. "Optical constants of the noble metals". *Phys. Rev. B*, 6:4370, 1972.

[195] N. Papasimakis, V. A. Fedotov, Y. H. Fu, D. P. Tsai, and N. I. Zheludev. "Coherent and incoherent metamaterials and order-disorder transitions". *Phys. Rev. B*, 80:041102, 2009.

[196] T. Zentgraf, J. Dorfmuller, C. Rockstuhl, C. Etrich, R. Vogelgesang, K. Kern, T. Pertsch, F. Lederer, and H. Giessen. "Amplitude- and phase-resolved optical near fields of split-ring-resonator-based metamaterials". *Opt. Lett.*, 33:848, 2008.

[197] P. D. Lacharmoise, N. G. Tognalli, A. R. Goni, M. I. Alonso, A. Fainstein, R. M. Cole, J. J. Baumberg, J. Garcia de Abajo, and P. N. Bartlett. "Imaging optical near fields at metallic nanoscale voids". *Phys. Rev. B*, 78:125410, 2008.

[198] S. I. Bozhevolnyi, I. I. Smolyaninov, and A. V. Zayats. "Near-field microscopy of surface-plasmon polaritons: Localization and internal interface imaging". *Phys. Rev. B*, 51:17916, 1995.

[199] V. A. Fedotov, P. L. Mladyonov, S. L. Prosvirnin, and N. I. Zheludev. "Planar electromagnetic metamaterial with a fish scale structure". *Phys. Rev. E*, 72:056613, 2005.

[200] S. L. Prosvirnin, S. Tretyakov, and P. L. Mladyonov. "Electromagnetic wave diffraction by planar periodic gratings of wavy metal strips". *J. Electromagn. Waves Appl.*, 16:421, 2002.

[201] S. Savo, N. Papasimakis, and N. I. Zheludev. "Light localization in disordered metamaterials". *Conference paper*, Quantum Electronics and Laser Science Conference (QELS), 2011.

[202] Y. Z. Cheng, H. L. Yang, Y. Nie, R. Z. Gong, and Z. Z. Cheng. "Investigation of negative index properties of planar metamaterials based on split-ring pairs". *Appl. Phys. A*, 103:989, 2011.

[203] V. V. Khardikov, E. O. Iarko, and S. L. Prosvirnin. "Trapping of light by metal arrays". *J. Opt.*, 12:045102, 2010.

[204] E. Plum, K. Tanaka, W. T. Chen, V. A. Fedotov, D. P. Tsai, and N. I. Zheludev. "A combinatorial approach to metamaterials discovery". *J. Opt.*, 13:055102, 2011.

[205] C. Janot. *Quasicrystal, A Primer.* Clarendon Press Oxford, 1992.

[206] E. A. Lord, K. Rrmakrishman, and S. Ranganathan. "An algorithm for generating quasiperiodic patterns and their approximants". *Bull. Mater. Sci.*, 23:119, 2000.

[207] D. Levine and P. J. Steinhardt. "Quasicrystals. I. Definition and structure". *Phys. Rev. B*, 34:596, 1986.

[208] J. E. S. Socolar and P. J. Steinhardt. "Quasicrystals. II. Unit-cell configurations". *Phys. Rev. B*, 34:617, 1986.

[209] "http://en.wikipedia.org/wiki/Penteract".

[210] S. Weber. "Nanotube modeler (version 1.5.0), JCrystalSoft [Online]".

[211] W. D. Montgomery. "Self-imaging objects of infinite aperture". *J. Opt. Soc. Am.*, 57:772, 1967.

[212] I. L. Ho, M. T. Lee, and Y. C. Chang. "Coupled-wave theory for birefringent photonic quasicrystal structures". *J. Opt. Soc. Am. B*, 29:382, 2012.